

# Photogrammetric techniques for characterisation of anisotropic mechanical properties of Ti-6Al-4V



**Matthew R. Arthington**  
Christ Church  
Department of Engineering Science  
University of Oxford

Trinity Term 2010

# Photogrammetric techniques for characterisation of anisotropic mechanical properties of Ti-6Al-4V

Matthew R. Arthington, Christ Church, University of Oxford  
For the degree of D.Phil. in Engineering Science, Trinity Term 2010

## Abstract

The principal aims of this research have been the development of photogrammetric techniques for the measurement of anisotropic deformation in uniaxially loaded cylindrical specimens. This has been achieved through the use of calibrated cameras and the application of edge detection and multiple view geometry. The techniques have been demonstrated at quasi-static strain rates,  $10^{-3} \text{ s}^{-1}$ , using a screw-driven loading device and high strain rates,  $10^3 \text{ s}^{-1}$ , using Split Hopkinson Bars. The materials that have been measured using the technique are nearly-isotropic steel, anisotropic cross-rolled Ti-6Al-4V and anisotropic clock-rolled commercially pure Zr.

These techniques allow the surface shapes of specimens that deform elliptically to be completely tracked and measured *in situ* during loading. This has allowed the measurement of properties that could not have been recorded before, including true direct stress and the ratio of transverse strains in principal material directions, at quasi-static and elevated strain rates, in tension and compression. The techniques have been validated by measuring elliptical prisms of various aspect ratios and independently measuring interrupted specimens using a coordinate measurement machine.

A secondary aim of this research has been to improve the characterisation of the anisotropic mechanical properties of cross-rolled Ti-6Al-4V using the techniques developed. In particular, the uniaxial yield stresses, hardening properties and the associated anisotropic deformation behaviour along the principal material directions, have all been recorded in detail not seen before. Significant findings include: higher yield stresses in-plane than in the through-thickness direction in both tension and compression, and the near transverse-isotropy of the through-thickness direction for loading conditions other than quasi-static tension, where significant anisotropy was observed.

## Acknowledgements

My deepest thanks go to my supervisor Dr Clive Siviour for his objective advice, wisdom and encouragement. Special thanks also go to my other supervisor, Dr Nik Petrinic, for inciting me to embark on this research, working behind the scenes to make it possible and for his eternal enthusiasm. I am also very grateful to Prof. David Hills, without whom this would still be a thesis in progress.

I am forever indebted to my partner, Kate Wilson. Her support and patience have been an invaluable contribution to this research.

Members of the Solid Mechanics group, past and present, have never failed to provide help and friendship when either was required. In particular I owe much to Ben Elliott, who's thoughtful approach to problems has always impressed me. I am also grateful to Euan Wielewski, Helen Sarsfield, Arin Jumpasut, Jens Wiegand and Robert Gerlach for all that they have done for me.

Many members of the Solid Mechanics group have helped me in a variety of ways over the years. I would like to thank the following people for their contribution: Stefan Schwindt, Robert Paynter, Felix Hoffman, Daniel Mulvihill, Daniel Drodge, Pete Hardy, Graham Hillsdon, Stuart Carter, Dick Froud, Richard Duffin, Phil Webb, Yunxin Gao, Peifeng Li, Amanda Bradbury, Petros Siegkas, Guy Edwards and Jon Gregory.

This research has been financially supported by the Engineering and Physical Sciences Research Council (EPSRC) and Rolls Royce plc. Without the EPSRC equipment loan pool the experimental work would not have been possible and my thanks go to Adrian Walker for his assistance. I am also grateful to the members of Christ Church and New College for entrusting me to teach the next generation of engineers and affording me the means to finish this research.

I would also like to thank my mother Christine, grandmother Gladys, uncle Trevor and sister Catherine for their unfailing support in whatever I have chosen to do. I dedicate this thesis to my father, who never got to know who I would become, but inspired me to perpetually strive to ask questions and learn about the world.

# Contents

---

<b>Abstract</b>	<b>i</b>
<b>Acknowledgements</b>	<b>ii</b>
<b>Contents</b>	<b>iii</b>
<b>List of Figures</b>	<b>v</b>
<b>Nomenclature</b>	<b>xiii</b>
<b>1 Introduction and literature review</b>	<b>1</b>
1.1 Statement of research . . . . .	1
1.2 Titanium alloys . . . . .	2
1.3 Titanium . . . . .	4
1.4 Deformation behaviour of transversely isotropic materials . . . . .	9
1.5 Characterisation of Ti-6Al-4V . . . . .	16
1.6 Uniaxial characterisation . . . . .	17
1.7 Extracting material properties from experimental data . . . . .	26
1.8 Layout of this thesis . . . . .	26
<b>2 Edge Detection and Image Calibration</b>	<b>29</b>
2.1 Edge detection . . . . .	30
2.2 Image calibration: sources of error . . . . .	37
2.3 Conclusions . . . . .	41
<b>3 Use of Photogrammetry to Infer Evolving Cross-Section of a Uniaxial Test</b>	<b>43</b>
3.1 Introduction . . . . .	43
3.2 Method . . . . .	46
3.3 Estimation of error . . . . .	59
3.4 Evaluating the Telecentric Assumption . . . . .	73
3.5 Mechanically loaded specimen reconstruction . . . . .	75
3.6 Conclusions . . . . .	76

---

<b>4</b>	<b>Surface Roughness Tracking</b>	<b>83</b>
4.1	Introduction and prior work . . . . .	84
4.2	Method . . . . .	85
4.3	Discussion . . . . .	99
4.4	Conclusion . . . . .	103
<b>5</b>	<b>Measurements of Cross-Sections in Specimens of CP-Zr and Steel</b>	<b>105</b>
5.1	Quantifying the ellipticity in interrupted steel and CP-Zr tensile specimens . . .	107
5.2	Comparison of elliptical cross-section measurement technique . . . . .	109
5.3	Ellipse orientation measurement . . . . .	113
5.4	QS and HR tensile results for CP-Zr and steel . . . . .	114
5.5	Taylor impact tests on Zirconium . . . . .	125
5.6	Conclusions . . . . .	130
<b>6</b>	<b>Experimental Results</b>	<b>134</b>
6.1	Results . . . . .	136
6.2	Comparisons of all strain rates and material directions . . . . .	159
6.3	Initial yield surface estimation . . . . .	161
<b>7</b>	<b>Discussion, Improvements and Future Research</b>	<b>171</b>
7.1	Comparison of standard measurements with elliptical cross-section measurement	171
7.2	Measurements of material response . . . . .	172
7.3	Further research . . . . .	175
<b>8</b>	<b>Conclusions</b>	<b>184</b>
8.1	Conclusion . . . . .	184
	<b>References</b>	<b>191</b>

# List of Figures

---

1.1	The phase diagram of Ti-6Al-4V from Donachie [1]. The formation of the $\alpha$ phase from prior $\beta$ grains is described. . . . .	4
1.2	EBSD image that qualitatively shows banding of similarly orientated $\alpha$ grains in CR-Ti-6Al-4V, [2]. Colours represent orientation. . . . .	7
1.3	The principal material directions. . . . .	8
1.4	The von Mises yield surface in principal stress space. The surface is truncated at finite hydrostatic pressures for clarity. The intersection of principal planes and the cylinder can be seen to produce ellipses. The view is from a position in negative $\sigma_2$ and positive $\sigma_1$ and $\sigma_3$ . The strain increments are shown in red. . . . .	10
1.5	A diagrammatic representation of the von Mises yield function shown in figure 1.4. The directions of the strain increments at the uniaxial yield stress states are shown for two views of the von Mises yield function. N.B. the direction of the strain increment for the $\sigma_2$ uniaxial-yield-stress state, which bisects the other two axes. . . . .	11
1.6	A diagrammatic representation of a transversely isotropic Hill yield function. The directions of the strain increments at the uniaxial yield stress states are shown for two views of the yield function. N.B. the direction of the strain increment for the 2 uniaxial yield stress state has rotated to be more in the direction of 3 than in figure 1.5b. . . . .	12
1.7	A diagrammatic representation of a transversely isotropic, kinematically hardened, von Mises yield function. The directions of the strain increments at the uniaxial tensile yield stress states are shown for two views of the yield function. N.B. the direction of the strain increment for the 2 uniaxial yield stress state has rotated to be <i>further from</i> the direction of 3 than in figure 1.5b. . . . .	13
1.8	A typical cylindrical dog-bone tensile specimen showing the dimensions used at all strain rates in this research. . . . .	18
1.9	A silhouette photo of an initially cylindrical specimen from steel bar that has necked during QS loading. . . . .	19
1.10	Diagram of the quasi-static loading device with the laser extensometer recording the positions of painted stripes. . . . .	23
1.11	The Split Hopkinson bar apparatus for high strain rate loading of tensile specimens, from Elliott [3]. . . . .	25
2.1	An example image from a HR tensile experiment. . . . .	30
2.2	Part 1 of 2: The edge detection procedure applied to the left hand edge of a typical QS specimen photo. The correlation surface was produced by normalised cross-correlation with a 1 by 22 binary template. . . . .	35

2.3	Part 2 of 2: The edge detection procedure applied to the left hand edge of a typical QS specimen photo. The thresholded NCCI is shown as is the NCCI image filtered by group dimension ranking. An example of a parabola fitting is shown that identifies the sub-pixel edge location for its row. . . . .	36
2.4	An expanded view of a specimen's edge. The 3mm gauge diameter of the specimen shown spans approximately 450 pixels and the expanded region is 6 pixels wide by 178 pixels high. The edge positions have been smoothed by a four-pixel averaging filter. . . . .	37
2.5	Fibre shearing in SIMX16 images. The red channel is a cropped region of the 4th frame of 16 and the green and blue channels are the same region of the 5th frame. Note that the central column of squares has a shear line running vertically, as indicated by the yellow arrows. . . . .	39
2.6	A HR tensile specimen during loading. The red box shows a region, inset, around a sheared section of the image that shows a sharp change in surface position that was not present in reality. . . . .	40
2.7	A calibration grid used to calibrate the cameras. Before and after rectification. . . . .	41
3.1	The overview of the elliptical cross-section reconstruction technique. Three cameras photograph the specimen from different angles. From these photographs, the shape of the specimen may be calculated. At the centre and inset are the reconstructed specimen, shaded with direct true stress/MPa. . . . .	47
3.2	The arrangement of the apparatus for multiple cameras as used in the QS experiments. The angular spacing of $45^\circ$ between the cameras is a limitation of the equipment and is shown later to be sub-optimal for elliptical fitting. . . . .	48
3.3	Schematic diagram and photo of the arrangement of the apparatus for single cameras as used in HR experiments here. Three views spaced at $120^\circ$ give well conditioned data for ellipse fitting. . . . .	49
3.4	The first image shows a composite photo of the specimen seen from the three different cameras, where the red channel is the left image, the green channel the centre image and the blue channel the right image. The second picture has the same colour mapping, and is a composite photo of the images after the radial distortion has been removed and they have been extrinsically aligned. Note that the second image has negligible coloured fringing around the gauge section and shoulders, demonstrating the accuracy of the alignment. . . . .	51
3.5	The images and the edges of the QS specimen calculated from them. . . . .	52
3.6	The images of the HR specimen, and the edges calculated from them. . . . .	53
3.7	The tangent lines for a single cross-section of the specimen in the QS configuration. In this diagram the lines are shown as if they were from a pinhole camera, in that they are not parallel, as they would be from a telecentric lens. . . . .	54
3.8	An exact fit of an ellipse to six tangent lines, and a least squares fit to lines after they have been perturbed slightly. The left and right plots show a closer view of the regions bounded by dashed (— · —) boxes in the central plot. . . . .	59
3.9	Photos of the calibration prisms used to validate the technique. . . . .	60
3.10	The calibration prisms with their differences from perfect ellipses. Error spikes are plotted at 20 times the size of the error they represent, for clarity. The mean difference displayed is the mean of the magnitude of the differences. All plots have the same scale. . . . .	62
3.11	The rotational stage, mounting device and a calibration prism are shown in plan view at the centre of this photo of the QS experimental configuration. . . . .	63

3.12	The error in the measurements of the calibration prisms, prisms 1 to 9. The prisms were rotated to an orientation, $\varphi$ , as defined in figure 3.16. The frequency distributions of the errors found in aspect ratio and area for each of the orientations along the length of the prisms are plotted. . . . .	65
3.13	The error in each prism fitting, prisms 10 to 13. These plots complete the set begun in figure 3.12. . . . .	66
3.14	The error in the measurements of the calibration prisms, prisms 1 to 9 recorded under HR conditions. 16 frames were captured by the SIMX16 camera and each of these plots shows the error distributions for each of these frames. As in figures 3.12 and 3.13 the grey distributions are of aspect ratio error and the black distributions are of area error. . . . .	67
3.15	The error in each prism fitting, prisms 10 to 13. These plots complete the set begun in figure 3.14. Although these plots have a smaller vertical scale. . . . .	68
3.16	The simulated experimental variables. . . . .	70
3.17	Simulated reconstruction of ellipses for cameras angularly spaced at $45^\circ$ . . . . .	71
3.18	Simulated reconstruction of ellipses for cameras angularly spaced at $60^\circ$ . The scale has been altered from figure 3.17 for clarity. . . . .	71
3.19	An ellipse with $e = 3$ has been simulated in the $45^\circ$ and $60^\circ$ camera arrangements for a range of orientations, $\phi$ . The trends in the error bars demonstrate that the most accurate determination of elliptical shape is when cameras are pointed along the directions of the ellipse's major and minor axes. It can be seen that the $45^\circ$ cameras have particularly large errors at $\phi = 90^\circ$ , because the data are poorly conditioned, as demonstrated in figure 3.20. These simulations were run with a factor of 10 lower variance than for figures 3.17 and 3.18 to allow for an easier comparison between the angles of $\phi$ . Other orientations outside these ranges of $\phi$ are symmetric and need not be shown here. . . . .	72
3.20	A simulation of an ellipse that gives rise to poorly conditioned data because the camera orientations and the ellipse's orientation cause the points of tangency to group around the extremities. Thus, the value of $a$ is well conditioned, whilst the value of $b$ is likely to be inaccurate. . . . .	73
3.21	A circular cross-section as seen by one pinhole camera and the true tangential rays through the image edge positions. When the image plane is assumed to lie at the specimen centre and the back-projected rays are assumed to be telecentric, the cross-sectional reconstructed shape is larger than the original. As the camera centre is moved away from the specimen, the error due to the telecentric assumption decreases. . . . .	74
3.22	Plots of the percentage error predicted when assuming parallel (telecentric) light rays for an orientation, $\phi = 90^\circ$ . The positive plots are the error in the area measurement, which is over-predicted for all aspect ratios. The negative plots are for the same simulated fits, but they show the error in the aspect ratio measurement, which is under-predicted for all aspect ratios but circular. . . . .	75
3.23	Quasi-static tension specimen at the last recorded time step before fracture. . .	77
3.24	High strain rate tension specimen, at the last recorded time step before fracture.	78
3.25	A specimen of cross-rolled Ti-6Al-4V cut with its axis lying in the plane of rolling. The plots show true direct stress with axial position for several time steps.	79
3.26	High strain rate direct true stress results for all time steps. . . . .	79
3.27	Quasi static maximum true direct stress with time. The inset plot shows the shape of the minimum area cross section at a few selected time steps. . . . .	80

3.28	High strain rate true direct stress with time. The inset plot shows the shape of the minimum area cross section at all recorded time steps. Image acquisition was deliberately started after the start of loading so that the limited available frames could be concentrated on plastic deformation. . . . .	81
3.29	QS data showing $r_a/r_b - 1$ with axial position and time. . . . .	81
3.30	High strain rate data showing $r_a/r_b - 1$ with axial position and time. . . . .	82
4.1	(a) Surface height of a specimen showing the pseudo-random undulations of surface roughness running axially due to the manufacturing process. The horizon of the surface is shown in (b), and the tangential positions of the horizon are shown as a line in (a). It is observed that the circumferential locations of the horizon vary significantly with axial position. . . . .	85
4.2	(a) A typical tensile specimen of gauge length 8 mm and gauge diameter 3 mm, its size was specified so that it could be used in both quasi-static and high strain rate ( $> 10^3 \text{ s}^{-1}$ ) experiments. (b) An image of this specimen <i>in situ</i> where the gauge length spans $\sim 1250$ pixels. . . . .	87
4.3	The original detected left-hand edge of the specimen ( $\dots\dots$ ) with the low-pass filtered edge and the high-pass filtered edge shown at offset positions for clarity. The large ‘bucket’ shaped bump is the outline of the paint marker required for the laser extensometer. The width of a pixel in the image, $6.5 \mu\text{m}$ , is also shown. . . . .	88
4.4	The edge data from within the parallel gauge section of the specimen. The data have been passed through a high-pass Butterworth filter to remove all frequencies below 7 periods per mm. The peak at 16.25 periods per mm is the frequency of the turning during manufacture. . . . .	89
4.5	The original, discrete, edge positions determined by cross-correlation and the continuous spline interpolating fit. The surface features used to track the material are the zero-crossings. . . . .	90
4.6	(a) ‘Raw’ feature tracks showing the motion of corresponding features plotted as a function of time in the camera frame of reference. The parallel gauge length of the specimen is between 2 mm and 9 mm. A 9 s by 1.5 mm sub-region is shown as a box surrounding a group of features. The lines either side of the box indicate the modal average displacement direction. (b) The histogram of displacement within the box in (a). The threshold displacement values are shown by dashed lines; the mean of the displacements between these values is taken as the sub-region’s modal average displacement. . . . .	91
4.7	(a) The displacement of overlapping sub-regions, 9 s by 1.5 mm, across the range of time and axial position in the camera frame of reference. The shading represents average displacement at that location between two subsequent frames. (b) A finer determination of displacement with non-overlapping sub-regions of 3 s by 1 mm (3 s was the inter-frame time). The time and vertical positions of the displacement are irregularly spaced because they are plotted at the mean location of the features found to be in that sub-region, and not the nominal location of the sub-region. . . . .	92
4.8	The position of specimen edge curve features that could be tracked throughout the experiment are plotted. At the left and right sides side of the tracks are photos of the specimen at the start and the end of the experiment; the negative of their images has been shown for clarity. Along the edges of the specimens, crosses indicate the initial and final locations of the tracked positions. The dashed lines show the laser extensometer tracked positions throughout the experiment. . . . .	94

4.9	The displacement of roughness tracks measured close to initial axial positions of 8.7 mm and 2.2 mm in the gauge section, shown in figure 4.8, are subtracted from the displacement of laser extensometer measured tracks at these locations. Due to the initial separation of laser-tracked and roughness-tracked positions the increasing strain in the specimen tends to increase the error. . . . .	95
4.10	The tracks of material positions from the finely determined displacement data of figure 4.7(b). . . . .	97
4.11	(a) Engineering strain, $\epsilon_s(x, t)$ , calculated using the displacement of the tracked surface roughness. (b) Engineering strain, $\epsilon_a(x, t)$ , calculated using the cross-sectional areas as a function of initial position and time. . . . .	99
4.12	Contours of strain as functions of axial position and time. The shaded contours represent the areal strain and the lines represent roughness tracking strain with different levels of smoothing. (a) Modal averaging taken over 1 mm of length and consecutive frames only. (b) Coarser modal averaging taken over 1.5 mm of length and 3 periods spanning 4 frames. (c) The data in (a) with spline smoothing applied. (d) The data in (b) with spline smoothing applied. Note that the roughness tracking strain data in (b) and (d) do not cover the entire duration of the experiment because of the broad filtering. . . . .	100
5.1	The interrupted QS tensile specimens of Zr and steel in the relaxed state from the left camera view. The yellow dashed line is at the 0 mm axial height. The other dashed lines indicate the gauge positions of data in figures 5.2 and 5.3. . .	109
5.2	The ellipse fits to CMM data at three positions along the axis of the interrupted specimen tests are plotted as solid ellipses. The CMM measurements around the perimeter of the gauge section are plotted as dots. Error spikes are plotted through the CMM measurements, starting at the closest position on the ellipse, at 20 times the the distance between the ellipse and the measurement. . . . .	110
5.3	The mean of the magnitude of the distance from the points measured by the CMM to the nearest elliptical fit as a function of axial position. . . . .	110
5.4	The areas $r_a r_b \pi$ measured in the interrupted CP-Zr and steel specimens. The data were obtained from ellipses fitted to CMM data, by the reconstruction technique and by the optical comparator. . . . .	111
5.5	The percentage difference in area, $100(A - A_D)/A_D$ (where D are either the CMM data or the OC data), between elliptical fits to CMM data or OC measurements and cross-section reconstructions of interrupted specimens during QS tensile loading. The circles indicate values at axial positions that approximately coincided for reconstruction data and CMM or OC data. . . . .	112
5.6	The aspect ratios $r_a/r_b$ (where $r_a > r_b$ always) measured in the interrupted CP-Zr and steel specimens. The data were obtained from ellipses fitted to CMM data, by the reconstruction technique and by the optical comparator. . . . .	113
5.7	The % difference in aspect ratio, $100((r_a/r_b) - (r_a/r_b)_D)/(r_a/r_b)_D$ (where D are either the CMM data or the OC data), between elliptical fits to CMM data or OC measurements and cross-section reconstructions of interrupted specimens during QS tensile loading. The circles indicate values at axial positions that approximately coincided for reconstruction data and CMM or OC data. . . . .	114
5.8	Mean distances from CMM data to cross-section reconstructions of interrupted specimens during QS tensile loading. . . . .	115
5.9	The orientation with respect to axial position in the interrupted CP-Zr specimen. Each plot has been shifted to have a mean of zero. . . . .	115

5.10	The original SHB analysis stress-strain curve, the DIC generated curve and the corrected SHB curve are shown for the HR CP-Zr specimen. . . . .	116
5.11	The nominal stress-strain history during tensile loading of the two materials. . .	117
5.12	For steel and CP-Zr the maximum mean true direct stresses are plotted with strain calculated by $\varepsilon = \ln(A_0/A_{min})$ where $A_{min}$ is the minimum cross-sectional area. The minimum semi-major and semi-minor radii of the specimens are shown against areal strain too. Also plotted is the R ratio of true strains calculated using $r_a$ and $r_b$ at the minimum cross-sectional area plotted with the same strain. The R ratio could not be calculated reliably for small strains. The UTS positions are indicated with crosses. . . . .	121
5.13	The shapes of the cross-section at the position of maximum strain (minimum area) throughout the deformation of the specimens. For the HR specimens all frames are shown, whereas for the QS specimens every 10th frame is shown as well as the first and last frame. The major axis direction ( $r_a$ ) is drawn with a heavier line than the minor axis direction ( $r_b$ ). . . . .	122
5.14	The maximum $r_a$ and minimum $r_b$ radii as functions of axial position from the lower shoulder corner for the four QS and HR CP-Zr and steel specimens. Filtering was applied to the HR specimens' edges before the reconstruction to remove high frequency data. The radii are coloured red to blue with respect to the frame number, red being the first frame and blue the last frame before fracture.	123
5.15	The results from figures 5.14e and 5.14g without filtering applied to the edges before the cross-section reconstruction. . . . .	124
5.16	The configuration of the Taylor impact of CP-Zr experiments. . . . .	126
5.17	Images from a Taylor impact experiment carried out on heavily textured high-purity zirconium plate, taken with a SIM-8 ultra-high-speed camera and showing the three views obtained using the two mirrors. . . . .	126
5.18	Three-dimensional surface geometry reconstruction showing the true cross-sectional area strain as a function of time and the axial position, [4]. . . . .	127
5.19	Semimajor and semiminor axes of the deforming cross-sectional shape as functions of time and the axial position, [4]. . . . .	128
5.20	(a) Final post-deformation image frame and (b) comparison of the semimajor and semiminor axes of cross-sectional shape from the recovered specimen using data from both a CMM and the optical measurement technique, taking the final post-deformation image frame as the reference. . . . .	129
5.21	The initial and final state of a rod that has been tested using the Taylor impact experiment. . . . .	129
5.22	The cross-sectional area of the Taylor Impact specimen against distance from the anvil at each frame captured during the experiment. . . . .	130
5.23	The salient lengths of the Taylor Impact specimen measured from the reconstruction of its cross-section. . . . .	131
5.24	The flow stress against time during the Taylor Impact test. . . . .	131
6.1	The principal material directions in the cross-rolled Ti-6Al-4V plate. . . . .	135
6.2	The nominal stress-strain results for the QS tensile specimens in all material directions. The strain was calculated by DIC of the specimen shoulders in the QS photographs. . . . .	136
6.3	Mean direct true stress plotted against minimum area strain. . . . .	137
6.4	The semi-minor and semi-major axes lengths at the minimum cross-section against areal strain. . . . .	138

6.5	The R-ratio at the minimum cross-sectional area as a function of areal strain at the minimum area. . . . .	139
6.6	These figures show the shape of the most strained region in the QS tension specimens in 10 frames, evenly spaced in time, during the experiment. . . . .	140
6.7	These photos show the fracture surface of the QS D1 tensile specimen where the vertical direction is in the plane of the CR-plate and the horizontal direction is through thickness, D3. Note that the fracture surface has formed a plane that contains the in-plane direction. . . . .	141
6.8	These photos show the fracture surface of the QS D2 tensile specimen. Note that the fracture surface has formed a plane that contains the in-plane direction. . . . .	142
6.9	These photos show the fracture surface of the QS D3 tensile specimen. The fracture plane is more pitted and much less flat than the D1 or D2 specimens and it has formed in a direction that nearly contains the 1 direction. . . . .	143
6.10	The true stress-strain in the QS compression specimens for all directions. The strain was calculated by DIC of the region where the anvils and specimen meet in the photographs, assuming a parallel gauge section throughout the loading. . . . .	144
6.11	Mean direct true stress at the minimum cross-sectional area plotted against minimum area strain and mean direct true stress at the maximum cross-sectional area plotted against maximum area strain in the QS compression specimens. . . . .	145
6.12	The semi-minor and semi-major axes lengths at the maximum cross-section against areal strain at the maximum area in the QS compression specimens. . . . .	146
6.13	The $R^{-1}$ at the maximum cross-sectional area as a function of areal strain at the maximum area in the QS compression specimens. . . . .	146
6.14	The magnitude of the QS compression true stress-strain behaviour as calculated by DIC of the anvil displacement and by the change in maximum area cross-section. Also plotted are the QS tension results. Note that the elastic stiffnesses all agree very well when strain is measured by change in cross-sectional area. . . . .	147
6.15	These figures show the shape of the most strained region in the QS compression specimens in 10 frames, evenly spaced in time, during the experiment. . . . .	148
6.16	Nominal stress strain results of the HR tensile specimens calculated by SHB analysis with scaling and shifting applied to make the strain match that obtained from DIC of the high speed photographs. . . . .	149
6.17	Mean direct true stress at the minimum cross-sectional area plotted against minimum area strain and mean direct true stress at the maximum cross-sectional area plotted against maximum area strain in the HR tension specimens. . . . .	150
6.18	The semi-minor and semi-major axes lengths at the minimum cross-section against areal strain at the minimum area in the HR tension specimens. . . . .	151
6.19	The R ratio at the minimum cross-sectional area as a function of areal strain at the minimum area in the HR tension specimens. . . . .	151
6.20	These figures show the shape of the most strained region in the HR tension specimens in all frames during the experiment. . . . .	152
6.21	These photos show the fracture surface of the HR D1 tensile specimen. Note that the fracture surface has formed a plane that contains the in-plane direction and has a step in the middle. . . . .	153
6.22	These photos show the fracture surface of the HR D2 tensile specimen. Note that the fracture surface has formed a plane that contains the in-plane direction and has a step in the middle. . . . .	154

6.23	These photos show the fracture surface of the HR D3 tensile specimen. The fracture plane is more pitted and much less flat than the D1 or D2 specimens and it can't be said to have formed in any particular direction. . . . .	155
6.24	The true stress-strain results from the three material directions in HR compression, obtained directly from SHB analysis. . . . .	156
6.25	Mean direct true stress at the minimum cross-sectional area plotted against minimum area strain and mean direct true stress at the maximum cross-sectional area plotted against maximum area strain in the HR compression specimens. . .	157
6.26	The semi-minor and semi-major axes lengths at the maximum cross-section against areal strain at the maximum area in the HR compression specimens. . .	158
6.27	The $R^{-1}$ at the maximum cross-sectional area as a function of areal strain at the maximum area in the HR compression specimens. . . . .	158
6.28	These figures show the shape of the most strained region in the HR compression specimens in all frames recorded during the experiment. . . . .	159
6.29	The true stress-strain paths for uniaxially loaded specimens of all three material directions at QS and HR strain rates in both compression and tension are plotted here. The magnitude of the stress and the strain for the compression results is shown for comparison with the tensile data. . . . .	160
6.30	The R ratios for tension and the $R^{-1}$ ratios for compression are plotted for all of the Ti-6Al-4V specimens. . . . .	161
6.31	These figures show the magnitudes of true stress and true strain for the three material directions on separate graphs for comparison of material behaviour at different strain rates. . . . .	162
6.32	These figures show the R (and inverted R) ratios for the three material directions on separate graphs for comparison of material behaviour at different strain rates.	163
6.33	A view of the deviatoric plane in principal stress space showing the uniaxial yield stress states and the plastic strain increment directions for CR-Ti-6Al-4V loaded quasi-statically at 9 % strain. The data are plotted in red and the mean fit von Mises yield surface is shown in blue. . . . .	164
6.34	The same view as in figure 6.33 showing the uniaxial yield stress states in red and the elliptical fit to them, representing a kinematically hardened Hill yield surface, shown in green. . . . .	166
6.35	The same view as in figure 6.33 showing the uniaxial yield stress states and the plastic strain increments in red. Also shown are the tangent lines (dashed) to the yield surface derived from the normal direction to the strain increments and passing through the uniaxial yield stress states. The best fit to these tangents is shown in blue. . . . .	167
6.36	The same view as in figure 6.33 showing the uniaxial yield stress states, the plastic strain increments and the tangent lines. The best-fit von Mises surface is shown in black, the best fit kinematically hardened Hill surface to the yield points is shown in green and the best fit to the tangent lines is shown in blue. . .	168
6.37	A deviatoric plane view of a hypothetical material with the same uniaxial yield stress states as the CR-Ti-6Al-4V here, but with inverted R ratios. The strain increments and yield surface tangents are shown in blue, as is the best fit to the tangents. The best fit to the yield points is shown in green and the von Mises surface fitting these points is shown in black. . . . .	169
7.1	An example of a higher order function than a conic section, $f = x^4 + y^4 - 1 = 0$ . It may be possible to measure this shape by a least squares method using an adaptation of the cross-section measurement technique. . . . .	178
7.2	A suggested improvement to the mirror configuration that provides equal path lengths to the specimen in all three views. . . . .	180

# Nomenclature

---

$\alpha$	The hexagonal close packed phase of titanium
$\beta$	The body centred cubic phase of titanium
$R_\theta$	Ratio of transverse strains in flat specimens, $\epsilon_w^p / \epsilon_t^p$
$r_a$	The length of the semi-major axis of an ellipse
$r_a$	The length of the semi-minor axis of an ellipse
$r_d$	Ratio of transverse strain rates, $D_w / D_t$
BCC	Body centred cubic crystal structure
CCD	Charge-Coupled Device
CMM	Coordinate Measurement Machine
CNC	Computer Numerically Controlled
CR	Cross-rolled
D1	The direction of the longest, in-plane, dimension of the cross-rolled Ti-6Al-4V plate
D2	The direction of the shortest, in-plane, dimension of the cross-rolled Ti-6Al-4V plate
D3	The through-thickness direction of the cross-rolled Ti-6Al-4V plate
DIC	Digital image correlation
FE	Finite element
HCP	Hexagonal close packed crystal structure
HR	High strain rate
NCCI	Normalised cross-correlation image
Optical comparator	OC
q	Negative ratio of width strain rate to axial strain rate, $-D_w / D_l$
QS	Quasi-static
R	The ratio of true strains in the major axis and the minor axis directions of an elliptical cross-section: $R = \ln(r_a/r_0) / \ln(r_b/r_0)$

SHPB	Split Hopkinson Pressure Bar
Ti	Titanium
TMP	Thermomechanical processing
UTS	Ultimate tensile strength
Ti-6Al-4V	Titanium - 6 wt% aluminium - 4 wt% vanadium by weight
CP-Zr	Commercially pure zirconium

# Introduction and literature review

---

## 1.1 Statement of research

The principal aims of this research have been the development of photogrammetric techniques for the measurement of anisotropic deformation in uniaxially loaded cylindrical specimens. Materials, such as cross-rolled titanium - 6% aluminium - 4% vanadium (Ti-6Al-4V) and clock-rolled commercially pure zirconium (CP-Zr), can be macroscopically homogeneous but exhibit anisotropy in mechanical properties such as Young's modulus and yield stress. The cross-sections of cylindrical specimens made from such materials will deform elliptically with applied loading [5–8]. The ability to measure this deformation was sought for a range of strain rates, from  $\dot{\epsilon} = 10^{-3} \text{ s}^{-1}$  to  $\dot{\epsilon} = 10^3 \text{ s}^{-1}$ , so that data that has not previously been measured in such detail would be available for developing and/or validating constitutive models.

Extensive validation of the new technique was performed using experimental and simulated measurements. It was then applied to cross-rolled Ti-6Al-4V specimens cut from plates to obtain new experimental data on its anisotropic mechanical behaviour at low and high strain rates in the three principal material directions. The method was also applied to specimens of clock-rolled CP-Zr plate and steel bar to measure the behaviour of materials that exhibited more

and less anisotropy than Ti-6Al-4V. Interrupted specimens of CP-Zr and steel were also measured using a coordinate measurement machine (CMM) to provide estimates of the accuracy of the new photogrammetric technique.

In addition to the technique for measuring the elliptical shape of specimen cross-sections as a function of axial position during loading, a technique has been developed to track the displacement of features in the surface roughness of a specimen. This technique allows the high spatial resolution measurement of specimen deformation without marking, and complements the cross-section measurement technique. In combination, these two methods record the complete surface shape of a deforming specimen during loading.

By measuring the dimensions of the evolving elliptical cross-sections in these specimens, these methods provide valuable data to help determine the form of the anisotropic yield function that models the constitutive behaviour of materials. Alternatively, these data provide a rich source of validation data or data for the calibration of numerical constitutive models at low and high strain rates.

The next three sections introduce the mechanical properties of Ti-6Al-4V investigated here, the nature of the yield behaviour of alloys like this, and experimental techniques for measuring parameters that govern this behaviour in material models.

## 1.2 Titanium alloys

Titanium (Ti) alloys are widely used in aerospace and bioengineering applications because of their high specific strength and resistance to corrosion [9]. The growth of the aerospace industry indicates [10] that improvement of complex engineering systems, such as aero engines, is set to continue, and consequently a deeper understanding of the requirements that govern their design will be required. Modern aero engines are composed of approximately 40% Ti alloy by volume,

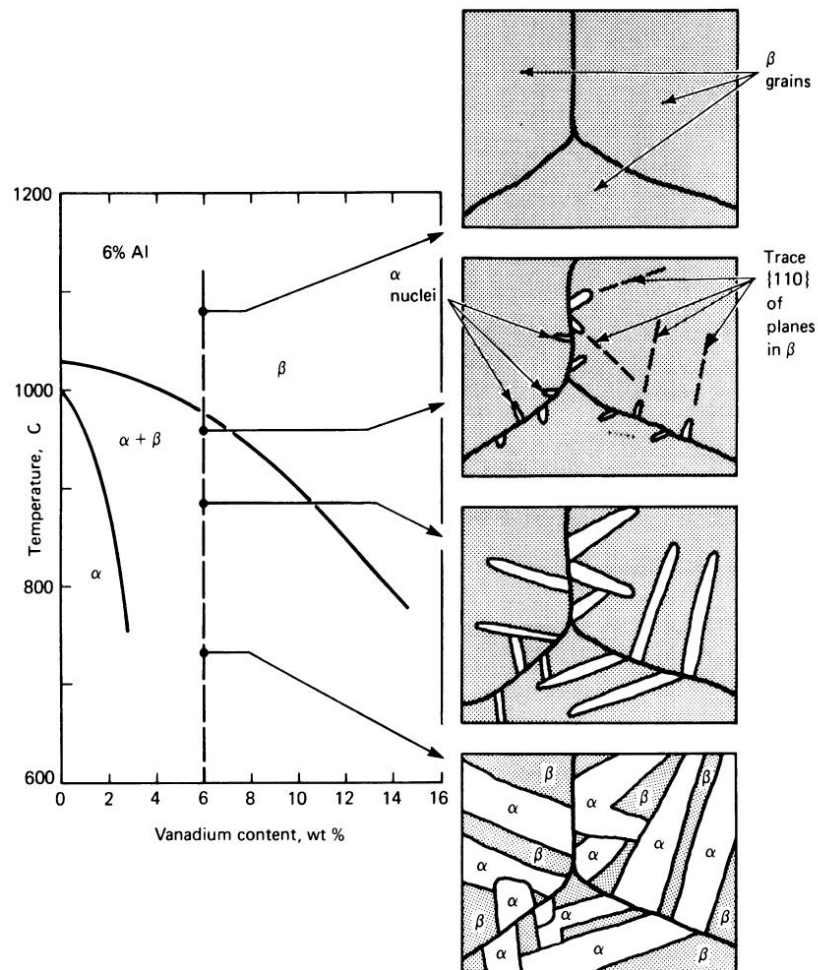
[11], or 36% by weight, [12]. Ti-6Al-4V, in particular, is one of the most extensively used Ti alloys due to favourable properties including weldability, ductility, toughness and forgeability.

Manufacturing Ti-6Al-4V is relatively costly compared to more widely used alloys such as steel and aluminium [9]. Moreover, in aerospace applications, the weight of components significantly affects the fuel efficiency of vehicles. These are the two main reasons why manufacturers strive to reduce the mass of Ti-6Al-4V required to meet the design criteria of their devices. In order to achieve optimum use of material, designers use numerical simulations and experimental prototypes to evaluate revisions that use less material but still meet the design criteria.

When considering the use of Ti-6Al-4V in aero engines, engineers must analyse the complex loading situations and interactions between objects that may take place under extreme events such as bird strikes, where a bird is ingested into the engine. Predictive techniques, such as finite element (FE) analyses, have greatly improved in their ability to model material behaviour over the past two decades and have provided tools with which to model new designs, predict their success or failure and make iterative improvements, without having to perform expensive real world tests.

There are still improvements to be made in the accuracy of FE simulations, which are limited in their ability to predict the behaviour of real components for several reasons. First, approximations are made because of the cost of simulating physical mechanisms that work at scales too computationally expensive to simulate in large components; second, the stochastic nature of the microstructure; third, loading conditions, geometry and the exact boundary conditions in a particular situation cannot be exactly known; and finally, the constitutive behaviour of the materials being simulated has to be well characterised, understood and modelled. It is this last limitation at which this research is aimed at helping to overcome, by improving characterisation techniques for anisotropic, rate-dependent, materials.

## 1.3 Titanium



Microstructures achieved at various intermediate temperatures by slowly cooling from above the  $\beta$  transus. Final microstructure consists of plates of  $\alpha$  (white) separated by the  $\beta$  phase (dark).

**Figure 1.1:** The phase diagram of Ti-6Al-4V from Donachie [1]. The formation of the  $\alpha$  phase from prior  $\beta$  grains is described.

Solid titanium exists as one of two allotropes: below 882 °C it forms the  $\alpha$  phase which has a hexagonal close-packed (HCP) crystal structure and between 882 °C and 1668 °C (the melting temperature) it forms the  $\beta$  phase which has a body-centred cubic (BCC) crystal structure [1, 9, 13, 14]. Alloying elements are added to titanium to alter its strength, ductility, fatigue and creep resistance and its forgeability. These elements are generally either  $\alpha$  or  $\beta$  stabilisers, that serve to adjust the quantity of the two phases found in the service-temperature microstructure.

As stated above, titanium alloys are relatively expensive compared to steel and aluminium alloys. This is due to the energy intensive Kroll process [1, 9], developed in the 1940s, required to create Ti ‘sponge’ from ore and the subsequent costs in further re-melting and processing. Thus titanium alloys are used only where their desirable properties justify their expense. These applications include, amongst others, aero-engines, aerospace airframes, biomedical implants, sporting goods, building materials and automobile components. As a result of their relative expense, titanium alloys have been widely studied from processing through to behaviour to ensure that they are used in the most efficient manner possible. See Lütjering [9] and/or Donachie [1] for reviews of Ti. However, due to the complexity of the microstructure developed during processing there is still research to be done to understand fully the mechanical behaviour of the wide variety of alloys possible.

This research is concerned with developing experimental techniques that can provide data to help improve the understanding of the constitutive behaviour of anisotropic materials at many strain rates. It is here applied to a cross-rolled Ti-6Al-4V that is used primarily in the production of compressor fan blades for jet engines that must respond to impact events such as bird strikes within specified parameters. As is usually the case, the better the material is characterised, the more efficiently engineers can design components using it because there is less uncertainty about its response.

### **Cross-rolled Ti-6Al-4V plate production**

Cast ingots of homogenised Ti-6Al-4V are commonly produced as cylinders measuring on the order of  $\sim 2$  m long by  $\sim 0.75$  m diameter in modern production facilities [1, 9, 15]. These ingots have a microstructure of  $\alpha$  grains that have nucleated from prior  $\beta$  grain boundaries, within a matrix of retained  $\beta$ , as shown in figure 1.1, or the martensitic  $\alpha'$  phase, depending on the cooling rate [9, 16]. This microstructure is called the  $\alpha + \beta$  structure. To achieve plate-shaped blocks of Ti-6Al-4V, thermomechanical processing (TMP) by heating, squashing and

rolling is used. This processing not only shapes the ingot, but also anneals and transforms large grains into smaller grains, which increases yield strength and alters ductility and fracture behaviour. The desired microstructure, and hence mechanical properties, are achieved through the strict control of this processing. Without this strict control, different batches of plate material may have different mechanical behaviour, which would not be appropriate where safety-critical components are manufactured, such as aero-engine compressor blades, and tight regulations exist for their performance.

TIMET produce Ti-6Al-4V plate for aero-engines compressor blades manufactured by Rolls Royce plc. in their mill in Swansea by repeated heating and compression stages before final cross-rolling. Cross-rolling comprises the repeated rolling of slabs of material in one direction and then in an orthogonal direction in the plane of the final plate, which shall be referred to as CR-plate from here on in. This reduces the cross-sectional area by up to 75%. The squashing and rolling ‘breaks’ down the initially large  $\alpha$  grains to produce smaller grains and hence an increased number of grain boundaries. The processing introduces many dislocations that, combined with the increased density of grain boundaries, tend to harden the alloy and increase its yield strength.

The rolling process has a significant effect on the texture of the microstructure, which is the distribution of crystallographic orientations. Within the texture of CR-plate there are bands of commonly orientated  $\alpha$  grains within prior  $\beta$  grains known as macro-zones. An electron back scattered diffraction (EBSD) image of CR-Ti-6Al-4V from Sarsfield [2] shows these macro-zones as similarly coloured (and hence similarly orientated) bands of  $\alpha$  grains (figure 1.2). The HCP  $\alpha$  phase has pyramidal, basal and prismatic slip planes with the pyramidal having the largest critical resolved shear stress (CRSS). This causes single crystals of  $\alpha$  to have anisotropic plastic flow behaviour. When similarly orientated  $\alpha$  grains are banded together, as they are in CR-Ti-6Al-4V, this microstructural anisotropic plastic flow behaviour is present at the macroscopic scale too.

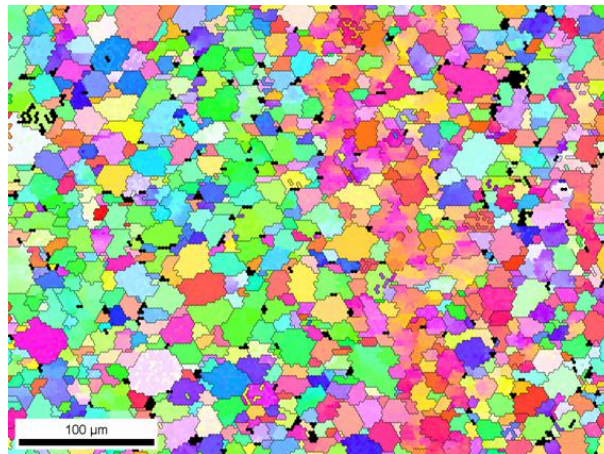


**Figure 1.2:** EBSD image that qualitatively shows banding of similarly orientated  $\alpha$  grains in CR-Ti-6Al-4V, [2]. Colours represent orientation.

The presence of macroscopic plastic anisotropy is therefore attributed to the low symmetry of the critically resolved shear stress on slip planes of the HCP  $\alpha$  phase and the tendency of the initially uniform polycrystalline structure to undergo lattice rotations that result in a preferred crystallographic orientation, or texture [5]. The texture in rolled Ti-6Al-4V has been observed to give rise to anisotropic mechanical properties in a number of studies, [2,5,7,17–19]. Sarsfield [2] has noted flattening of grains, due to the TMP, anisotropically reduces the lengths available for dislocation glide and alters hardening behaviour due to dislocations being held at grain boundaries.

To develop predictive modelling capabilities for the CR-plate, the relevant mechanical behaviour needs to be included in constitutive relationships, and the strength of all the parameters in these models needs to be fully characterised. The events that need to be modelled in aero-engine compressor blades include: the linear elastic loading due to the dynamic forces from the high-speed rotation and the interaction with the air flow that provides the main function as a turbo-machine; the wearing and corrosion of the blades due to foreign object damage and particulate ingestion (such as dust, sand and ice); and, of most importance to the current research, bird strike and blade release events in which the high strain rate mechanical behaviour of Ti-6Al-4V play a crucial role in determining the overall response of the engine.

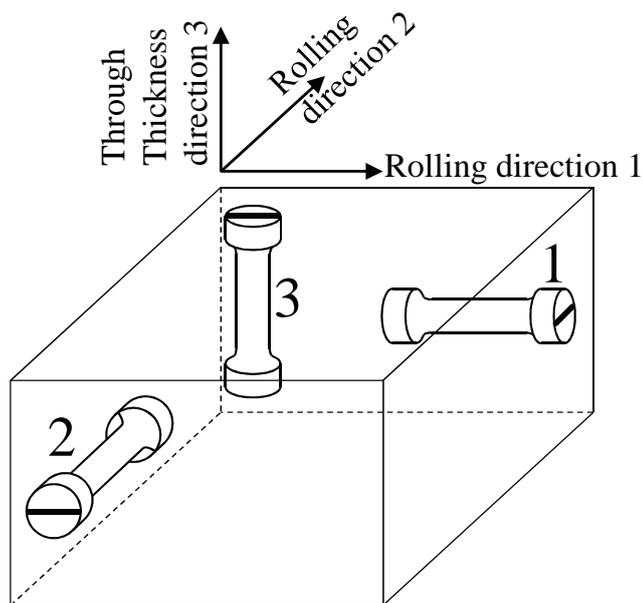


**Figure 1.3:** The principal material directions.

Prediction of the properties of Ti-6Al-4V based on the modelling of the microstructure, including its texture, using crystal plasticity theory and multi-grain models, at least for homogenisation, has been suggested by several researchers (see, for instance [2]). However, the results of these predictions will always need to be validated. Mechanical testing remains the principal method for determining properties of materials at an appropriate scale for successfully modelling impact events.

In order to help determine the high strain rate anisotropic mechanical properties and calibrate and/or validate models of cross-rolled Ti-6Al-4V and materials like it, experimental techniques have been developed here. For general characterisation of CR-plate under impact events, and similar homogeneous materials, established techniques exist to examine some of the uniaxial behaviour at a variety of strain rates. § 1.4 describes the behaviour of anisotropic materials in general and § 1.5 details the important techniques for uniaxial characterisation.

## 1.4 Deformation behaviour of transversely isotropic materials

The uniaxial stress-strain response of metallic alloys can generally be described as having an initial linear elastic response with a stiffness governed by Young's Modulus until yield, an initial yield stress and then an increasing flow stress upon increasing strain. After the strain rises above the yield strain there will be an amount that cannot be recovered after unloading: the plastic strain. The initial yield stress is usually defined as the stress reached so that, were the material to be unloaded, it would recover to retain a permanent strain of 0.2%. The flow stress is the stress that the material supports after increasing the strain above the initial yield strain.

The degree of anisotropy in Young's Modulus of the CR-plate is not as significant, if not negligible, as the differences in yield stress and hardening curves of the alloy when deformed in in-plane and out-of-plane (through-thickness) directions [2, 19]. Figure 1.3 shows the principal material directions in the CR-plate in relation to the uniaxial specimens obtained from it. The 1 and 2 directions were initially assumed to have equal uniaxial yield stresses, whilst the 3 direction has been shown to have a lower yield stress [19]. From now on, in this chapter, we will adhere rigorously to this numbering convention, i.e. direction 1 and 2 are in-plane and expected to be equivalent and direction 3 is through-thickness.

In 1928 von Mises [20] suggested that the plastic potential and the normal to the yield function of a metal were the same. This has been shown to hold true for nearly all metallic alloys [5]. Thus, for a metal, the plastic strain increment will be normal to the yield surface. From here on in when strain increment is discussed, this means the increment in *plastic* strain, unless explicitly stated otherwise.

In a material that obeys the von Mises yield criterion ( $(\sigma_1 - \sigma_2)^2 + (\sigma_2 - \sigma_3)^2 + (\sigma_3 - \sigma_1)^2 = 2\sigma_y^2$ , when shear stresses are zero), if, for example, a uniaxial state of stress in direction 1 is applied then  $[d\varepsilon_1, d\varepsilon_2, d\varepsilon_3]^T \parallel [1, -0.5, -0.5]^T$ , where  $d\varepsilon_1$ ,  $d\varepsilon_2$  and  $d\varepsilon_3$  are the increments in

plastic strain their respective directions. Figures 1.4 and 1.5 show the von Mises yield function, in a principal stress space, and the strain increment directions for the three uniaxial stresses. Note that the strain increment direction at yield when loading along the 2 axis, in the view of figure 1.5b, bisects the other two axes equally.

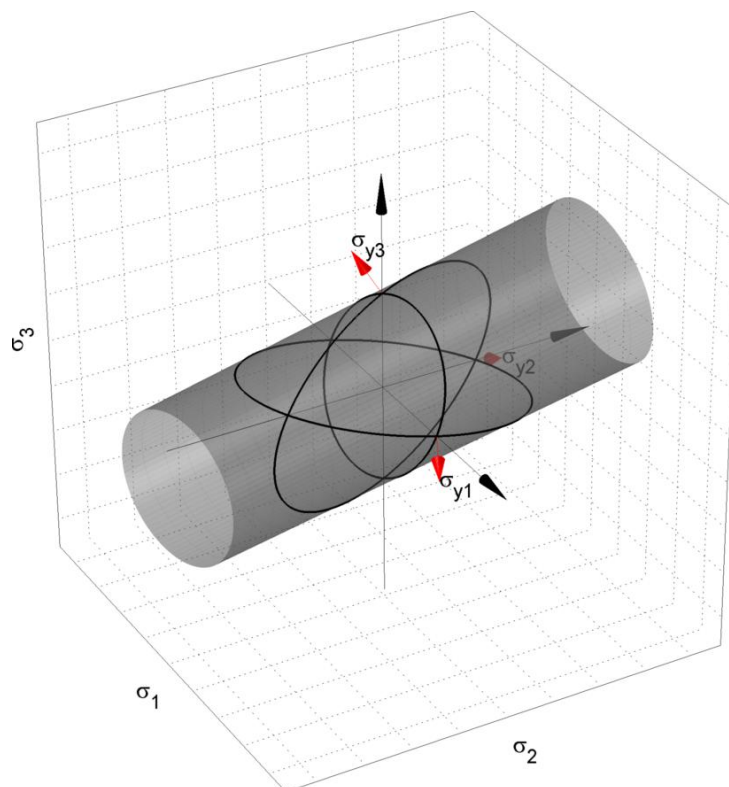


**Figure 1.4:** The von Mises yield surface in principal stress space. The surface is truncated at finite hydrostatic pressures for clarity. The intersection of principal planes and the cylinder can be seen to produce ellipses. The view is from a position in negative  $\sigma_2$  and positive  $\sigma_1$  and  $\sigma_3$ . The strain increments are shown in red.

In anisotropic alloys, such as many rolled plates, the yield function that describes the yield behaviour usually changes shape, size and/or position and hence some or all of the strain increment directions change too. In 1948 Hill [21] suggested an extension of the von Mises yield surface to describe anisotropic plasticity in metals ( $H(\sigma_1 - \sigma_2)^2 + F(\sigma_2 - \sigma_3)^2 + G(\sigma_3 - \sigma_1)^2 = 1$ , when shear stresses are zero and  $H$ ,  $F$  and  $G$  are material parameters). This extension has been widely considered and many further extensions to the Hill model have been proposed to include the behaviour of materials that behave in ways not predicted by the Hill yield function,

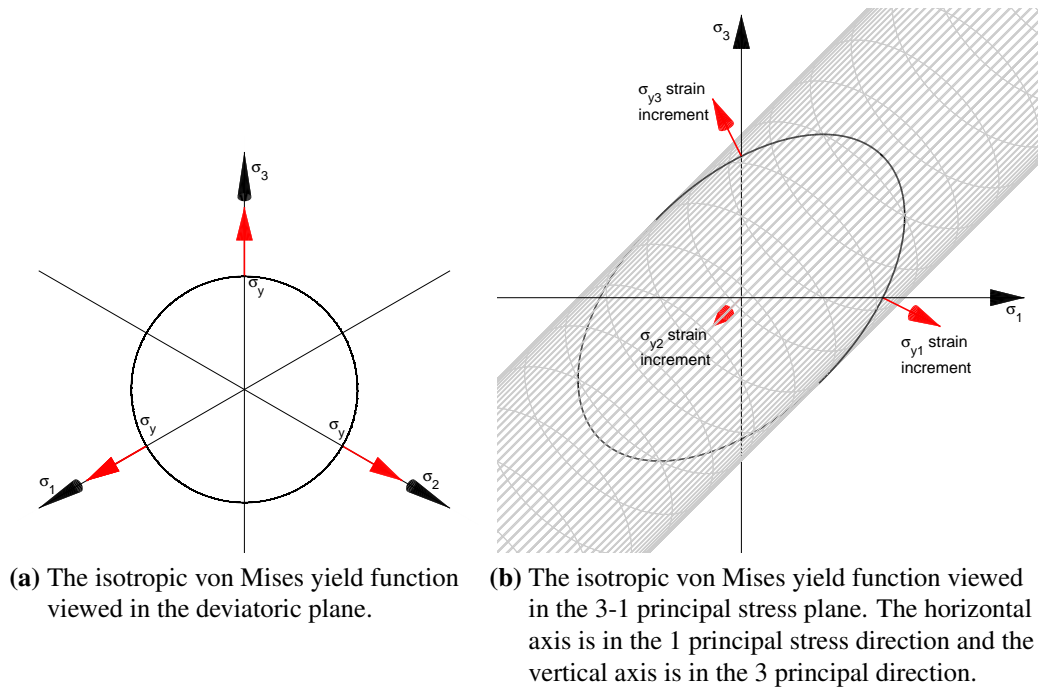


**Figure 1.5:** A diagrammatic representation of the von Mises yield function shown in figure 1.4. The directions of the strain increments at the uniaxial yield stress states are shown for two views of the von Mises yield function. N.B. the direction of the strain increment for the  $\sigma_2$  uniaxial-yield-stress state, which bisects the other two axes.

e.g. for transversely isotropic (also called orthotropic in the literature) metals [8, 22–24]. However, as a first approximation, the Hill yield function is a suitably flexible model of anisotropic plastic behaviour.

As mentioned above, and measured by Dyson [19], the cross-rolled Ti-6Al-4V under investigation here can be assumed to be transversely isotropic due to the TMP it has been through. Therefore, the present description will concentrate on the reduction of the Hill yield function to transversely isotropic metals. When the 1, 2 and 3 principal stress directions are aligned with the 1, 2 and 3 material directions, given in figure 1.3 for the CR-plate, figure 1.6 demonstrates a possible Hill yield function for a transversely isotropic material such as the cross-rolled Ti-6Al-4V, where, hypothetically,  $\sigma_{y1} = \sigma_{y2}$  and  $\sigma_{y3} = 0.8\sigma_{y1}$ . Note that the strain increment direction at yield when loading along the 2 axis (as well as the 1-yield-stress strain increment direction) has changed to point more in the direction of the 3 axis because of the lower  $\sigma_{y3}$ ,

which has altered the gradient of the yield function at the intersections with the  $\sigma_1$  and  $\sigma_2$  axes, which represent the uniaxial yield stresses.

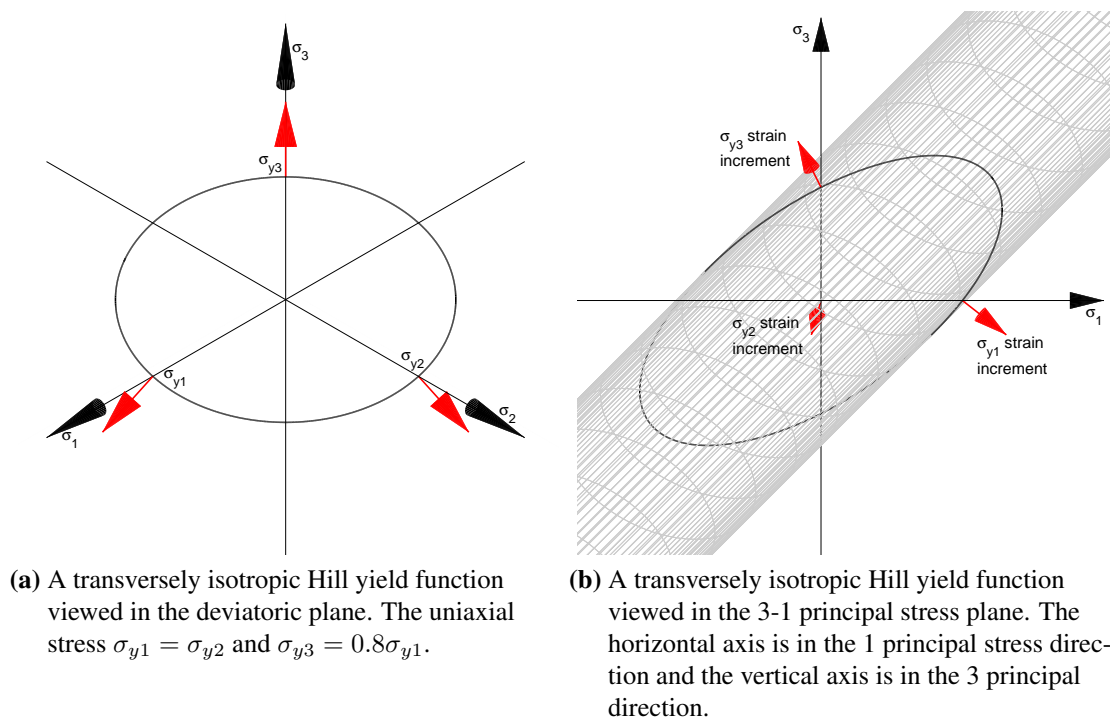


**Figure 1.6:** A diagrammatic representation of a transversely isotropic Hill yield function. The directions of the strain increments at the uniaxial yield stress states are shown for two views of the yield function. N.B. the direction of the strain increment for the 2 uniaxial yield stress state has rotated to be more in the direction of 3 than in figure 1.5b.

In uniaxial experiments these strain increment directions would present themselves as anisotropic deformation of the cross section. Initially cylindrical cross-sections of transversely isotropic materials are known to deform into elliptical cross-sections [5–7] when loaded in the 1 or 2 material directions. Uniaxial specimens loaded along the 3-axis, the through-thickness direction, exhibit axisymmetric deformation.

Another simple type of transversely isotropic anisotropy that could, in theory, arise in metals is that of a kinematically hardened von Mises yield surface. Hypothetically, if the rolled plate material could be modelled entirely by such a yield function then its yield surface would appear as shown in figure 1.7. This figure demonstrates that if the through-thickness com-

pression during the processing of the plate had reduced the 3 direction tensile yield stress and simultaneously increased the magnitude of its compressive yield stress, the strain increment in the 1 and 2 directions would be rotated in the opposite direction to that of the Hill transversely isotropic surface. Providing an opportunity to distinguish between the two cases through experimental observation.

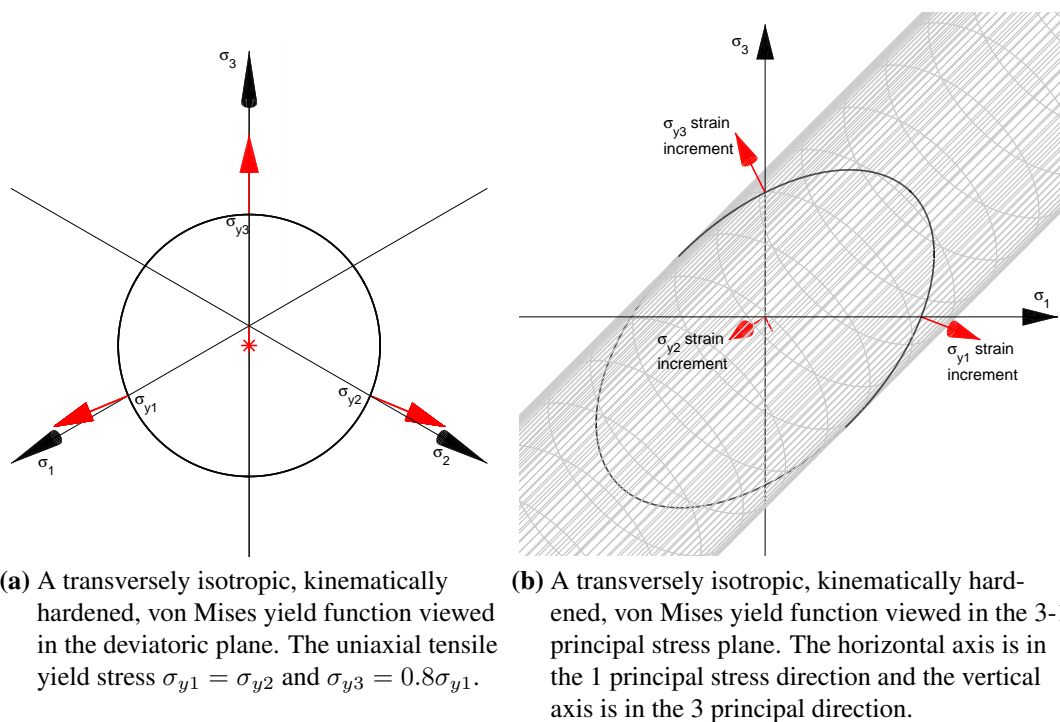


**Figure 1.7:** A diagrammatic representation of a transversely isotropic, kinematically hardened, von Mises yield function. The directions of the strain increments at the uniaxial tensile yield stress states are shown for two views of the yield function. N.B. the direction of the strain increment for the 2 uniaxial yield stress state has rotated to be *further from* the direction of 3 than in figure 1.5b.

### 1.4.1 Measuring the strain increment direction in uniaxial experiments

Plastic anisotropy has been frequently characterised by the transverse strain ratios in flat tensile uniaxial specimens [5, 22, 25–27] and there exists an ASTM Standard, ASTM E517-00(2006) [28], that defines good practice in its measurement. The ‘ $R_\theta$ -value’ (as it shall be known here)

or ‘Lankford Coefficient’ [25] is defined for uniaxial tensile tests on flat specimens as:

$$R_{\theta} = \varepsilon_w^p / \varepsilon_t^p, \quad (1.1)$$

where  $\varepsilon_w^p$  is the plastic strain in the plane of the sheet perpendicular to the tensile direction and  $\varepsilon_t^p$  is the plastic strain in the through-thickness direction.  $R_{\theta}$  is thus the same as the ratio of the integrals of the transverse plastic strain increment directions  $\int d\varepsilon_2 / \int d\varepsilon_3$ .

Measuring the strain ratio decides immediately whether the yield function is of the Hill type, figure 1.6, or a kinematically hardened von Mises type, figure 1.7, because the strain ratios for these types of function are in opposite directions if the  $R_{\theta}$  ratio does not change significantly with straining. It has been noted [21,27], that measuring  $R_{\theta}$  is an indirect way of finding the principal yield stresses when the material is known to behave according to the Hill yield function.  $R_{\theta}$  is also used to estimate forming limits for die forming processes [5].

It has been noted by Kocks [5] that the  $R_{\theta}$  value often does change with strain, and hence a better measure is the strain *rate*,  $D$  (where  $D=\dot{\varepsilon}$ ), ratio,  $r_d$  :

$$r_d = D_w / D_t. \quad (1.2)$$

The two extreme values of  $R_{\theta}$  and  $r_d$ , zero and infinity for no widening and no thinning, respectively, do not lend themselves well to simple comparison; in addition it can be difficult to measure the small displacement of through thickness deformation in flat specimens, hence the ratio of widening strain rate to axial strain rate has been proposed:

$$q = -D_w / D_l, \quad (1.3)$$

which follows from  $r_d$  using the assumption of constant volume, where  $D_l$  is the length strain rate [29]. The value of  $q$  normally has a range between 0 and 1, which is more suitable for

comparison of materials, but there is a functional relationship between each measure.

It has been noted in Gedney [30] and Osman [31] that non-rectangular deformation of the cross-section of flat specimens through edge-curling after necking can prevent accurate measurement of transverse dimensions in uniaxial experiments. Yang [6] has shown that measuring the  $R_\theta$  ratio using the ratio of transverse radial strains in initially cylindrical specimens is equivalent to measuring the ratio in flat specimens. However, the focus of Yang's work was the estimation of the validity of the assumption that  $R_\theta$  did not change with small strains and that the true stress could be calculated by taking measurements from only a single transverse extensometer; using a correction factor to compensate for the assumption made that the cross-sectional shape remained circular, and Yang did not make explicit measurements of the elliptical shape of the cross-section during deformation. Kocks [5], page 447, concerning the elliptical deformation of anisotropic, initially cylindrical specimens in uniaxial experiments to determine the yield stresses observed that:

Such 'ovaling' (of an initially circular cross-section) has been observed, but it has not been studied with great care. Inasmuch as it provides valuable information on the material's plastic anisotropy without an additional test, it should be routinely measured in both tension and compression tests.

In Kocks's review, he states that traditional methods of measuring  $R_\theta$ ,  $r_d$  or  $q$  ratios, using post fracture measurements or transverse extensometers are not sufficiently sophisticated. He describes the use of surface mounted strain gauges for the collection of width strain data, which is part of the ASTM specification [28]. However, he goes on to state that at high strains these are unsuitable due to loss of cohesion between the gauges and the specimen. This is compounded by the emphasis that correct yield surface determination requires measurement of the plastic strain increment vectors throughout loading and not just the state of stress at yield.

Measurement of transverse deformation by contacting techniques or strain gauges is even less suited to high strain rate experiments. The photogrammetric techniques developed in the

current study allow quantification of the elliptical shape of deforming uniaxial cylindrical specimens. This provides data on the strain ratios in uniaxial experiments at all rates of strain, whether in tension and compression, as a function of uniaxial strain with high data resolution. These data can be used to expose the nature of the yield function at the uniaxial yield stress states by providing the direction of the strain increment. Such measurements have not been performed before. Estimates of the accuracy of the technique have also been made.

## 1.5 Characterisation of Ti-6Al-4V

Ti-6Al-4V is widely used in industry and the mechanical behaviour of some of its microstructures have been reasonably well characterised, see, for instance [19, 32–37]. However it does not attract the same level of attention as more common alloys such as steel and aluminium. Much research attention on the anisotropy in Ti-6Al-4V has focused on its anisotropic response during superplasticity - see for instance [7, 38] - due to the relative difficulty in forming it into components when compared to other alloys. There is a lack of research into the room temperature anisotropic mechanical behaviour of cross-rolled Ti-6Al-4V at low and high strain rates, of the sort that is required for modelling impact events.

Whilst previous research, [19, 37], has made progress towards finding some accurate material parameters that define the behaviour of this particular form of cross-rolled Ti-6Al-4V, the detailed measurements of anisotropic deformation that are necessary to create anisotropic material models is lacking. This is why one of the main aims of this research has been to record the material deformation behaviour in great detail with an increased number and variety of measurements. Dyson [19] has recorded the uniaxial stress-strain response of this form of Ti-6Al-4V in tension and compression at strain rates of  $\dot{\epsilon} = 10^{-3} \text{ s}^{-1}$ ,  $\dot{\epsilon} = 1.7 \times 10^2 \text{ s}^{-1}$  and  $\dot{\epsilon} = 4 \times 10^3 \text{ s}^{-1}$ , and noted that the orientation of specimens with respect to the rolling direction significantly affects the material response and suggested that more research should be performed to quantify

this behaviour further. Dyson did not record the plastic increment directions during these experiments. Characterisation of cross-rolled Ti-6Al-4V in a report by Wang [37], also showed that this anisotropic behaviour is apparent in specimens taken from CR-Ti-6Al-4V plates tested in tension, but again no record was made of the plastic strain ratios.

## 1.6 Uniaxial characterisation

In order to determine the mechanical behaviour of a material through uniaxial loading, specimens are cut from representative samples. These specimens need to have sufficiently large gauge diameters relative to their grain size so that there are a sufficient number of grains to assume homogeneity. Siviour [39] has quoted a figure of 10 grains across the diameter as the minimum required for homogeneity, Safford [40] has quoted 20 and Drodge [41] has presented a figure of 4 grains, from (1.4), as being sufficient to ensure that the majority of grains do not touch the surface in a tensile specimen, whereas 19 grains are required for less than 10% of grains to be cut. The Ti-6Al-4V specimens in this research had more than 60 grains across the 3 mm diameter, which should have ensured that they were homogeneous.

The calculation in Drodge [41] to calculate the fraction of grains that are cut by the circumference of a cylindrical specimen is:

$$\frac{\text{Cut grains}}{\text{Uncut grains}} = \frac{d}{D} \left( 2 - \frac{d}{D} \right), \quad (1.4)$$

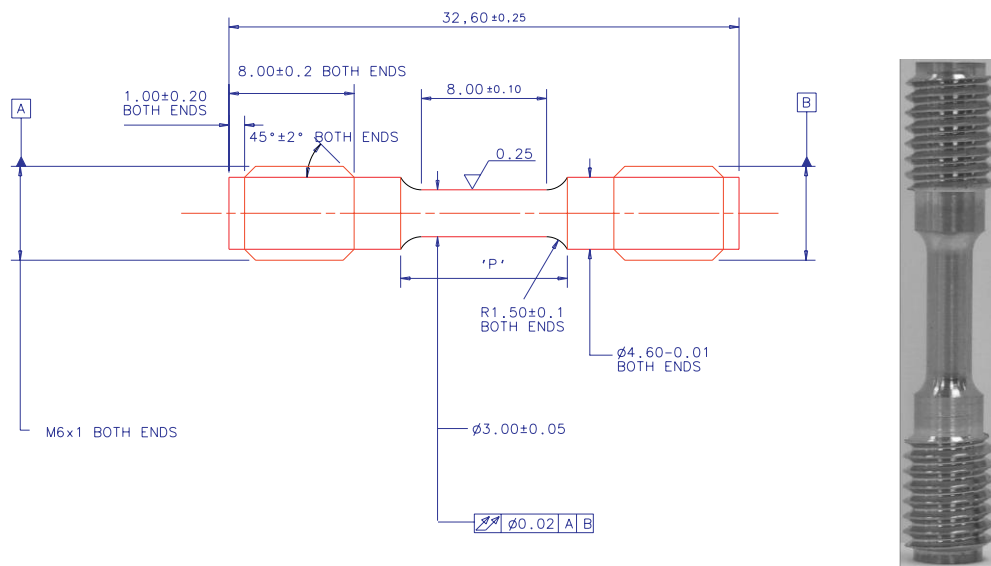
where  $d$  is the mean diameter of a grain and  $D$  is the gauge diameter of a specimen.

If there is a larger microstructural length scale inherent to a material, such as the macro-zones seen in the EBSD image figure 1.2, then the gauge width should be large enough so that the response is not influenced by that inhomogeneity. From the EBSD image, these macro-zones are approximately 100  $\mu\text{m}$  across, and hence there were 30 of these units across the 3 mm diameter, which should still be sufficient for homogeneity.

### Tensile specimens

To determine the tensile mechanical behaviour of materials, standard tensile tests are performed on samples of material using dog-bone flat or cylindrical specimens [42] (see figure 1.8). These specimens have a long parallel gauge section, within which the stress is assumed uniaxial and constant over the gauge width, and a smooth transition to wider shoulders where the testing machine can apply the load without causing stress concentrations in the gauge section. The length of the specimen should be sufficient to ensure a uniaxial stress state, however the length is limited in high strain rate testing due to the requirements of specimen equilibrium, see § 1.6.2 below. The specimens used here are shorter than the ASTM standard [42] so that the specimens could be used, and the deformation directly compared, for both QS (quasi-static) and HR (high strain rate) experiments and yet still reach equilibrium at high strain rates.

In most ductile metals the tensile deformation behaviour can be divided into regions of linear elasticity, yield, plastic flow, necking and fracture.



(a) The dimensions of the specimen.

(b) A photograph of the specimen.

**Figure 1.8:** A typical cylindrical dog-bone tensile specimen showing the dimensions used at all strain rates in this research.

### Necking in tensile specimens



**Figure 1.9:** A silhouette photo of an initially cylindrical specimen from steel bar that has necked during QS loading.

Necking in tensile specimens, see figure 1.9, is a result of a plastic instability in the specimen where the rate of increasing strength of the material through strain hardening is no longer sufficient to support the rate of increasing load. The weakest location along the gauge length of the specimen starts to narrow, which causes further concentration of the stress and further narrowing of that neck.

This curvature of the neck results in a triaxial stress state within the specimen which cannot be analysed by simply assuming a prismatic cross-section. Bridgman [43] suggested a correction factor to obtain the effective uniaxial stress from a necking isotropic specimen using the curvature of the neck:

$$\sigma_{eff} = \frac{\sigma_{avg}}{\left(1 + \frac{2R}{r}\right) \left[\ln\left(1 + \frac{r}{2R}\right)\right]} \quad (1.5)$$

where  $\sigma_{eff}$  is the effective stress that would be present if the gauge section were parallel,  $\sigma_{avg}$  is the total axial force divided by the cross-sectional area,  $r$  is the radius of the cross-section and  $R$  is the radius of the profile. Using this approximation a better estimate of the true stress during loading can be found for many materials.

G'Sell [44], describes the use of photogrammetry for the purposes of measuring the radial deformation of isotropic cylindrical specimens throughout the necking range for video control of tensile strain rate. However that method only works for specimens that deform axisymmetri-

cally.

The Bridgman correction relies on the cross-section remaining circular and the von Mises yielding criterion applying. Eisenberg [45] presented a modification of the Bridgman correction to include anisotropic materials with initially circular cross-sections that deform into ellipses. A complex equation was derived that requires integration through numerical quadrature for the general case, however his results indicated that simple averaging of the pseudo-anisotropic Bridgman correction evaluated for the maximum and minimum radii directions and their corresponding profiles is very close to, if not indistinguishable from, the general solution. This suggested that the modified Bridgman factor for elliptical cross-sections should be calculated as:

$$\sigma_{eff} = \frac{\sigma_{avg}}{\frac{1}{2} + \frac{1}{4} \left(1 + \frac{R_a}{r_a}\right) \ln \left[1 + \frac{r_a}{R_a}\right] + \frac{1}{4} \left(1 + \frac{R_b}{r_b}\right) \ln \left[1 + \frac{r_b}{R_b}\right]} \quad (1.6)$$

where  $r_a$  and  $r_b$  are the lengths of the semi-major and semi-minor axes respectively at the minimum cross-sectional area, and  $R_a$  and  $R_b$  are the profile radii corresponding to the major and minor axes of the ellipse.

When (1.6) is valid, the correction from  $\sigma_{avg}$  to  $\sigma_{eff}$  can be made for elliptical cross-sections when measurements are made of the cross-section dimensions. Hartley and Eisenberg [45, 46] used prior knowledge of the anisotropy of the material to estimate the elliptical shape after measuring the major dimension of the cross-section, but this is not required using the technique developed in chapter 3 of this thesis, where all dimensions of the elliptical cross-section are measured directly in all specimens.

If the necking deformation is recorded accurately then numerical simulations of the experiment may be used, through inverse identification techniques, § 1.7, to obtain constitutive parameters that cannot be directly obtained through the simple uniaxial deformation.

### 1.6.1 Compression specimens

Compression specimens are usually made as cylinders of material with an aspect ratio of height/diameter at or slightly above 1 [5, 47]. If the specimen is too slender then buckling may occur.

The specimen must be lubricated to reduce friction between its surfaces and the anvils. Designs for specimens that include shallow cups cut into the ends or concentric grooves scribed into the ends have been suggested [47] to prevent the lubricant from being squeezed out during loading. Without adequate lubrication the specimen will be constrained by the friction and barrel during loading. If the specimen's aspect ratio is too short then the friction between the anvils and the specimen may become too large to obtain meaningful results under uniaxial assumptions. Characterising the frictional forces during the experiments [48] can allow numerical simulations of the experiment to be accurate and the deformation behaviour of the specimen may be used to calibrate constitutive parameters using inverse identification, see § 1.7.

### 1.6.2 Mechanical testing machines

Mechanical testing machines have been used since at least as far back as the industrial revolution, and the first commercial machine was made available in 1886 [49]. Modern uniaxial testing machines generally fall into three categories: screw-driven, servo-hydraulic or wave propagation (Split-Hopkinson Pressure Bar, SHPB) machines, listed in order of increasing strain rate capability.

Most simply, the strain in specimens in screw-driven or servo-hydraulic machines is calculated by measuring the displacement of the moving cross-head,  $u_c$ , and then calculating nominal strain as:

$$e = u_c/L_o, \quad (1.7)$$

where  $L_o$  is the initial length of the gauge section. However, contacting extensometers were developed that can measure the displacement of the specimen shoulders or the compression

anvils, which removes the compliance of the fixtures from the strain calculation. More advanced extensometers can measure displacements within the parallel gauge section, and hence should only respond with the exact uniaxial displacement,  $u$ , in the specimen, until necking begins.

Force in the specimens is measured using a load-cell that outputs a voltage proportional to the load by means of strain gauges that respond to its linear elastic deformation. In the SHPB stress wave analysis is used to determine both the displacement and the force in the specimen.

### Screw-driven machines

Screw driven machines, [49], use geared electric motors to move a ball-and-screw drive connected to a cross-head. A uniaxial force can be applied to specimens attached between a static cross-head and the moving cross-head either in compression or tension. The rate of loading is controlled by feedback controllers that usually measure the cross-head speed and/or load to achieve the desired rate, but other measurements gathered by extensometers can be used in the control loop too. The strain rates achieved by this type of machine are usually quasi-static and the magnitude of the forces generated depends on the machine's size.

In this research, a screw-driven Hounsfield testing machine was used to deform specimens in compression and tension at nominal strain rates of approximately  $\pm\dot{\epsilon} = 10^{-3} \text{ s}^{-1}$ .

### QS extensometers

As stated previously, flat dog-bone specimens are frequently used to measure anisotropic tensile properties of materials. However the cross sectional shape of flat dog bone specimens can change to that of a non-rectangular section after necking during the experiment, making true stress measurements difficult [42]. This is not a drawback of cylindrical specimens, providing that the cross-sectional shape can be measured. Therefore, chapters 3 and 4 develop a methodology which, using digital cameras combined with computer vision calibration tools,

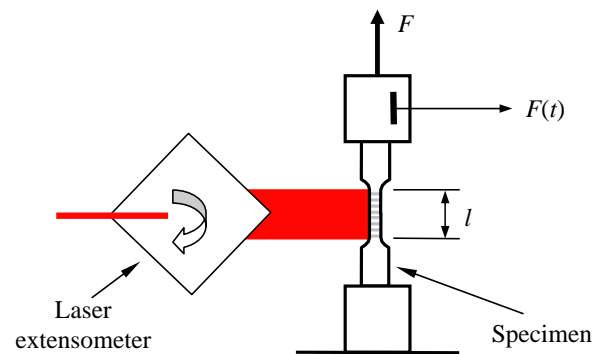


**Figure 1.10:** Diagram of the quasi-static loading device with the laser extensometer recording the positions of painted stripes.

can capture the surface deformation in standard cylindrical dog bone specimens of anisotropic, homogeneous materials without marking. This is a significant advance in measurement techniques considering the drawbacks associated with marking such as specimen preparation time, paint cracking and surface obscurement. The techniques can also be applied to high strain rate experiments using a high speed camera.

Many devices have been used to record the extension of a specimen during its deformation in a uniaxial experiment [42]. Linear variable differential transformers (LVDTs), laser extensometers and more recently, video extensometers, have all been used to measure the positions of various points along the specimen's geometry and analysed to obtain strain measurements. In order to obtain full field rather than discrete measurements, laser speckle interferometry, [50], may be used. However this method has limitations in terms of the size of the observable region and equipment cost. A more realistic method is speckle metrology, which can give a strain field with a much higher resolution than other measurements, however specimens with a uniform colour need to be marked, which obscures the surface when measuring deformation normal to it. In chapter 4, the use of tracking surface profile features from silhouette images to measure surface displacement and strain is developed.

Thus, the two techniques developed in chapters 3 and 4 allow an almost full estimate of the surface deformation in homogeneous, uniaxially loaded, cylindrical specimens to be obtained.

### Servo-hydraulic machines

Servo-hydraulic machines, [49], use a pressurised reservoir of fluid and electronically controlled valves to control the speed of a piston. Specimens can be loaded in compression or tension between the piston and a fixed cross-head. Again, the magnitude of the applied loads is dictated by the size of the machine and the maximum pressures allowed. Strain rates achievable are typically between  $\dot{\epsilon} = 10^{-1} \text{ s}^{-1}$  and  $\dot{\epsilon} = 10^2 \text{ s}^{-1}$ , although repeatable strain rates above  $\dot{\epsilon} = 10^1 \text{ s}^{-1}$  are difficult to obtain [51] because of the ability of the valves to control accurately the high speed flow required.

### Split-Hopkinson pressure bars

SHPB, [51, 52], are used to apply loads at strain rates from  $\pm\dot{\epsilon} = 10^2 \text{ s}^{-1}$  up to  $\pm\dot{\epsilon} = 10^4 \text{ s}^{-1}$  using wave propagation techniques. First developed by Hopkinson [53] in 1914, then Davies [54] and Kolsky [55], the most commonly used form of the SHPB today comprises two long instrumented bars that sandwich a specimen between them. A striker bar, propelled by a gas gun, impacts into the end of one of the instrumented bars (either directly for compression or into a flange for tension) which creates a stress wave that propagates along the bar into the specimen. Strain gauges, amplifiers and high speed data acquisition components are used to record the (linear elastic) stress at certain points in the bars at high acquisition rates (a sampling rate of 5 MHz with a 5 mm strain gauge in this research) as the waves propagate along them. See figure 1.11 for a diagram of the tensile form of the SHPB apparatus used in this research.

Equilibrium in the specimen is required for meaningful mechanical behaviour determination. As the wave propagates from the relatively large diameter input bar into the smaller diameter specimen and then into the output bar, several reflections at each of the interfaces occur due to changing impedance from differences in size that create free surfaces and differences in material stiffnesses. In order to achieve equilibrium in the specimens, their gauge length must be kept short. The specimen dimensions used in this research have been chosen so that they can

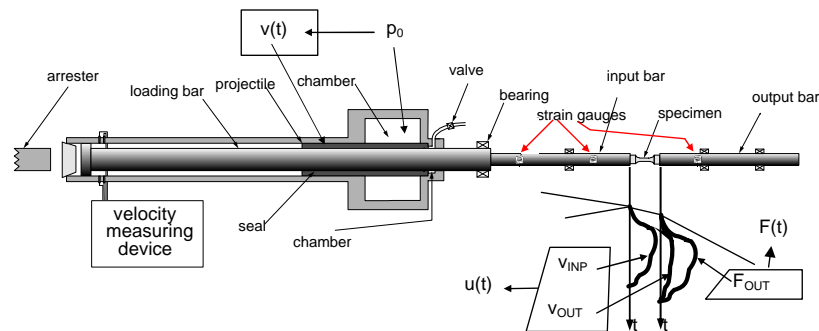


**Figure 1.11:** The Split Hopkinson bar apparatus for high strain rate loading of tensile specimens, from Elliott [3].

be used at high strain rates. The dimensions were not altered for quasi-static (QS) experiments so that direct comparisons between the specimen deformation measurements could be made. Ideally, more slender QS specimens would be used to reduce end effects, but the measurement of the complete surface shape overcomes this deficiency somewhat.

One dimensional wave analysis is used to determine the stress and strain in the specimen using the principal result that  $\sigma = \rho cv$ , where  $\sigma$  is the uniaxial direct stress in the bar,  $\rho$  is its density,  $c$  is the speed of sound in the bar and  $v$  is the velocity of the bar material. The displacements of the ends of the input and output bars as functions of time are calculated by integration of the  $v = \sigma/\rho c$  values recorded in each bar at the strain gauges and shifted in time to represent the values at the bar ends. The force in the specimen as a function of time is usually taken as the force transmitted through it and recorded in the output bar, but it can also be calculated by wave separation in the input bar which permits the checking of equilibrium between the two ends of the specimen. Once the force and bar end displacements (and hence the equivalent specimen shoulder or anvil displacements) are known then the nominal strain and uniaxial nominal stress can be determined. A more detailed description of this analysis can be found in, for example, Harding [56]. More sophisticated strain measurements may be obtained by digital image correlation (DIC) in high speed photography to achieve the equivalent of video extensometry and avoid the errors inherent in calculating displacement by wave analysis.

The loads that can be applied by this kind of apparatus are limited by the strength of the

materials used for the bars and the speed of the impact bar. In this research the experiments were performed at nominal constant strain rates of approximately  $\pm\dot{\epsilon} = 10^3 \text{ s}^{-1}$ .

## 1.7 Extracting material properties from experimental data

FE analyses allow more data from experiments to be used to calibrate material parameters. In the traditional measuring methods given above, the resolution of these strain measurements is limited to around 10 or fewer recorded positions in the gauge length of specimens used in both HR and QS tests. Using machining marks to track surface positions could add one or two orders of magnitude more measurable positions.

With the incorporation of FE techniques into the characterisation of materials, there are many more opportunities for determining material parameters in models by comparison of experimental results with simulation results. Doyle and Elliott [3, 57] describe and demonstrate how experimental data may be used by ‘inverse identification’ techniques to find material properties that were previously difficult to determine accurately. Of particular relevance to this research in Elliott it is stated how measurement of specimen strain fields with higher spatial resolution, combined with reconstruction of specimen geometry, as functions of time, provides better characterisation of post UTS behaviour and further improves the characterisation of materials.

## 1.8 Layout of this thesis

Chapter 2 describes the edge detection algorithm developed to automatically detect the edges of uniaxial specimens to sub-pixel accuracy in the presence of noise and poor illumination. This algorithm is used in the two subsequent chapters. Also described in this chapter are the

techniques used to calibrate cameras for use in photogrammetry and some of the difficulties in using high speed cameras for this purpose and methods to overcome them.

Chapter 3 describes the technique developed to measure elliptical cross-sectional shape by using three cameras to photograph a specimen *in situ* during QS or HR loading. A description is given of the method used to extrinsically calibrate the cameras using only an undeformed specimen. Also described are the experiments and numerical simulations used to estimate the accuracy of the technique. Representative specimens of CR-Ti-6Al-4V are measured during QS and HR loading to provide examples of the measurements that may be made.

Chapter 4 describes the technique developed to measure the axial displacement of a specimen during loading with a high spatial resolution. The technique makes use of the profile of the surface roughness, created during the manufacture of the specimens, to discover features that may be tracked over many images to provide a measurement of displacement, and subsequently strain. The technique complements the cross-section measurement technique because it does not require marking and allows the simultaneous measurement of a specimen's outline, cross-sectional shape and axial displacement.

Chapter 5 describes experiments performed on highly anisotropic CP-Zr and transversely orthotropic steel where the cross-section measurement technique was applied during QS and HR tensile loading. These experiments demonstrated the range of alloys that may be characterised using the new techniques and obtained data not published before. Further validation of the technique is given through the independent measurement of interrupted, necked, QS specimens.

Chapter 6 presents the results of uniaxial experiments performed on CR-Ti-6Al-4V in compression and tension at quasi-static and high strain rates in the three principal plate directions. These data have not been published before and represent a significant improvement in the characterisation of this form of Ti-6Al-4V.

Chapter 7 presents a discussion of the contents of the thesis, suggests improvements to the techniques and outlines the directions for future research. Chapter 8 presents conclusions of

the research.

## Edge Detection and Image Calibration

---

In this chapter the method used to find the edges of a specimen in silhouette images is described. This method is common to both the cross-section reconstruction and edge tracking techniques used later.

Three separate views of the specimen outline are required for the cross-section reconstruction technique in chapter 3. Further, these are required at all strain rates for the current study. The primary objective of edge detection here is to locate the edges of a specimen in all views as accurately as possible, with secondary objectives of high efficiency and speed of computation. The experiments were designed to make edge detection straightforward by using silhouette views of specimens. In principle, this creates two high contrast edges with a step change in pixel intensity at the edges of a specimen, as can be seen in a QS image in figure 2.2a, on page 35.

However, in experiments at high strain rates, where the image acquisition rate changes from three frames per second at QS to about  $10^5$  frames per second, other difficulties arise. Figure 2.1 shows an example of an image of a HR specimen, which comprises three views of the specimen in a single photo obtained using mirrors. Because of short exposure times in these experiments image intensification is required in the camera, which contributes to the high level of noise. Furthermore, the use of mirrors causes each view to have different depths of field,

which gives rise to loss of focus and blurring. The lighting arrangement in mirrored views also gives rise to highlights in the specimen surface which can confuse a ‘dumb’ algorithm into choosing these positions as specimen edges. These difficulties have been overcome in the research presented, resulting in a robust and accurate edge detection method for photos of uniaxial experiments.

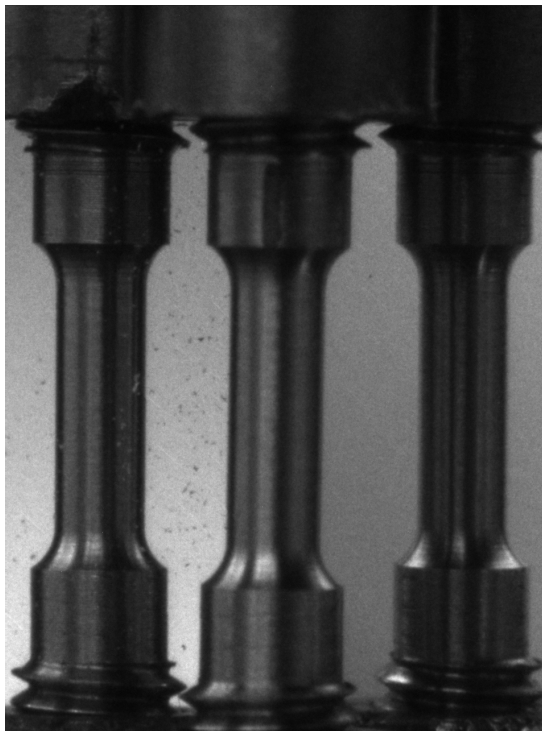


**Figure 2.1:** An example image from a HR tensile experiment.

## 2.1 Edge detection

There are many methods for detecting edges in images. For the current research, methods devised by Canny [58], Harris [59], Prewitt [60] and Sobel, as well as the SUSAN [61] detector were investigated to assess their edge detection capabilities. Canny found many false edges in the images along with the correct edges, as did Harris. Harris also had a notable constant offset in the results for the implementation tested here. Both the Canny and Harris methods

are based on smoothing by convolution with a Gaussian template to remove noise and then use the maximum gradient of intensities revealed as the best estimates of edge locations. Prewitt and Sobel are commonly implemented using 3 by 3 kernels which identify sharp edges well, but in the presence of noise there were far too many false edges detected. SUSAN is more robust to the presence of noise than the other methods as it is based on an integral approach, but this comes at the cost of blurring the edge definition. All of the edge detection algorithms are 2 dimensional in their approach and are deliberately designed so that they are as invariant as possible to edge orientation. When using images of uniaxial specimens (figure 2.2a) it is known *a priori* that the orientation of the edges is vertical or almost vertical, that there are two of them and that they are continuous. The images should not suffer from occlusions or significant noise and other corruption that may be associated with ‘real-world’ images of cluttered scenes. An edge detection algorithm has been developed here that takes cues from Canny’s, using a difference-of-boxes approach, but exploits the properties of the images to provide robust edge detection with sub pixel accuracy.

Methods have been proposed, [62–65], to provide edge detection that can locate edges to sub-pixel accuracy. After reviewing the current methods, it was decided that a template matching strategy was most appropriate for these experiments.

### 2.1.1 Filtering and sub-pixel edge detection using template matching

In perfect silhouette images of specimens, the edges change from full intensity to zero intensity within one pixel width, the ‘step-edge’ model. Ideal silhouette images of specimens also have flat intensity either side of the edge. The template chosen to locate these edges was therefore a row of an even number of pixels with the first half full intensity and the second half of zero intensity.

The standard normalised cross-correlation,  $c(u, v)$ , of this template,  $t(x, y)$  with the images,  $f(x, y)$ , filters the image. The result of the filter is that step-edges respond strongly

(where  $c(u, v) \rightarrow 1$ ) along each row. Patterns in the image that aren't step edges respond less strongly and inverse step edges respond with  $c(u, v) \rightarrow -1$ . The cross-correlation image,  $c(u, v)$ , referred to from here on in as NCCI, is computed from the following equation, given in Lewis [66]:

$$c(u, v) = \frac{\sum_{x,y} (f(x, y) - \bar{f})(t(x - u, y - v) - \bar{t})}{\left\{ \sum_{x,y} [f(x, y) - \bar{f}]^2 \sum_{x,y} [t(x - u, y - v) - \bar{t}]^2 \right\}^{0.5}}, \quad (2.1)$$

where the sum is over the  $(x, y)$  region where the template and the image overlap by shifting the template  $t(x, y)$  to  $t(x - u, y - v)$ .  $\bar{t}$  is the mean of  $t(x, y)$  and  $\bar{f}$  is the mean of  $f(x, y)$  in the region.

Ideally, the location of the maximum value on each row of the NCCI would locate the edge in a perfect silhouette to the nearest pixel, and then the brightness of that pixel would determine where the sub-pixel edge position lay. However, in real images the camera spreads the information about the location of the edge across several pixels due to loss of focus. This is one of the reasons for the long length of the template used. To determine the underlying true position of the edge, the maximum value of the NCCI was interpolated. This interpolation was performed in each row of pixels by taking NCCI values around the maximum and fitting a parabola to them by least-squares. The location of the peak of this parabola was taken as the location of the edge.

The second reason for the long length of the template is that the greater the length of the template, the more robust the detector is to noise in the pixel intensities, because small variations in regions of uniform intensity are averaged. Even some of the best silhouette images here have edges like those in figure 2.2b, where a highlighted section of the surface causes a short peak in the nominally dark region. This type of image artefact reduces the maximum length of the template because it pulls the peak in the NCCI values away from the true edge location if the template's span covers the artefact whilst lying over the exact location of the

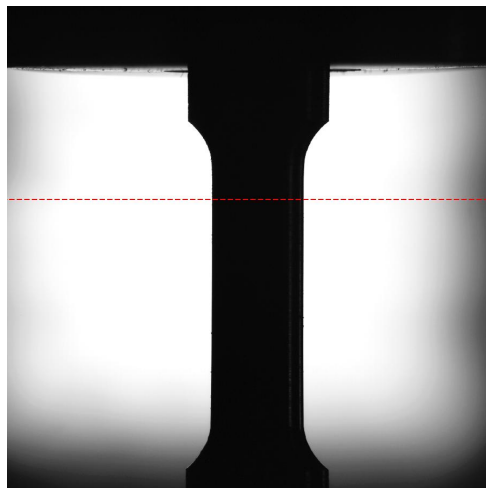
edge. The final size of the template was chosen for each experiment based on the resolution of the images and the extent of the uniform intensity regions either side of an edge. The template size used, after some optimisation, was 22 pixels wide for QS specimens and 40 pixels wide for the HR specimens.

There was an additional problem present in real images due to the combination of edge blurring by loss of focus and noise throughout, which meant that sometimes that the true edge on each row was not necessarily the location of the maximum value in the NCCI for that row. This led to the development of a strategy to find the true edge maximum: (1) The NCCI was first thresholded so that only pixels of the NCCI with a value above 0.9 in high quality QS images and 0.8 in lower quality HR images remained. (2) To identify which regions in this binary image were true edge peaks and which were peaks from noise, the contiguous regions of the binary image were identified and ranked according to their longest dimension, see image figure 2.3c in the demonstration provided by figures 2.2 and 2.2. (3) In each row the peaks that did not belong to the highest ranked region in that row were discarded and the single remaining region was taken to be the true edge peak location, because the true edge is continuous and long, whereas peaks due to noise and highlights are generally short. (4) The values in the peak were then used to find the location of the sub-pixel peak through parabola fitting.

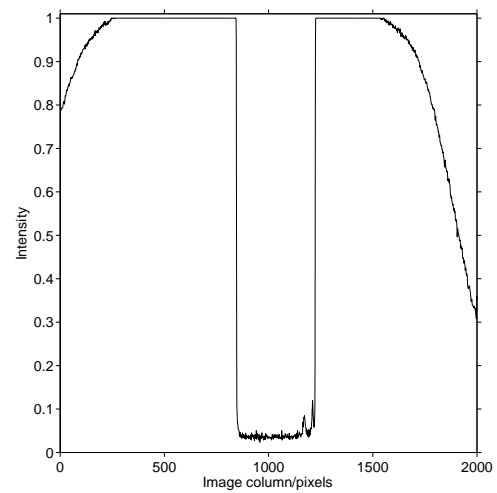
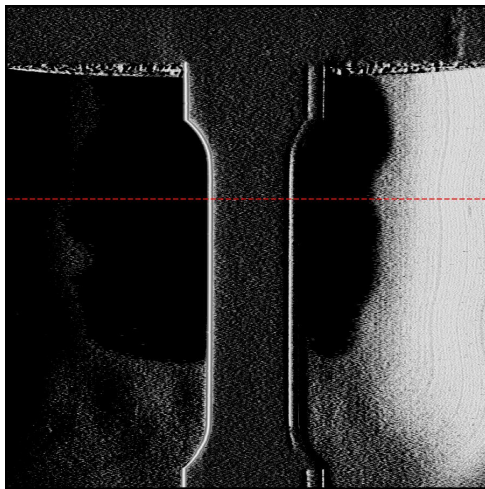
The whole process for edge detection relevant to the uniaxial test specimen geometry can be summarised with an example as follows. First, the image (figure 2.2a) was cross correlated with a template to produce a NCCI (figure 2.2c). The values for example pixel row 800 of this image can be seen in figure 2.2c. Second, the NCCI was thresholded (figure 2.3a) so that only correlation values above 0.9 remained. Third, contiguous two dimensional groups of non-zero correlation values were ranked according to their longest dimension and for every row only the correlation values belonging to the largest group spanning that row were retained, resulting in figure 2.3c. Finally, for every row, a parabola was fitted by least-squares to the non-zero correlation values and the location of its peak was taken to be the sub-pixel edge location, as

shown in figure 2.3e. Figure 2.3f shows the detected left hand edge in the exemplary photo and figure 2.4 shows the result of edge detection in a similar specimen photo with a 4 pixel row averaging filter applied to the edge location data.

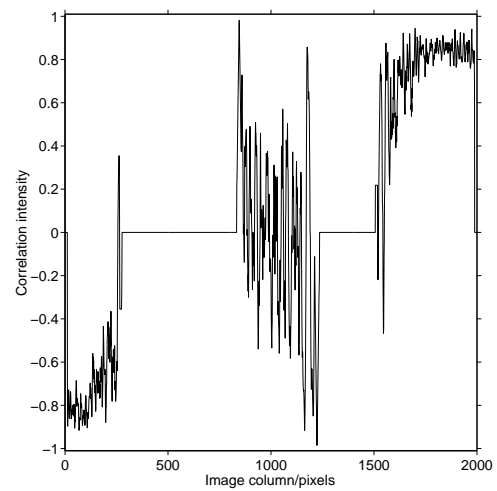
After the left hand specimen edge had been found in this way, the right hand one was found by applying the same process, but multiplying the NCCI by -1. This would have been the result if the template had first been reflected, but it was more computationally efficient to re-use the NCCI.



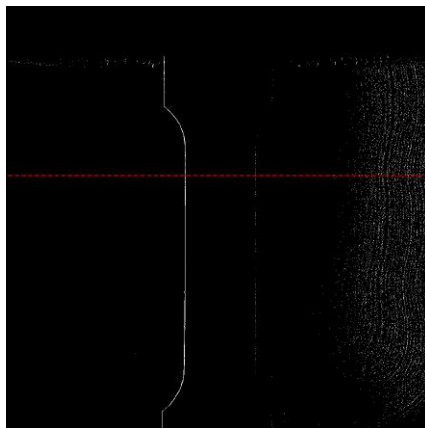
(a) Original image.

(b) Original image, 800<sup>th</sup> pixel row values.

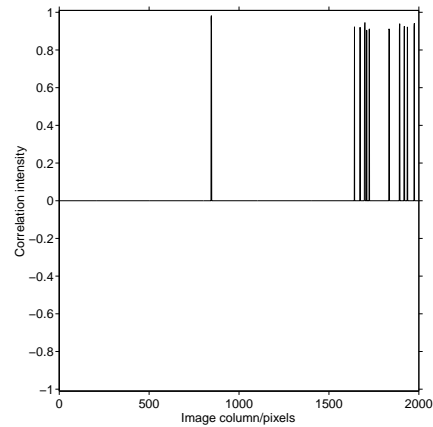
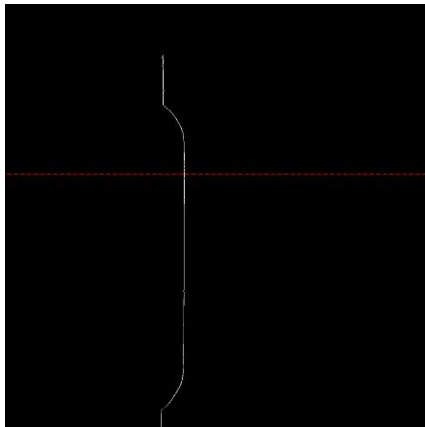
(c) Correlation surface.

(d) Correlation surface, 800<sup>th</sup> pixel row values. The peak value is at column 845.

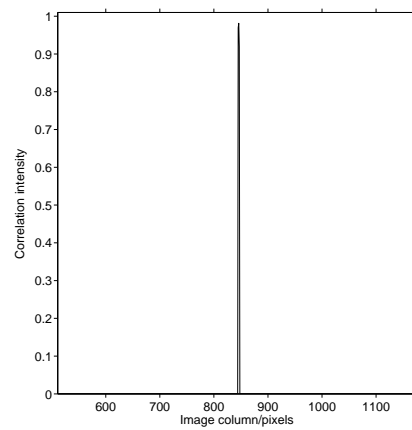
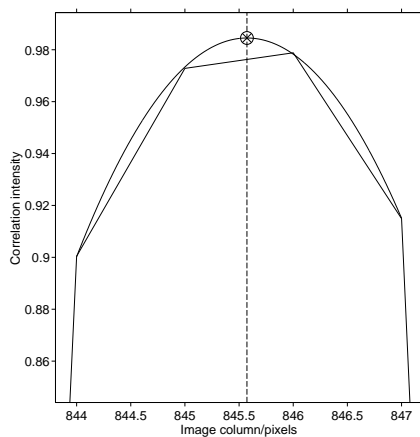
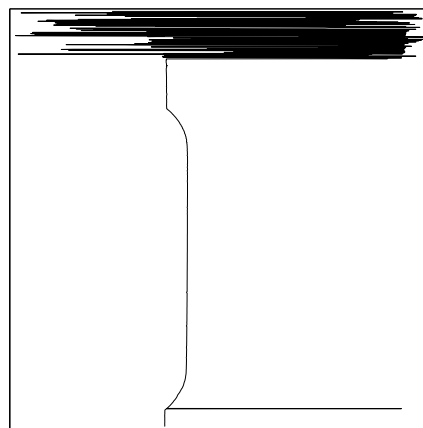
**Figure 2.2:** Part 1 of 2: The edge detection procedure applied to the left hand edge of a typical QS specimen photo. The correlation surface was produced by normalised cross-correlation with a 1 by 22 binary template.



(a) Thresholded correlation surface.

(b) Thresholded correlation surface, 800<sup>th</sup> pixel row values.

(c) Reduced correlation surface.

(d) Reduced correlation surface, 800<sup>th</sup> pixel row values.(e) Parabola fit to the peak on the 800<sup>th</sup> pixel row.

(f) Left edge position in image.

**Figure 2.3:** Part 2 of 2: The edge detection procedure applied to the left hand edge of a typical QS specimen photo. The thresholded NCCI is shown as is the NCCI image filtered by group dimension ranking. An example of a parabola fitting is shown that identifies the sub-pixel edge location for its row.

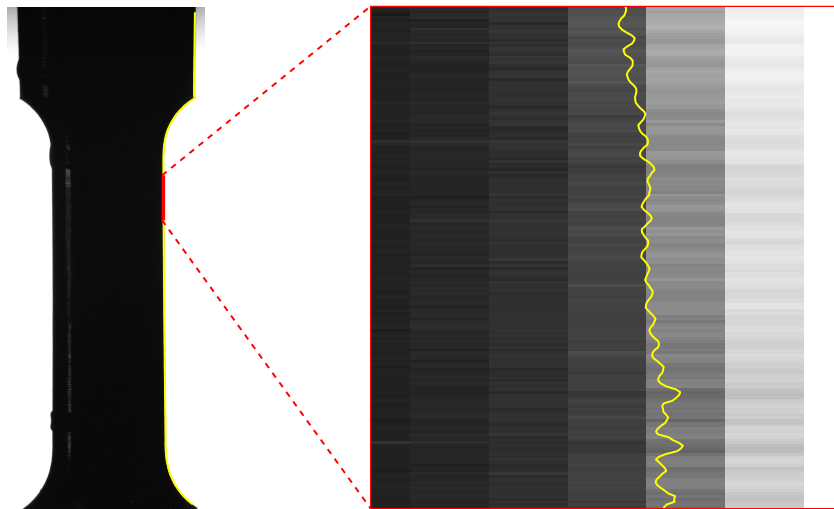


**Figure 2.4:** An expanded view of a specimen's edge. The 3mm gauge diameter of the specimen shown spans approximately 450 pixels and the expanded region is 6 pixels wide by 178 pixels high. The edge positions have been smoothed by a four-pixel averaging filter.

### Similarity of edges between frames

When the image acquisition rate is sufficiently high, the location of the edges of a specimen do not move very far between frames. This provides an opportunity to increase simultaneously the robustness and the speed of computation during edge detection for all but the first image. Given the maximum distance a specimen can displace between frames, study of the subsequent images can be reduced to a region that surrounds the previous location of the edges on each row, plus the potential displacement increment, plus the length of the template. This reduces the possibility of false edge peaks being confused for the true edge peak in the NCCI and it also reduces the computation time for calculating the NCCI and ranking the contiguous regions.

## 2.2 Image calibration: sources of error

Ideally, the lens and CCD (Charge-Coupled Device) arrangement in a digital camera can repeatedly record perfect pinhole-camera [67] images of the object to be photographed. However

---

there are several sources of error that alter the image from this ideal.

### 2.2.1 Lens distortion

Owing to the finite size of the lens aperture, to allow light to enter, the focal distance is fixed so that only objects within a certain depth of field from the lens will be in sharp focus. Reducing the aperture size increases the depth of field, but at the cost of reducing the amount of light reaching the CCD, which causes other problems (see ‘CCD distortion’ below). Another source of error from the lens is that of the lens curvature required to offer a range of magnifications and focusing depth in variable lens configurations. These configurations invariably cause either barrel or pincushion radial distortion, where objects in the image away from the camera’s optical centre will appear, respectively, smaller or larger than they would at the centre. See figure 2.7a for an example of the pincushion distortion encountered in QS images.

### 2.2.2 Multiple CCD distortion

Another type of distortion that can arise in multiple CCD cameras, such as the Ultra-High-Speed SIMX16 camera used here, is projective distortion due to misalignment of the CCDs. This most commonly presents itself as the shift and rotation of images relative to one another, but can also include anisotropic scaling leading to a full projective misalignment. This distortion was rectified by aligning all frames to the first frame in the series. To do this a checkerboard grid pattern was photographed in all 16 frames. The corners of the pattern were located in the images using DIC. The projective homography that transformed the coordinates of the points from their location in each image to their location in the initial frame was computed using the least squares homography fitting given by Zisserman [67].

### 2.2.3 Fibre-discontinuity image shearing

The projective distortion, however, does not take into account fibre-discontinuity shearing of the images. Ultra-High-Speed cameras often use optical fibres to guide the light separately to the CCDs, which provides a more efficient optical coupling, but introduces the possibility of discontinuity shearing because of fibre misalignment. Figure 2.5 shows an example of fibre shearing in the SIMX16 by representing two different images as different colour channels in a single image. Figure 2.6 shows an example of a specimen photographed at HR during tensile loading; a region has been highlighted that has clearly sheared whilst the specimen remained unchanged in reality.

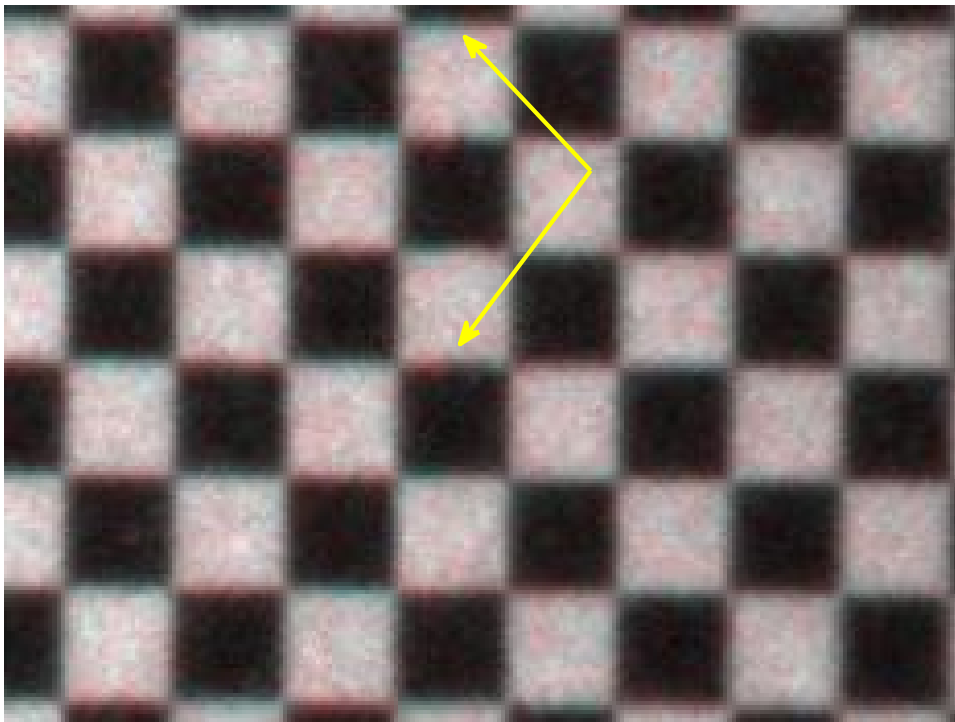


**Figure 2.5:** Fibre shearing in SIMX16 images. The red channel is a cropped region of the 4th frame of 16 and the green and blue channels are the same region of the 5th frame. Note that the central column of squares has a shear line running vertically, as indicated by the yellow arrows.

Correction for shearing distortion was not implemented in the current research, however a proposal for its rectification is given in § 7.3. The degree of distortion created by this problem is assumed to be small, but potentially significant when the data are used for validation of material

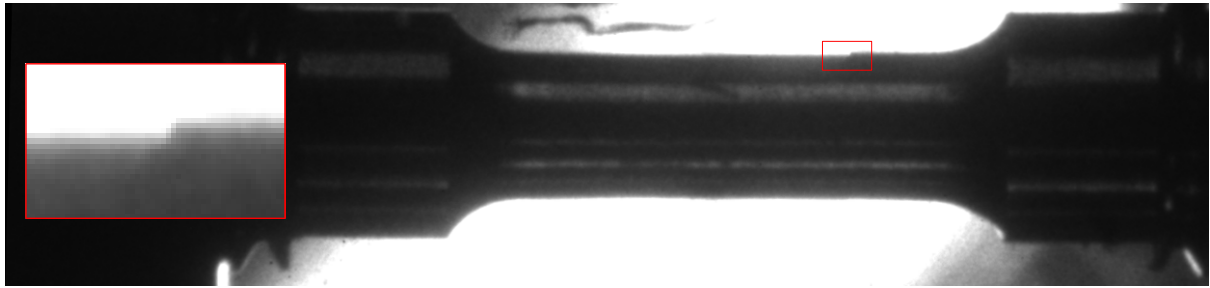


**Figure 2.6:** A HR tensile specimen during loading. The red box shows a region, inset, around a sheared section of the image that shows a sharp change in surface position that was not present in reality.

models.

### 2.2.4 CCD distortion

The CCDs convert photons to an electrical signal which is stored as a digital value to create the digital images. When there are few photons reaching the CCD, which is often the case when the exposure time is very short and/or the aperture is small, the signal generated has to be amplified and will invariably be noisy. Hence a fraction of the intensity of the pixel values will be random, or at least unrepresentative of the number of photons reaching the detector. See [68] for more analysis of the various types of noise present in images and its effect on image analysis. Other types of CCD noise include dead pixels, where a pixel always reports the same intensity value. Whilst dead pixels are a manufacturing defect, in practice it is very difficult to eliminate them completely and they must either be ignored or compensated for.

### 2.2.5 Radial distortion rectification

Methods for rectification of radial distortion were investigated. The algorithm presented in [69] and [67] was implemented in Matlab, but it was found to be poorer at rectifying the radial distortion than the implementation provided by the Matlab Calibration Toolbox [70], which

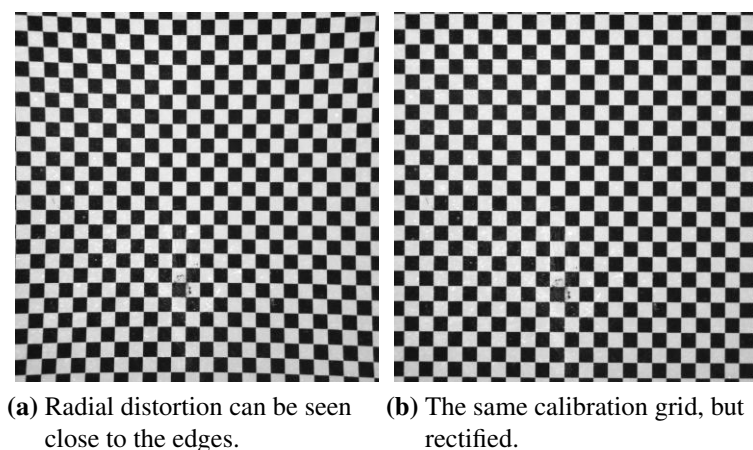


**Figure 2.7:** A calibration grid used to calibrate the cameras. Before and after rectification.

was adopted and customised for this research. The results of a rectification using the toolbox can be seen in figure 2.7.

During the photogrammetric processing the radial rectification was applied only to the detected edge locations, as there were far fewer calculations to perform: In QS images ( $2000 \times 2000$  resolution) there were 4000 edge locations, whereas the images had  $4 \times 10^6$  pixel locations. To rectify an entire image the location of each pixel in the undistorted image had to be calculated and then, because the pixels moved to non-integral locations, two dimensional interpolation had to be performed to produce a raster image once more. Whereas to rectify edge locations required simply calculating the undistorted position and storing that location.

## 2.3 Conclusions

This chapter has presented a robust and accurate method for obtaining the sub-pixel location of the edge outline of a silhouetted specimen in digital images where noise, blurring and artefacts can significantly influence the results. A template matching strategy was used to filter images so that positions of the underlying edge would respond most strongly. Criteria for choosing the correct length of template were given. A method for filtering out the regions that were not the true edge locations but still responded strongly to the template matching was presented.

Also described in this chapter were the reasons why acquiring edges in real images can result in different results from the ideal situation of a perfect pinhole camera model. Radial distortion had the greatest influence and the method used to correct for this error was described.

## Use of Photogrammetry to Infer Evolving Cross-Section of a Uniaxial Test

---

### 3.1 Introduction

The use of any material in structural applications requires a knowledge of its mechanical properties, in particular its response to applied loading at different strain rates and temperatures [31]. A common technique for measuring these properties is the uniaxial tensile test on cylindrical dog-bone specimens. Calculation of true stress in these specimens requires knowledge of the variation of the cross-section as a function of time.

The inelastic response of materials to applied uniaxial deformation is typically measured using tensile or compressive specimens of initially circular cross-section. Under deformation, this cross-section may no longer be axisymmetric if the material behaves anisotropically. If the anisotropic material properties have certain symmetry properties, such as homogeneity, then the cross-section may deform into an ellipse. In order to determine the parameters that govern plastic anisotropy in metals, it has been shown [71] that the ratio of the strains perpendicular to the loading axis may be used, which may be determined from the shape of the cross-section.

Initially cylindrical specimens, manufactured from the in-plane directions of rolled Ti-6Al-4V plate, have been demonstrated to deform elliptically by McDarmaid [7] and Yang [6].

Both McDarmaid and Yang have shown how the ellipticity in Ti-6Al-4V specimens can be used to measure the degree of anisotropy. However there are significant drawbacks to McDarmaid's method; because the test was interrupted and the specimen major and minor axes measured in the unloaded state. Yang's method involved a "diametral strain-gauge (extensometer) with two parallel arms", which was used to measure the diametral strain at either a fixed angle or a fixed surface position around the circumference of the specimen cross-section. Owing to the use of a single diametral measure, Yang had to make assumptions concerning the constancy of the anisotropic ratios in order to approximate the axial strain and the true stress at a particular elliptical cross-section.

The variation in anisotropic deformation after the UTS (ultimate tensile strength), in the necking region, provides useful data for identification of model parameters or validation of constitutive relationships simulated using FE modelling.

Optical methods offer the best means of measuring these cross-sections, since multi-point measurements can be made. They operate at all strain rates for which photographs can be taken, without significant alteration to the post processing, and can be applied to environmentally controlled experiments. Optical techniques for measuring two dimensional geometry from a single view of the specimen are commonplace, e.g. [44]. However a means of constructing the 3D specimen shape from 2D images is required for anisotropic deformation of specimens.

The measurement technique proposed here uses an optical method to determine the elliptical cross-section plane by plane *in situ* through a multi-point measurement that does not require assumptions about material response or the direction of the specimen w.r.t. the material axes. It is applicable to anisotropic, homogeneous specimens undergoing uniaxial loading at any strain rate.

Previous work on cross-sectional reconstruction has often concentrated on computing arbitrary contours [72] into generalised 3D surfaces. Tubular cross-section measurements can be achieved using a single camera by rotating the specimen [73] or the camera [74] to acquire

many views for reconstruction. However, these methods cannot be applied to materials characterisation experiments, where tensile loads of many kN would prevent rotation of the specimen and, at least at high strain rates where acquisition is required on  $\mu\text{s}$  time scales, rotation of the camera is impossible.

Hartley *et. al* [45,46] developed an optical method for measuring the profile of a necking specimen and suggested applying it to measure the elliptical shape of an anisotropic specimen using two orthogonal views aligned with the major and minor axes of the cross-section. The technique was to project a silhouette of the specimen onto a vibrating mirror which scanned the image past a vertical slit, behind which a photo diode converted the light intensity into an electrical signal. This signal then contained information about the minimum radius of the current projection in its peak-to-peak value and the neck profile curvature in the second differential. The signal was calibrated so that it could be used to control the strain rate in necking specimens. This technique has the disadvantages of requiring a vibrating mirror, which means its range of deformation velocities is limited, and of assuming longitudinal symmetry of the specimen about its neck, which may be an oversimplification for certain experiments. The measurements obtained by this method for one view of the specimen can now be obtained by edge detection, such as that in chapter 2, in digital images. The technique also had the disadvantage that it could be used only when the major and minor axes of deformation were known prior to the experiment and any rotational misalignment of the specimen would reduce the apparent ellipticity, which is the case for all techniques that measure elliptical shapes using only aligned views.

In the method outlined here, at least three views of a deforming specimen are used to find tangent edge rays from its silhouette. An algorithm that can incorporate any number of tangential rays is used to find the least-squares fit of an arbitrary ellipse to them.

The method has been evaluated using simulations of the experimental procedure with stochastic error estimations and by measuring similarly sized elliptical prisms that have been

accurately measured using a CMM. The method has been applied to tensile dog bone specimens of the CR-Ti-6Al-4V alloy which were loaded quasi-statically and at a high strain rate.

## 3.2 Method

The edge position data, derived from the images and corrected for any lens distortion (as described in chapter 2) and for misalignment of the positions of the cameras, were used to calculate surface tangents to specimens at all discernible axial positions. Ellipses were found that best-fit these tangents using a least-squares technique. The varying elliptical cross-sections of the specimen were then found. The following sections describe the processes involved in the reconstruction of specimen shapes, a general overview of the method is given in figure 3.1 for a specimen measured using three silhouetted views.

### 3.2.1 Image Capture and Processing

The process of obtaining 2D specimen surface profiles from images has been given in chapter 2. From these profiles, tangent lines from the camera centres to the specimen are constructed, which are then taken forward into the reconstruction process.

In both the quasi-static (QS) and high strain rate (HR) experiments presented here, cylindrical dog bone tensile specimens with a gauge diameter of 3 mm and a gauge length of 8 mm were used, as seen in figures 1.8, 3.5a and 3.6a, on pages 18, 52 and 53.

In the QS experiments, three TELI Digital Cameras (CSB4000CL) with 4 megapixel 10-bit greyscale CMOS sensors, using Computar Megapixel lenses, were used to capture three views of a specimen from angles at  $-45^\circ$ ,  $0^\circ$  and  $45^\circ$  w.r.t. the centre camera's central axis, figure 3.2. One end of the specimen was displaced at  $5.6 \times 10^{-6} \text{ ms}^{-1}$ , which corresponds to a plastic strain rate of  $7 \times 10^{-4} \text{ s}^{-1}$ ; frames were recorded simultaneously on all cameras at a rate of one every three seconds. The resolution of the images was  $6.5 \mu\text{m}/\text{pixel}$ .

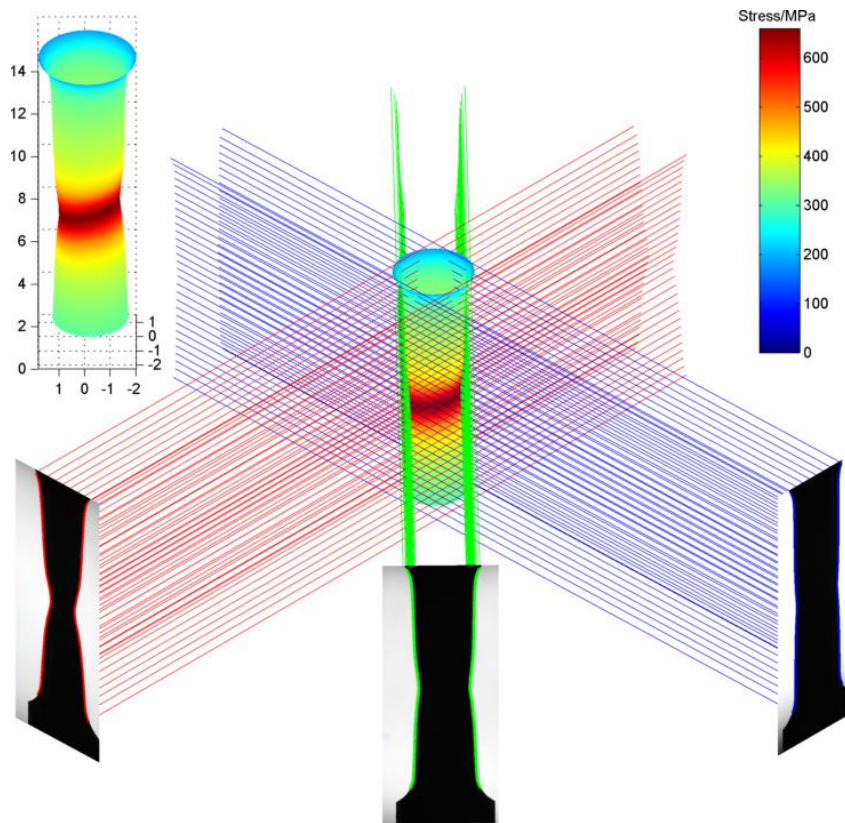


**Figure 3.1:** The overview of the elliptical cross-section reconstruction technique. Three cameras photograph the specimen from different angles. From these photographs, the shape of the specimen may be calculated. At the centre and inset are the reconstructed specimen, shaded with direct true stress/MPa.

For HR experiments, a Specialised Imaging SIMX16 camera was used with two mirrors to give views at  $-120^\circ$ ,  $0^\circ$  and  $120^\circ$ , figure 3.3. HR experiments were performed at a strain rate of  $3 \times 10^3 \text{ s}^{-1}$  in the plastic region; 16 images were recorded at a frame rate of 76 000 frames per second. The resolution of the images was  $13 \mu\text{m}/\text{pixel}$ . Strain rates in both QS and HR are quoted  $\pm 10\%$ .

In the QS experiments described in this chapter, the specimen was reverse lit to give a silhouette view for the two side cameras and front lit for the centre camera, to allow good contrast of the edges in all images. In HR experiments in this chapter, the specimen's edges are front lit in all views, as shown in figure 3.6a. In later chapters the technique was modified to allow silhouettes to be recorded at all strain rates, in all views, which has been found to produce better results.

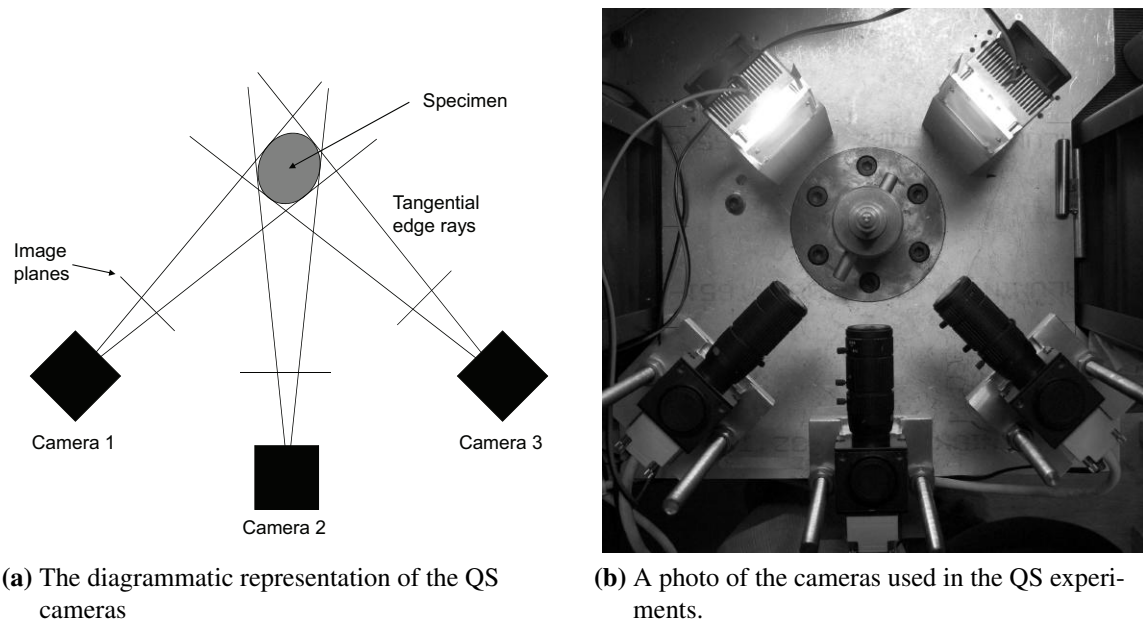


**Figure 3.2:** The arrangement of the apparatus for multiple cameras as used in the QS experiments. The angular spacing of  $45^\circ$  between the cameras is a limitation of the equipment and is shown later to be sub-optimal for elliptical fitting.

The camera lenses were assumed to be telecentric, in that the cameras were assumed to be infinitely far from the specimen, with no parallax error, to simplify the extrinsic calibration. The error due to this assumption is explored in 3.4 and found to be negligible for the focal lengths used here. Photographs and edges of the undeformed QS and HR specimens in this chapter are shown in figures 3.5b and 3.6b.

### 3.2.2 Extrinsic calibration

The description that follows is valid for either the multiple-camera configuration used during QS experiments or the single-camera-and-two-mirror configuration used in HR deformation where two of the cameras are virtual, but reference will be made to three “cameras”.

The cameras were extrinsically calibrated so that their location relative to one another and the specimen was known. This calibration was performed partly using measurements of the configuration and partly by image analysis. Firstly, it could be reasonably assumed, after the

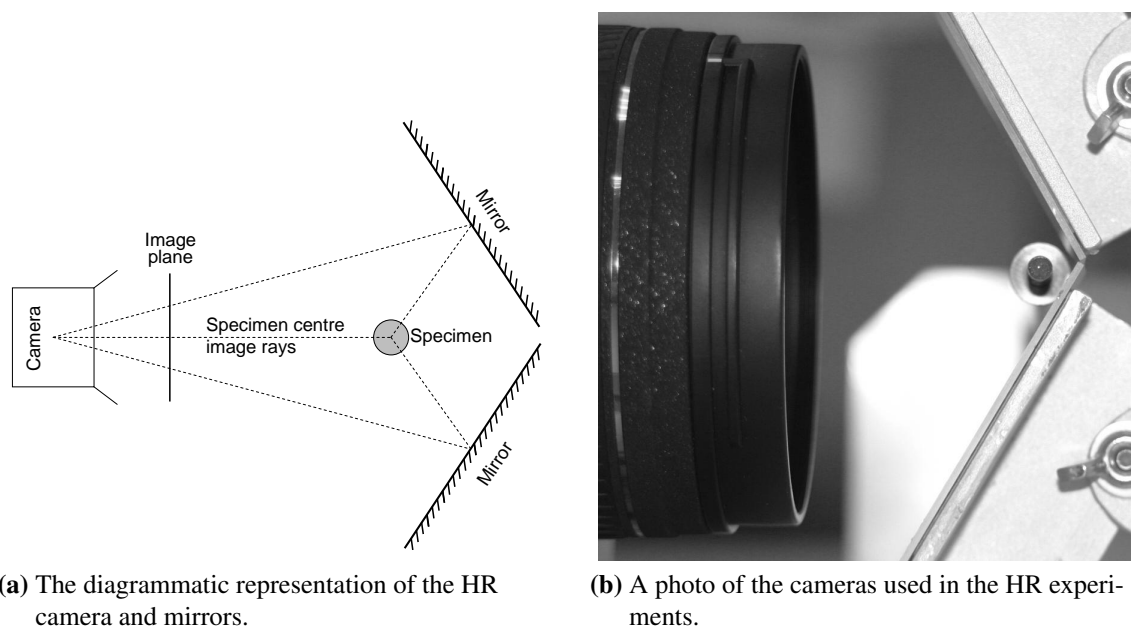


**Figure 3.3:** Schematic diagram and photo of the arrangement of the apparatus for single cameras as used in HR experiments here. Three views spaced at  $120^\circ$  give well conditioned data for ellipse fitting.

application of the rectification described in § 2.2.5, that planar objects scale linearly with the pixel dimensions in the digital images. Secondly, the camera optical axes were perpendicular to the specimen axis, i.e. in the radial direction, because the cameras were mounted on stands that locked them in place so that they looked directly at the specimen. The relative angles of the three cameras were measured from the apparatus. A final assumption was that the camera centres were very far from the specimen, the validity of which is investigated in 3.4. The remaining parameters for extrinsic calibration were the position of the camera centres along the specimen axis and the scale and orientation (with respect to camera-roll) of the specimen in the images. Whilst care was taken to position the cameras in exact known locations with the same optical settings, small differences will always remain that have to be taken into account for accurate photogrammetric processing.

The initial dimensions of the specimens were always measured before the experiments. If all three cameras were perfectly aligned then the initially cylindrical specimen would have appeared exactly the same in each one. Hence the dimensions of the unloaded specimen in the

initial frames of the experiment could be used to find the scale, roll-angle and camera position for alignment purposes. This meant that a camera calibration by calculation of the complete fundamental matrix [67] was unnecessary.

The edges in the parallel gauge section were fitted, using least-squares, with straight lines. The gauge diameter was divided by the average separation of these lines in pixels to find the scale of the images in mm/pixel. The orientation of the bisector of these two lines was used to find the true loading axis of the specimen. In QS images the edges were parallel because the cameras were enforced to be looking along a radius. However, in HR images the gauge section could appear smaller at one end than the other if the mirrors or camera were slightly off-axis. To overcome this, the HR edges were first linearly scaled so that the edges of the gauge section were made parallel again.

For tensile specimens the positions of the corners of the shoulders of the specimen in the images were found by DIC. The mean position of the bottom shoulders was taken to be the origin. In compression specimens the top of the lower anvil was taken to be the origin.

After radial distortion had been removed and extrinsic calibration parameters had been found, the coordinates of specimen dimensions in each of the images of the undeformed specimen became the same. Figure 3.4 demonstrates the result of this calibration and rectification procedure by applying the rectification directly to the images used for calibration of a specimen photographed with three silhouetted views. This figure clearly shows the degree of initial misalignment and the extent to which it has been corrected.

For computational efficiency, the rectification of the edge data was performed on the edge position data and not on the images prior to edge detection (as in figure 3.4).

### 3.2.3 Elliptical fitting

After rectifying and transforming the edge data from pixel coordinates (which had sub-pixel resolution horizontally and integer pixel resolution vertically) into extrinsically calibrated mm

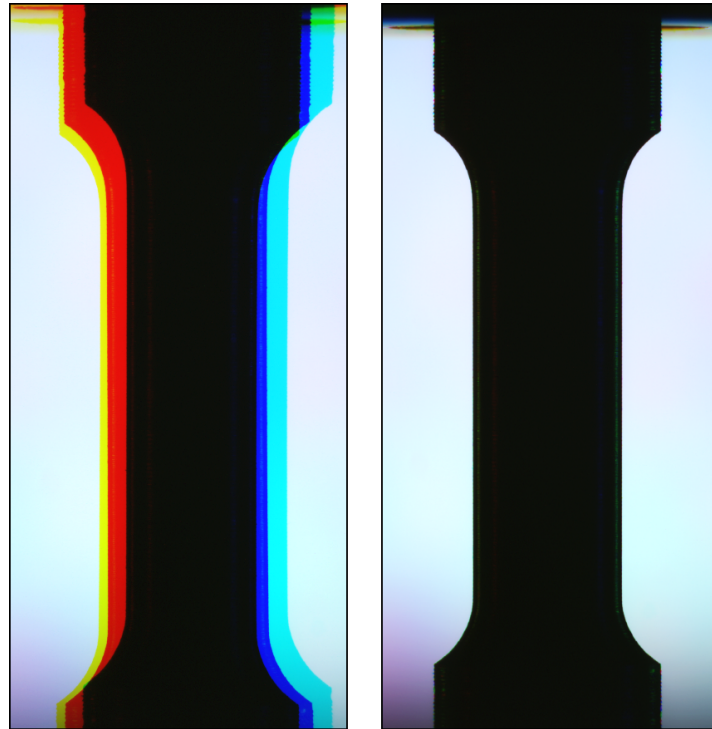
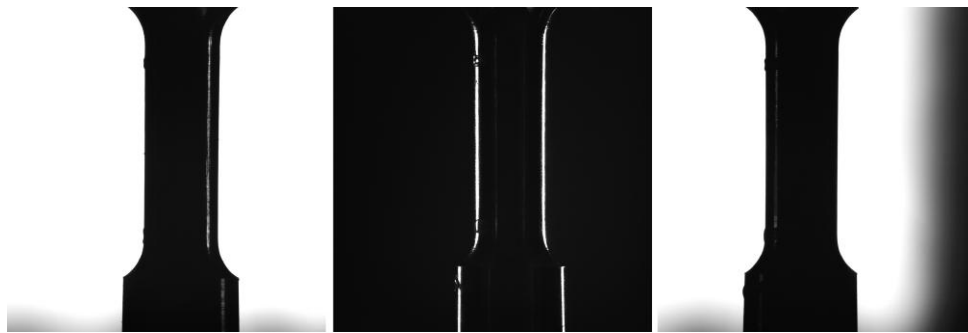


**Figure 3.4:** The first image shows a composite photo of the specimen seen from the three different cameras, where the red channel is the left image, the green channel the centre image and the blue channel the right image. The second picture has the same colour mapping, and is a composite photo of the images after the radial distortion has been removed and they have been extrinsically aligned. Note that the second image has negligible coloured fringing around the gauge section and shoulders, demonstrating the accuracy of the alignment.

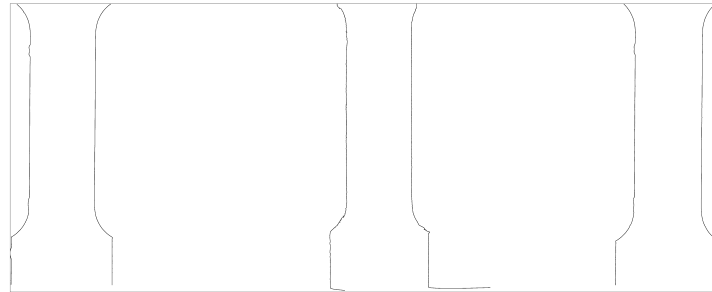
coordinates, the two edges in each of the three cameras had discrete vertical ordinates. To calculate the elliptical fit to a cross-section, at a particular axial position in the specimen, searches were conducted to find the horizontal position of each of the six edge positions that had corresponding vertical positions closest to that desired. These horizontal positions were then assumed to lie on the intersection of the camera image plane and the cross-sectional plane. Back projected edge rays were formed that passed through the edge positions in the direction normal to the image plane. These lines were tangential to the specimen, as shown in figure 3.2, and will be called tangent lines. The tangent lines were used to reconstruct the elliptical shape of the specimen as a function of axial position and time.

The edge data could have been interpolated by splines to estimate the horizontal edge locations at vertical positions that didn't match discrete datum points, but this was deemed

unnecessary because the axial pixel resolution was sufficiently high (approximately 1000 pixels over the 8 mm gauge length in QS images) to capture the relatively smooth variation in the cross-sectional shape of the specimens here. The error introduced by fitting ellipses to positions that could range vertically by up to one pixel is unlikely to be significant. However if the technique were applied to cross-sections with sharp discontinuities, the interpolation may be required. This meant that cross-sectional shape of the specimens was only calculated with an axial resolution that corresponded directly to the pixel resolution of the cameras.



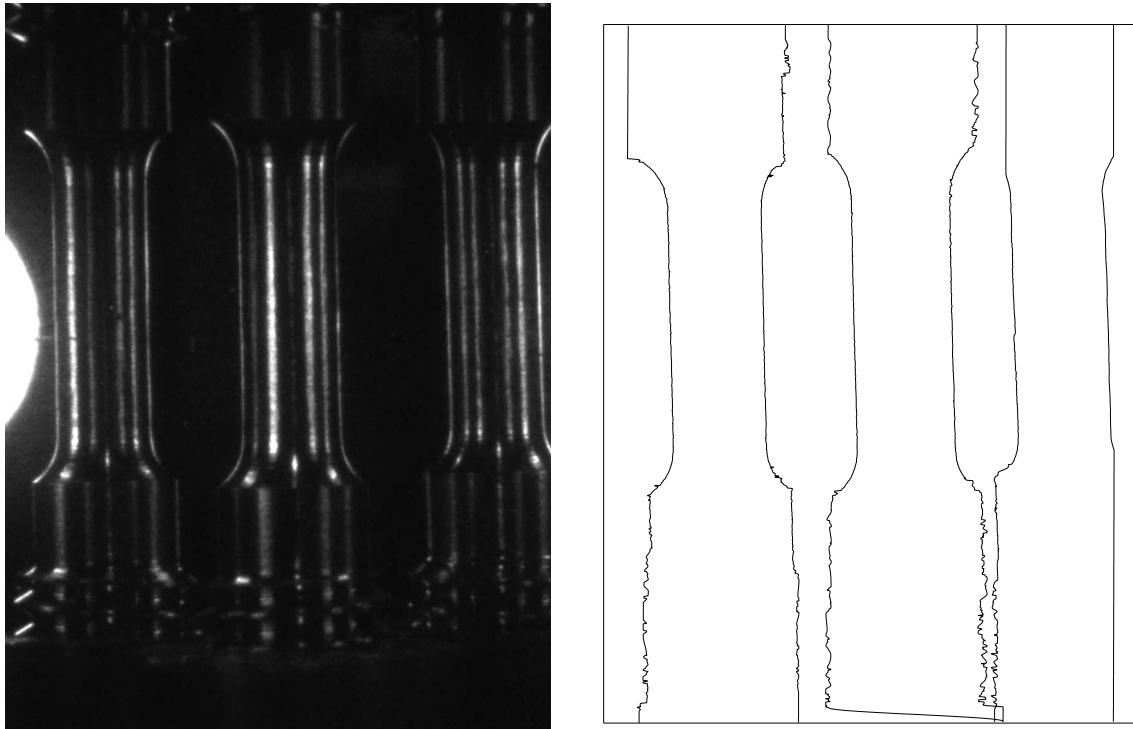
(a) An example of the images captured in one time step in the QS experiments.



(b) The edges of the QS specimen.

**Figure 3.5:** The images and the edges of the QS specimen calculated from them.

The problem of fitting ellipses to inaccurate data points has been explored thoroughly in the literature. There are several methods of finding a best fit to data points. Wynn [75] shows that least squares fitting using one of several measures of distance to the ellipse can give good results with low residuals. Gander [76] presented a least squares solution and Fisher and Halir [77, 78] have shown that *direct* least squares fitting of ellipses to data points is possible, which offers the possibility of improving computation speed over iterative methods. However,



(a) An example of an image captured in one time step in the HR experiments.

(b) The edges of the HR specimen.

**Figure 3.6:** The images of the HR specimen, and the edges calculated from them.

the problem here is not one of fitting ellipse to points, but to tangent lines. Eagles [79] gives a graphical method of constructing an ellipse from five planar tangent lines, which uses the intersections of these lines with further construction lines to find the tangent points of the ellipse that lies between them. This method is useful for the case when there are only five tangent lines, as is the general solution to exact conic section fitting which is derived and explained below.

Only five lines tangent to an ellipse, or any conic section, are required to define its shape fully [79]; the six line configuration described has a redundancy and requires an optimum fitting method. Where tangent lines and not points are given, it is known that the error is in the measured position of edge points, so one fitting method could have been to use the sum of the shortest distances (squared) between the lines and the ellipse as the objective for minimisation. However an iterative scheme that does not involve the non-linear step of choosing the smaller of the two possible distances from the tangent points to the ellipse could not be found. Instead,

the algebraic distance squared, equation (3.9), presented later in the chapter, was used as an objective function. The algebraic distance was found to be a good measure to use for ellipse fitting in both [75] and [80].

To make the fitting possible, and to reduce the number of steps that the iterative procedure took, a good initial estimate of the parameters was required. The initial estimate was taken to be a circle centred at the centroid of a triangle formed by the three (for these experiments) lines bisecting each camera's pair of tangent lines, which are shown in figure 3.7. The circle's radius is taken as the mean distance from this centre to all of the rays.

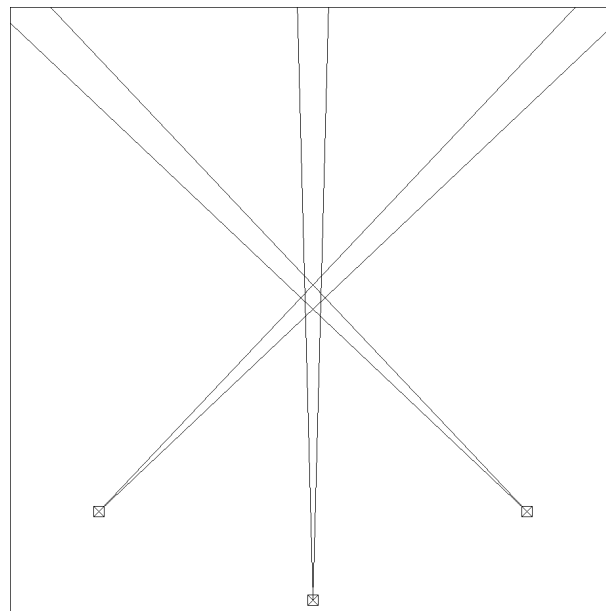


**Figure 3.7:** The tangent lines for a single cross-section of the specimen in the QS configuration. In this diagram the lines are shown as if they were from a pinhole camera, in that they are not parallel, as they would be from a telecentric lens.

An alternative initial estimate can be found by choosing five of the six available rays and computing the ellipse that exactly touches them all. Using this method did not significantly improve the total computation time needed to make the initial estimate and derive the least squares fit. Further, such a fit could have caused the minimisation to have reached a local minimum that was not the true minimum. This would have caused orientation biasing, which was prevented somewhat by using a circle.

### Derivation of iterative solutions

The derivation of the conic equation for an ellipse written in the space of the tangent line gradients  $m$  and their  $y$ -axis intercepts,  $c$ , was as follows.

The lines, projected onto a horizontal plane, become, with an appropriate choice of coordinate system orientation, six lines in a plane, two from each camera, of the form:

$$y = m_j x + c_j \quad j = 1, \dots, 6 \quad (3.1)$$

or

$$q(x, y) = -y + m_j x + c_j = 0 \quad (3.2)$$

If the intersection of the specimen's vertical axis (i.e. the centre of the ellipse) with the horizontal plane is taken to be the origin of the coordinate system, the ellipse never passes through the origin and the elliptical conic section can be represented as an implicit second order polynomial of the form:

$$p(x, y) = Ax^2 + Bxy + Cy^2 + Dx + Ey + 1 = 0. \quad (3.3)$$

At the points of tangency  $(X_i, Y_i)$ , where the lines touch the ellipse, the tangent lines, (3.2), and the ellipse, (3.3), have equal gradients, and hence equal normal directions,

$$\nabla p(X_i, Y_i)_i = \begin{bmatrix} 2AX_i + BY_i + D \\ BX_i + 2CY_i + E \end{bmatrix} = \lambda \nabla q(X_i, Y_i)_i = \lambda \begin{bmatrix} m_i \\ -1 \end{bmatrix}, \quad (3.4)$$

where  $\lambda$  is an arbitrary scalar. From (3.4):

$$\frac{2AX_i + BY_i + D}{BX_i + 2CY_i + E} = -m_i, \quad (3.5)$$

$$X_i(2A + Bm_i) + Y_i(B + 2Cm_i) + Em_i + D = 0.$$

Substituting (3.1) at the tangent points,  $(X_i, Y_i)$ , into (3.5) gives:

$$X_i = \frac{-(Bc_i + 2Cm_i c_i + Em_i + D)}{2(A + Bm_i + Cm_i^2)}. \quad (3.6)$$

Substituting (3.1) and then (3.6) into (3.3) at the points of tangency gives:

$$\begin{aligned} p(X_i, Y_i) &= f(A, B, C, D, E, F) \\ &= A\mu^2 + B\mu(m_i\mu + c_i) + C(m_i\mu + c_i)^2 + D\mu + E(m_i\mu + c_i) + 1 = 0, \end{aligned} \quad (3.7)$$

when  $m_i$  and  $c_i$  are tangent to the ellipse, where:

$$\mu = \frac{-(Bc_i + 2Cm_i c_i + Em_i + D)}{2(A + Bm_i + Cm_i^2)}.$$

### Fitting to five tangent lines

If an exact solution to the fitting of an ellipse to five lines is required, as it may be when finding better initial estimates for the least squares solution, then five equations of the form of (3.7) must be solved simultaneously. Effort was put into finding an explicit form for the solution of the five ellipse constants,  $A, B, C, D, E$ , in terms of the ten line parameters,  $m_i, c_i \quad i = 1, \dots, 5$ , but it could not be found. Instead Newton's method was implemented:

$$\mathbf{a}_{n+1} = \mathbf{a}_n - \mathbf{J}^{-1}\mathbf{f}, \quad (3.8)$$

where:

$$\mathbf{a} = \begin{pmatrix} A \\ B \\ C \\ D \\ E \end{pmatrix}, \mathbf{f} = \begin{pmatrix} f_1(\mathbf{a}) \\ f_2(\mathbf{a}) \\ f_3(\mathbf{a}) \\ f_4(\mathbf{a}) \\ f_5(\mathbf{a}) \end{pmatrix}, \mathbf{J} = \frac{\partial(f_1, f_2, f_3, f_4, f_5)}{\partial(A, B, C, D, E)}.$$

This iterative scheme still required an initial estimate,  $\mathbf{a}_0$ , which was taken as the conic equation parameters given by the average circle created by the five lines, described earlier. With this circular estimate, it was found that this scheme often requires fewer than 3 steps to compute the exact ellipse fit to a sufficient accuracy in practical examples.

### Fitting to more than five tangent lines

When many ( $> 5$ ) lines from many camera views are available, non-linear least squares fitting using gradient descent can be used to find the optimum ellipse. The procedure for fitting an ellipse to the lines that over-define it begins with the square of equation (3.7), the algebraic distance squared:

$$g(m_i, c_i : \mathbf{a}) = f^2(m_i, c_i : \mathbf{a}). \quad (3.9)$$

$g(m_i, c_i : \mathbf{a})$  is a positive, non-zero valued, function when the line it is a function of is not a true tangent to the ellipse fit. The best fit is obtained when the sum of all  $g(m_i, c_i : \mathbf{a})$  is a minimum and an exact fit is obtained when all  $g = 0$ . Writing the  $g$  equations in vector form,

$$\mathbf{g}(\mathbf{a}) = [g(m_1, c_1 : \mathbf{a}), \dots, g(m_p, c_p : \mathbf{a})]^T, \quad (3.10)$$

allows the difference between the desired value of the equations,  $\mathbf{0}$ , and their value at a particular  $\mathbf{a}$  to be defined as  $d\boldsymbol{\beta} = (\mathbf{0}) - \mathbf{g}(\mathbf{a}) = -\mathbf{g}(\mathbf{a})$ . To obtain a linearised estimate of the change,  $d\mathbf{a}$ , required to reduce  $\mathbf{g}(\mathbf{a})$ , following the derivations in, for instance, [67] and [76] the Jacobian of (3.10) is multiplied by a small change in  $\mathbf{a}$ :

$$d\boldsymbol{\beta} = \begin{pmatrix} \frac{\partial g}{\partial A} \Big|_{m_1, c_1, \mathbf{a}} & \frac{\partial g}{\partial B} \Big|_{m_1, c_1, \mathbf{a}} & \dots & \frac{\partial g}{\partial E} \Big|_{m_1, c_1, \mathbf{a}} \\ \frac{\partial g}{\partial A} \Big|_{m_2, c_2, \mathbf{a}} & \frac{\partial g}{\partial B} \Big|_{m_2, c_2, \mathbf{a}} & \dots & \frac{\partial g}{\partial E} \Big|_{m_2, c_2, \mathbf{a}} \\ \vdots & \vdots & \ddots & \vdots \\ \frac{\partial g}{\partial A} \Big|_{m_p, c_p, \mathbf{a}} & \dots & \dots & \frac{\partial g}{\partial E} \Big|_{m_p, c_p, \mathbf{a}} \end{pmatrix} d\mathbf{a}, \quad (3.11)$$

which can be written

$$d\boldsymbol{\beta} = \mathbf{A}d\mathbf{a}. \quad (3.12)$$

Then:

$$\mathbf{A}^T d\boldsymbol{\beta} = \mathbf{A}^T \mathbf{A} d\mathbf{a}. \quad (3.13)$$

Defining:

$$\mathbf{r} = \mathbf{A}^T d\boldsymbol{\beta},$$

and

$$\mathbf{q} = \mathbf{A}^T \mathbf{A},$$

gives:

$$\mathbf{q}d\mathbf{a} = \mathbf{r}, \quad (3.14)$$

which was solved by Gaussian elimination to give  $d\mathbf{a}_n$ , for the  $n^{\text{th}}$  state of  $\mathbf{a}$ . Applying the change  $\mathbf{a}_{n+1} = \mathbf{a}_n + d\mathbf{a}_n$  in an iterative manner finds the conic parameters,  $\mathbf{a}$ , that gave the least squares fit for  $\mathbf{g}(\mathbf{a})$  by gradient descent. During the iterative procedure the corrector,  $d\mathbf{a}_n$ , can be too large when the current fit is far from optimum because the ‘gradient’ is too large, therefore a fraction of  $d\mathbf{a}_n$  is usually applied to prevent overshooting the optimum state. It has been found, in this research, that  $0.5d\mathbf{a}_n$  allows fitting to ellipses with aspect ratios up to 3 at any angle in three camera configurations.

The criterion for stopping the scheme was when the norm of  $\mathbf{g}(\mathbf{a})$  changed by a sufficiently small amount between consecutive iterations. The results of a least squares fit to six non-exact tangent lines is shown in figure 3.8

After the optimum fit has been obtained a check must be made to ensure that an ellipse, and not a different form of conic section, has been found. The solution is an ellipse if the

discriminant of (3.3) is less than zero:

$$B^2 - 4AC < 0 \quad (3.15)$$

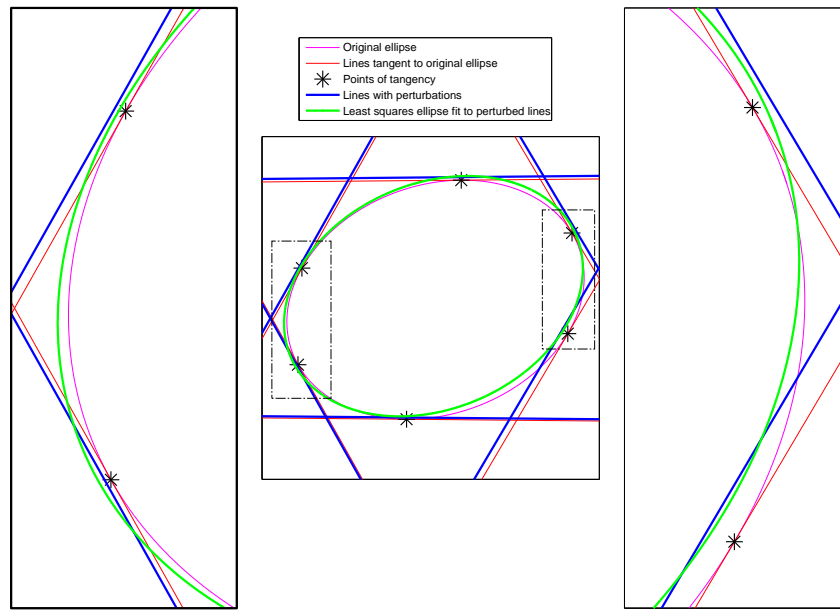
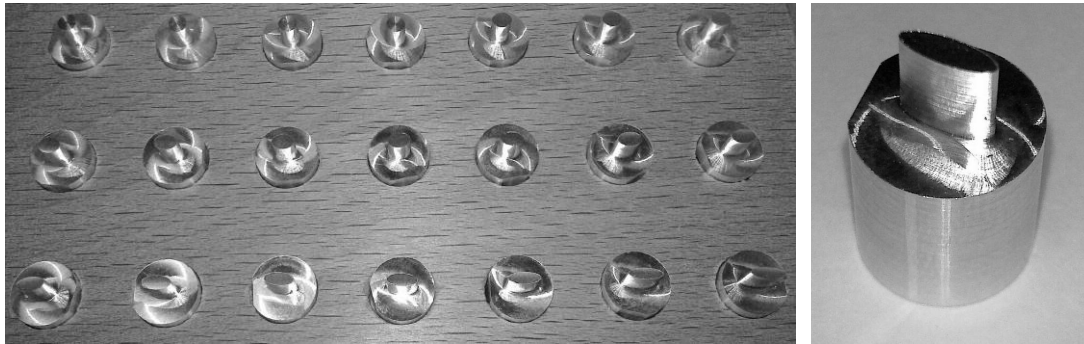


**Figure 3.8:** An exact fit of an ellipse to six tangent lines, and a least squares fit to lines after they have been perturbed slightly. The left and right plots show a closer view of the regions bounded by dashed (— · —) boxes in the central plot.

### 3.3 Estimation of error

Elliptical prisms of precisely known dimensions were measured using the technique described above to estimate the achievable accuracy using the specified equipment. The experiment was also simulated to estimate the optimum values of certain parameters to obtain data of the highest accuracy and to obtain a generic estimate of the accuracy likely to be achieved.



(a) The full range of aluminium calibration prisms created for this research. Only 13 were selected for their dimensions. (b) Calibration prism 20, aspect ratio = 3, major axis length = 2.60 mm

**Figure 3.9:** Photos of the calibration prisms used to validate the technique.

### 3.3.1 Static reconstruction of elliptical prisms

5 mm long elliptical prisms of aluminium with the same cross-sectional area as a 3 mm diameter cylinder were manufactured, by CNC (Computer Numerically Controlled) milling, with a range of aspect ratios to create calibration specimens, the ‘calibration prisms’, as shown in figure 3.9. The dimensions of the calibration prisms were measured using a Mitutoyo SERIES 191 CNC Coordinate Measurement Machine (CMM) , with a quoted accuracy of better than  $\pm 2 \mu\text{m}$ . Approximately 360 evenly spaced positions around the circumference were measured at 1, 2 and 3 mm below the top end of each prism. For all of the prisms the three circumferences were found to have indistinguishable differences and were combined into one set of coordinate measurements.

Ellipses were fitted to these coordinates for each prism. The variation of the points from their elliptical fits can be seen in figures 3.10a through 3.10m. These plots show the CMM measured positions and the elliptical fits to them, which were derived using the method given in [78]. The plots also show ‘error spikes’, which are vectors from the CMM recorded positions to their nearest points on the ellipse, and have a magnitude of 20 times the distance between the two positions to emphasize the distribution of difference from elliptical (otherwise they would not be visible). The pattern seen in the error spikes around the apogees and perigees is due to

the backlash, inherent in the CNC process. However, the deviation from true ellipses in all of the calibration prisms can be seen to be small, and hence they proved to be valid shapes for evaluating the cross-section measurement technique.

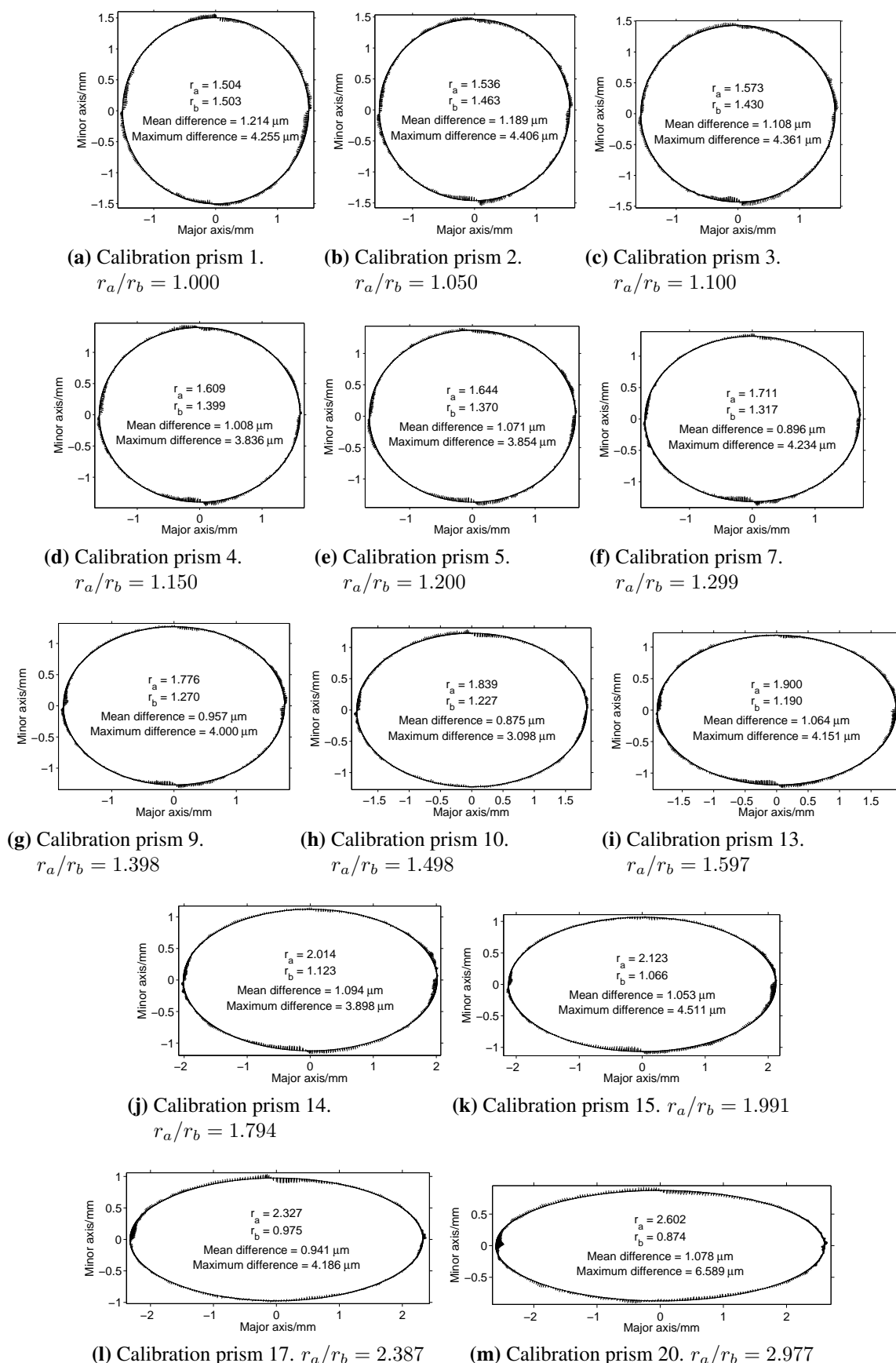


**Figure 3.10:** The calibration prisms with their differences from perfect ellipses. Error spikes are plotted at 20 times the size of the error they represent, for clarity. The mean difference displayed is the mean of the magnitude of the differences. All plots have the same scale.

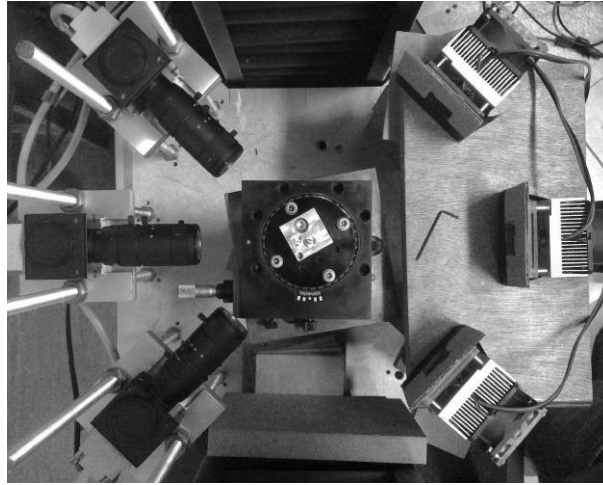


**Figure 3.11:** The rotational stage, mounting device and a calibration prism are shown in plan view at the centre of this photo of the QS experimental configuration.

The calibration prisms were mounted onto a rotational stage at the centre of the QS camera configuration, where their central axes coincided with the usual location of the uniaxial specimen axes. The experimental configuration can be seen in figure 3.11. The three views were all silhouettes. About 440 distinguishable axial positions were measured using the technique for each prism to obtain multiple measurements for validation. The prisms were rotated by  $10^\circ$  and photographed, repeatedly, until they had been rotated through  $180^\circ$  to ascertain whether there was any dependence of accuracy on ellipse orientation.

The rotational stage was only accurate to  $\pm 0.5^\circ$  and hence the orientation could only be known to that accuracy. The error in orientation measured by the technique was always found to be within the error of positioning the rotational stage, and so can be said to be better than  $\pm 0.5^\circ$ , even for the prism with the smallest aspect ratio here, but not for the cylindrical prism. The percentage error in area,  $r_a r_b \pi$ , and in aspect ratio,  $r_a / r_b$ , was calculated at each height along the prism according to  $E = 100(x - \hat{x}) / \hat{x}$  where  $x$  is the measured value and  $\hat{x}$  is the value obtained from the fit to CMM coordinates. The distribution of these percentage errors are shown as vertical frequency distributions at their corresponding orientations in figures 3.12a to 3.12g and figures 3.13a to 3.13f. The errors and the variance can be seen to increase as the aspect ratio increases.

The calibration prisms were designed to cover the range of aspect ratios encountered in the tensile specimens of CP-Zr and Ti-6Al-4V shown in chapters 5 and 6. The results indicate that there is some dependence of the error on the angle of the ellipse relative to the cameras, but the majority of the results have errors that overlap to a greater or lesser extent. It is suggested that in practice the accuracy of the results does not depend very strongly on orientation.

For the HR configuration the prisms were measured in only one orientation. To estimate the discrepancy caused by using multiple CCDs, which have to be calibrated, as described in chapter 2, the results of reconstructing the cross-sections of the same prism using each of the 16 frames of the SIMX16 camera are given in figures 3.14a to 3.14g and figures 3.15a to 3.15f. The errors can be seen to vary slightly with frame, but the most significant result is that the error is greater using the high speed camera under HR loading conditions than when using the QS camera under QS loading conditions, which was expected. There were approximately 180 axial positions for cross-section measurement of the prisms in the HR configuration.

In experiments on Ti-6Al-4V, aspect ratios,  $e = r_a/r_b$ , of no more than 1.18 were observed, which should allow the area and aspect ratio to be determined to within an accuracy of better than the  $\pm 1\%$  for QS loading and  $\pm 4\%$  for HR loading due to the error seen for the prism of  $e = 1.2$ .

Further QS validation of the technique when applied to real specimens is described in chapter 5.

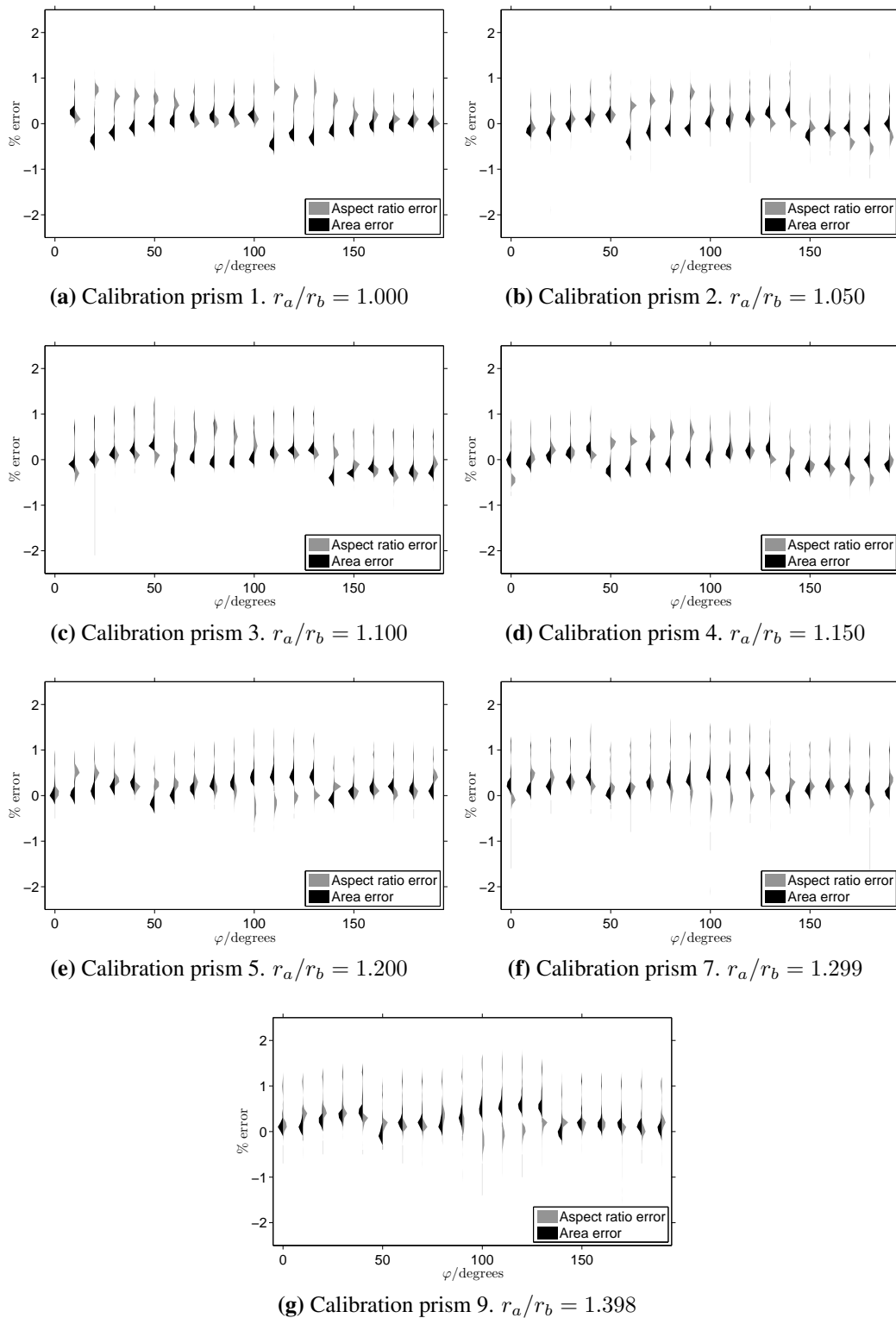


**Figure 3.12:** The error in the measurements of the calibration prisms, prisms 1 to 9. The prisms were rotated to an orientation,  $\varphi$ , as defined in figure 3.16. The frequency distributions of the errors found in aspect ratio and area for each of the orientations along the length of the prisms are plotted.

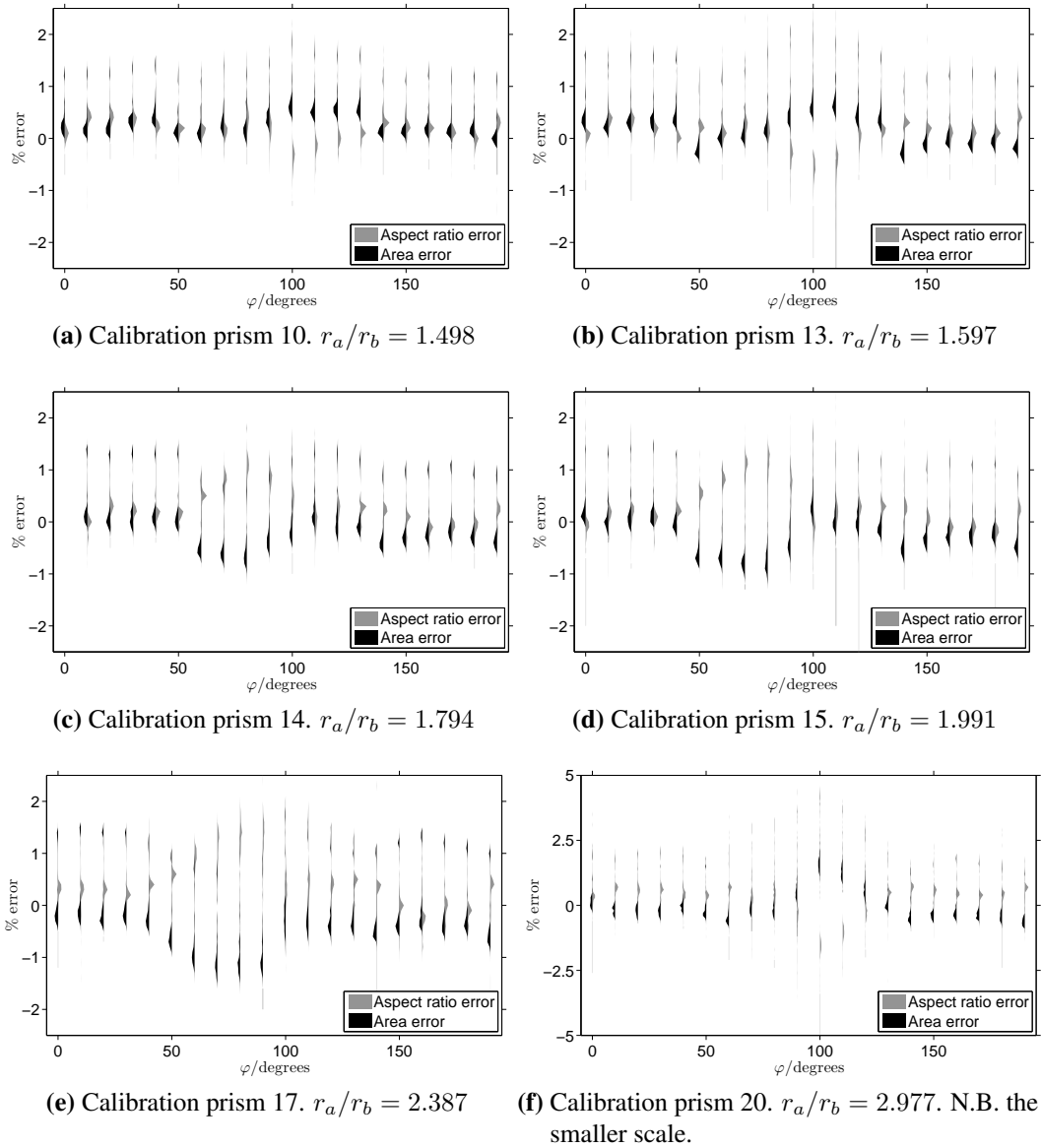


**Figure 3.13:** The error in each prism fitting, prisms 10 to 13. These plots complete the set begun in figure 3.12.

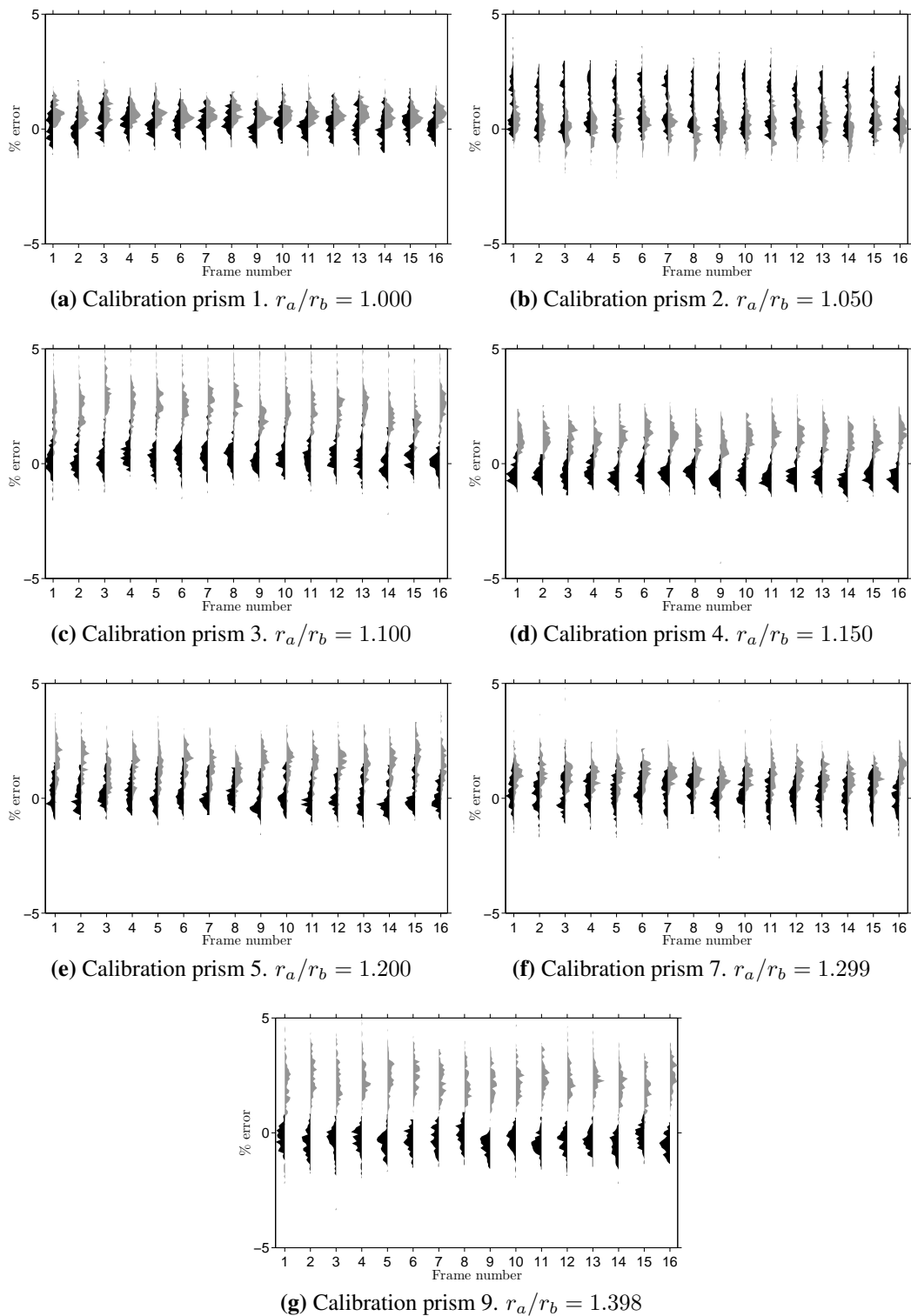


**Figure 3.14:** The error in the measurements of the calibration prisms, prisms 1 to 9 recorded under HR conditions. 16 frames were captured by the SIMX16 camera and each of these plots shows the error distributions for each of these frames. As in figures 3.12 and 3.13 the grey distributions are of aspect ratio error and the black distributions are of area error.

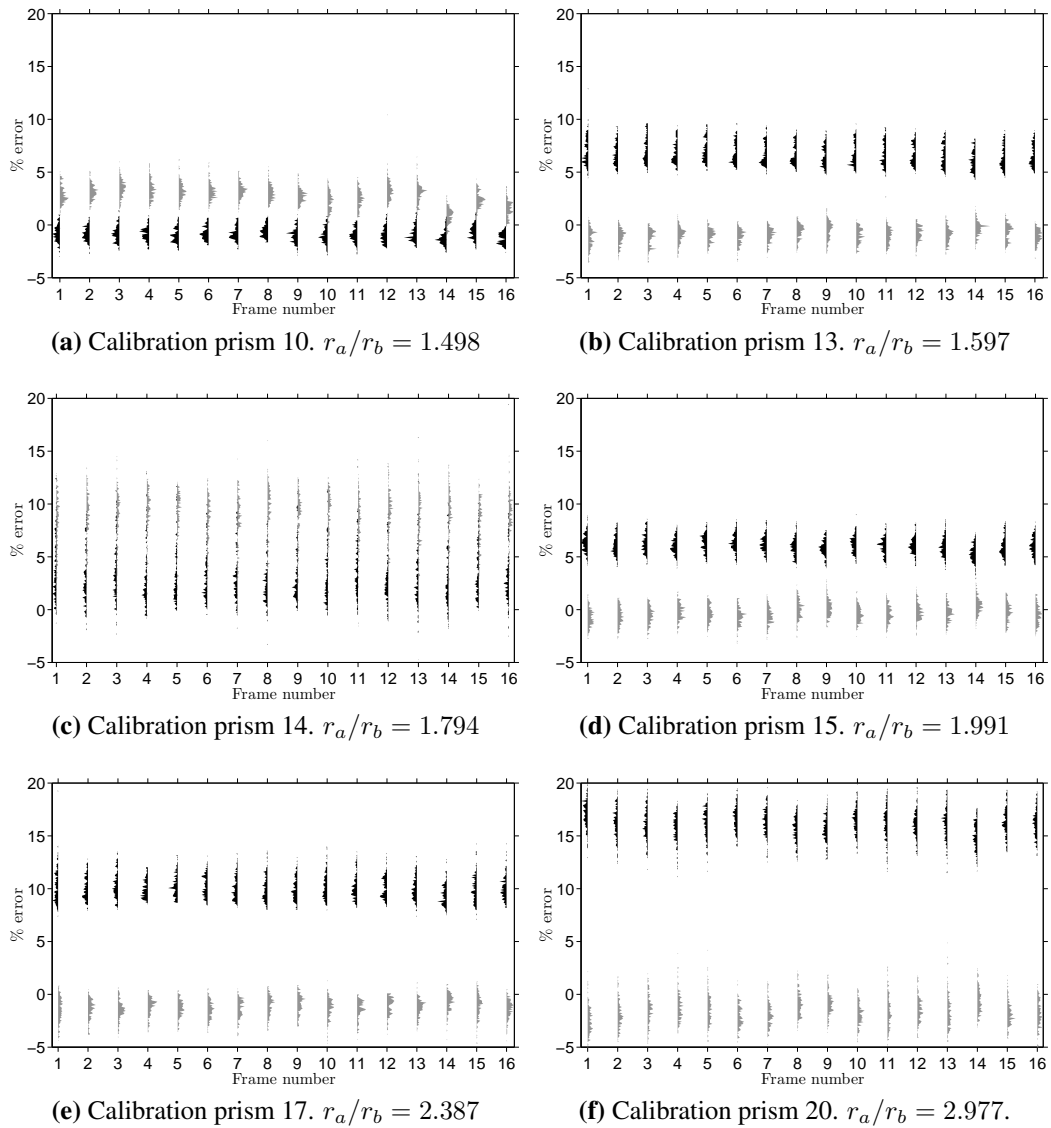


**Figure 3.15:** The error in each prism fitting, prisms 10 to 13. These plots complete the set begun in figure 3.14. Although these plots have a smaller vertical scale.

### 3.3.2 Statistical simulations of the fitting process

The effect of varying camera positions and specimen shape was also investigated using a stochastic method. The experiment was simulated for a single cross section given different edge positions to estimate errors. The simulated experimental variables can be seen in figure 3.16. For a particular ellipse, each tangent line was perturbed perpendicularly to itself by a normally-distributed random value to mimic the errors encountered during real experiments. The perturbed lines were used to fit ellipses using the method described in § 3.2.3. The simulations assumed that the cameras were pinhole cameras.

This process was repeated 1000 times, each time choosing six perturbations, representing noise, randomly from a set of 100 normally distributed random values. These values had a mean  $\mu = 0^1$  and standard deviation  $\sigma = 0.01$  and were normally-distributed to represent the accumulated error from all possible sources, including lens calibration, extrinsic calibration and lighting changes, amongst others. The percentage errors,  $E_i$ , were calculated using the resultant value from each of the 1000 simulated reconstructions,  $x_i$ , and the true value,  $\hat{x}$ , to give  $E_i = 100(x_i - \hat{x})/\hat{x}$ ,  $i = 1, 2, \dots, 1000$ , for each variable. The means,  $\mu$ , and error bars  $\pm 2\sigma$  of these values are shown in figure 3.17 for a simulation where  $L=1000$ ,  $\phi = 90^\circ$ ,  $\theta = 45^\circ$  and ellipse area =  $\pi$ . The value of  $\theta$  matches those used in the QS configuration reconstruction of elliptical prisms discussed in 3.3.1. These simulations provide an insight as to whether there is any biasing present in the camera configuration when there are random errors in the edge positions

It will be shown later that  $\phi = 90^\circ$  and  $\theta = 45^\circ$  are the most poorly conditioned combination of orientation and spacing. This can be seen as a larger variance in the errors in figures 3.12 and 3.13 around  $\phi = 90^\circ$ . Comparison of figures 3.17 and 3.18 show that cameras equally spaced at  $60^\circ$  (or equivalently  $120^\circ$ ) from one another, are typically of the order of 10 times

<sup>1</sup>These values are dimensionless as they represent ellipses with an area of  $\pi$ , and all lengths are relative to the mean radius of 1.

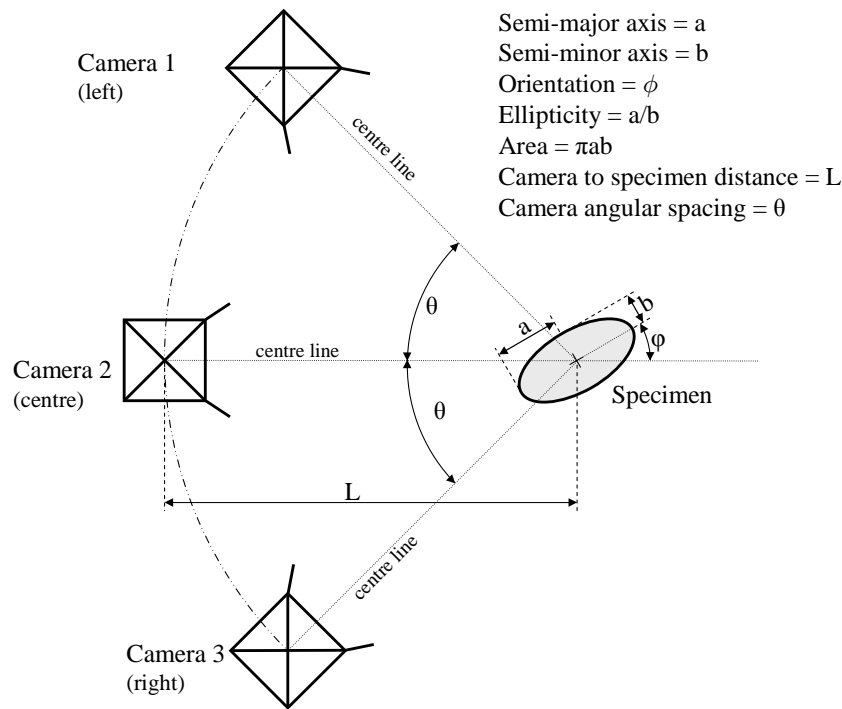


**Figure 3.16:** The simulated experimental variables.

more accurate than cameras placed at  $45^\circ$  for large aspect ratios, given the same errors in edge positions.

Figure 3.19 shows a comparison of the error as a function of  $\phi$  between cameras spaced at  $\theta = 45^\circ$  and  $\theta = 60^\circ$  (QS and HR configurations). It was observed that  $\phi = 90^\circ$  and  $\theta = 45^\circ$  gives the greatest errors, as these values give rise to poorly conditioned data for the least squares fitting with large aspect ratios. In this state, many of the data are concentrated around two points on the ellipse, figure 3.20, and as a result, the value of  $b = r_b$  is poorly conditioned whilst  $a = r_a$  is well determined. The least errors are encountered in the QS configuration when the side cameras observe the full width of the major or minor axis, which is to be expected as  $r_a$  and  $r_b$  will then be measured directly whilst the centre camera will be adding additional information. Similarly, the least errors are encountered in the HR configuration when one of the cameras observes the major or minor axis and the other two cameras are evenly spaced and capture the

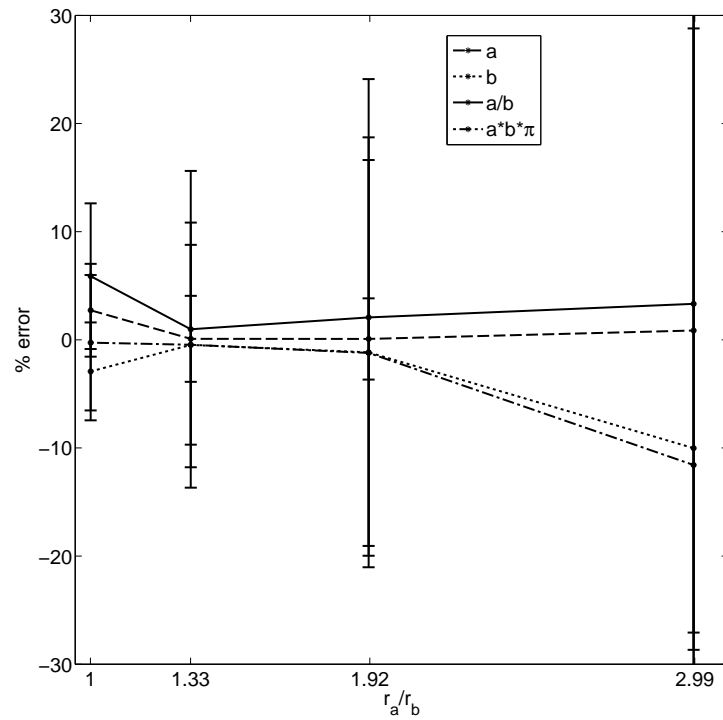


**Figure 3.17:** Simulated reconstruction of ellipses for cameras angularly spaced at  $45^\circ$ .

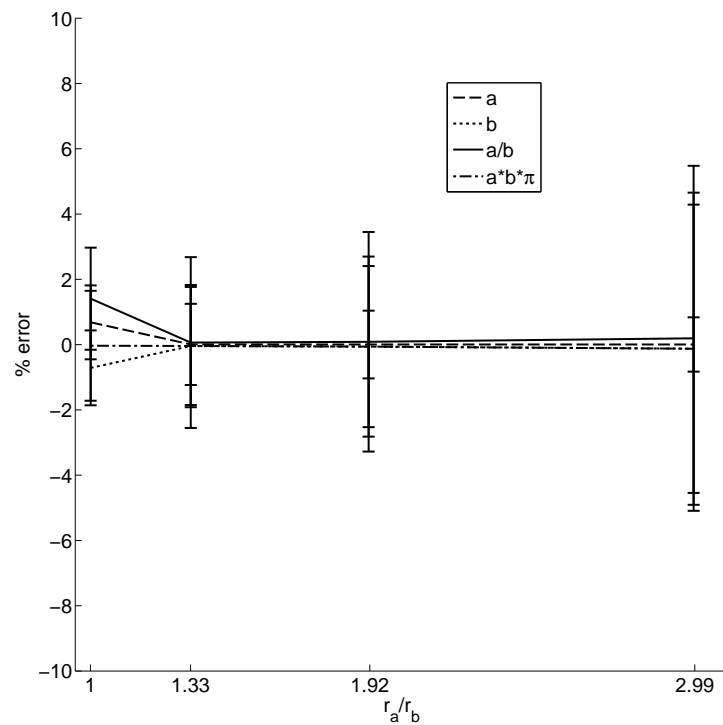


**Figure 3.18:** Simulated reconstruction of ellipses for cameras angularly spaced at  $60^\circ$ . The scale has been altered from figure 3.17 for clarity.

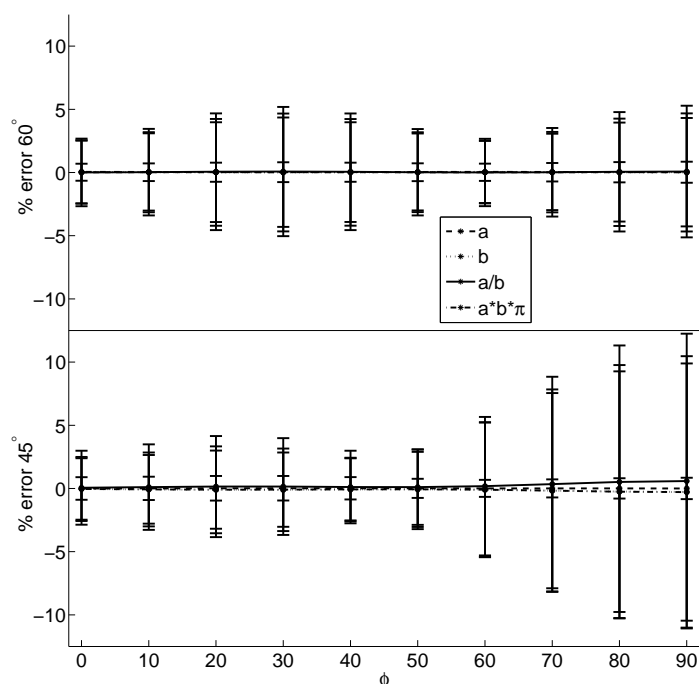


**Figure 3.19:** An ellipse with  $e = 3$  has been simulated in the  $45^\circ$  and  $60^\circ$  camera arrangements for a range of orientations,  $\phi$ . The trends in the error bars demonstrate that the most accurate determination of elliptical shape is when cameras are pointed along the directions of the ellipse's major and minor axes. It can be seen that the  $45^\circ$  cameras have particularly large errors at  $\phi = 90^\circ$ , because the data are poorly conditioned, as demonstrated in figure 3.20. These simulations were run with a factor of 10 lower variance than for figures 3.17 and 3.18 to allow for an easier comparison between the angles of  $\phi$ . Other orientations outside these ranges of  $\phi$  are symmetric and need not be shown here.

other dimension reasonably well in combination. The HR configuration has no unique 'worst' ellipse orientation like the QS configuration does.

The poor result for error in aspect ratio  $e = 1$  in the simulations, figures 3.17 and 3.18, compared to the reconstruction of the real prisms in 3.3.1 is because the simulations are biased so that any deviation from circular, at  $e = 1$ , whether positive or negative, will increase the positive error because  $e$  is defined to be positive for all shapes. Whereas random perturbations for shapes with higher aspect ratios result in shapes that vary around their positive value and can have positive and negative differences that will have a mean closer to zero. However, one would expect a similar result in the real experiments, but this has not been seen in § 3.3.1.

It would seem apparent from these simulations that they are not totally representative of

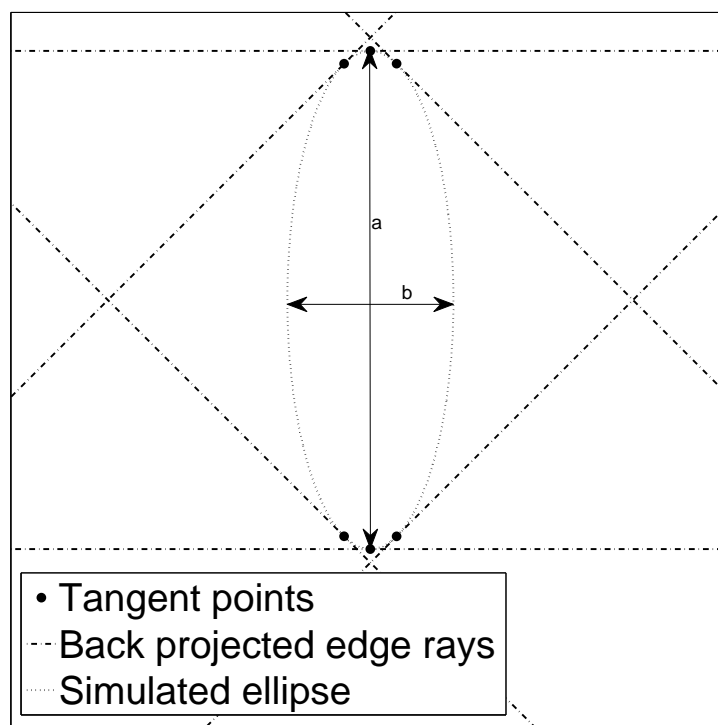


**Figure 3.20:** A simulation of an ellipse that gives rise to poorly conditioned data because the camera orientations and the ellipse's orientation cause the points of tangency to group around the extremities. Thus, the value of  $a$  is well conditioned, whilst the value of  $b$  is likely to be inaccurate.

the errors encountered during the experiment. The current hypothesis for this discrepancy is that the model of the error - normally-distributed random values - is not wholly correct, and some other estimate that takes into account possible systematic errors due to poor lighting and calibration may be required to reduce this difference. However, the simulations do provide valuable, generic insight into the optimum experimental set-up.

### 3.4 Evaluating the Telecentric Assumption

To simplify extrinsic calibration of cameras, an assumption can be made that the cameras are infinitely far from the specimen. This means that light rays entering them are treated as parallel and the back-projected edge rays for elliptical fitting are parallel to the direction in which the camera is pointing. This assumption has been validated and the errors have been quantified by

running simulations of the experiment, figure 3.21. In these simulations the true ellipse tangents to ‘near’ cameras were calculated. The edge positions of these tangents in images were assumed to lie at the same distance from the camera as the specimen’s centre. Parallel rays projected from the image edge positions provide tangents for fitting a reconstructed elliptical shape.

The normalised distance between the camera and the specimen centre,  $L$ , figure 3.16, was varied with differing values of aspect ratio and orientation. An example of the results for the orientation  $\phi = 90^\circ$  is shown in figure 3.22. It was found that for all orientations, camera spacings and aspect ratios  $< 3$  the error in the cross-sectional area measured was  $< 0.04\%$  for cameras spaced at  $L \geq 100$  specimen radii from the specimen centre. For the same range of parameters, the error in ellipticity measured (which was always  $\leq 0$  by definition, because  $e \geq 1$ ), for the worst case orientations, was  $> -0.017\%$ . The error in measuring the orientation of the ellipses was negligible for  $L = 100$ . In the experiments in this research, no camera centre was closer than 105 specimen radii to the specimen.

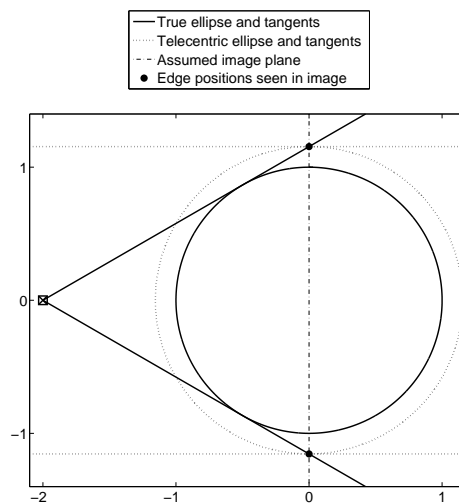


**Figure 3.21:** A circular cross-section as seen by one pinhole camera and the true tangential rays through the image edge positions. When the image plane is assumed to lie at the specimen centre and the back-projected rays are assumed to be telecentric, the cross-sectional reconstructed shape is larger than the original. As the camera centre is moved away from the specimen, the error due to the telecentric assumption decreases.

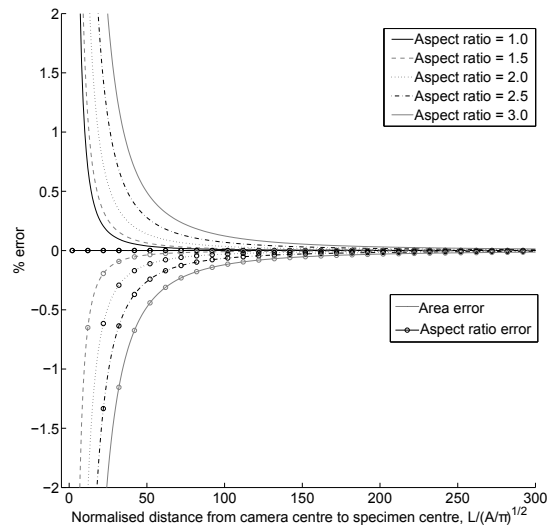


**Figure 3.22:** Plots of the percentage error predicted when assuming parallel (telecentric) light rays for an orientation,  $\phi = 90^\circ$ . The positive plots are the error in the area measurement, which is over-predicted for all aspect ratios. The negative plots are for the same simulated fits, but they show the error in the aspect ratio measurement, which is under-predicted for all aspect ratios but circular.

### 3.5 Mechanically loaded specimen reconstruction

Cylindrical tensile dog-bone specimens of CR-Ti-6Al-4V were manufactured in the D1 direction, parallel to the first rolling direction. The specimens were loaded quasi-statically and at high strain rate, with images acquired as described above. Figures 3.23 and 3.24 show full reconstructions of these specimens in the final frame before fracture. The specimens for which experimental results are presented were orientated to give the best conditioned data. As well as the reconstructed shape, stress and aspect ratio are shown as functions of position. It should be observed that the specimens form an elliptical cross-section that is most elliptical in the region of greatest plastic strain. The reconstructions demonstrate the capabilities of this method and the data obtainable through its use.

In order to examine stress distribution as a function of time, graphs such as those in figures 3.25 and 3.26 are used. Here, the true direct stress is calculated using the measured force on the specimen and the reconstructed cross-sectional area. In the QS experiment, figure 3.25, the stress generally increases monotonically as a function of time, until necking is observed. The

same trend is observed in HR loading; however there are fewer photographs of the event. In both cases the peak stress in the frame before failure is indicated. It is interesting to note the elastic only (no shape change) unloading of the end of the parallel section after the UTS, as expected, by comparing figures 3.25 and 3.29.

From the peak stress in each frame, a true-stress-time curve can be produced, figures 3.27 and 3.28. These curves are essentially continuous for QS loading, where many images are available, but less so at HR, as shown. However, comparison with traditional HR data analysis will allow the user to relate this discrete true stress data to more continuous nominal stress measurements. Further, the technique allows aspect ratio to be calculated as a function of time and position, figures 3.29 and 3.30. § 7.2 shows how these data can be used to inform material models.

## 3.6 Conclusions

An optical technique for estimating cross-sectional shape by measuring planar surface contours of elliptical specimens has been presented. The technique has been shown to work in both quasi-static and high strain rate experiments to quantify anisotropic plasticity behaviour of a titanium alloy for which useful quantitative stress and aspect ratio data have been produced.

The technique has been evaluated using computational simulations of the physical conditions that may be encountered in experiments. Stochastic error estimates have been obtained by perturbing the data to mimic the likely deviations of measurements from the true positions. These have shown that the optimal angular spacing of the minimum of three views is  $60^\circ$  or  $120^\circ$ .

Elliptical calibration prisms of precisely known dimensions were reconstructed using the technique, to evaluate both the equipment and the method. It was found that elliptical cross-sections with a variety of aspect ratios could be measured accurately at a variety of orientations.

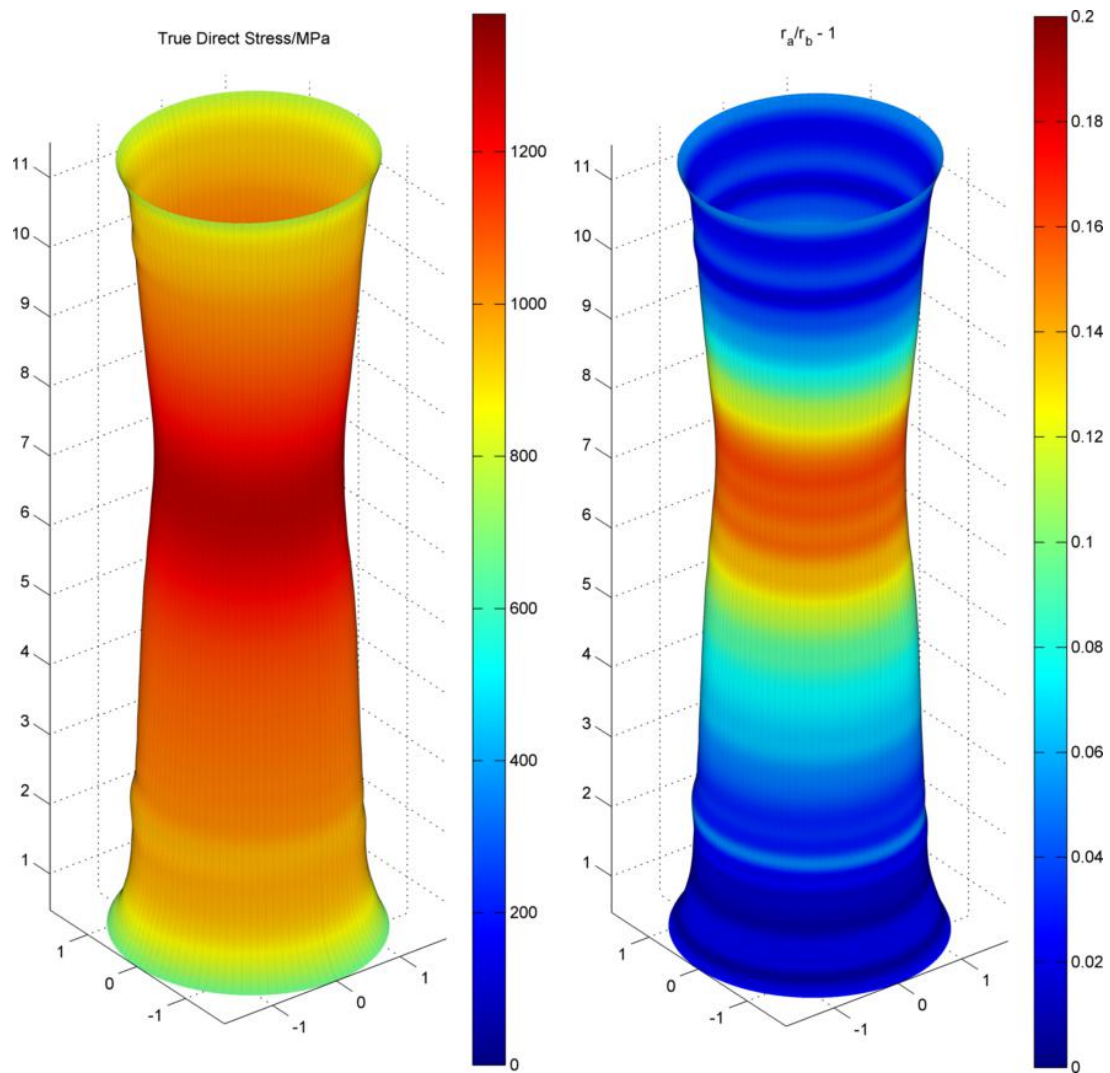


**Figure 3.23:** Quasi-static tension specimen at the last recorded time step before fracture.

This technique allows the measurement of cross-sectional area along the axis of the specimen and subsequently calculation of the total volume, of specimens of anisotropic, homogeneous materials in experiments where three or more views of a cylindrical specimen can be obtained. The technique is applicable in tension or compression tests without the need for contact with the specimen or marking its surface. The technique is well suited to environmentally controlled and high strain rate experiments and may be applied to the measurement of any planar conic section and is not limited to the field of mechanical materials testing.

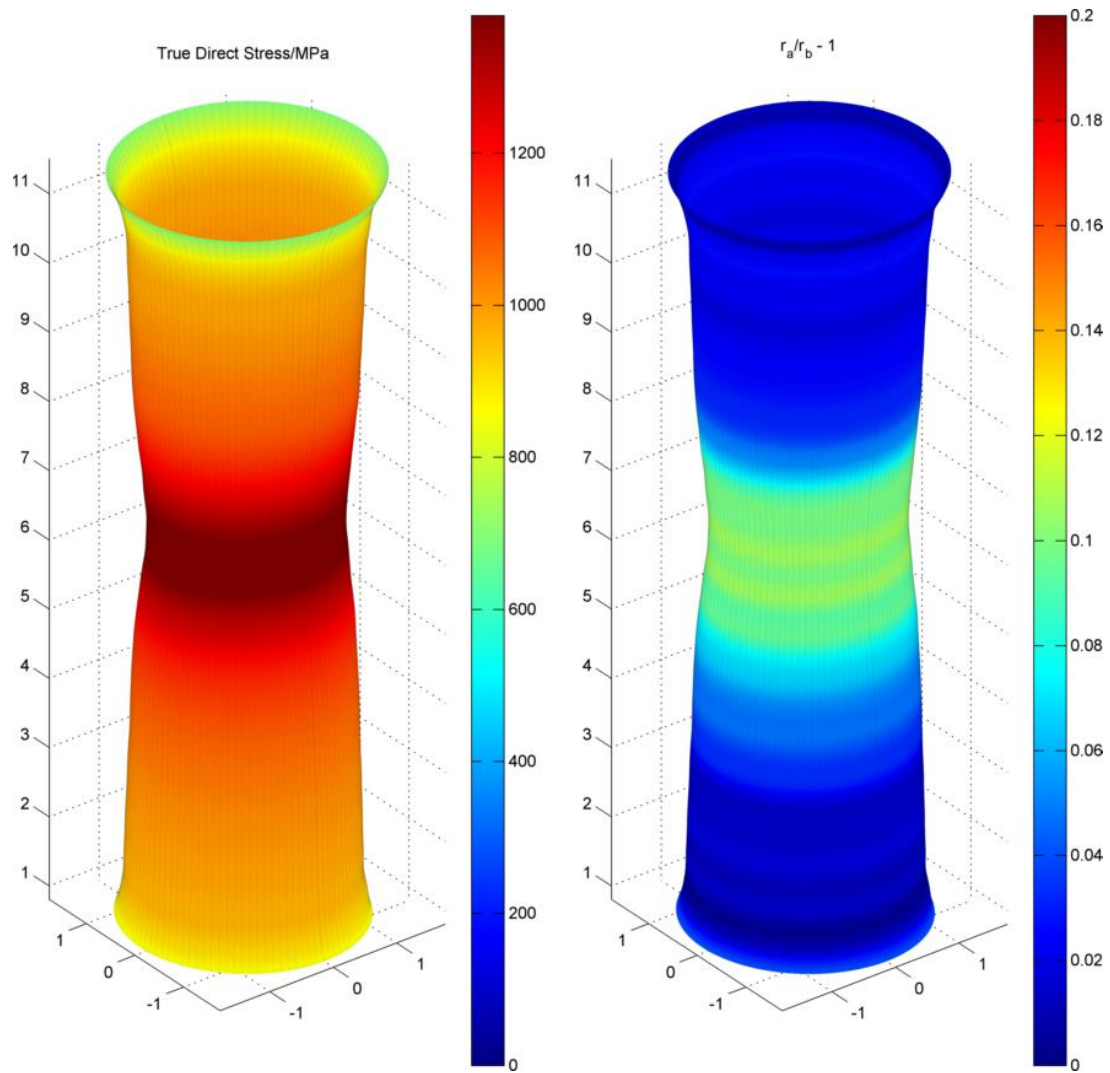


**Figure 3.24:** High strain rate tension specimen, at the last recorded time step before fracture.

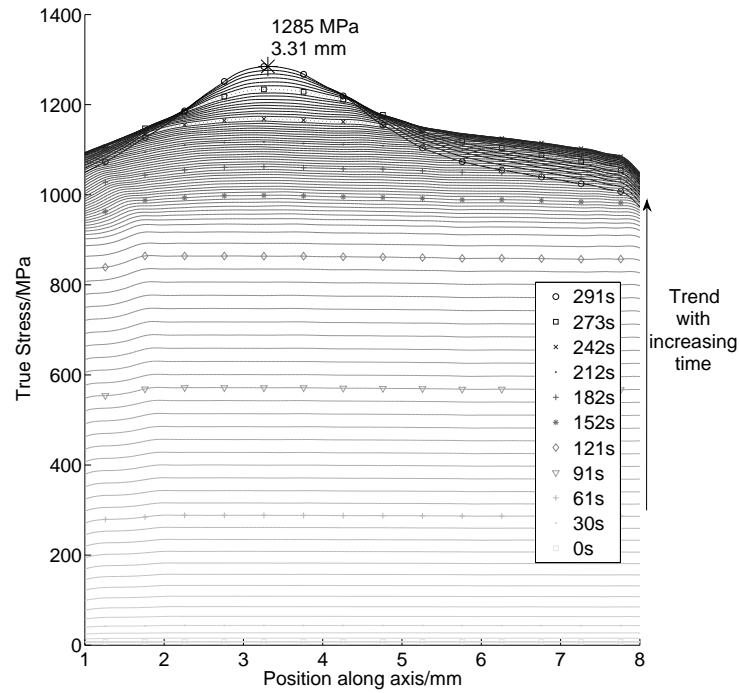


**Figure 3.25:** A specimen of cross-rolled Ti-6Al-4V cut with its axis lying in the plane of rolling. The plots show true direct stress with axial position for several time steps.

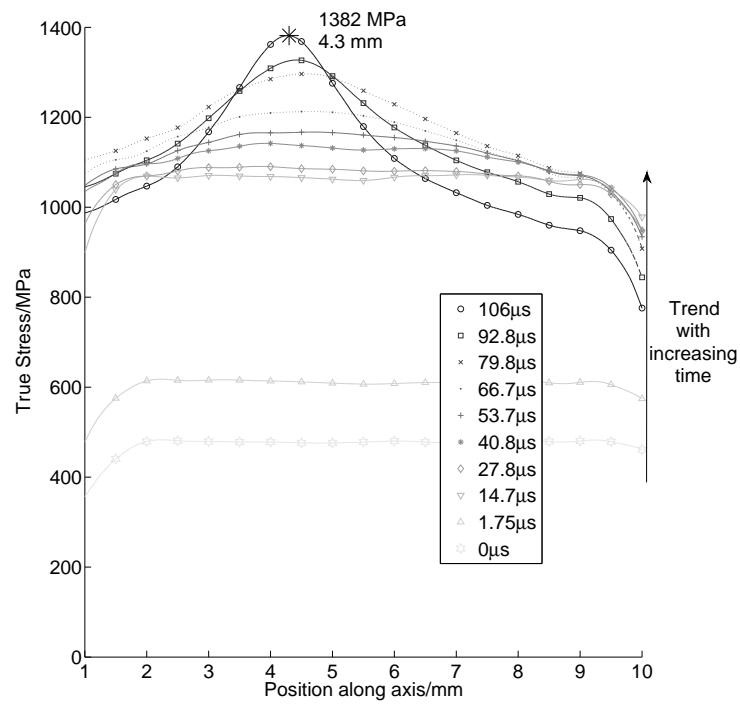


**Figure 3.26:** High strain rate direct true stress results for all time steps.

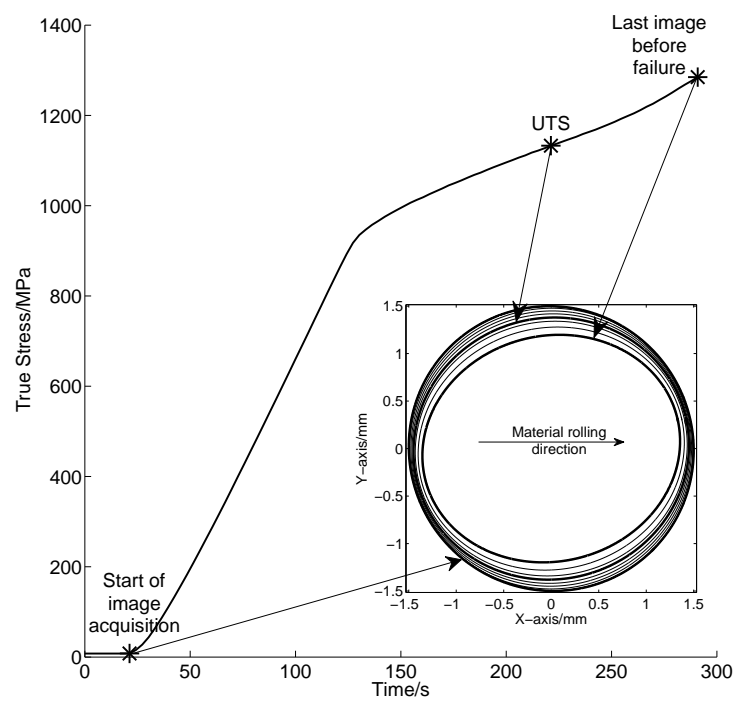


**Figure 3.27:** Quasi static maximum true direct stress with time. The inset plot shows the shape of the minimum area cross section at a few selected time steps.

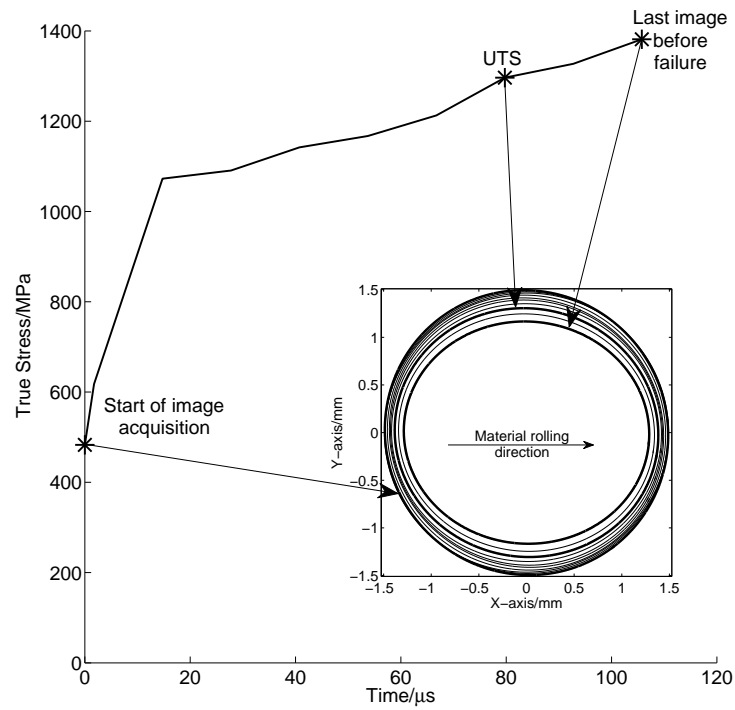


**Figure 3.28:** High strain rate true direct stress with time. The inset plot shows the shape of the minimum area cross section at all recorded time steps. Image acquisition was deliberately started after the start of loading so that the limited available frames could be concentrated on plastic deformation.

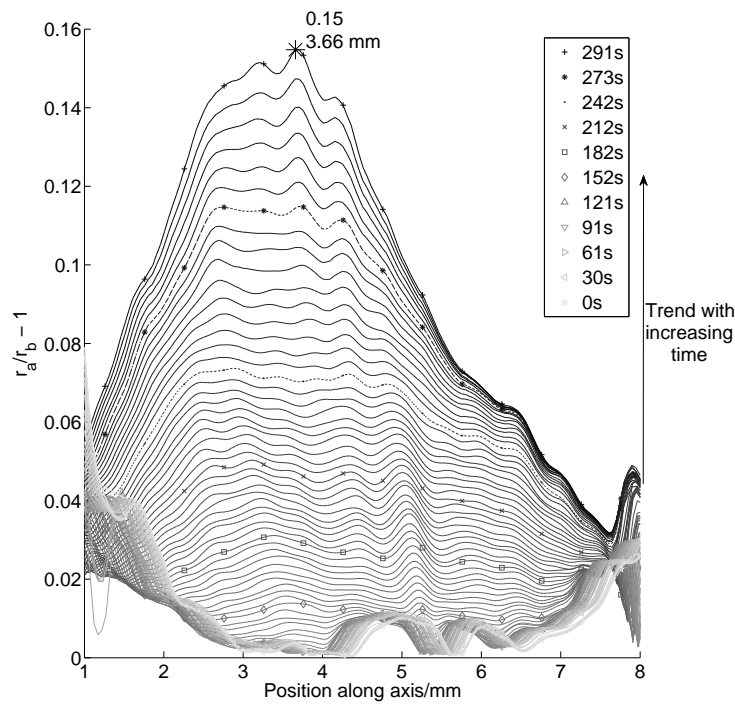


**Figure 3.29:** QS data showing  $r_a/r_b - 1$  with axial position and time.

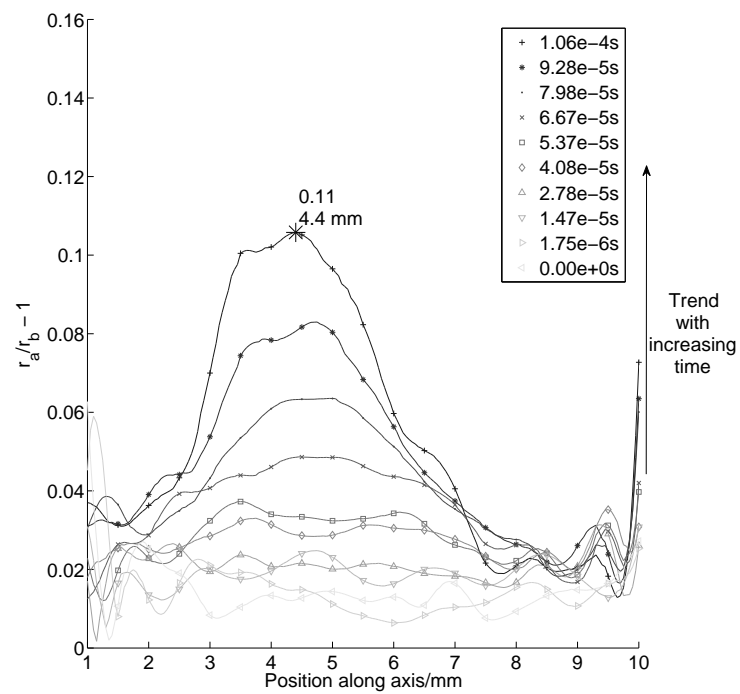


**Figure 3.30:** High strain rate data showing  $r_a/r_b - 1$  with axial position and time.

## Surface Roughness Tracking

---

In this chapter a technique for measuring the displacement and strain of specimens with high resolution is presented. The technique tracks features within the surface profile of a specimen seen silhouetted against a contrasting background, such as that seen in the uniaxial specimens in this research (see chapter 2). The technique requires discernible roughness on the specimen's surface that can be measured from photographs.

In the uniaxial, initially cylindrical, specimens of Ti-6Al-4V the surface roughness was the product of manufacturing by turning on a lathe. The slight but discernible surface features, which could have been removed by grinding and polishing, to an extent, were instead used to obtain the axial displacement of the surface without extra marking. This permitted the simultaneous determination of surface height from images in chapter 2, that in turn allowed the computation of the evolving elliptical cross-section, whilst measuring axial deformation too. The combination of the technique in this chapter with the technique described in chapter 3 provides data on the elliptical cross-sections at axial positions in a material frame of reference, rather than the camera frame of reference.

---

## 4.1 Introduction and prior work

There are a number of well-established optical techniques that may be used for measurement of displacement in material characterisation experiments. Digital Image Correlation (or Speckle Metrology, or Particle Image Velocimetry) tracks the motion of applied or natural random features on the specimen surface, and is capable of achieving sub-pixel displacement resolution, at the expense of spatial resolution. Laser speckle metrology uses similar analysis, but here the pattern is provided by the laser speckle effect, which occurs when coherent light impinges on a textured surface. For small displacements, laser speckle interferometry may be used, and the Moiré and Fine Grid methods also provide excellent displacement resolution, although only in one direction in the case of Moiré. Reviews of these techniques may be found in [81–87].

However, there is a class of material characterisation experiments that are (a) uniaxial, so that data are only required in one direction, and (b) difficult to photograph face-on. Further, if the method from chapter 3 to reconstruct the geometry of a uniaxially deformed specimen is used, views of the specimen from three angles are required with *no* artificial markings on the specimen surface. For this reason, a method for measuring axial displacement, and calculating axial strains, by tracking the profile of the surface roughness to obtain displacements has been developed. As well as removing the requirement for specimens to be marked, this technique will be shown to provide very high spatial data densities which allow high quality strain calculations.

Visual feature tracking is a broad field of research (see e.g. [88–90]) and two-dimensional features in images are often tracked through a combination of methods which include cross correlation. For surface profile feature tracking a one dimensional method is required, but many of the problems encountered, such as occlusions and noise, and the strategies used to overcome them, are applicable here too. The features tracked in this chapter primarily suffer from the picket fence problem, in that they look very similar to their neighbours due to the periodicity of lathe turning. In addition to this, noise in the images and changing specimen surface roughness due to elongation makes matching features from one frame to the next, using anything other

than their position, problematic. Strategies have been developed to overcome the challenges of this task that should prove useful to others who would like to implement this technique.

## 4.2 Method

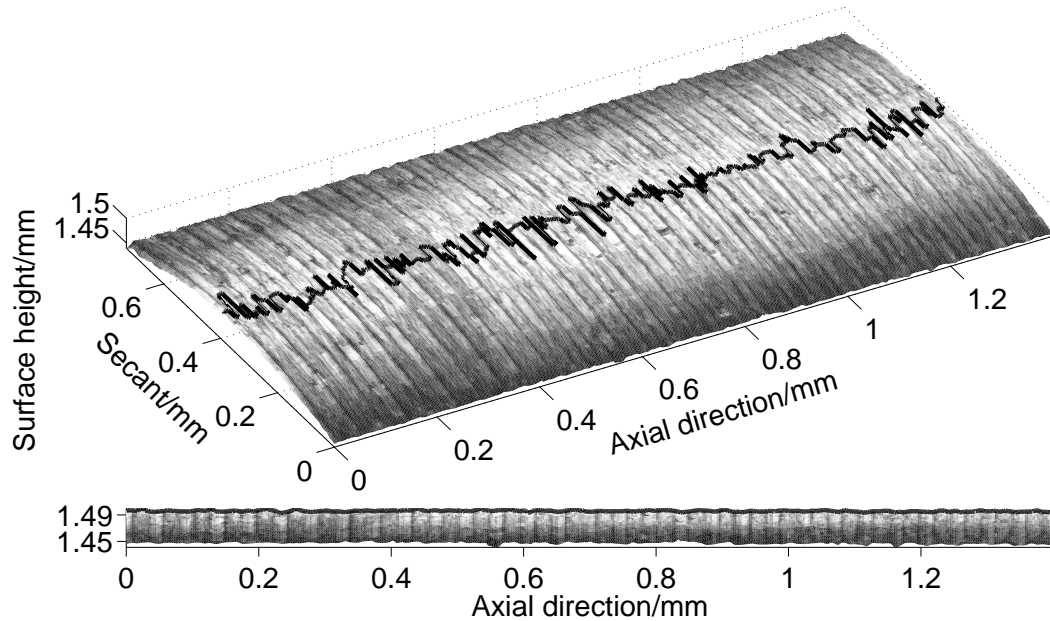


**Figure 4.1:** (a) Surface height of a specimen showing the pseudo-random undulations of surface roughness running axially due to the manufacturing process. The horizon of the surface is shown in (b), and the tangential positions of the horizon are shown as a line in (a). It is observed that the circumferential locations of the horizon vary significantly with axial position.

### 4.2.1 Obtaining specimen edge features

Specimens manufactured by turning on a lathe have surface roughnesses that are approximately periodic with axial position, overlaid with irregular variations due to random fluctuations in the process. This chapter will use a single tensile test specimen as an example of the new measurement technique. The surface height of a patch from this specimen has been measured using an Alicona Infinite Focus Surface Profiler, and is shown in figure 4.1. The edge seen

in an image of the specimen is ideally a visible horizon of this surface, figure 4.1(b). The peaks, troughs and zero crossings of this edge, after high-pass filtering, are used to generate displacement data. In reality, the surface seen is close to the horizon shape, but will differ because the camera lens is not a true pinhole camera and rays of light from the horizon reach the sensor from multiple angles.

Data are analysed from the quasi-static, uniaxial tensile experiment on a specimen of CR-Ti-6Al-4V, which was also one of the subjects of chapter 3, with nominal gauge length 8 mm and gauge diameter 3 mm, figure 4.2(a). Specimens were loaded using a commercial screw driven Hounsfield Tensometer with a cross-head speed of 0.5 mm/min. Photographs were acquired at a rate of one every three seconds using a TELI Digital Camera (CSB4000CL), with a 4 megapixel 10-bit greyscale CMOS sensor, and a Computar Megapixel lens. The edge detection and surface peak tracking was implemented in Matlab. For comparison, laser extensometer measurements were also performed using a FIEDLER Optoelektronik model P-50, which had a sampling frequency of 50 Hz and was found to have an accuracy of  $\pm 3 \mu\text{m}$  in practice. This device works by tracking the position of a series of white lines which are painted onto the relatively dark specimen surface.

Using this apparatus, digital images, figure 4.2(a), of the cylindrical specimen were acquired with a sufficiently high resolution to discern the surface roughness in the edges. The specific resolution that is required depends on both the specimen and the apparatus;  $6.5 \mu\text{m}$  per pixel was used in this experiment. The acquisition equipment was focused on the edges of the specimen and the lens was calibrated so that radial distortions could be removed by rectification as described in § 2.2.

The edges of the specimen in the images were found as described in chapter 2. An example section of edge data is given in figure 4.3 (dashed line).

A data set consisting of the radial positions of the left and right hand edges of the specimen as functions of axial position along the specimen length was thus created. In order to calculate

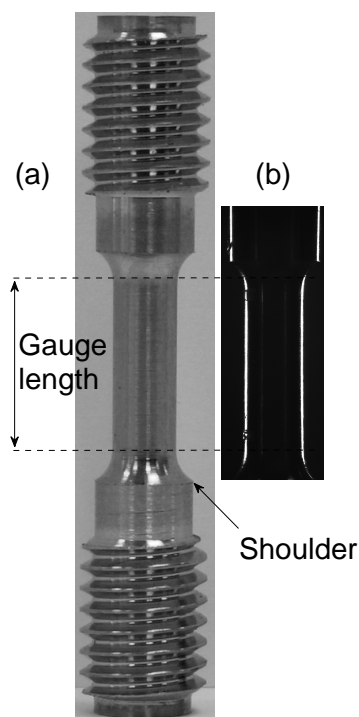


**Figure 4.2:** (a) A typical tensile specimen of gauge length 8 mm and gauge diameter 3 mm, its size was specified so that it could be used in both quasi-static and high strain rate ( $> 10^3 \text{ s}^{-1}$ ) experiments. (b) An image of this specimen *in situ* where the gauge length spans  $\sim 1250$  pixels.

specimen displacement it was necessary to track material positions by following the movement, between images, of features in these edges. The discernible features that were most likely to be present throughout the experiment, and not to move with respect to the material, were the zero-crossings of the high-pass filtered curve that had a positive gradient (although negative gradient features were equally valid). The frequencies present in the edge data are shown in figure 4.4, where it can be seen that the dominant frequency was  $\sim 16.25$  samples per mm. This frequency is indicative of the number of cuts the lathe tool made in each mm along the surface during manufacturing. Features with this frequency should be the most persistent throughout the experiment, albeit with some reduction in frequency as the specimen was elongated.

In order to locate these features, the edge curve was filtered using a high-pass Butterworth filter with a cut-off frequency chosen so that the detected shape of the nominal specimen geometry could be removed, but the underlying surface roughness would remain with a zero mean.

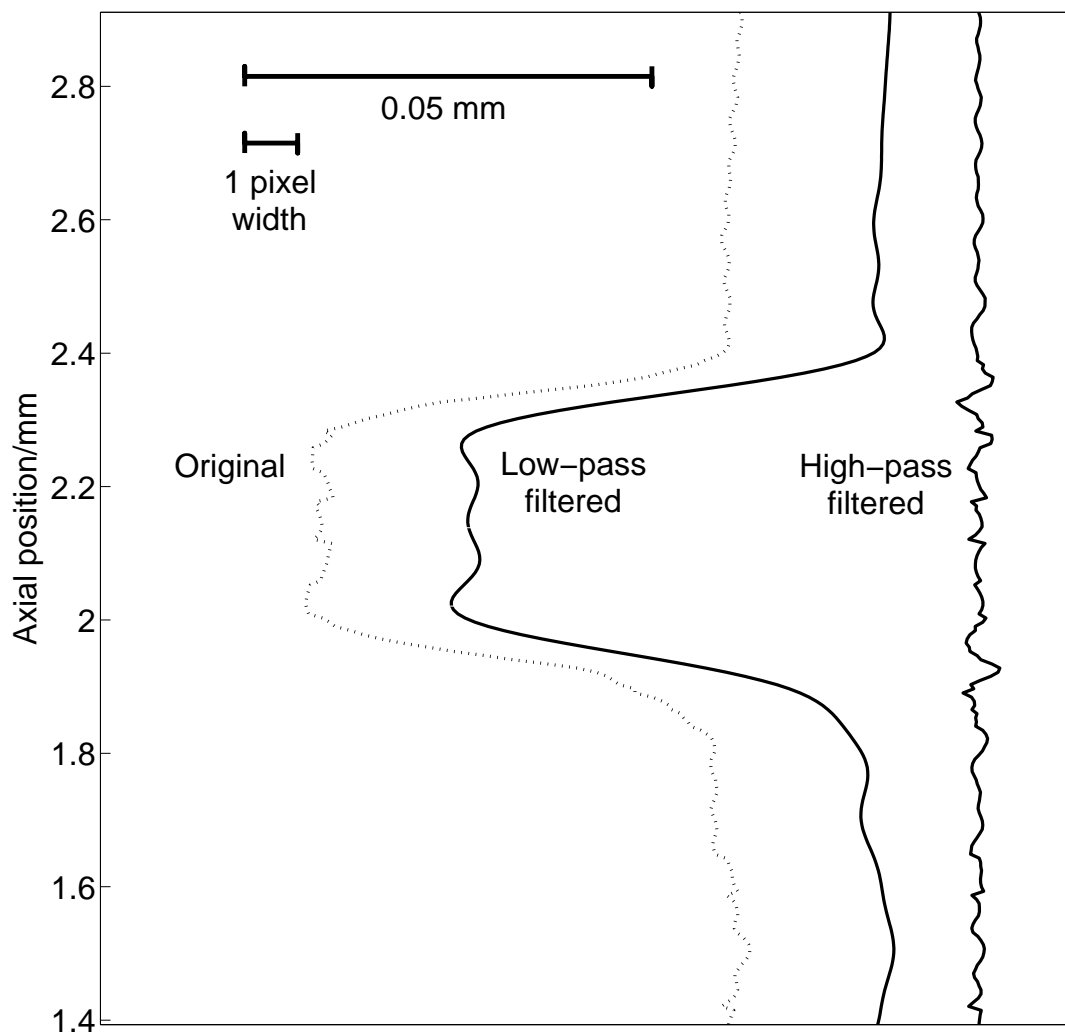


**Figure 4.3:** The original detected left-hand edge of the specimen ( $\cdot\cdot\cdot\cdot\cdot$ ) with the low-pass filtered edge and the high-pass filtered edge shown at offset positions for clarity. The large ‘bucket’ shaped bump is the outline of the paint marker required for the laser extensometer. The width of a pixel in the image,  $6.5\ \mu\text{m}$ , is also shown.

In this experiment the cut-off frequency was determined to be 6 periods per mm.

To improve the repeatability of locating the zero-crossing at the same material position in each frame, a least-squares spline fit to the detected edge of the specimen was calculated using the Matlab ‘csaps’ function [91]. This also allowed the determination of the position of zero-crossings in the surface roughness to an accuracy better than the nearest pixel, which is the best resolution obtainable from the original, pixelated, data. Figure 4.5 shows the result of spline fitting and the calculation of the zero-crossings in a small region of the edge curve.

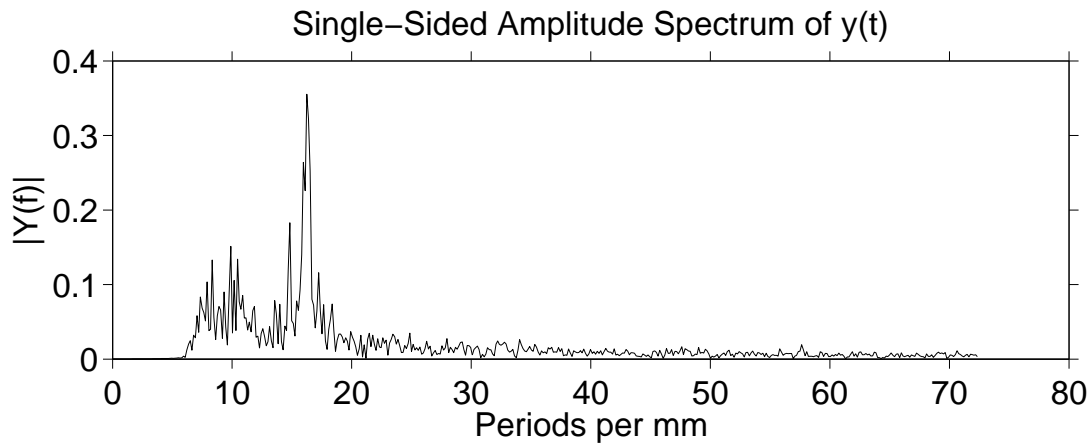


**Figure 4.4:** The edge data from within the parallel gauge section of the specimen. The data have been passed through a high-pass Butterworth filter to remove all frequencies below 7 periods per mm. The peak at 16.25 periods per mm is the frequency of the turning during manufacture.

#### 4.2.2 Robust tracking of features between frames

Once zero-crossings had been located, they were tracked between frames. If the zero-crossings had been farther apart, making the inter-frame displacement of the material less than the wavelength of the roughness, and noise had had less of an influence on the edge data, then tracking them would have been a relatively simple matter of matching one feature to its closest neighbour in a subsequent frame. In the current example, the surface roughness wavelength,  $\sim 60 \mu\text{m}$ , was short enough in some sections of the gauge length so as to make matching to closest neighbours produce too many false matches to be useful. In order to overcome this limitation, the cross-head displacement of the loading device was used to produce a model of expected displacement. Matches between zero crossings were only made when the feature in the second frame was within a given distance of the predicted position. Figure 4.6(a) shows the matches found using this guided matching. By assuming that one end of the specimen moved with the cross-head, whilst the other was stationary and the displacement was otherwise linear in position, a predicted displacement was obtained for each axial position.

Using this method, many features were matched correctly, but false matches remained. False matches were found and removed using a similar prediction method, this time using

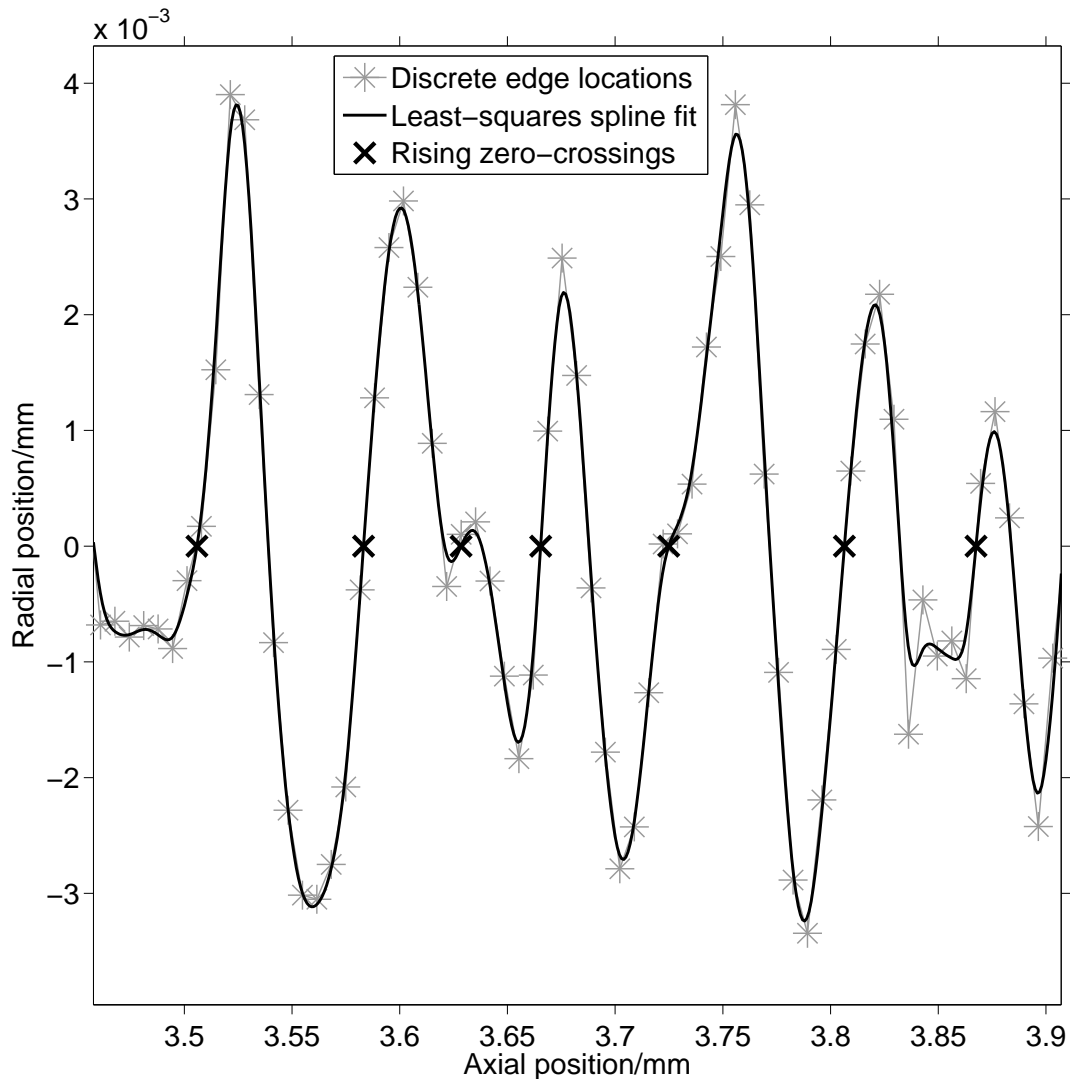


**Figure 4.5:** The original, discrete, edge positions determined by cross-correlation and the continuous spline interpolating fit. The surface features used to track the material are the zero-crossings.

the modal-average displacement of regions that spanned a fraction of the whole length and time of the experiment. Figure 4.6 demonstrates the process, whereby the displacements of all features within a certain region of axial length and time, 1.5 mm and 9 s, were binned to produce a histogram of displacement, shown in figure 4.6(b). Features were accepted as correctly matched if their displacements were within a threshold of the most frequent displacement, otherwise they were rejected. This threshold was determined by the maximum expected strain rate in the specimen and the region's time span and axial length; a threshold of  $\delta = \pm \dot{\epsilon}(\Delta t)(\Delta L)/2 = \pm 0.015$  mm was used in this experiment. The displacements of the

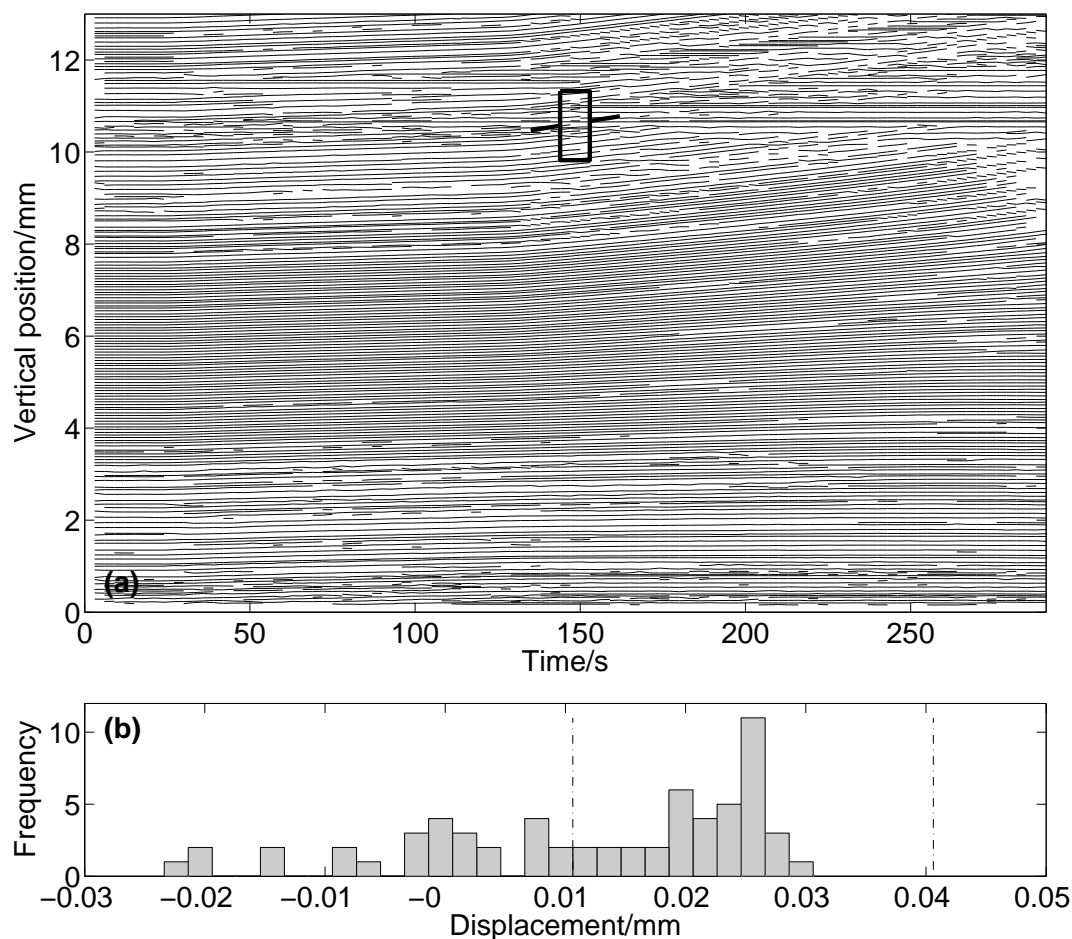


**Figure 4.6:** (a) ‘Raw’ feature tracks showing the motion of corresponding features plotted as a function of time in the camera frame of reference. The parallel gauge length of the specimen is between 2 mm and 9 mm. A 9 s by 1.5 mm sub-region is shown as a box surrounding a group of features. The lines either side of the box indicate the modal average displacement direction. (b) The histogram of displacement within the box in (a). The threshold displacement values are shown by dashed lines; the mean of the displacements between these values is taken as the sub-region’s modal average displacement.

acceptably matched features were averaged and taken to be the displacement of that region. The centre of the region was recalculated as the average location of the acceptable features. The modal-average displacement was calculated at a grid of time and axial positions using overlapping sub-regions across the whole set of features, which produced the displacement data shown in figure 4.7. This method of filtering relied on the strain within the region being approximately constant, which was the case for the regions selected, which were sufficiently small, and the

homogeneous material.

Figure 4.7 plots material displacement over time in the vertical image position. It can be seen that at around 11 mm and 250 s, the displacement has been incorrectly determined, showing that this technique could not be relied upon to obtain correct displacements for all locations within the experiment. To ensure the validity of the results, a manual check for erroneous data, such as this, had to be performed.

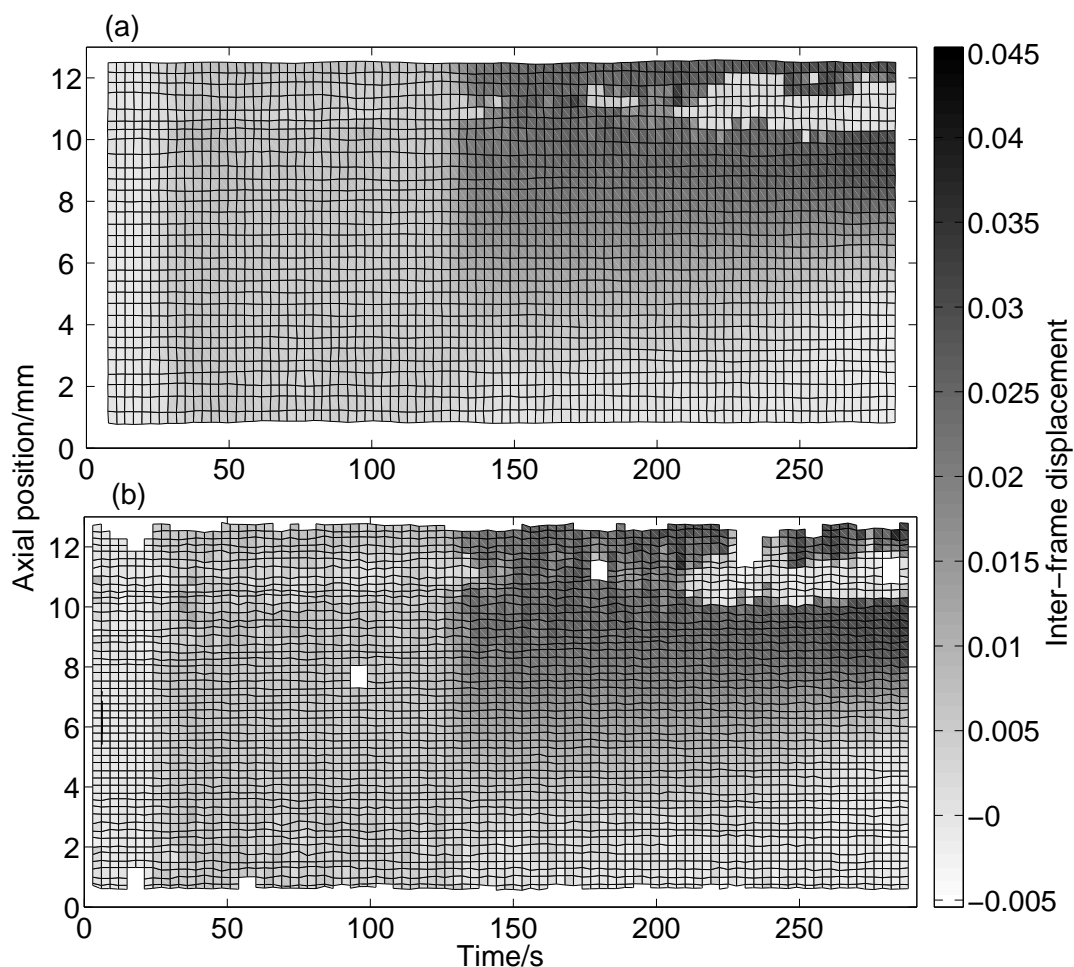


**Figure 4.7:** (a) The displacement of overlapping sub-regions, 9 s by 1.5 mm, across the range of time and axial position in the camera frame of reference. The shading represents average displacement at that location between two subsequent frames. (b) A finer determination of displacement with non-overlapping sub-regions of 3 s by 1 mm (3 s was the inter-frame time). The time and vertical positions of the displacement are irregularly spaced because they are plotted at the mean location of the features found to be in that sub-region, and not the nominal location of the sub-region.

After filtering, features that were previously unmatched or incorrectly matched could then be guided using the displacement data in figure 4.7(a), with more precision than the linearly interpolated cross-head data, and consequently the allowed threshold in matching could be reduced, preventing the majority of false matches. The resulting set of matches was filtered using a smaller region size, 3 s by 1 mm, to give a finer representation of displacement of the material in the camera frame of reference, as shown in figure 4.7(b). Using this even finer description to guide the matching process yet again, with an even further reduced threshold for guidance, a detailed set of matching features could be found.

The average number of pixel rows between consecutive positive-gradient zero-crossings was 10 pixels and within one period of roughness there are more positions that can be tracked than just the positive-gradient zero-crossings: these are the zero-crossings with negative gradient and the local maxima and minima. The fine displacement data in figure 4.7(b) could also be used to guide matches for these three feature types as they all had similar displacements. Given the matches for features of all four types, a detailed measurement of specimen displacement along the gauge length could be obtained by following features that were successfully tracked throughout the experiment. These data are shown in figure 4.8 where 252 features were tracked at a mean initial spacing of 31  $\mu\text{m}$  and a median initial spacing of 16  $\mu\text{m}$ . This figure does not show features that could not be tracked for the entire experiment, but if those that could be tracked continuously for at least two thirds of the time were considered, the mean initial spacing would decrease to 26  $\mu\text{m}$  while the median would be unchanged.

### 4.2.3 Laser extensometer validation

To validate the new method against an established position measurement technique, the position of two locations within the gauge section, highlighted in figure 4.8, were measured with a laser extensometer. The comparison data are shown in figure 4.9, which shows the difference between the two laser displacement measurements and the displacement measurements derived

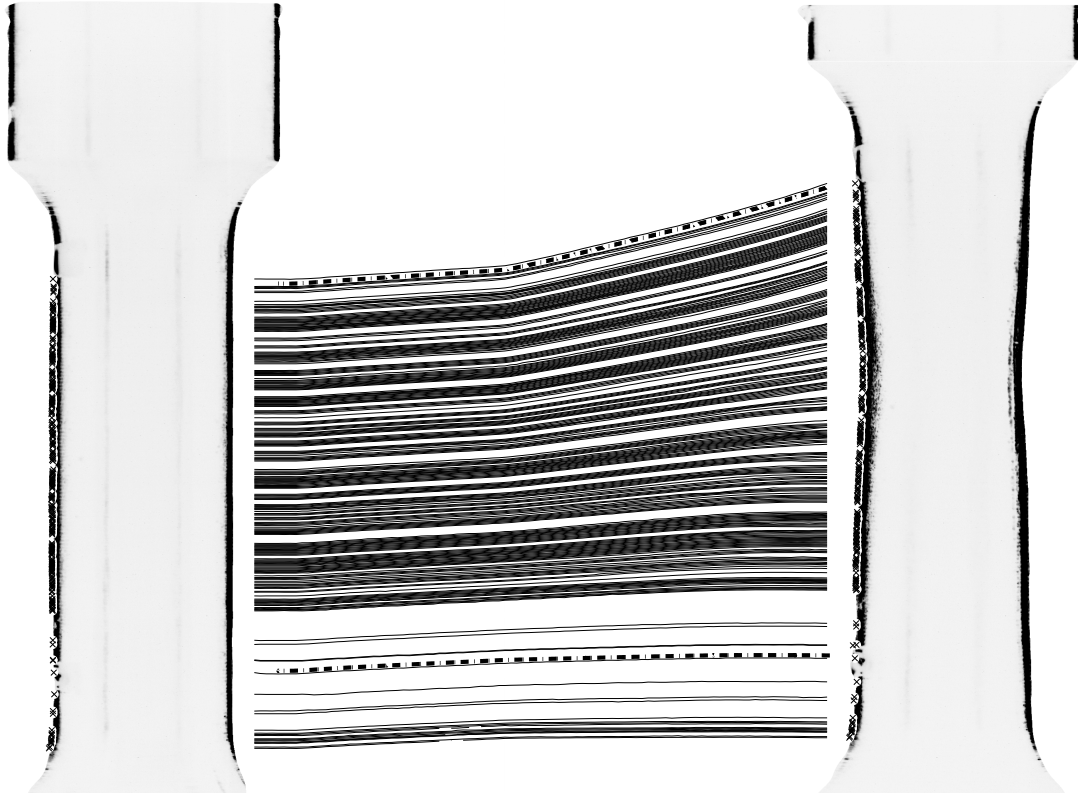


**Figure 4.8:** The position of specimen edge curve features that could be tracked throughout the experiment are plotted. At the left and right sides side of the tracks are photos of the specimen at the start and the end of the experiment; the negative of their images has been shown for clarity. Along the edges of the specimens, crosses indicate the initial and final locations of the tracked positions. The dashed lines show the laser extensometer tracked positions throughout the experiment.

from the closest tracks. The laser positions,  $y_L$ , were initially at 8.66 mm and 2.23 mm and the roughness tracks,  $y_C$ , were initially at 8.74 mm and 2.18 mm. The laser extensometer recorded its measurements at a rate of 50 Hz, whilst the inter-frame time of the cameras was 3 s, and therefore the laser extensometer data was smoothed with an averaging filter of 150 samples to obtain more accurate values for comparison. A maximum error of 23  $\mu\text{m}$  was seen in these results. However, some of this error is due to the strain of the samples which tends to move the lines apart.

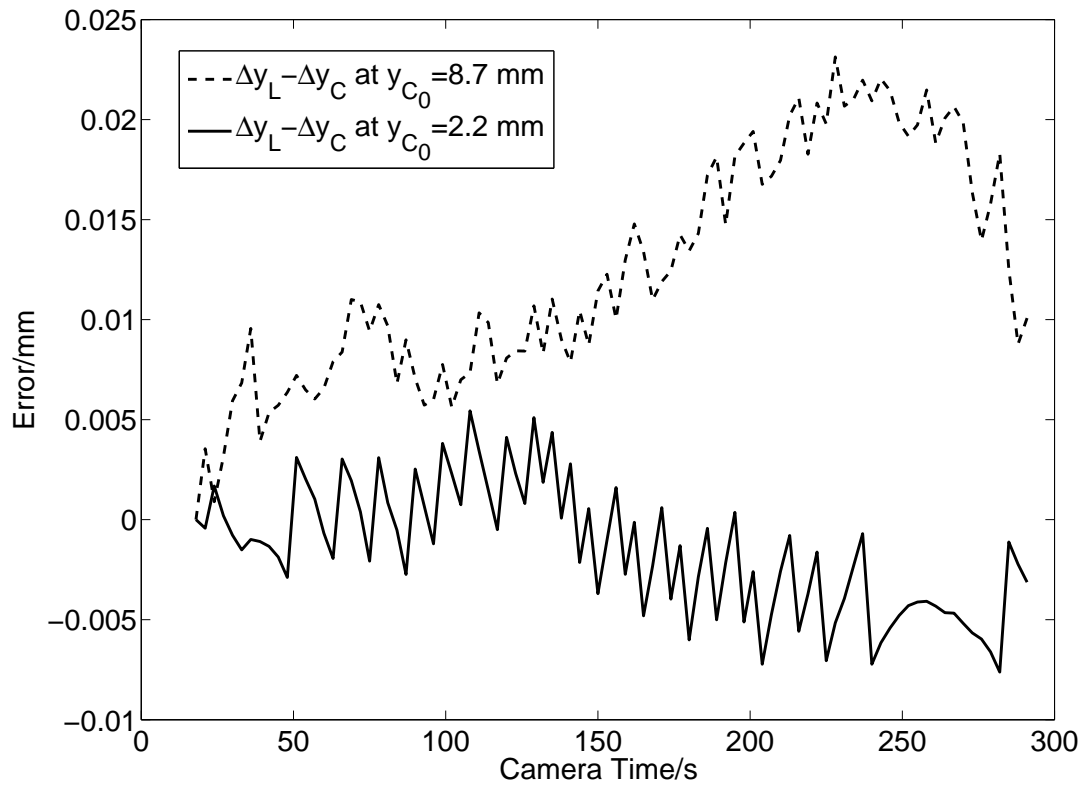


**Figure 4.9:** The displacement of roughness tracks measured close to initial axial positions of 8.7 mm and 2.2 mm in the gauge section, shown in figure 4.8, are subtracted from the displacement of laser extensometer measured tracks at these locations. Due to the initial separation of laser-tracked and roughness-tracked positions the increasing strain in the specimen tends to increase the error.

#### 4.2.4 Calculation of specimen strain

The high resolution displacement data contain a certain amount of noise; when differentiating these data to obtain strain, the noise will have a significant effect on the results. Smoothing of one sort or another is often employed in these situations to extract the underlying derivative. Here, a method of smoothing is presented that allows computation of strain.

To calculate strain from the continuously tracked material positions shown in figure 4.8 would have ignored the displacement data from tracks that could not be followed for the duration of the experiment; however, such partial tracks still contribute useful data some of the time. The Eulerian displacement plotted in figure 4.7(b) includes *all* data, with averaging of displacements over an axial length of 1 mm. Using the averaged representation of the material

displacement allowed the calculation of strain that included all of the available displacement data combined with an averaging filter that prevented the differentiation of measurements becoming too noisy.

Knowledge of the Lagrangian displacement, as opposed to the Eulerian displacement seen in figure 4.7, allows the calculation of strain as a function of initial axial position. The Lagrangian form is commonly required for the comparison of material strain at different times during an experiment. The paths of material movement can be derived from the Eulerian displacement. The location of a material point,  $x_i(t)$ , initially at  $x_i(0)$ , can be found by adding its inter-frame displacement,  $u(x_i(t), t)$ , interpolated at  $x_i(0)$  and  $t = 0$  because the discrete locations of  $x_i(t)$  may not coincide with the discrete locations of  $u(x_i(t), t)$ . This means that  $x_i(\Delta t) = x_i(0) + u(x_i(0), 0)$ , where  $\Delta t$  is the inter-frame time, i.e. the time at the second frame. The material's subsequent position can be found by further additions of the interpolated Eulerian displacement at those positions, giving  $x_i(t + \Delta t) = x_i(t) + u(x_i(t), t)$ . The tracked material paths derived in this way are shown in figure 4.10, where it can be seen that the regions in the data set with poorly determined displacement (around  $t = 250$ ,  $x = 10.5$  mm) result in poorly tracked material positions, as expected. The displacement from the initial position for a point within the material can be found as  $U_i(x_i(0), t) = x_i(t) - x_i(0)$ .

It should be noted that this method also allows estimation of material displacement in regions of the specimen where features cannot be robustly tracked and axial gaps are left in the tracking record, as seen in figure 4.8. The data in figure 4.10 are not simply an interpolation of those in figure 4.8, because more information has been included. This is the preferable method of calculating material displacement when individual features cannot be tracked continuously.

The reconstructed displacement data were then smoothed using a least-squares spline-fit (see the `csaps` function of Matlab [91]) in the time and axial dimensions and then differentiated to obtain the engineering strain,  $\varepsilon_s(x_i, t) = \frac{\partial U_i}{\partial x}|_t$ , shown in figure 4.11(a). The level of smoothing was chosen to qualitatively achieve a representative strain field. The extremes in

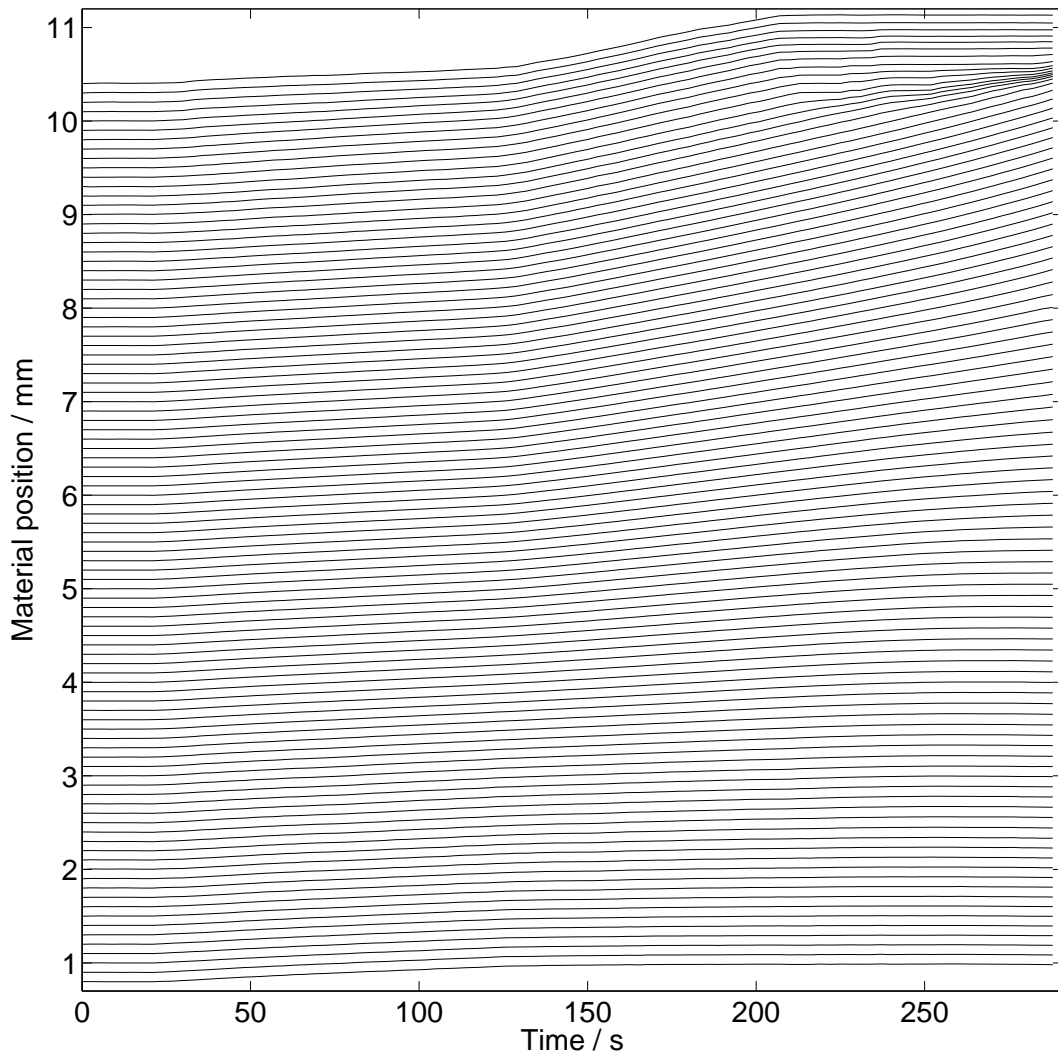


**Figure 4.10:** The tracks of material positions from the finely determined displacement data of figure 4.7(b).

the choice of smoothing level were no smoothing (csaps parameter = 1), which resulted in the differentiation of very noisy results that produced meaningless strain data, and complete averaging (csaps parameter = 0) to a single constant value of displacement and hence zero strain. The smoothing level chosen was a compromise chosen to find the most representative strain field and for figure 4.11(a) the csaps parameters were 0.99 in the time dimension and 0.9 in the axial dimension. More sophisticated smoothing could have used the displacement to inform the smoothing process and smooth regions where the displacement had a high gradient less than other regions. This would help capture the detail in the strain field and obtain more accurate

values of strain in more uniform regions of the displacement field.

In order to validate these data, strain was also calculated as a function of initial axial position using the areas of the cross-section, which were calculated using the technique presented in chapter 3. Before calculating the areas, the edge curves were also smoothed axially by low-pass filtering with a roll-off frequency of 17 periods per mm. Since the elastic strain is small, the volume of the specimen was assumed constant, allowing the engineering strain to be calculated at time  $t$  as  $\varepsilon_a(x_j, t) = (A(x_j(0), 0) - A(x_j(t), t))/A(x_j(t), t)$ , where  $A(x_j(0), 0)$  and  $A(x_j(t), t)$  are the original and current cross-sectional areas respectively, for the material at axial position  $x_j(t)$ . The initial area could not have been found without the derived material paths shown in figure 4.10, since the initial axial position corresponding to each current axial position could not have been known. Knowing the paths also allowed the strain,  $\varepsilon(x_j, t)$ , to be calculated as a function of the initial location of the material, and not only its current location. The result of the areal strain calculation is shown in figure 4.11(b).

Comparison of the two methods for calculating engineering strain: areal and modal averaged displacement, provides validation of the new technique. Figure 4.12 shows the comparison of the shaded contours of areal strain with four different representations of strain from the tracks. Shown in figure 4.12(a) and figure 4.12(c) is the strain from the finely determined displacement in figure 4.7(b). Figure 4.12(b) and figure 4.12(d) show the strain from the coarser displacement data of figure 4.7(a) (both smoothed with csaps parameters equal to 0.9999 in the time and axial dimensions). Figure 4.12(c) and figure 4.12(d) show how smoothing with a least squares spline function can improve the appearance of the data by removing noise (the csaps parameters were 0.99 in the time dimension and 0.9 in the axial dimension).

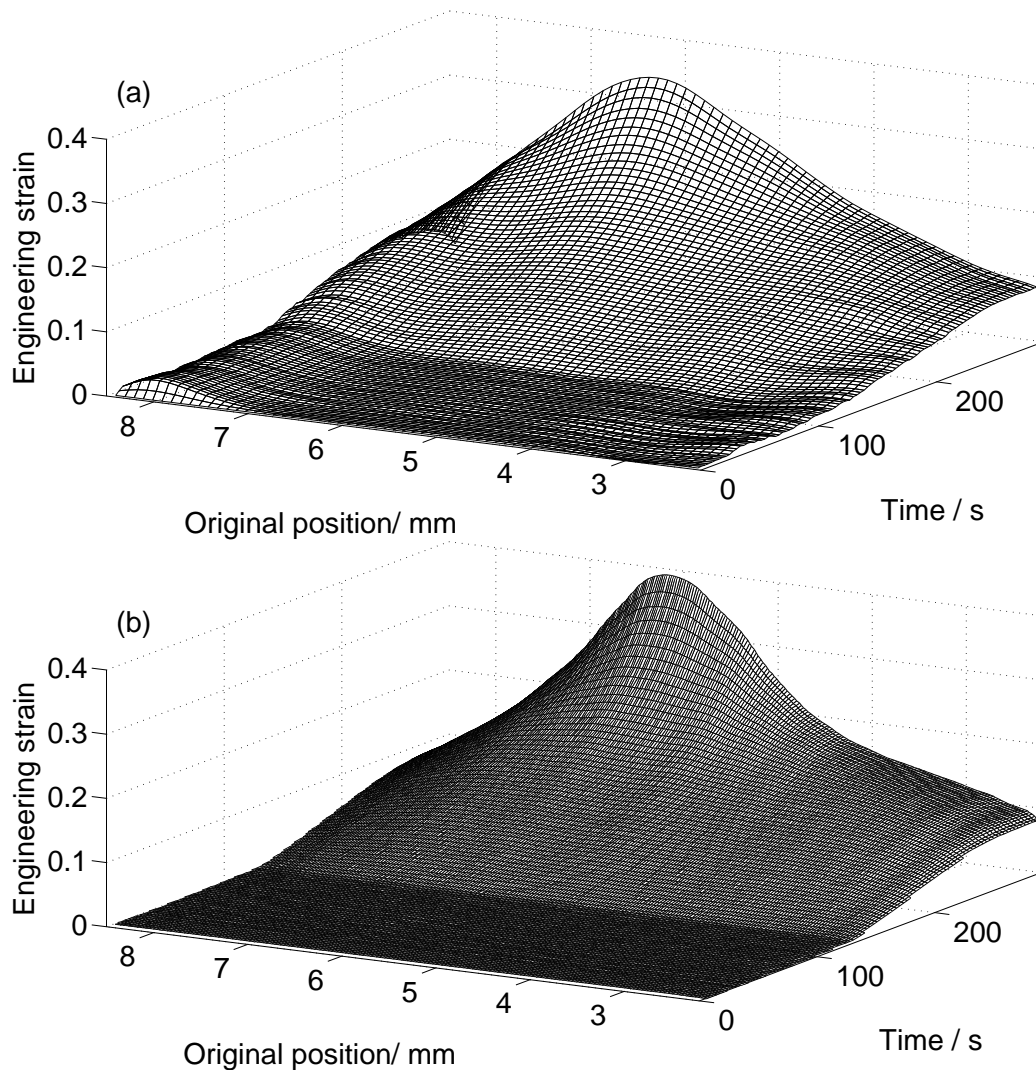


**Figure 4.11:** (a) Engineering strain,  $\varepsilon_s(x, t)$ , calculated using the displacement of the tracked surface roughness. (b) Engineering strain,  $\varepsilon_a(x, t)$ , calculated using the cross-sectional areas as a function of initial position and time.

### 4.3 Discussion

The new technique constitutes a method for the determination of material displacement and strain with high spatial data resolution. It is applicable in situations where the roughness on the surface of a specimen is discernible in the edge profile, moves with the deforming material, and photographs can be obtained at a sufficiently high rate. A strategy for tracking features in this profile has been presented that can reduce false matches and allow the continuous tracking of material positions. For regions in the profile that cannot be confidently tracked throughout

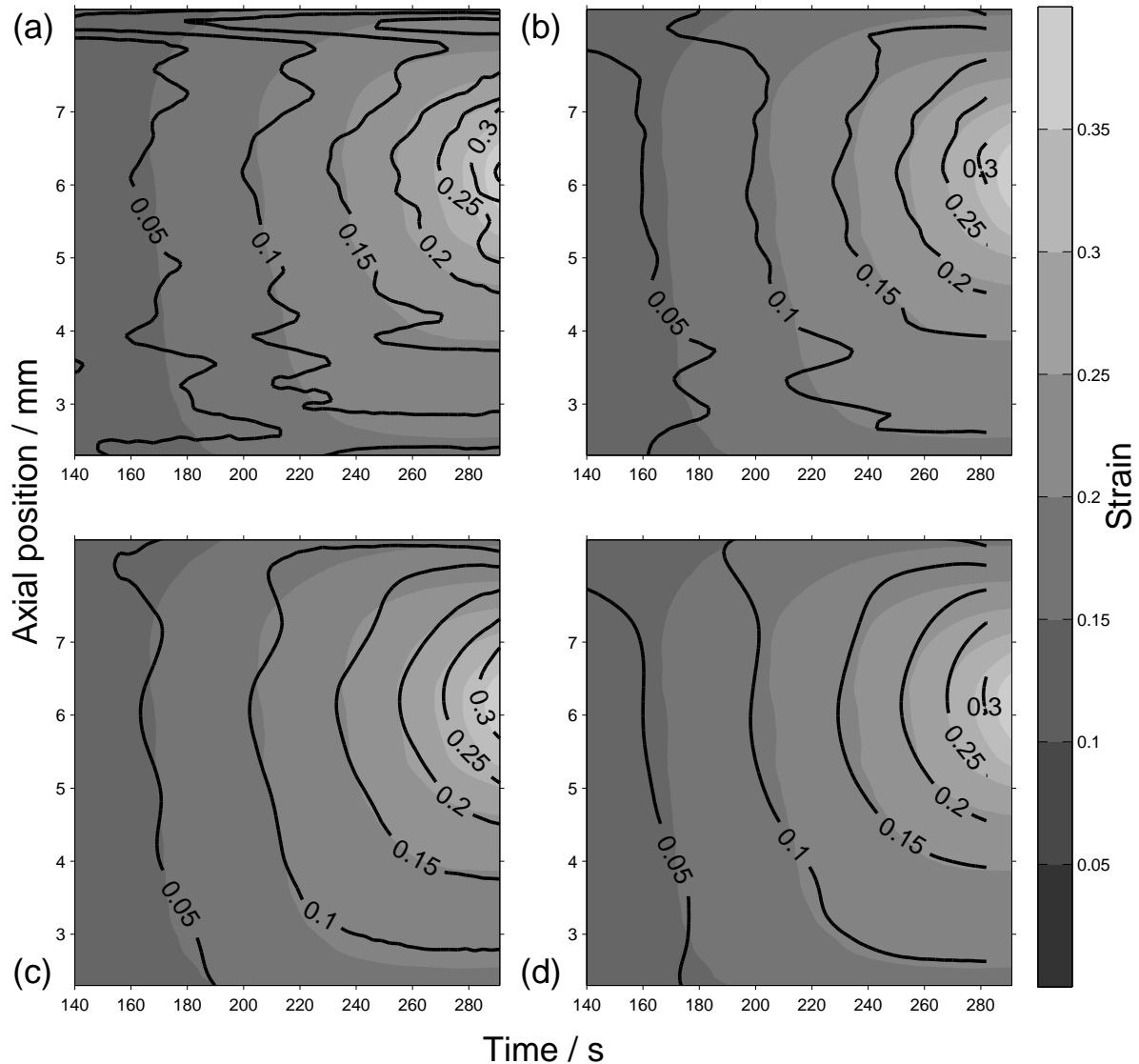


**Figure 4.12:** Contours of strain as functions of axial position and time. The shaded contours represent the areal strain and the lines represent roughness tracking strain with different levels of smoothing. (a) Modal averaging taken over 1 mm of length and consecutive frames only. (b) Coarser modal averaging taken over 1.5 mm of length and 3 periods spanning 4 frames. (c) The data in (a) with spline smoothing applied. (d) The data in (b) with spline smoothing applied. Note that the roughness tracking strain data in (b) and (d) do not cover the entire duration of the experiment because of the broad filtering.

the experiment, a method for determining average displacement and expected material paths has also been presented. These data have also been shown to provide a reliable method for calculating strain with a high spatial resolution.

This technique presents advantages over speckle digital image correlation because it does not require the specimen to be marked, which obscures the surface and prevents accurate simultaneous measurement of radial position. Marking also obscures potentially important failure mechanisms. As the technique is non-contacting, it has the associated advantages of other non-contacting techniques in that it can be used in high speed and/or high temperature experiments. The surface roughness in this experiment was the result of the manufacturing process (turning on a lathe) which left a smoothly varying surface roughness with peaks separated by an average of  $\sim 60 \mu\text{m}$ , allowing the technique to track material positions with a high spatial resolution that may be difficult to achieve by digital image correlation of speckles. The equipment required to implement this technique is also readily available.

Data from a cylindrical specimen have been displayed. However, the technique need not be limited to this geometry. This method provides an accurate technique for measuring localised strain at an abundance of locations throughout the gauge length of any specimen.

The new technique compares well against displacement measurements from a laser extensometer and calculation of strain from specimen area. Figure 4.12 shows good agreement between areal strain and roughness tracked strain.

The low frequency component of the difference in displacements shown in figure 4.9 could have been caused by the initial disparity in the position being tracked by the two methods. Because the surface roughness was not uniform, and hence did not guarantee a distinct feature at a certain location, the two locations under comparison were not the same; in fact they were separated in these two cases by 0.08 mm and  $-0.05$  mm. Given that the strain at these locations rose to  $\sim 10\%$  during the experiment, part of the difference can be attributed to this disparity, rather than a fault with the roughness tracking.

One proposed reason for small differences between the measurements is that the separation of neighbouring features,  $\sim 30 \mu\text{m}$ , is similar to the structural length scale in the material, *viz.* the grain size. Thus the material is inhomogeneous on this scale and some noise may be due to the different axial strain of neighbouring grains. However further experiments would be required to determine the extent of this effect. Further sources of error are discussed in § 7.3.2.

Removing false matches is an important part of this technique. Whilst the matching strategy is designed to prevent these, it cannot be verified that any particular match is true. Part of the problem with making correct matches is that the edge curve changes shape from one frame to the next: noise in the images; the changing shape of the surface due to its elongation; and a changing horizon due to radial motion of the surface, all affect the apparent shape. Much effort was exerted in investigating solutions to obtain even fewer false matches. For example, cross-correlating patches of the edge curve with the edge curve in the next frame partially helps to make correct matches, but the length of the edge curve required to make a sufficiently unique patch reduces the resolution of the tracking through an averaging effect and provides diminishing returns on the information gathered. Therefore cross-correlation was found to be of insubstantial assistance and was not used. Better tracking was also sought by adapting stochastic methods such as RanSAC [92] and MLESAC [93] where the gradients of the zero-crossings and the heights of maxima and minima were used as *a priori* descriptors for these features so that groups could be found that agree on general displacement and false matches removed. However this was only of benefit when the descriptors had persistent values, which was found not to be the case for most of the features detected in the edge curves here, as the descriptors are second order and are affected more by noise.

In future applications of this technique, the occurrence of false matches can be reduced by better estimates of expected displacement for matching guidance. This estimate could come from extra measurement by, for instance, sparse extensometer measurement, from predictive modelling of displacement or manual estimation. However these may not be readily available

---

and simple linearly interpolated cross-head displacement should be adequate in most experiments where the wavelength of surface roughness is shorter than the inter-frame displacement and a prediction is therefore required.

## 4.4 Conclusion

A method for measuring displacement in uniaxially loaded specimens with high position resolution,  $\sim 30 \mu\text{m}$ , has been developed. The profile of surface roughness is seen in images of a specimen captured by high resolution digital cameras. This profile is measured in the images using sub-pixel accuracy edge detection. Features within this edge are detected using data from its high frequencies, ignoring the nominal specimen dimensions and using only surface roughness information. A method for tracking these features that copes with problems inherent in feature tracking where the features are not designed to be tracked is given. This method uses an estimate of the specimen displacement from the cross-head of the loading device to guide the matching of features between image frames and then using modal-average filtering in sub-regions that span a range of time and axial length to identify incorrect matches.

For specimens with a mean surface roughness wavelength shorter than the maximum material displacement between frames, it has been found that to obtain an accurate matching of features, an estimate of displacement is required. This could be obtained through external displacement measurement, approximate finite element modelling or manual estimation of some of the matching. Here, the cross-head displacement was used and found to be suitable.

Once the features had been matched correctly, material displacement for positions at high resolution was obtained. In practice the average separation of features that could be tracked throughout the experiment was  $\sim 30 \mu\text{m}$ . The displacement information was also differentiated to calculate the strain in the specimens.

The technique does have drawbacks, one of which is that some of the strain resolution that could theoretically be achieved by measuring the displacement of all of the features in the edge curve must be sacrificed in order to gain higher accuracy through smoothing.

Difficulties also arise due to noise in images, which is a factor in most photogrammetric applications, and can be reduced by appropriate lighting conditions and equipment.

## Measurements of Cross-Sections in Specimens of CP-Zr and Steel

---

Ti-6Al-4V is the main material of interest to this research. However, the photogrammetric techniques developed are applicable to a range of anisotropic materials. To demonstrate the applicability of this method to materials that exhibit even greater anisotropic behaviour under applied deformation, specimens of clock-rolled commercially-pure zirconium (CP-Zr) have been loaded in tension at QS (quasi-static) and HR (high strain rate) and their cross-sections have been measured using the reconstruction technique developed in chapter 3. The clock-rolled CP-Zr is similar to the CR-Ti-6Al-4V, in that it is a rolled HCP material. Clock-rolling is a rolling process whereby a plate of material is repeatedly rolled in evenly spaced directions to produce a transversely isotropic microstructure.

To further assess the capabilities of the developed techniques, tensile specimens made from threaded mild steel bar, which should have transverse isotropic symmetry perpendicular to the bar axis, have also been loaded in tension at QS and HR and measured using the technique to demonstrate its sensitivity when measuring near-circular cross-sections. Ti-6Al-4V and the CP-Zr are also expected to exhibit transversely isotropic mechanical behaviour. The use of steel, rather than Ti-6Al-4V specimens cut from the 3-direction, is a demonstration of the technique's applicability to other alloys that deform nearly axisymmetrically.

---

In addition, interrupted tests were performed in which a specimen of steel and one of CP-Zr were loaded quasi-statically until they necked significantly and were then unloaded, before fracture occurred. The surface shapes of these “interrupted specimens” were measured using the CMM described in chapter 3 and the semi-major and semi-minor axes were measured using an optical comparator (OC). In § 3.3.1 elliptical prisms were independently measured using the CMM and then used to estimate the errors inherent in the technique under experimental conditions, which provided a level of confidence for measuring uniaxial specimens before the necking instability had begun. In this chapter, the independent measurements of the interrupted specimens are used to estimate the errors in measuring the cross-sectional shapes of specimens that have necked, and hence no longer have transverse-plane symmetry within the gauge section. This final comparison completes the process of verifying that the measurements correspond to specimen dimensions that was begun in chapter 3.

The results from three CP-Zr specimens will be discussed here: one that was loaded at the QS strain rate until it had significantly necked but not fractured, and two that were loaded in tension until fracture at QS and high strain rates. The results from three steel specimens with the same loading conditions are also given.

### 5.0.1 Outline

The CMM data of the interrupted specimens are first analysed to verify that the cross-sections of these homogeneous samples deform elliptically throughout the gauge section. Symmetry arguments about the operations during material manufacture can be made to predict ellipticity in the cross-sections of initially cylindrical specimens until voids are created or fracture occurs. The data presented in this chapter provide a more rigorous experimental confirmation of this theory than that given in any of [6, 7, 94], where elliptical sections of zircalloy and Ti-6Al-4V were measured. This is given in § 5.1.

The CMM data from the interrupted CP-Zr specimen are then analysed to determine whether the ellipse orientations change observably with axial position. If they did, this would indicate that the material orientation changed with strain due to the different strain levels reached throughout the neck. The CMM and OC data from both the CP-Zr and steel interrupted specimens are finally compared to the measurements obtained from the cross-section reconstruction technique to estimate the errors in measuring a necked specimen under real experimental conditions. The data are compared individually and elliptical fits of the CMM data are also compared to the cross-section reconstruction ellipses.

QS and HR tensile experiments taken to fracture were performed on the two materials and cross-section reconstruction applied. Experimental results are presented and significant features are discussed in § 5.4.

Research has also been carried out in collaboration with Euan Wielewski *et al.*, to measure the elliptically deforming cross-section of Taylor impact specimens of the CP-Zr material [95]. This work is described in a recent paper [4]. CMM measurements taken after the impact on one of these Taylor impact specimens have been compared to measurements obtained from a cross-section reconstruction using high-speed photography and mirrors. The results of this comparison are given in § 5.5. The author's principal intellectual contribution to this research was the method of measurement, the design of the optical configuration and the analysis tools. This research demonstrates some of the wider applicability of the technique and the new types of measurement that may now be made.

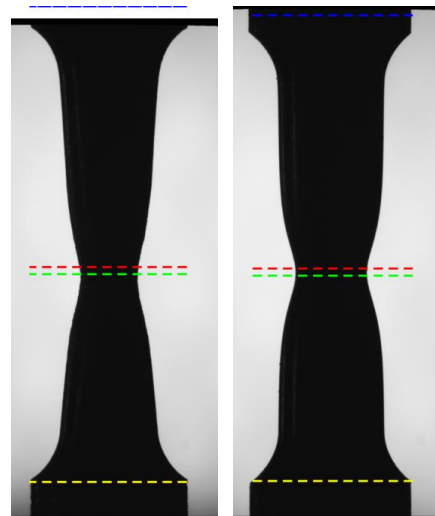
## **5.1 Quantifying the ellipticity in interrupted steel and CP-Zr tensile specimens**

In order to verify that the cross-sectional shapes of the interrupted specimens were elliptical, specimens with the dimensions given in figure 1.8, page 18, were extended to a nominal strain

of 23 %, after which the tensile force was reduced to zero at the negative of the initial strain rate. These specimens were then measured by the CMM at 0.2 mm axial intervals to give points around their circumferences. Ellipses were fitted to these points at each height. The results of differences between the measured positions and the least-squares ellipse fit to them can be seen in figure 5.3. In this figure, green squares indicate the position of minimum cross-sectional area, blue asterisks indicate the position of largest area and red crosses indicate largest error. The colouring scheme corresponds to that in figures 5.1 and 5.2 which respectively show the positions of the highlighted cross-sections along the specimen, and the distributions of the points with respect to the ellipses. The irregular axial spacing of the data in figure 5.3 is due to the omission of obviously erroneous measurements in the CMM data where only part of the circumference could be measured.

Figure 5.2 shows the deviation of the CMM data points from elliptical. The length of the spikes in this figure are scaled to 20 times the distance between the fitted ellipses and the CMM measurements. The outer, blue, plots correspond to the axial locations indicated by a blue asterisk in figure 5.3. The green plots correspond to the axial locations indicated by a green square in figure 5.3. The red plots correspond to the largest differences in figure 5.3, indicated by red x. These three positions can be seen in photos of the specimen in figure 5.1.

A similar verification has been performed by Rittenhouse *et. al* [94] on specimens of anisotropic Zircaloy-2 (an alloy of zirconium), where specimens were measured using an optical comparator after fracture to evaluate their cross-section's deviation from elliptical at several axial positions. In the Rittenhouse report the ellipses were measured by measuring the major and minor diameters, whereas in this research a least squares fitting of an ellipse to the 2 dimensional points is made, which is a better estimate of the true ellipse because it uses many more measurements to estimate the elliptical shape.



(a) The interrupted CP-Zr specimen. (b) The interrupted steel specimen.

**Figure 5.1:** The interrupted QS tensile specimens of Zr and steel in the relaxed state from the left camera view. The yellow dashed line is at the 0 mm axial height. The other dashed lines indicate the gauge positions of data in figures 5.2 and 5.3.

## 5.2 Comparison of elliptical cross-section measurement technique

The optical comparator (OC) used was a Mitutoyo Profile Projector, type PV-600 with a quoted uncertainty in measurement of the diameters as  $\pm 4 \mu\text{m}$ . The measurements were made such that the narrowest diameter that could be found anywhere in each specimen, i.e. at the neck, at the orientation showing the  $r_b$  direction, was taken to be across the dimension of the narrow profile. The wide profile, showing  $r_a$ , was taken to be at  $90^\circ$  to this first orientation. Measurements were made of the diameters across these profiles at 0.3 mm intervals. Given that the elliptical orientations did not change significantly with axial position, as shown in § 5.3, these diametral measurements provide data on  $r_a$  and  $r_b$  with axial position. Using these radii, the area and aspect ratios were calculated.

In figure 5.8 the difference between the CMM position data and the cross-sectional reconstructions for the CP-Zr and the steel specimens are shown. It is suggested that the accuracy of

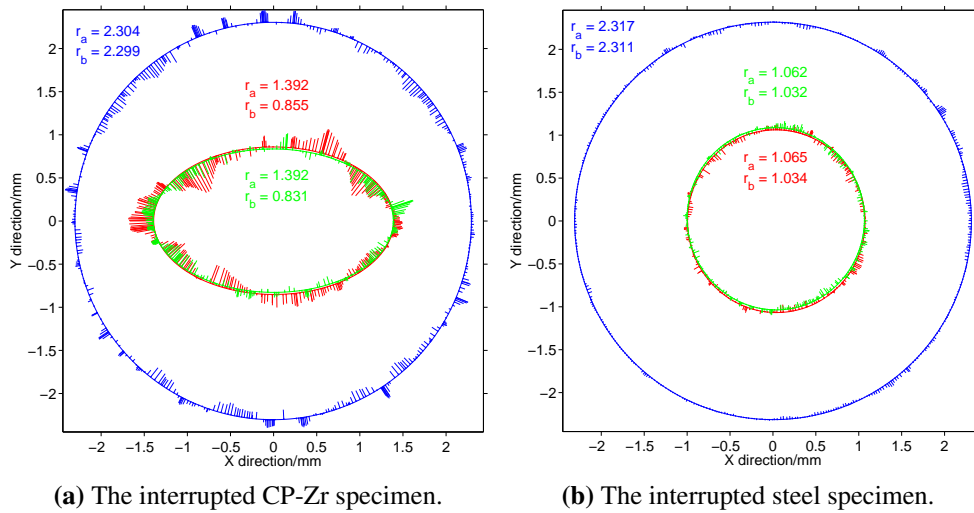


**Figure 5.2:** The ellipse fits to CMM data at three positions along the axis of the interrupted specimen tests are plotted as solid ellipses. The CMM measurements around the perimeter of the gauge section are plotted as dots. Error spikes are plotted through the CMM measurements, starting at the closest position on the ellipse, at 20 times the the distance between the ellipse and the measurement.

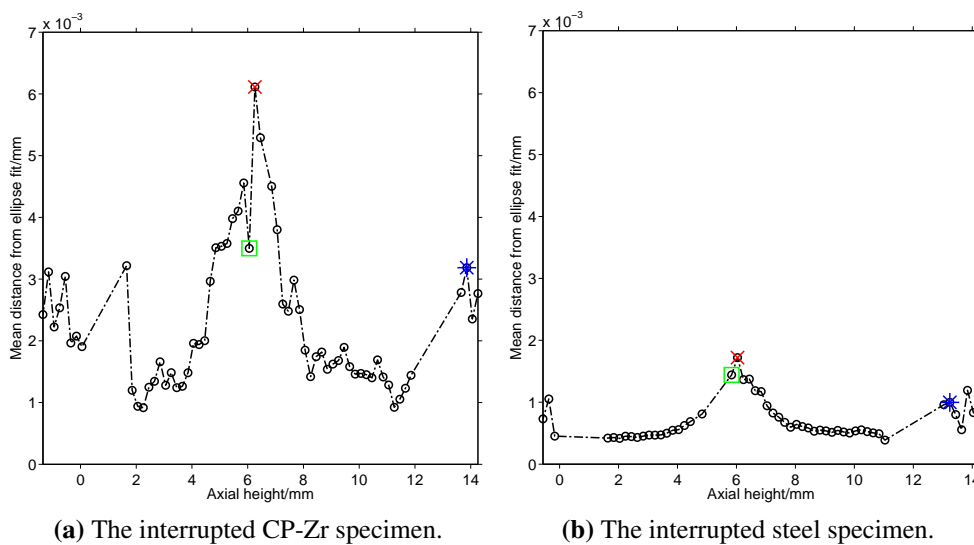


**Figure 5.3:** The mean of the magnitude of the distance from the points measured by the CMM to the nearest elliptical fit as a function of axial position.

the CMM data is below its specified value because of the roughness of the specimen's surface (due to pitting) and the high curvature around the necked region, which have both combined to cause a systematic error in the axial location of the measurements due to offsetting of the CMM probe. Hence it is suggested that the CMM data, and not the cross-sectional measure-

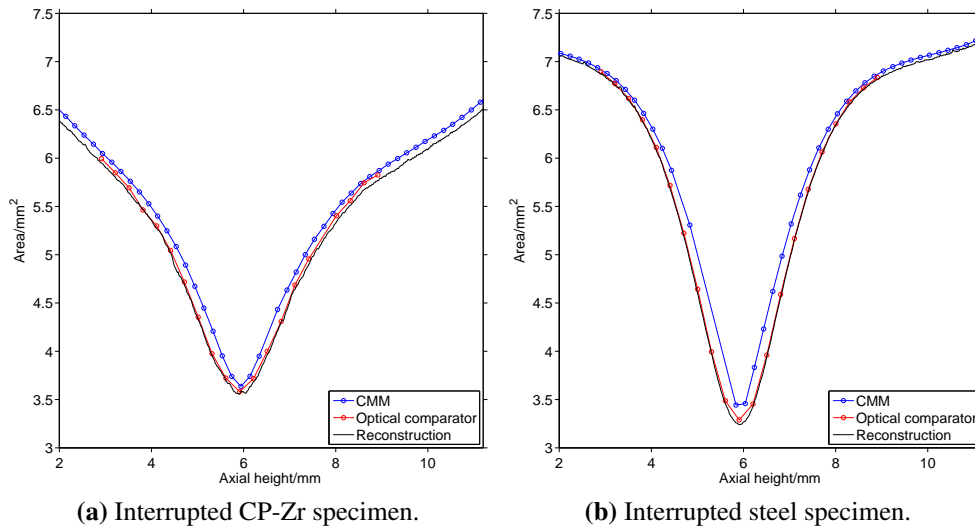


**Figure 5.4:** The areas  $r_a r_b \pi$  measured in the interrupted CP-Zr and steel specimens. The data were obtained from ellipses fitted to CMM data, by the reconstruction technique and by the optical comparator.

ment technique, are responsible for the large differences. This is supported by the data from the OC, which is in much closer agreement with the reconstruction data than the CMM data.

The CMM data and the ellipse cross-sectional data have also been compared using the elliptical fits to the CMM data and the reconstructed elliptical cross-sections. The area with position data and aspect ratio with position data from the OC and the reconstruction technique have also been compared. The percentage difference in these measurements have been calculated using linearly interpolated CMM and OC data because there were far fewer measurements from these devices. The values of these differences at axial positions that approximately coincided for the reconstruction technique and the CMM or OC have been highlighted in the plots.

Figure 5.4 shows the area with position from the elliptical fits to the CMM data, the OC data and the reconstructed elliptical data from the interrupted specimens. Figure 5.5 shows the percentage differences in these areas.

Figure 5.7 shows the percentage differences between the aspect ratios, which are shown in figure 5.6a and figure 5.6b. It can be seen in figures 5.4a and 5.6a that the CMM data have a narrower peak in area and aspect ratio, probably due to CMM's probe not being able to correctly

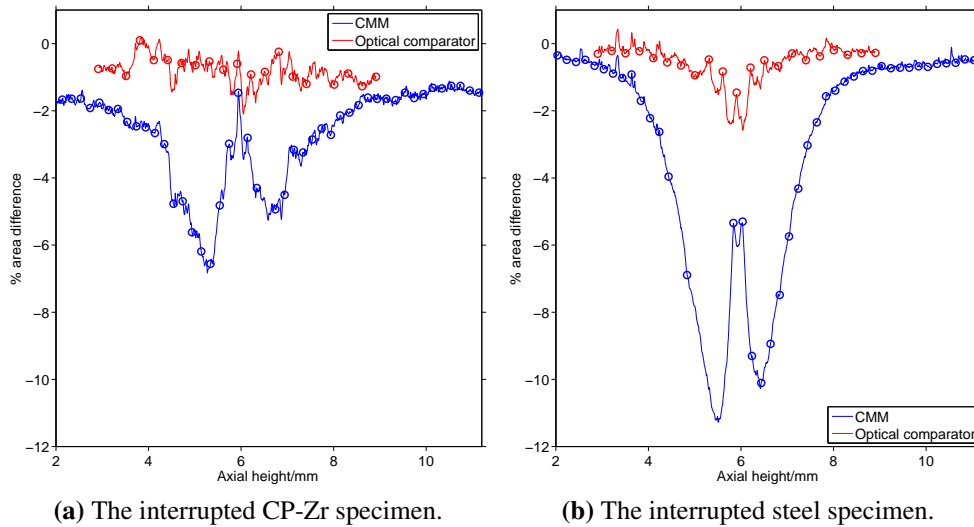


**Figure 5.5:** The percentage difference in area,  $100(A - A_D)/A_D$  (where D are either the CMM data or the OC data), between elliptical fits to CMM data or OC measurements and cross-section reconstructions of interrupted specimens during QS tensile loading. The circles indicate values at axial positions that approximately coincided for reconstruction data and CMM or OC data.

follow its height when in contact with the concave profile of the specimen, whereas the OC data follows the reconstruction data more closely. This difference in narrowing between the CMM data and the reconstruction data can be seen to cause the largest errors in figure 5.7. The location of the largest differences are consistently in the region immediately above and below the neck in figures 5.8 and 5.5, where there is the greatest curvature in the profile. This is also evidence that the error is in the CMM measurement because the OC and the reconstruction technique are independent of location, unlike the CMM measurement, which is affected by the curvature.

If the CMM data are assumed to be offset axially, then the measurements are valuable in verifying the ellipticity of the shape of the cross-section and the constant elliptical orientation with axial position. However, the CMM data are not likely to be useful for verification of the reconstruction technique's ability to measure aspect ratio and elliptical cross-section area with position. The OC data is more useful for those comparisons and can be seen to have a worst-case error of  $\pm 1\%$  in measuring aspect ratio and a  $\pm 2\%$  in measuring area for both the CP-Zr and the steel specimens. This verifies the technique's ability to measure these properties for real

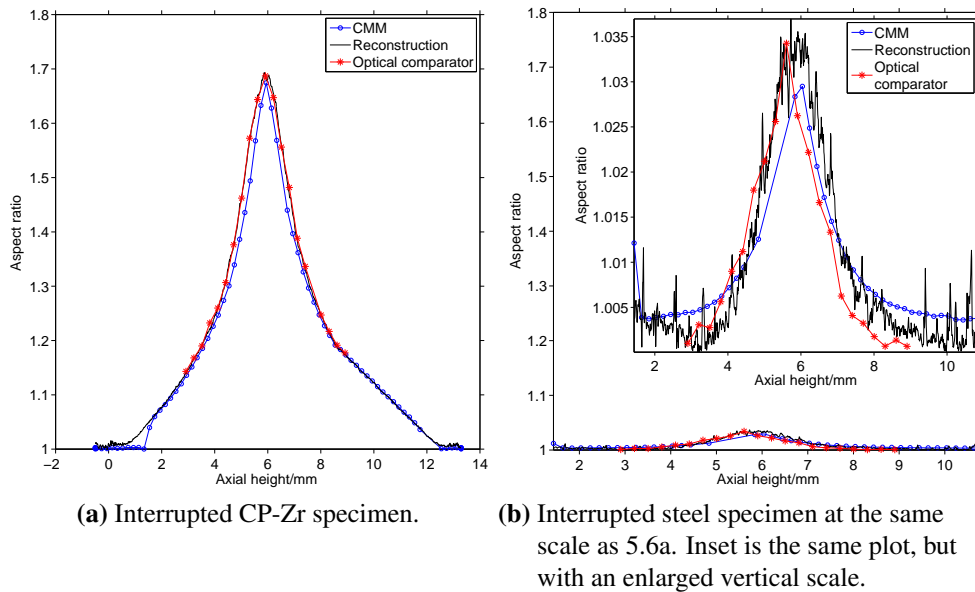


**Figure 5.6:** The aspect ratios  $r_a/r_b$  (where  $r_a > r_b$  always) measured in the interrupted CP-Zr and steel specimens. The data were obtained from ellipses fitted to CMM data, by the reconstruction technique and by the optical comparator.

specimens with varying cross-sectional shapes as well as prisms of various aspect ratios, which were measured in § 3.3.1.

### 5.3 Ellipse orientation measurement

The interrupted steel specimen had a cross-section that was very close to circular, as is shown in figure 5.2b, so it did not have a meaningful elliptical orientation, or at least one that could be measured very accurately. The CP-Zr specimen, on the other hand, had a strongly elliptical cross-section, the aspect ratio of which varied with axial position, and hence strain (because it had necked).

The relative orientation of the elliptical cross-sections is shown in figure 5.9. The orientation of the specimen in the CMM relative to the material direction could not be accurately determined due to errors in aligning the specimen in the apparatus. Therefore, the data in figure 5.9 have been plotted with an offset so that each set has a zero mean. This permits a relative

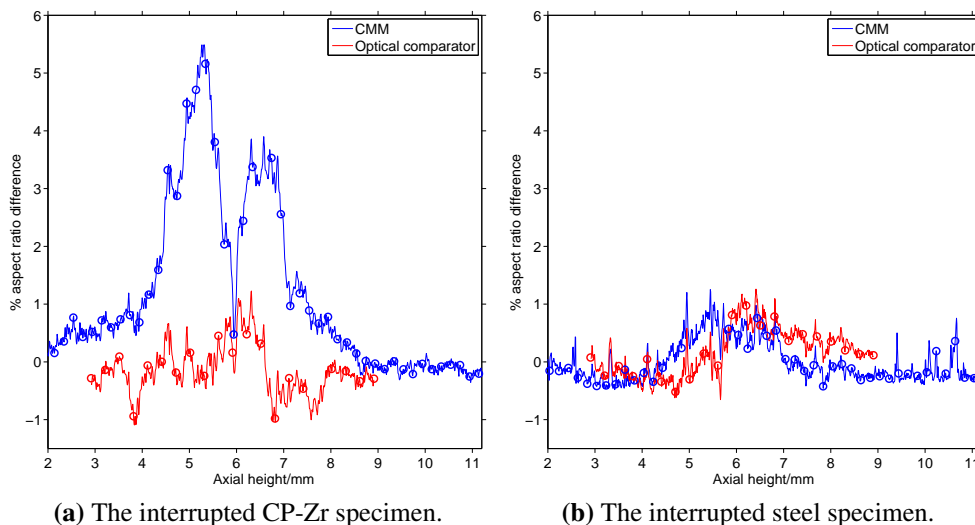


**Figure 5.7:** The % difference in aspect ratio,  $100((r_a/r_b) - (r_a/r_b)_D)/(r_a/r_b)_D$  (where D are either the CMM data or the OC data), between elliptical fits to CMM data or OC measurements and cross-section reconstructions of interrupted specimens during QS tensile loading. The circles indicate values at axial positions that approximately coincided for reconstruction data and CMM or OC data.

comparison of orientation variation throughout the gauge length. It can be seen that, although there is some random variation, both sets of data have reasonably constant cross-sectional orientations along the axial direction. A suggestion for improving the alignment of the specimen in the apparatus is presented in § 7.3.2.

## 5.4 QS and HR tensile results for CP-Zr and steel

Two uniaxial tensile specimens, one of CP-Zr and one of steel, were deformed quasi-statically and another two specimens, again one each of CP-Zr and steel were deformed at the high strain rate whilst applying the experimental method described in chapter 3. The mean QS total strain rate in the plastic region for CP-Zr was  $1.6 \times 10^{-3}$  and at HR was  $4.4 \times 10^3$ . The mean QS plastic strain rate for steel was  $3.3 \times 10^{-3}$  and at HR was  $5.6 \times 10^3$ . The optical configuration of the QS experiments consisted of the three TELI digital cameras fixed at an angular spacing of  $45^\circ$ . All three QS camera views were of specimen silhouettes.

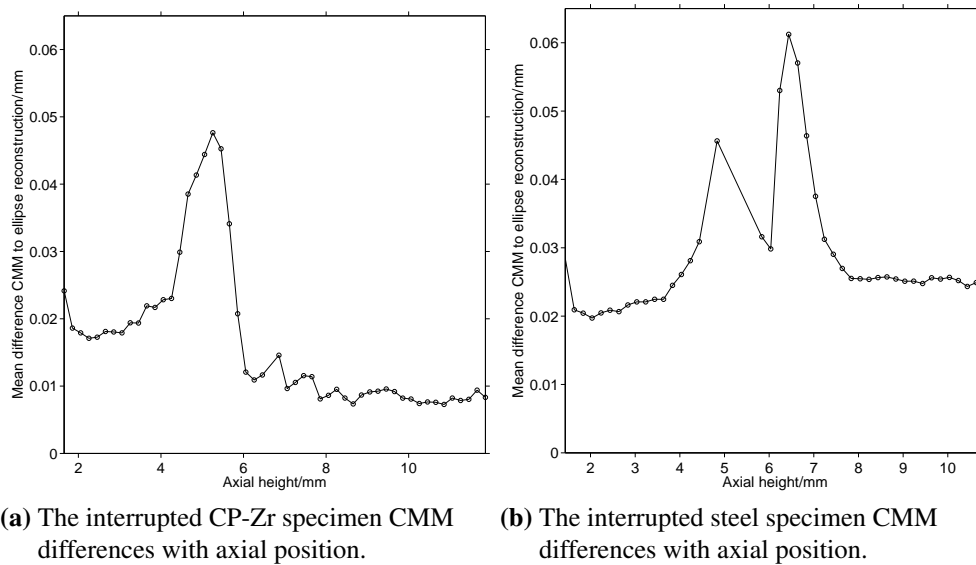


**Figure 5.8:** Mean distances from CMM data to cross-section reconstructions of interrupted specimens during QS tensile loading.

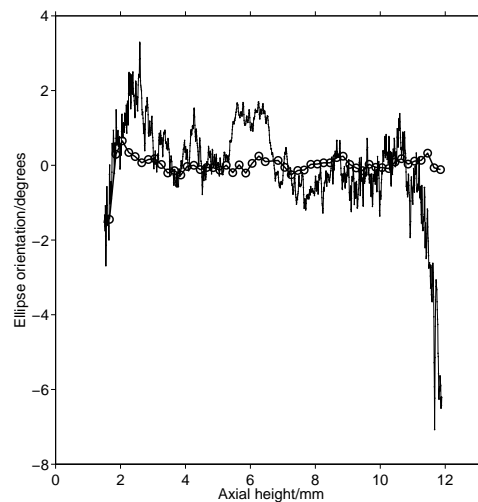


**Figure 5.9:** The orientation with respect to axial position in the interrupted CP-Zr specimen. Each plot has been shifted to have a mean of zero.

The HR views were of the silhouetted specimen and two mirrored side views using mirrors fixed at  $120^\circ$ . The silhouette lighting was achieved in the limited space available by pointing the flashes at panels of projector screen material to create a diffuse bright background for all three views.

### 5.4.1 Strain calculation from DIC

The strain in wave based SHB analysis of HR tensile specimens is often subject to a certain amount of error due to the stress wave reflections from various surfaces in the more complex geometry of tensile specimens. In order to correct for these errors, DIC of the specimen shoulders in the high-speed photographs was performed to calculate the correct strain in the specimen when the photos were taken. This allows the strain calculated in the SHB analysis to be scaled and shifted to obtain more accurate overall strain values. The results of this correction are shown in figure 5.10 where the shifting and scaling has been performed manually.

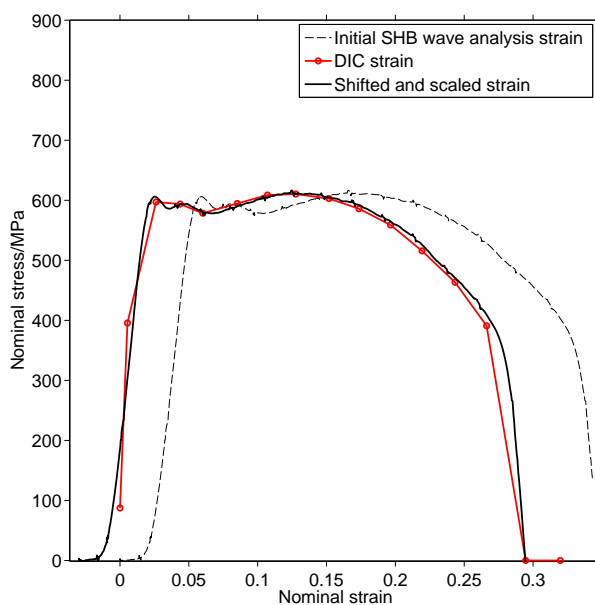


**Figure 5.10:** The original SHB analysis stress-strain curve, the DIC generated curve and the corrected SHB curve are shown for the HR CP-Zr specimen.

Figure 5.11 shows the nominal uniaxial stress-strain curves of the two materials at the two rates. The HR strain data in these plots have been corrected by the method outlined above.

### 5.4.2 Data calculation

The cross-sectional reconstruction data were collected in a calibrated-camera frame of reference, so the measurements are in mm, but the cameras are fixed and the specimen moves rela-

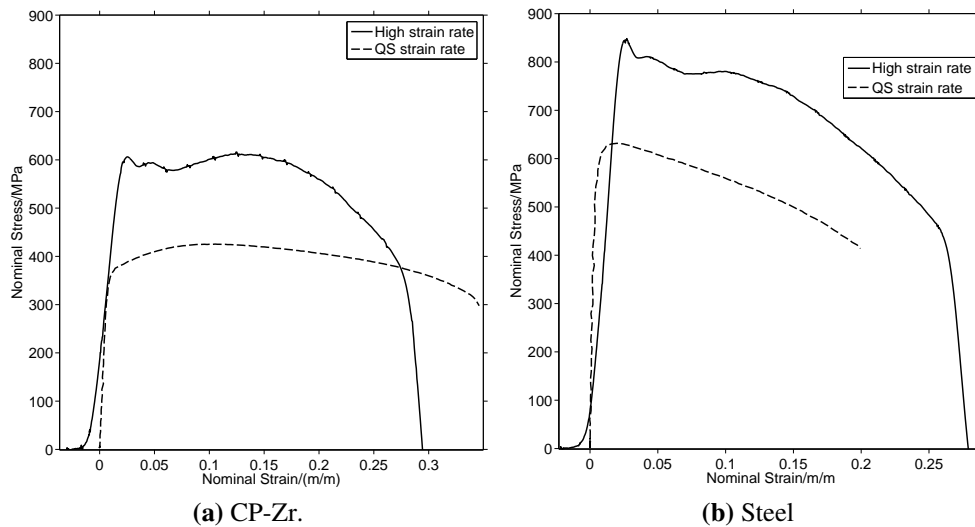


**Figure 5.11:** The nominal stress-strain history during tensile loading of the two materials.

tive to the coordinate system; an Eulerian frame of reference. The position of one end of each specimen was found by DIC of the shoulder shapes and the edges in all frames were translated vertically so that the 0 mm position was at the lower shoulder corner for tensile specimens or the lower anvil for compression specimens (described in chapter 6).

The reconstruction data comprised of elliptical parameters for all discernible axial locations (that corresponded to discrete vertical pixel ordinates, see § 3.2.1) in the static frame of reference. The technique described in chapter 4 was developed to determine how the cross-sectional shape of the specimens changed for surface material positions by tracking them. The combination of tracking the motion of material positions on the surface and the evolving elliptical shape of those positions has the potential to provide a great deal of data for comparison with numerical models of experiments such as these. Taking these measurements during an experiment and comparing them with modelling results allows the computation, using inverse identification techniques, of several modelling parameters simultaneously because of the number of measurements obtained.

In the following descriptions of the results of the experiments performed on CP-Zr, steel and Ti-6Al-4V the data will be presented in three simplified forms. All of the data are taken

from the location within the gauge length that has strained the most, according to its change in area. Assuming constant volume in plasticity allows the longitudinal strain to be calculated for cross-sectional area:  $\epsilon_A = \ln(A_0/A)$ , where  $A_0$  is the original gauge cross-sectional area. This location is at an arbitrary position in the uniform cross-section of the tensile specimens until necking begins and then it becomes the centre of the necking region until fracture. The most strained position in compression specimens is normally in the centre of the gauge length, farthest from the constraint imposed by friction with the anvils. In all of the data presented in this thesis, the minimum and maximum area positions were searched for, rather than assuming any particular location. This prevents any inequality in frictional effects on the two ends of a compression specimen from altering the data, and also takes into account the random positioning of the necking instability.

The three forms of the data presented will be:

1. The true stress against longitudinal strain,  $\epsilon_A$ , at the maximum strain position. It is noted that this is a true, material, stress strain curve and has not been measured previously.
2. The length of the semi-major and semi-minor radii,  $r_a$  and  $r_b$ , of the specimen at the maximum strain position, plotted against  $\epsilon_A$ .
3. The R ratio, defined as the ratio of total radial strains in the two principal axis directions of the elliptical cross-section  $R = \ln(r_a/r_0)/\ln(r_b/r_0)$ , where  $r_0$  is the radius of the initial gauge cross-section, at the maximum strain position; plotted against  $\epsilon_A$ . The inverse of this value is plotted for compression specimens, for direct comparison.

R is defined differently from  $R_\theta$ , defined by Kocks and the ASTM standard, in that it is always a measurement of the strain in the major-axis over strain in the minor axis, rather than the ratio of strains in material directions. This allows for the principal strain directions to differ from the material strain directions, but it also requires the orientation of the cross-section ellipse w.r.t. material axes to be quoted for all measurements of R.

These plots provide valuable information about the development of anisotropy in the materials with increasing strain. The length of the semi-major axis,  $r_a$ , is always greater than the semi-minor axis,  $r_b$ , so knowing the orientation of the elliptical cross-section relative to the material it was derived from is important. Typically the major axis of a specimen's deformed shape is aligned with the in-plane or through thickness direction for plate materials as these are the principal material directions.

Figure 5.12a shows the mean true direct stress in CP-Zr specimens under QS and HR loading as a function of true strain. It can be seen that the flow stress and ductility of CP-Zr has a strong strain rate dependence. Figure 5.12b shows the same output but for the steel specimens. Again there is a strong dependence of flow stress on strain rate, but not as significant a reduction in ductility at the high strain rate. The similarity of the true strain reached by the QS steel and CP-Zr specimens before fracture is coincidental.

Figure 5.12e shows the R ratio, as a function of the true minimum area strain, calculated at the minimum cross-section for the QS and HR CP-Zr specimens. The R value varied significantly before the UTS where the axial strain was still small. During purely elastic deformation the R value is poorly calculated as it is a ratio of small values close to the noise band of the data. The R ratio in the QS CP-Zr specimen changed from 0.058 at the UTS to 0.135 at the last frame before fracture ( $\epsilon = 0.78$ ), suggesting that the anisotropy reduced with increasing axial strain. The result is repeated at HR but with slightly greater initial anisotropy. The major axis of the deformation was in the through-thickness direction for both strain rates.

Figure 5.12f shows the results of the same calculation but for steel. Again the R ratio changed significantly before the UTS was reached but settled to a relatively constant value thereafter, changing from 0.882 just after the UTS to 0.896 just before fracture ( $\epsilon = 0.79$ ). The R ratio in the QS steel specimens had been expected to be 1. The aspect ratio of the elliptical cross-section of the interrupted steel specimen measured by the CMM is in agreement with the degree of anisotropy measured in the steel and it is therefore postulated that the threaded steel

bar from which the specimens were made had a TMP history that left it more anisotropic than expected (or indeed intended, for these comparison measurements). The orientation of the elliptical cross-sections in the steel specimens was not known in any meaningful way because the threaded bar had no markings to indicate its material direction. EBSD imaging could determine the presence of texture in the material, and this could be correlated with the orientation of the specimen, but this was not a goal of this research.

The major and minor radii of the cross-sections of the four specimens used to derive the data in figure 5.12 are shown in figure 5.14. The HR radii in these plots are derived from filtered edge reconstructions - where the edges were smoothed by a 10 pixel long averaging filter before cross-section computation - to remove the influence of surface texture and noise in the edge detection. The radii of the HR CP-Zr specimen from the *unfiltered* edges are shown in figure 5.15 for comparison. These data could be used to calculate the radius of curvature for the major and minor directions of the specimens and then the modified Bridgman correction could be made to calculate the effective uniaxial stress, as described in § 1.6, rather than simply the mean direct true stress, which has been presented thus far.

Data describing the R ratio and true-stress true-strain curves for CP-Zr and steel under QS and HR loading have not been seen before in the literature.

The shape of the maximum strain cross-sections are plotted in figure 5.13. These plots show the principal strain directions relative to the known material axes in the case of CP-Zr and relative to arbitrary transverse bar directions for steel. The similarity of maximum strain direction between the two steel samples at QS and HR is coincidental.

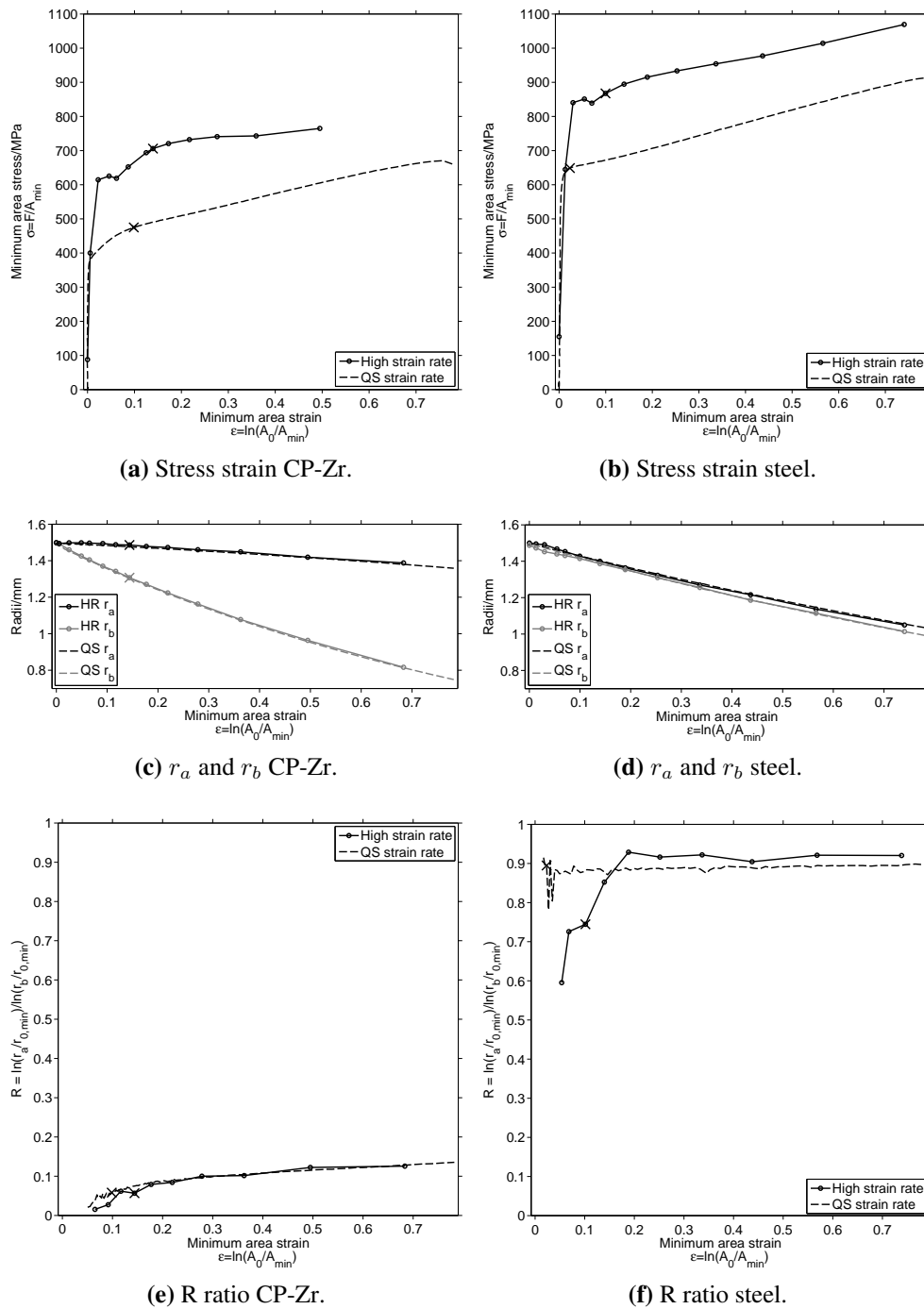


**Figure 5.12:** For steel and CP-Zr the maximum mean true direct stresses are plotted with strain calculated by  $\epsilon = \ln(A_0/A_{min})$  where  $A_{min}$  is the minimum cross-sectional area. The minimum semi-major and semi-minor radii of the specimens are shown against areal strain too. Also plotted is the R ratio of true strains calculated using  $r_a$  and  $r_b$  at the minimum cross-sectional area plotted with the same strain. The R ratio could not be calculated reliably for small strains. The UTS positions are indicated with crosses.

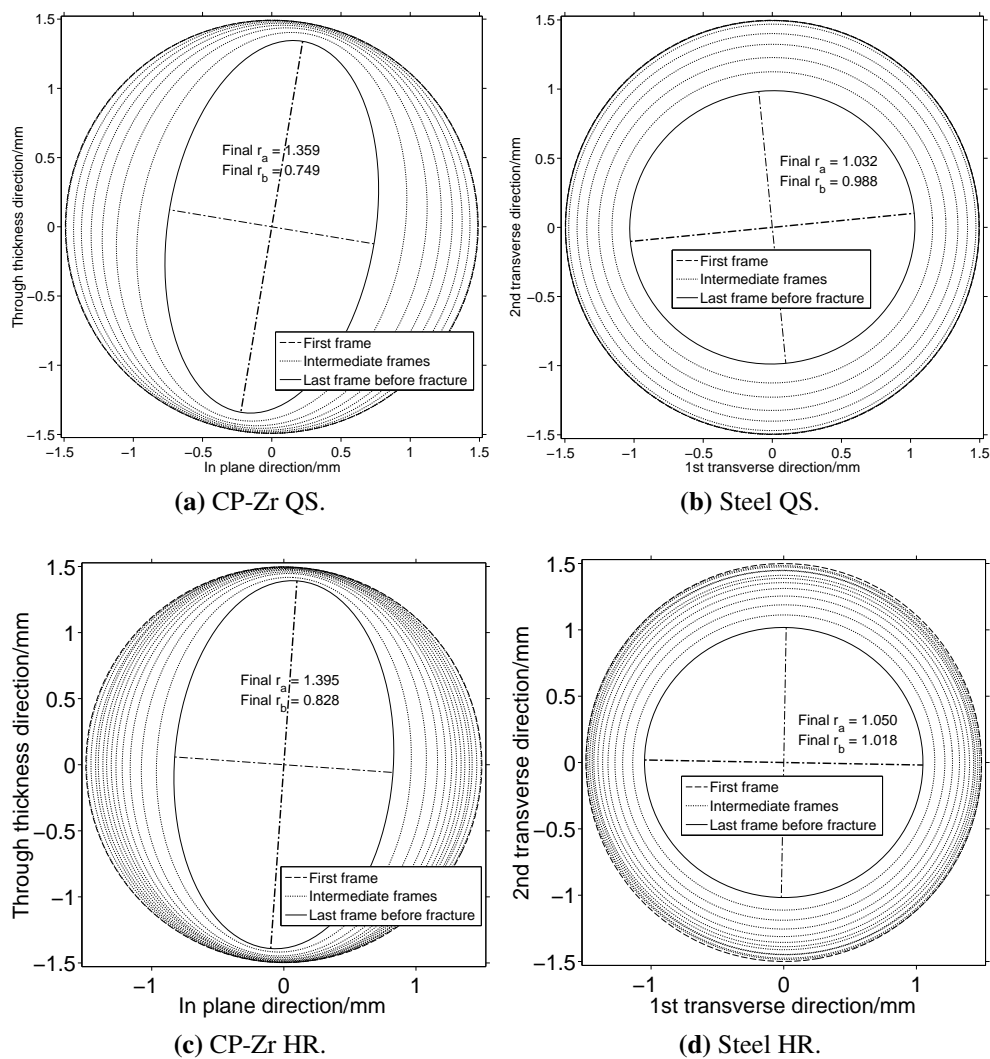


**Figure 5.13:** The shapes of the cross-section at the position of maximum strain (minimum area) throughout the deformation of the specimens. For the HR specimens all frames are shown, whereas for the QS specimens every 10th frame is shown as well as the first and last frame. The major axis direction ( $r_a$ ) is drawn with a heavier line than the minor axis direction ( $r_b$ ).

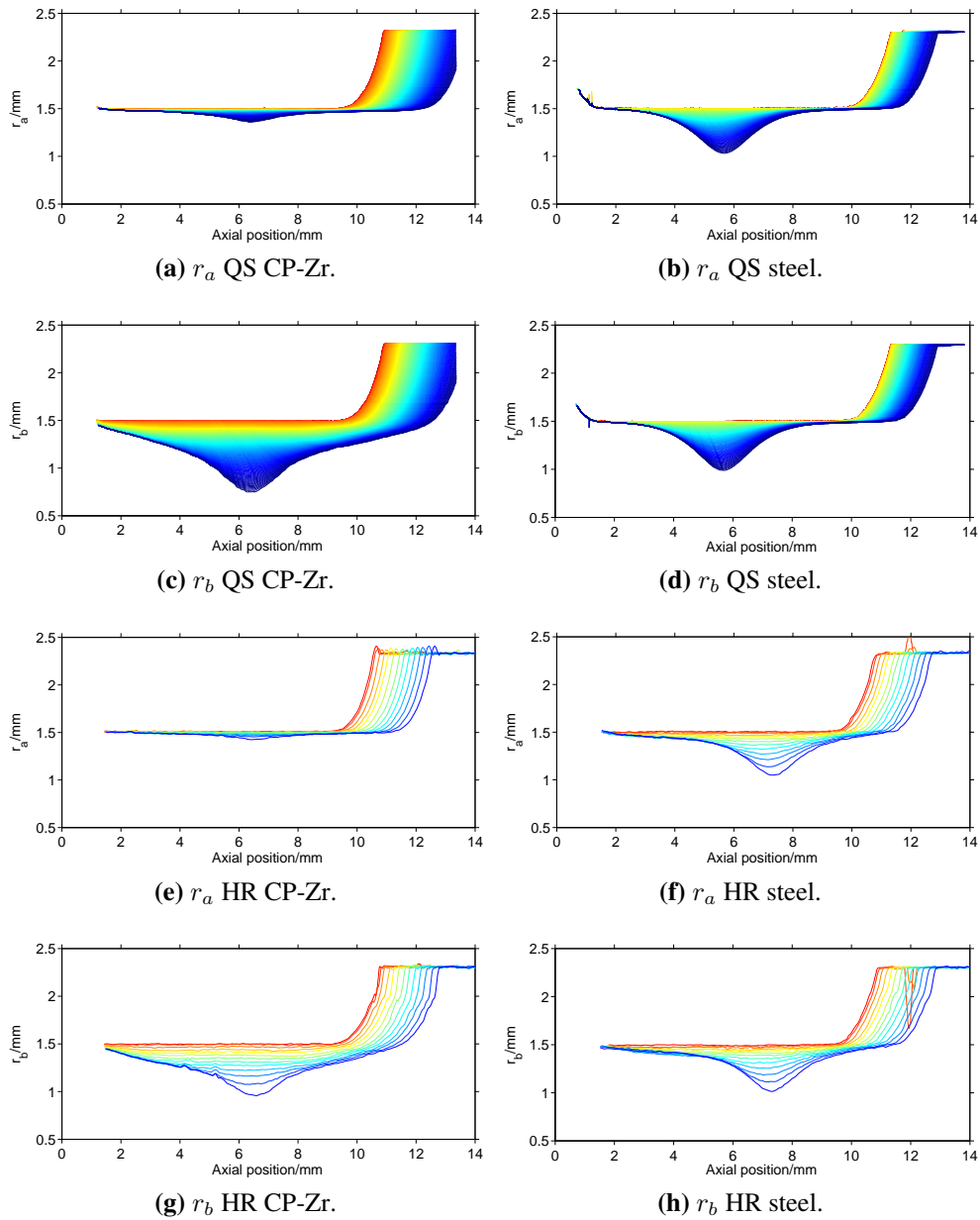


**Figure 5.14:** The maximum  $r_a$  and minimum  $r_b$  radii as functions of axial position from the lower shoulder corner for the four QS and HR CP-Zr and steel specimens. Filtering was applied to the HR specimens' edges before the reconstruction to remove high frequency data. The radii are coloured red to blue with respect to the frame number, red being the first frame and blue the last frame before fracture.

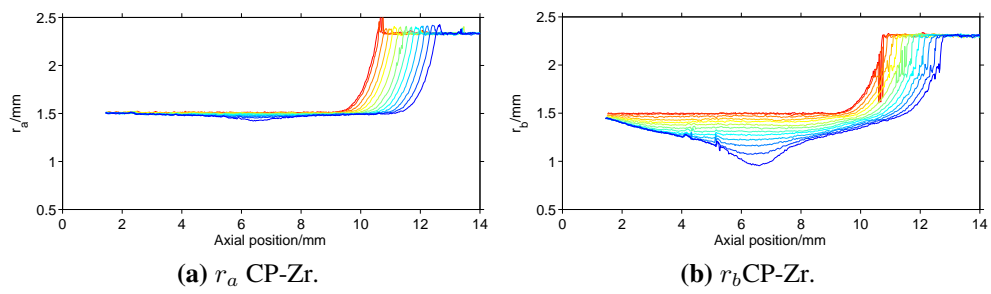


**Figure 5.15:** The results from figures 5.14e and 5.14g without filtering applied to the edges before the cross-section reconstruction.

## 5.5 Taylor impact tests on Zirconium

Taylor impact experiments on samples of CP-Zr were performed using a gas-gun to propel a cylindrical specimen into a massive instrumented hardened steel bar at approximately  $200 \text{ ms}^{-1}$ . See Field et al. [96] for a review of the Taylor impact procedure. The modern use of these experiments is usually to validate constitutive models of material behaviour. During a Taylor impact on a ductile material there is a variety of strain rates in the elastic and plastic regimes that provide good exercise for models.

High speed photography has been used in recent years to provide more data on the evolution of the axisymmetric deformation [83, 96]. Further advances have been made [97, 98] in which Taylor impact experiments have been carried out on CP-Zr and the results used to validate the results of finite element models by comparing the dimensions of the elliptical cross-sections of the specimens after impact. The application of the technique in chapter 3 to these experiments has permitted the measurement of the developing ellipticity in the cross-sections during impact that was not possible before.

A SIM8 ultra-high-speed camera with two mirrors was used to acquire images in the configuration shown in figure 5.16. Figure 5.17 shows 6 photographs taken during the impact of a CP-Zr specimen at  $7 \mu\text{s}$  intervals. Figure 5.18 shows 3D renderings of the results of applying the reconstruction technique to these photographs, where they have been shaded according to the strain calculated from the change in cross-sectional area,  $\varepsilon = \ln(A_0/A)$ . Figure 5.19 shows plots of the semi-major and semi-minor axes lengths as functions of axial position for the 6 photos. The ‘wiggles’ at the ends of the specimen are due to the application of smoothing to the edges where there had been a sharp curvature at the specimen corners.

Figure 5.20b shows the results of scanning the post-impact specimen (a photo of which is given in figure 5.20a) using the CMM and fitting ellipses to the data to obtain an independent measurement of the specimen’s dimensions. It can be seen that figure 5.20b shows good agreement between the CMM data and the reconstructed cross-section data.

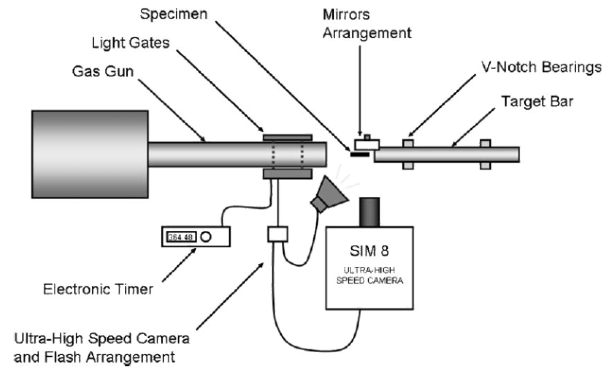


**Figure 5.16:** The configuration of the Taylor impact of CP-Zr experiments.

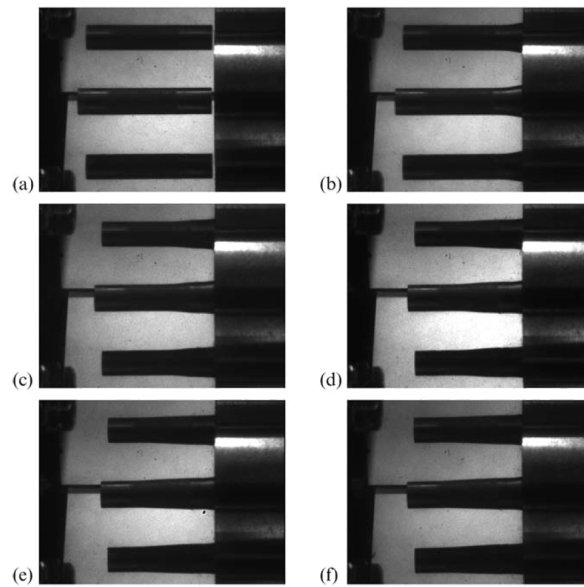


**Figure 5.17:** Images from a Taylor impact experiment carried out on heavily textured high-purity zirconium plate, taken with a SIM-8 ultra-high-speed camera and showing the three views obtained using the two mirrors.

No comparison with modelled experiments is provided here, but this is suggested in the section on future research, § 7.3. One of the simplest material modelling parameters that can be obtained from the Taylor impact experiment is an approximation of flow stress, derived by Taylor [95], using initial and final length measurements as shown in figure 5.21 and the equation,

$$\sigma = \frac{\rho V^2 (L - X)}{2(L - L_1) \ln(L/X)}. \quad (5.1)$$

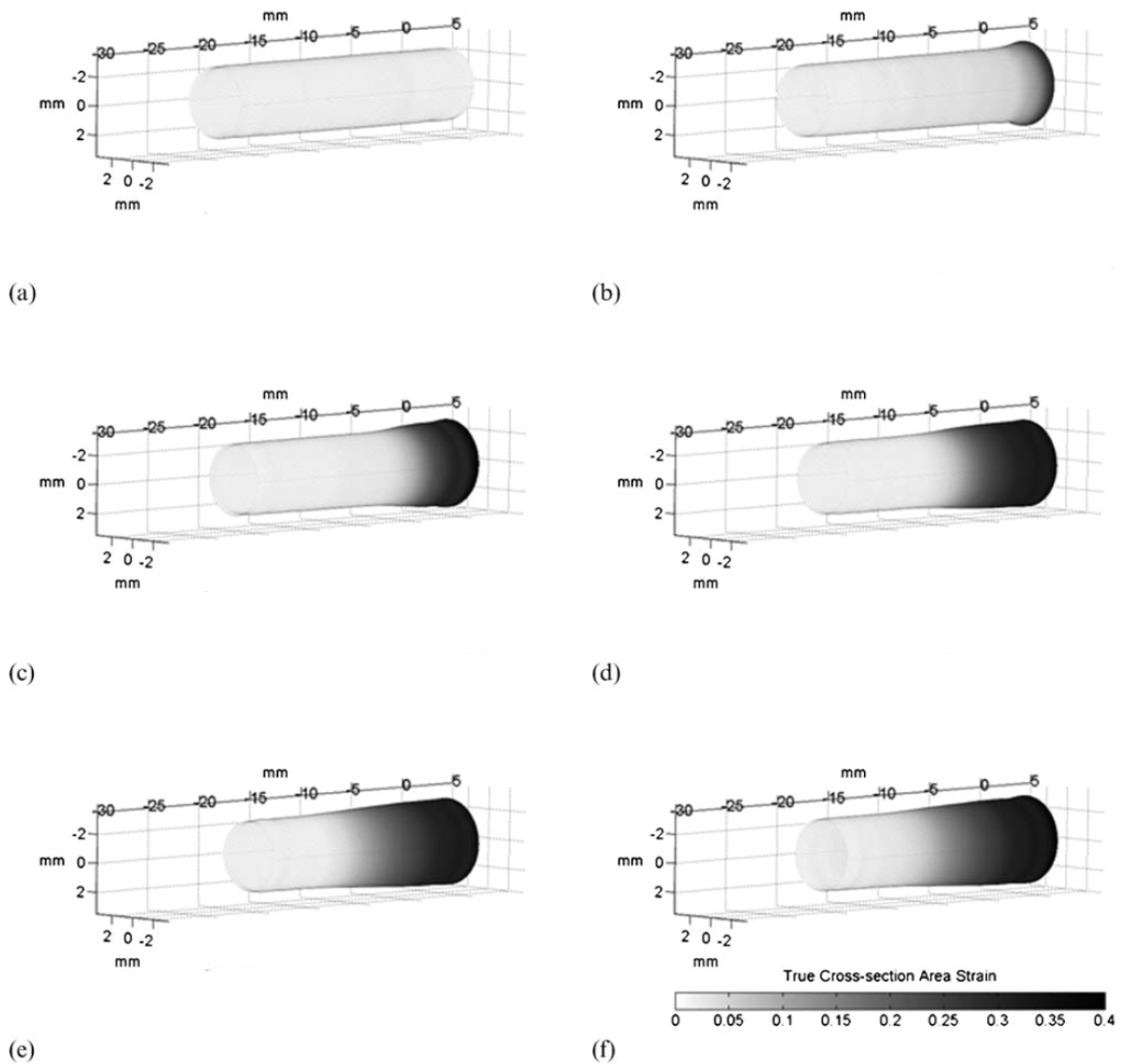


**Figure 5.18:** Three-dimensional surface geometry reconstruction showing the true cross-sectional area strain as a function of time and the axial position, [4].

Given the accurate geometric measurements obtained during the Taylor impact experiment shown here, the measurements usually made post-deformation in figure 5.21 can be made throughout the experiment. For the Taylor Impact test here the area of the cross-section is shown against distance from the anvil face in figure 5.22. In this figure markers indicate positions where the area in the deformed section first reaches 5% of the mean original area. These positions have been used to calculate the geometric lengths required for (5.1), which are shown in figure 5.23. Given these lengths, the flow stresses at each frame time can be calculated ac-

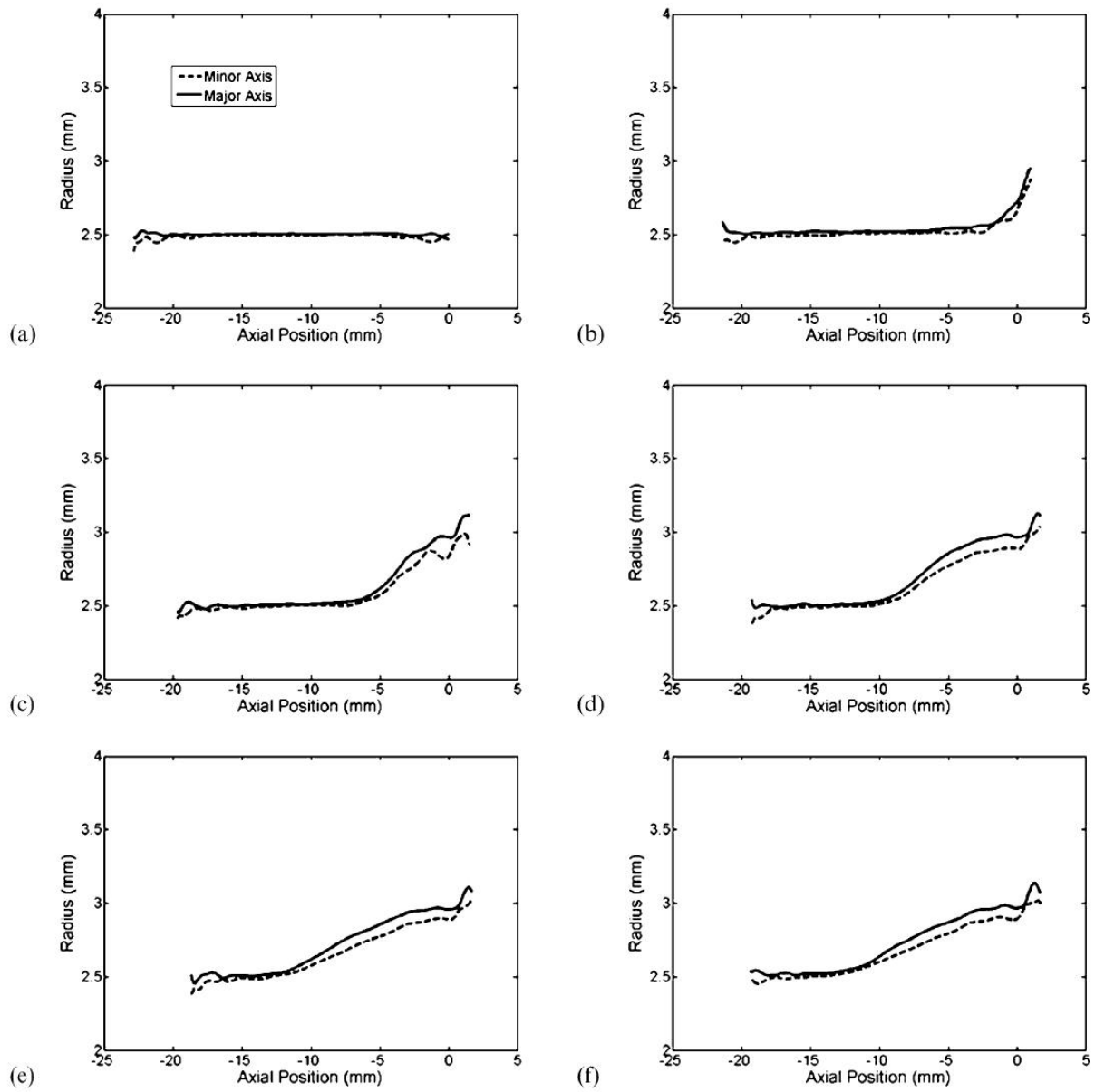


**Figure 5.19:** Semimajor and semiminor axes of the deforming cross-sectional shape as functions of time and the axial position, [4].

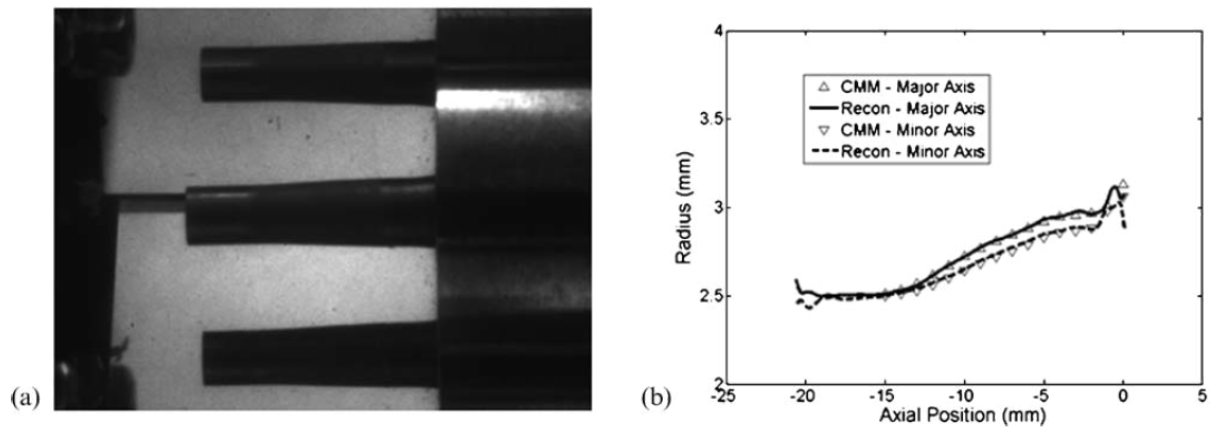


**Figure 5.20:** (a) Final post-deformation image frame and (b) comparison of the semimajor and semiminor axes of cross-sectional shape from the recovered specimen using data from both a CMM and the optical measurement technique, taking the final post-deformation image frame as the reference.

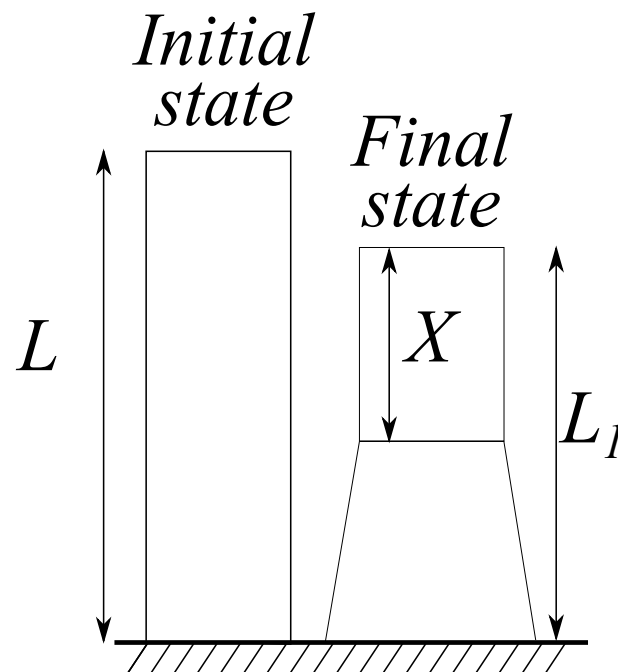


**Figure 5.21:** The initial and final state of a rod that has been tested using the Taylor impact experiment.

ording to (5.1), these are given in figure 5.24. However, (5.1) is known to be a poor indicator of flow stress when the flow stress changes with hardening, and the assumptions used in deriving the equation are violated when applied to a specimen that is still moving. It should therefore be noted that the flow stress calculated is only expected to be valid for the last three frames, where the plastic deformation had ceased to propagate and the flow stress ranges from 515 MPa and 555 MPa. These stresses are relatively low compared to the value of 600 MPa achieved in HR compression and 630 MPa in HR tension, shown in figure 5.12a, but they are fairly close.

The true value in using the geometric reconstruction data is anticipated not to lie in using the Taylor stress equation, but in comparison of numerical models of the experiment with the data. These should permit a fairly rigorous test of the model being used for the material.

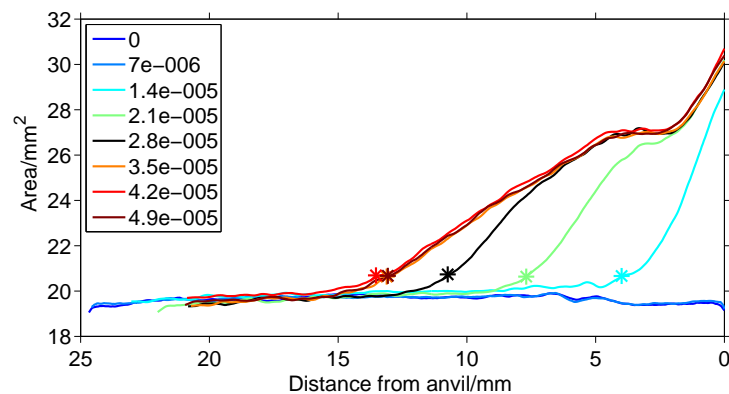


**Figure 5.22:** The cross-sectional area of the Taylor Impact specimen against distance from the anvil at each frame captured during the experiment.

## 5.6 Conclusions

In this chapter specimens of plastically anisotropic CP-Zr and steel have been deformed and measured by the reconstruction technique described in chapter 3, a coordinate measurement machine (CMM) and an optical comparator (OC). Using interrupted quasi-statically loaded tension specimens that had necked, the CMM data confirmed that the shape of the cross-sections in

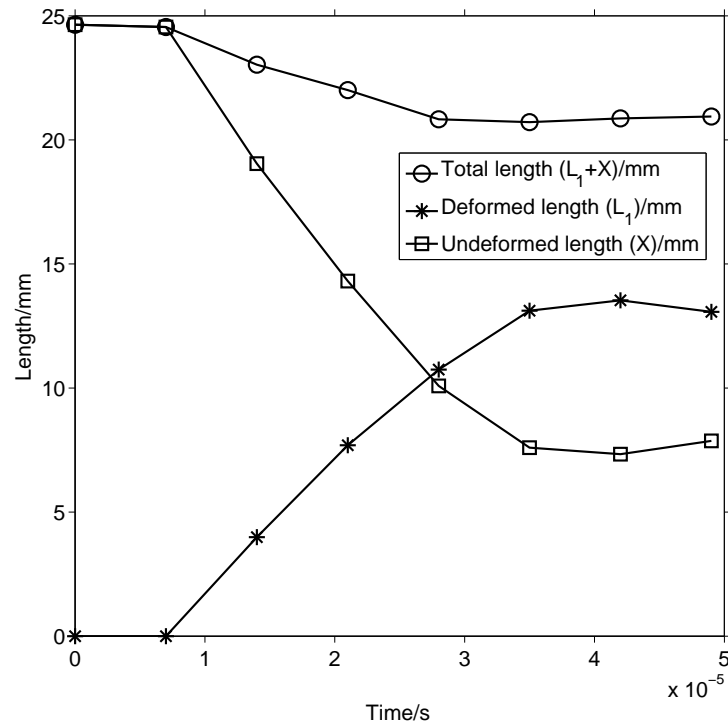


**Figure 5.23:** The salient lengths of the Taylor Impact specimen measured from the reconstruction of its cross-section.

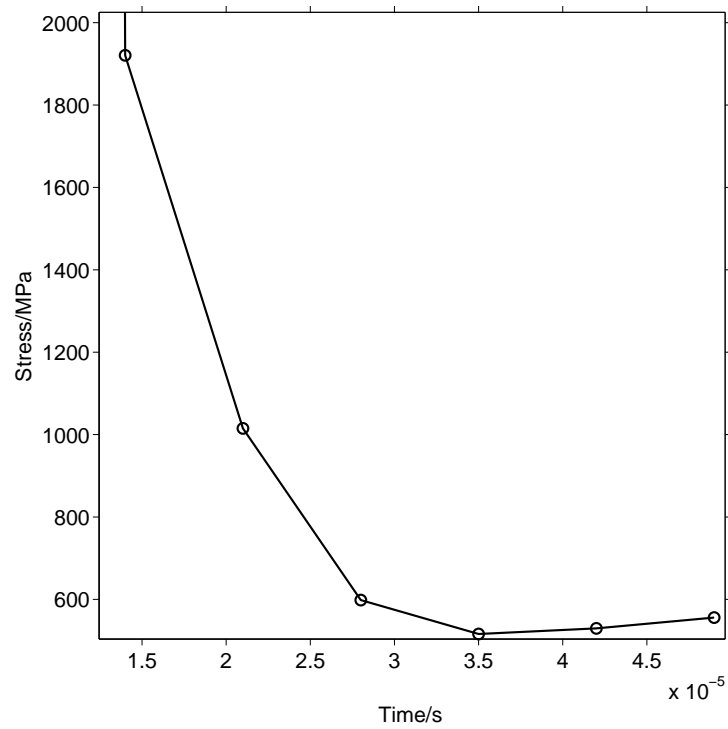


**Figure 5.24:** The flow stress against time during the Taylor Impact test.

both materials was nominally elliptical, and the steel specimen's cross-section was nearly circular. The CMM data was also used to confirm that the elliptical orientation of cross-section in the interrupted CP-Zr specimen did not significantly change with axial position, as was recorded in the reconstruction data.

The CMM data and the OC data were compared to the reconstructed measurements in terms of their area and aspect ratios. The CMM data was found to be a poor record of surface dimensions due to the concave curvature of the specimen profile and subsequent systematic error in axial position measurement. However, the OC data followed the reconstruction data much more closely, and these provided an independent measurement to verify that the reconstruction technique can capture the surface shape of a real specimen accurately. The difference between the OC measurements and the reconstruction measurements was found to be, in the worst case,  $\pm 1\%$  for aspect ratio and a  $\pm 2\%$  for area.

Data has also been presented on the deformation behaviour of these two materials in tension at QS and HR. The technique was shown to provide measurements of maximum true stress vs. true-strain until fracture in the highly elliptical CP-Zr specimens and the nearly circular steel specimens. Also presented were the maximum and minimum radii of these specimens at the minimum cross-sectional area throughout loading. These radii allowed the calculation of the R ratio for the specimens at QS and HR. The evolving radii of the specimens were shown, which would provide valuable data for validating constitutive models in simulations of these experiments.

A description of the reconstruction technique's application to the Taylor test was given. In this work the cylindrical impact specimen was fired at an anvil and the evolving cross-sectional shape was captured. Calculations of flow stress in the specimen during deformation using the standard Taylor equation in conjunction with the accurate measurements of cross-sectional area with position were made, but the values are not expected to be of significant use for characterisation due to violations of the assumptions made in Taylor's derivation.

The Taylor impact test is used as a tool for validation of material models as many strain rates are present throughout the experiment. Using the reconstruction technique in conjunction with this test provides even more data for validation. This means that comparisons can be made between the deformed shape and the model of the experiment not just at the final state of the specimen, but at intermediate states too, constraining the model further.

# 6

## Experimental Results

---

Experiments reported in this chapter were performed on cross-rolled Ti-6Al-4V plates with three principal material directions orientated as shown in figure 6.1 (also shown in figure 1.3) which will be referred to as D1, D2 and D3 . The plate was provided in two different forms; one was a 20 mm thick rectangular single plate, the other was a pack of three of these, diffusion bonded together to make a 60 mm thick plate. This provided a thick enough plate to manufacture through-thickness (D3) tensile specimens. Whilst the diffusion bonding process added further thermo-mechanical processing, it is not expected to have altered the microstructure significantly. The D1 direction was parallel to the longer side of the rectangular plate.

12 different types of experiment were performed on the material; for each of the three directions in figure 6.1 compression and tension experiments were performed at two strain rates, QS,  $10^{-3} \text{ s}^{-1}$  and HR,  $10^3 \text{ s}^{-1}$ . Three experiments were performed for each loading condition, apart from HR tensile experiments, where only one specimen from each direction could be analysed due to equipment problems. In this chapter the significant findings from the 12 different configurations will be presented. Only one representative specimen from each set of three experiments will be described.

The tension specimens had nominal dimensions given in figure 1.8a (page 18) and the compression specimens were right cylinders of nominal dimensions 3.0 mm diameter by 3.5 mm

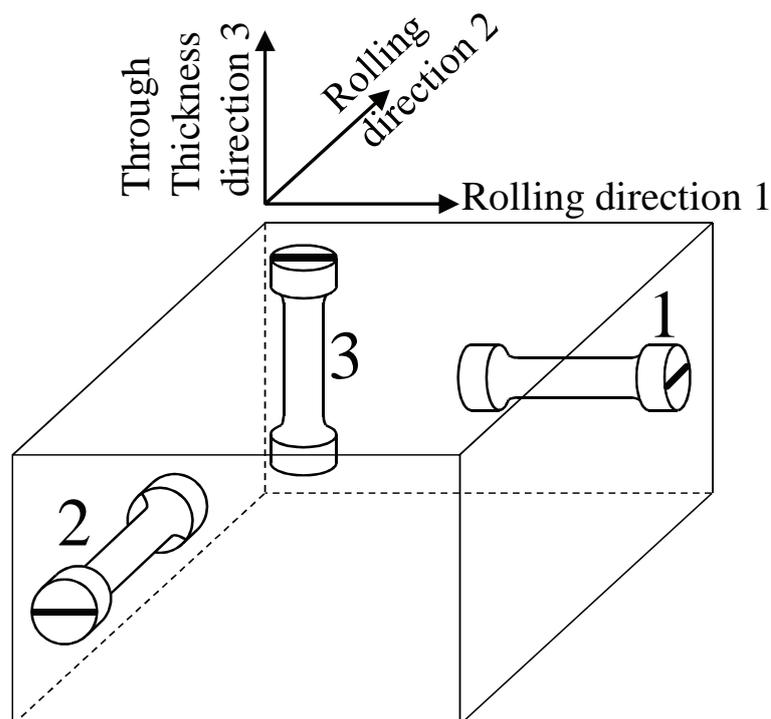


**Figure 6.1:** The principal material directions in the cross-rolled Ti-6Al-4V plate.

length.

The optical configuration of the QS experiments consisted of the three TELI digital cameras fixed at an angular spacing of  $45^\circ$ . The left and right cameras looked at silhouettes and the centre view was of the specimen illuminated only at its edges by the lights that illuminated the side views. This configuration can be seen in figure 3.5a. The centre view could not be reverse-lit, as the QS CP-Zr and steel specimens described in chapter 5 were, because the laser extensometer would have been obscured by the light source and simultaneous recording of lengths using the laser was desired<sup>1</sup>.

The difference in illumination between the centre and side views has the potential to distort the results. However, care was taken to ensure the specimen in the central view was illuminated sufficiently brightly at the edges. Illuminating all views as silhouettes is the preferred method and the edge data from the centre view has more noise in it when the specimen

<sup>1</sup>The laser extensometer and the cameras were used at the same time because the cross-sectional measurement technique hadn't yet been fully tested and so the laser extensometer was used as a precaution

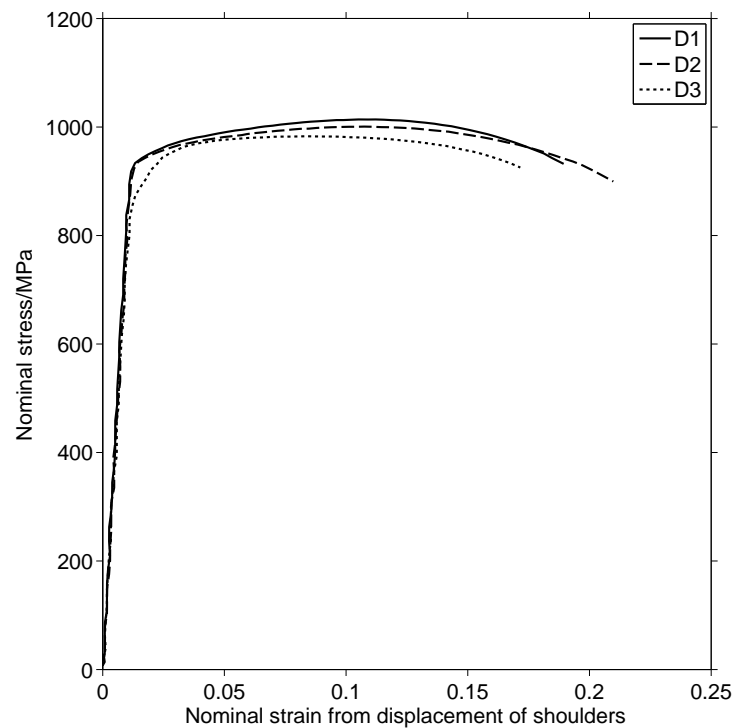
is illuminated, and not the background.

The HR images, captured using a SIM16 Ultra High Speed camera, were of the specimen and two mirrored views of it through mirrors fixed at  $120^\circ$ . The HR specimens were illuminated directly by the light from the flashes.

## 6.1 Results

### 6.1.1 QS tension tests

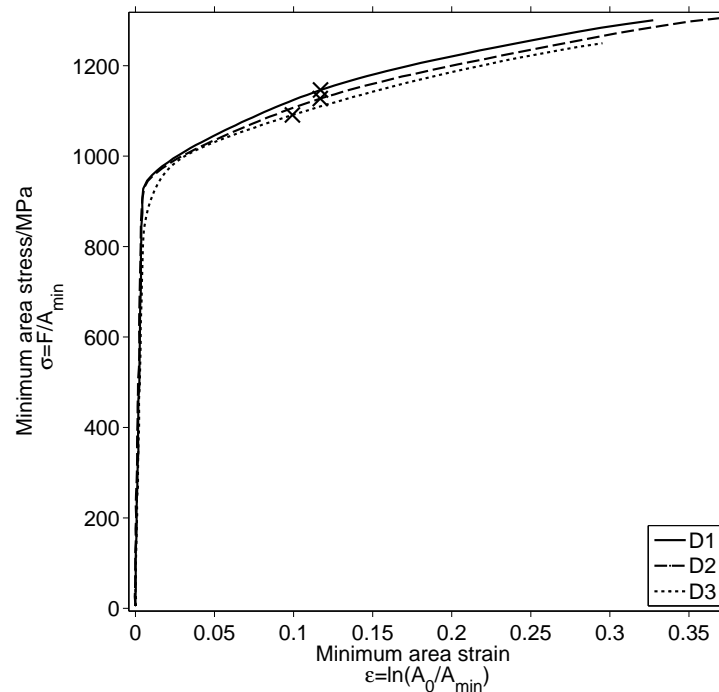
Figure 6.2 shows nominal stress-strain results for representative QS tensile specimens in the 3 material directions. The strain was calculated by tracking the positions of the specimen shoulders in the QS photographs using digital image correlation (DIC).



**Figure 6.2:** The nominal stress-strain results for the QS tensile specimens in all material directions. The strain was calculated by DIC of the specimen shoulders in the QS photographs.

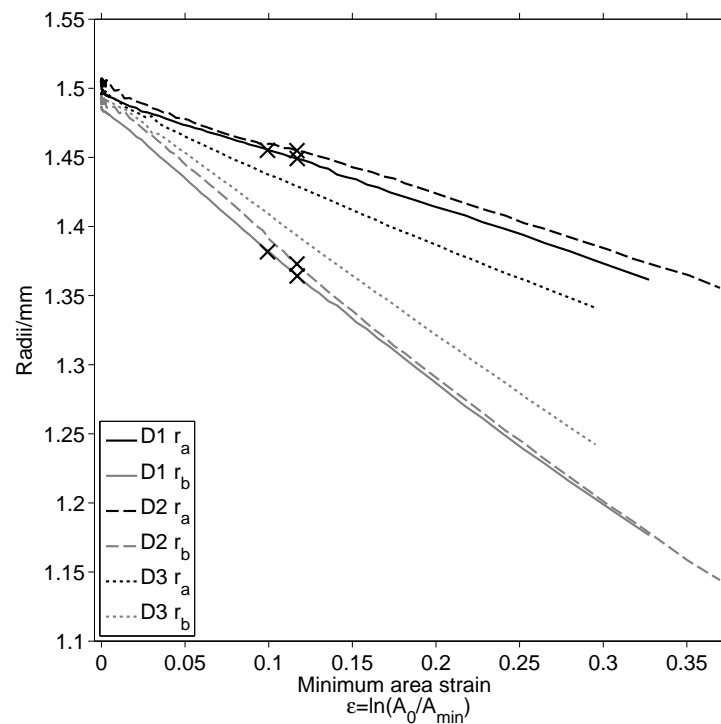
Figure 6.3 shows the true-stress vs. areal-strain for the three different directions of the plate material in QS tension. Markers (x) are used to indicate the position of the UTS in these plots and all other plots of tensile data in this chapter. The true stress was calculated as force over minimum cross-sectional area,  $\sigma = F/A_{min}$  and the areal strain was calculated as  $\epsilon = \ln(A_0/A_{min})$ , where  $A_0$  is the original area, also at the minimum area. D1 and D2 have very similar initial yield stresses and plastic flow stress behaviour, as expected, although the rate of hardening in the D2 specimen is lower than D1. D3 has a lower initial yield stress but hardens more rapidly on increased loading and approaches the same flow stress as D2, but then the hardening rate decreases again producing the lowest flow stress of all. The D3 specimen is less ductile than D1, which in turn is less ductile than D2.

Whilst these data are not a record of the complete state of 3 dimensional stresses within the material, they do provide more information than could be obtained without measuring the elliptical cross-section throughout the gauge length.



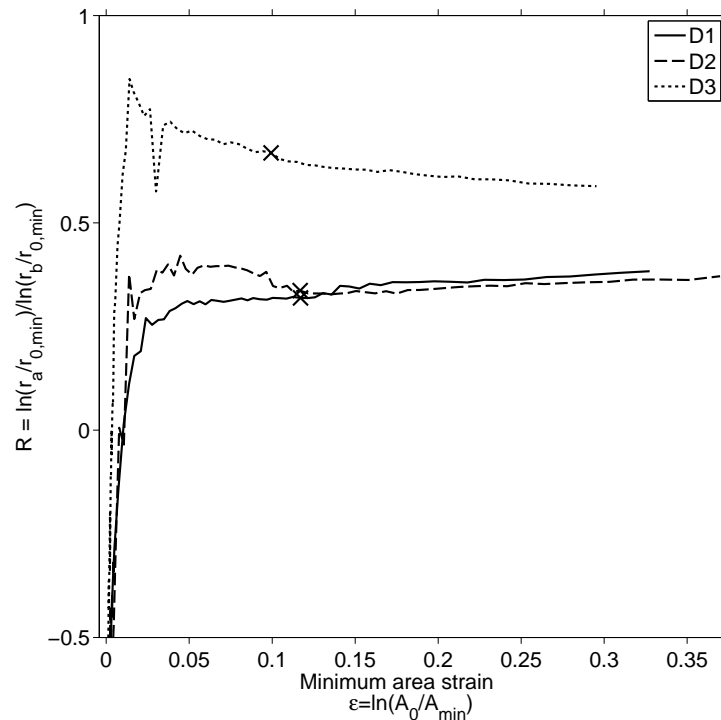
**Figure 6.3:** Mean direct true stress plotted against minimum area strain.

Figure 6.4 shows the lengths of the semi-major ( $r_a$ ) and semi-minor ( $r_b$ ) axes as a function of the areal strain. Measurements were performed at the section of minimum area (maximum strain) on the specimen; i.e. the centre of the neck. It can be seen that for D3  $r_a \neq r_b$  and it does not possess the assumed cross-sectional isotropy. Figure 6.5 shows the R ratio calculated from these radii, and it demonstrates the similarity of the D1 and D2 specimens whilst also showing that the D3 specimen has large differences in its straining directions at large axial strain. This is contrary to the result that would be expected from a cross-rolled plate that had achieved in-plane isotropy.



**Figure 6.4:** The semi-minor and semi-major axes lengths at the minimum cross-section against areal strain.

Figure 6.6 shows the evolving shape of the most strained position in the gauge section for each of the three QS tension specimens. The orientations of the final shapes before fracture are not exactly coincident with the principal material directions in the D1 and D2 specimens, as they were expected to be. This could be either because of systematic experimental error in inserting the specimens into the loading device at the correct initial orientation, or it could be



**Figure 6.5:** The R-ratio at the minimum cross-sectional area as a function of areal strain at the minimum area.

an artefact of the material behaviour. However, repeated tests would have to be performed in order to assert which is the case.

If the angles can all be assumed to be systematically offset, then the D1 and D2 specimens can be seen to strain the most in the through-thickness (D3) direction, whilst the D3 specimen has strained most at an angle that is closer to the D1 direction than the D2 direction.

Figures 6.7, 6.8 and 6.9 show, respectively, photos of the D1, D2 and D3 QS tensile specimens after fracture. The definite preferred fracture direction of the D1 and D2 specimens is likely a consequence of the elliptical shape immediately prior to fracture. The D3 specimen did not show as strong a dependency of fracture direction on material direction, and this is probably because of its lower anisotropy.

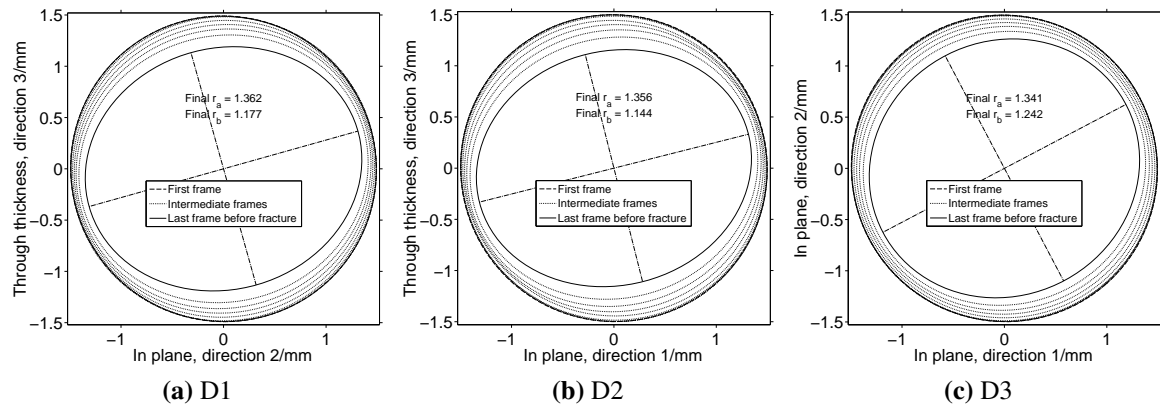
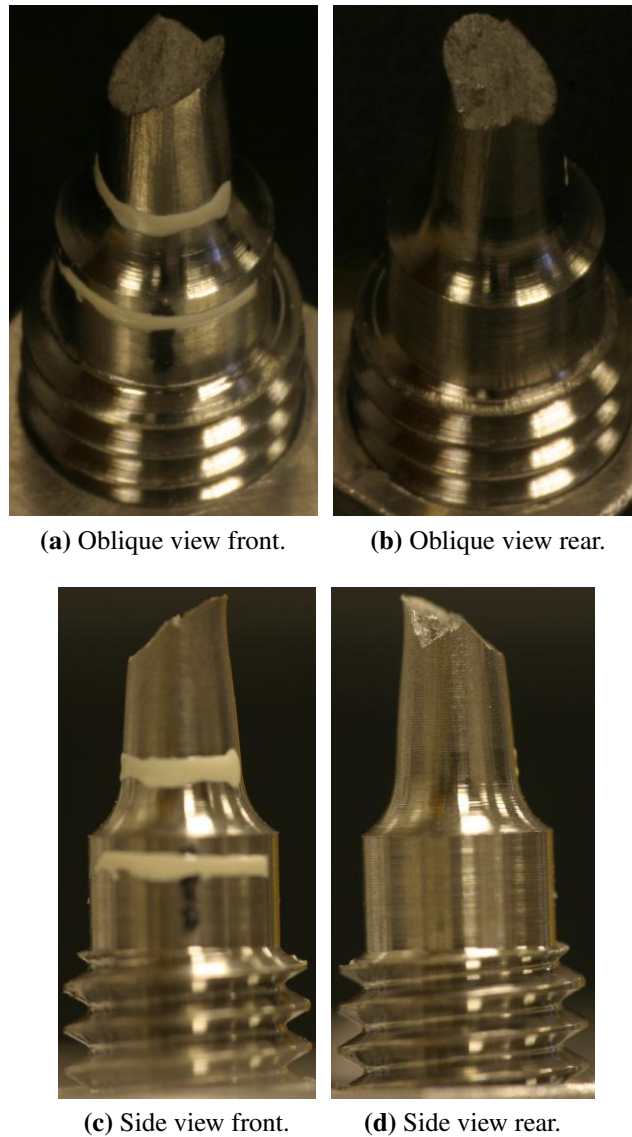


**Figure 6.6:** These figures show the shape of the most strained region in the QS tension specimens in 10 frames, evenly spaced in time, during the experiment.

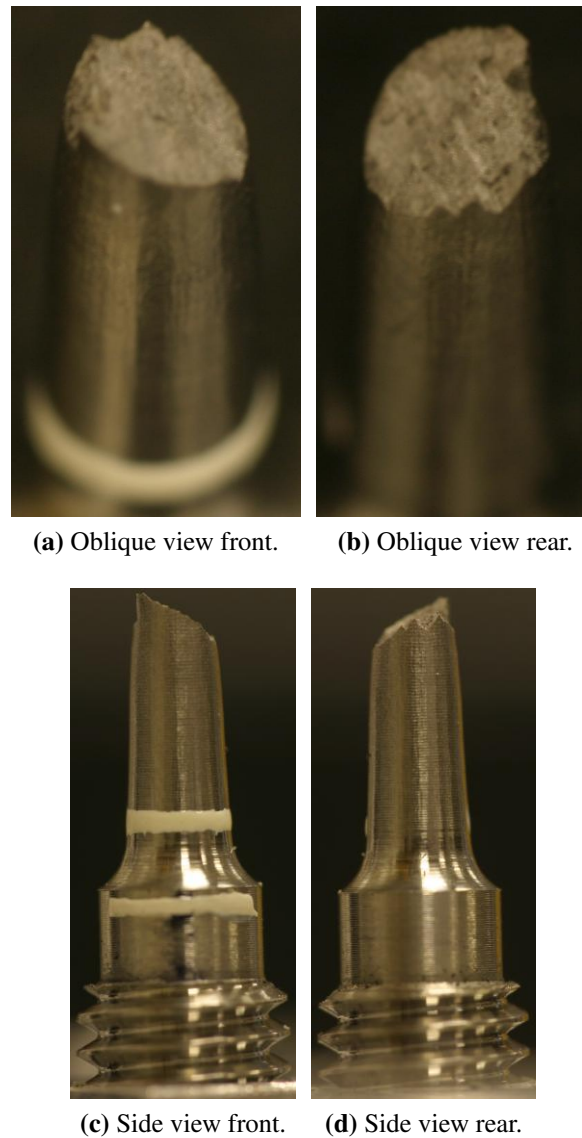
### 6.1.2 QS compression tests

Figure 6.10 shows the true stress-strain results for each of the three material directions. The strain in these plots was calculated by DIC of the region where the anvils and specimen meet in the photographs of the specimen, whilst stress was calculated assuming constant volume and that the cross-section remained uniform throughout, i.e. no barrelling. Barrelling of compression specimens, due to friction with the anvils, is very difficult to eliminate in practice. Castrol LMX grease was used to lubricate the interfaces between the compression specimens and the anvils. However, some barrelling was present in all of the compression specimens in this study and therefore the data were further analysed by calculating the stress at two significant cross-sectional positions rather than assuming the ideal uniform cross-section. These positions are at the maximum and minimum cross-sectional areas. Figure 6.11 shows the mean true direct stress at these axial positions during QS compression loading of specimens taken from each of the three material directions. These two sets of data are plotted against the areal strain calculated at the same cross-sections. The minimum area position is always at one of the two ends of the specimen where it is constrained by friction and the maximum area is furthest from the constraints of the anvils, usually at the centre of the specimen.

The initial yield stress of the D3 specimens in compression also has a smaller magni-



**Figure 6.7:** These photos show the fracture surface of the QS D1 tensile specimen where the vertical direction is in the plane of the CR-plate and the horizontal direction is through thickness, D3. Note that the fracture surface has formed a plane that contains the in-plane direction.



**Figure 6.8:** These photos show the fracture surface of the QS D2 tensile specimen. Note that the fracture surface has formed a plane that contains the in-plane direction.

tude than the other two directions, the same as observed in tensile data, but with a much larger difference. This suggests that the principal hardening mechanism during manufacture is not kinematic hardening, because of the reduction in magnitude of the yield stress for the D3 direction in both compression and tension. However, the D3 direction in compression did not harden as quickly as it did in tension, and nowhere do the specimens come close to achieving the same flow stress as the D1 or D2 directions. The D1 flow stress is greater in magnitude than the D2 specimen, as observed in the tension specimens, although the difference is small.

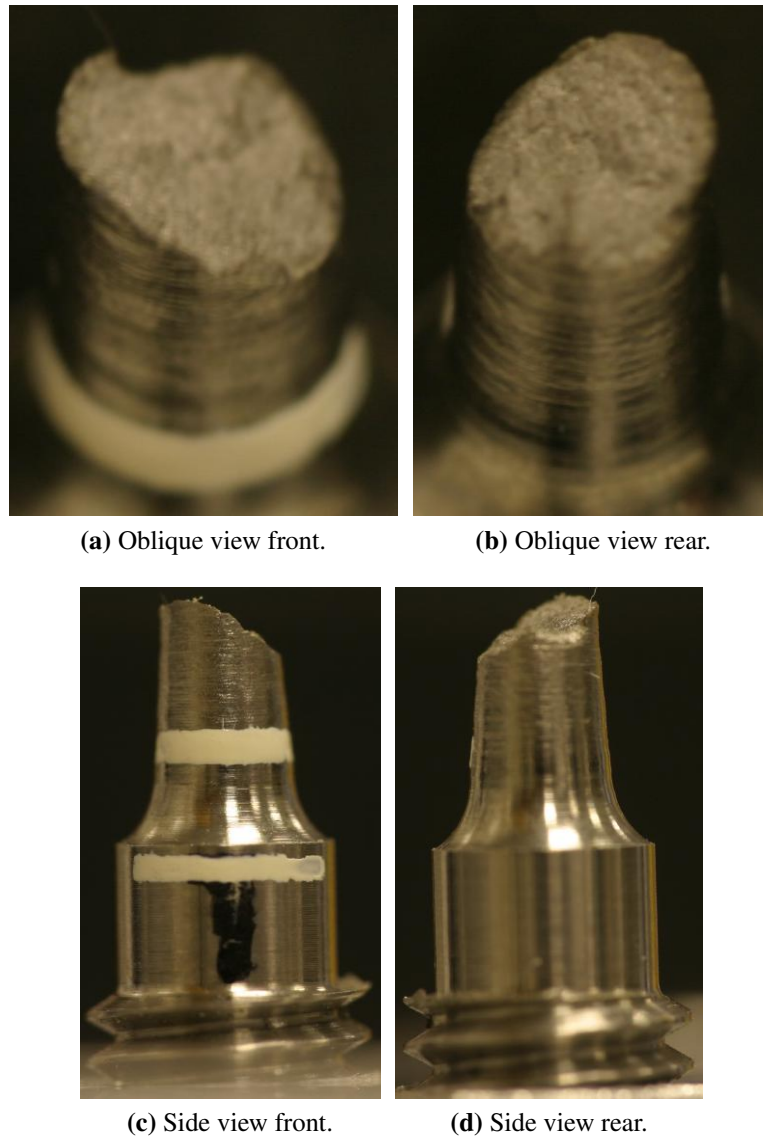


**Figure 6.9:** These photos show the fracture surface of the QS D3 tensile specimen. The fracture plane is more pitted and much less flat than the D1 or D2 specimens and it has formed in a direction that nearly contains the 1 direction.

The ratios of true stress between the two different cross-sections in each specimen are approximately equal for all three directions, indicating that the ratios of areas, and hence the degrees of barrelling, are also similar.

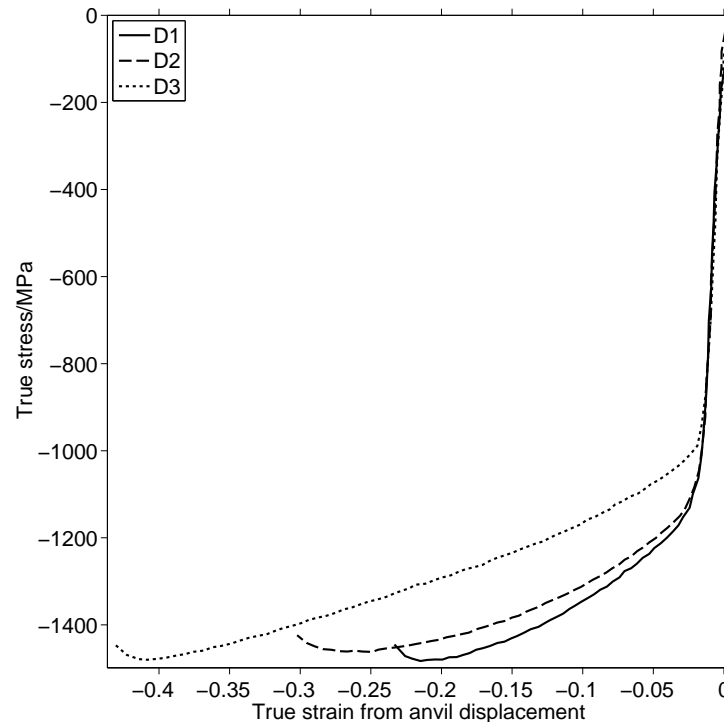


**Figure 6.10:** The true stress-strain in the QS compression specimens for all directions. The strain was calculated by DIC of the region where the anvils and specimen meet in the photographs, assuming a parallel gauge section throughout the loading.

Figure 6.12 shows the major and minor radii of the specimens at the maximum cross-section against areal strain at that position. The ratio of radii of the D3 specimen is near unity throughout; the ratios found in the D1 and D2 specimens were similar to each other but much larger than D3.

Figure 6.13 shows the  $R^{-1}$  values calculated at the maximum cross-sectional area, where there is most strain, for all three material directions.  $R^{-1}$  rather than  $R$  has been plotted because  $R^{-1} = R_{\theta}$  (the traditional ratio of strains between width and thickness directions) for compression specimens when the principal deformation axes match the material axes. Using  $R^{-1}$  also means that the compression and tension plots (e.g. figure 6.5) are more readily comparable.

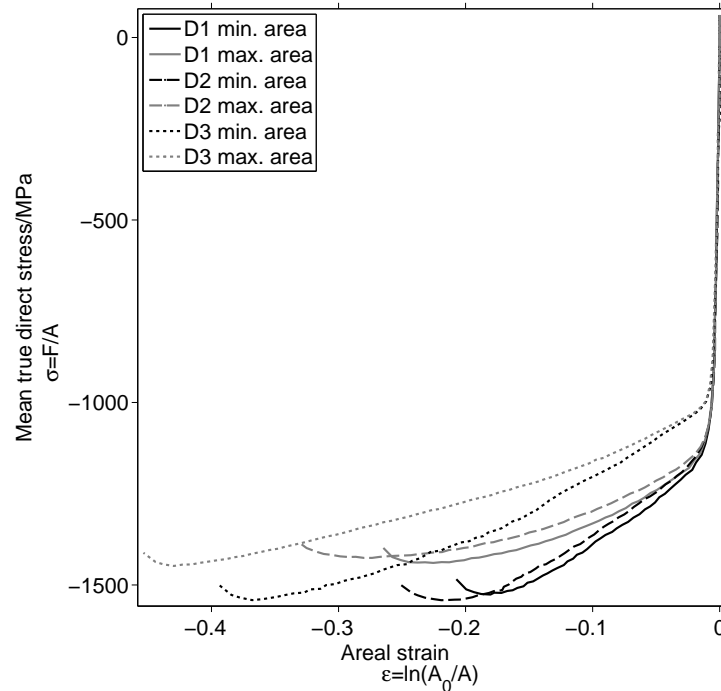


**Figure 6.11:** Mean direct true stress at the minimum cross-sectional area plotted against minimum area strain and mean direct true stress at the maximum cross-sectional area plotted against maximum area strain in the QS compression specimens.

The  $R^{-1}$  value for D3 in QS compression can be seen to be much closer to 1 than in QS tension. It is also a more constant value, indicating that the rate of increasing anisotropy with strain is smaller than in QS tension. The D1 and D2 directions exhibit significant anisotropy, indicated by  $R^{-1}$  values that start at around 0.5 for small strain but then increase upon further straining, at a faster rate than in tension, to become less anisotropic (D1 = 0.55 and D2 = 0.63 at failure).

The accuracy of strain obtained by DIC and that obtained by measuring the change in cross-sectional area is compared in figure 6.14. It can be seen, by the close agreement of the stiffness in tension and compression using the areal strain, that the strain measured by DIC of the anvil displacement overestimates the strain. This is due to the compliance of the lubricant and the anvils themselves increasing the apparent strain. Measuring the change in area to obtain strain has produced better estimates of strain in this research. However accurate measurements of the area would not have been possible without the elliptical cross-section measurements.

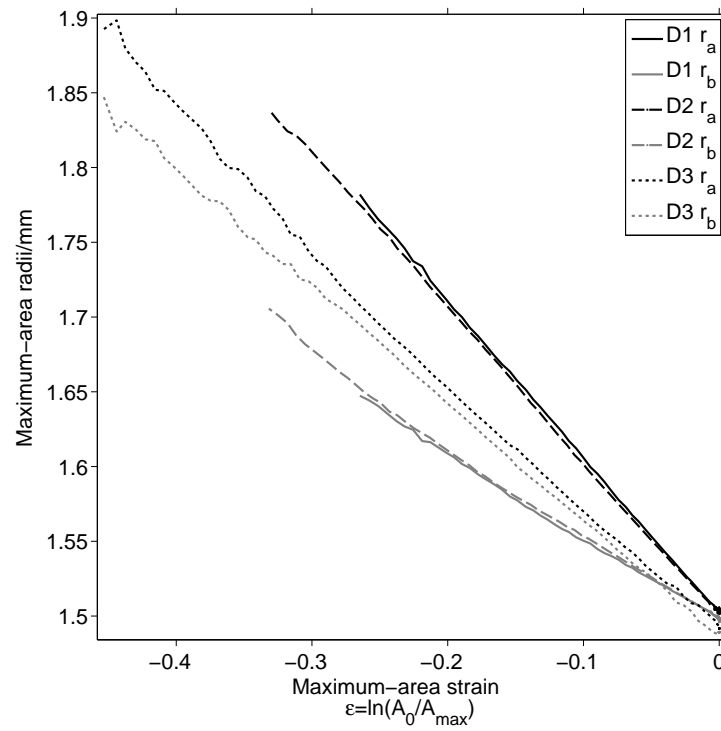


**Figure 6.12:** The semi-minor and semi-major axes lengths at the maximum cross-section against areal strain at the maximum area in the QS compression specimens.

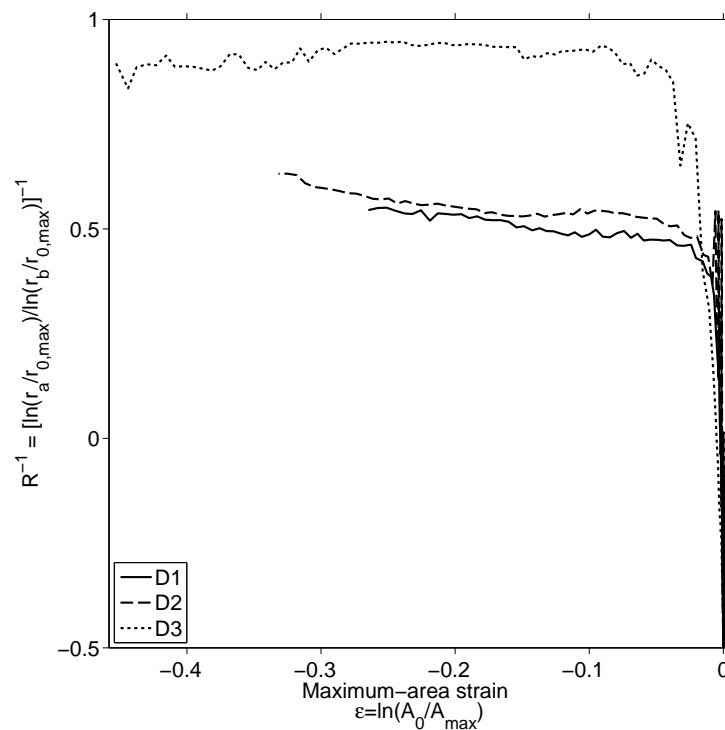


**Figure 6.13:** The  $R^{-1}$  at the maximum cross-sectional area as a function of areal strain at the maximum area in the QS compression specimens.

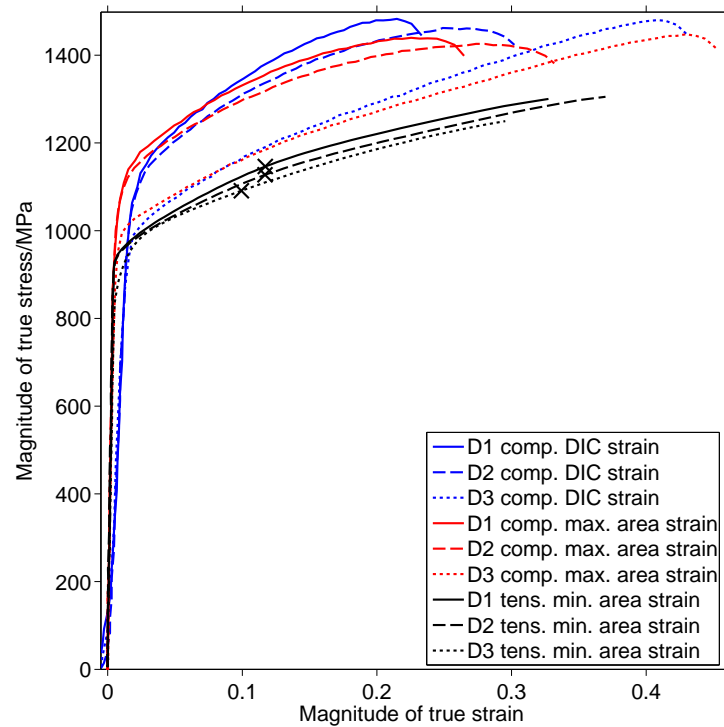


**Figure 6.14:** The magnitude of the QS compression true stress-strain behaviour as calculated by DIC of the anvil displacement and by the change in maximum area cross-section. Also plotted are the QS tension results. Note that the elastic stiffnesses all agree very well when strain is measured by change in cross-sectional area.

Figure 6.15 shows the evolution of the cross-sectional shape of the most strained position in each of the three material directions for the QS compression specimens. The D1 and D2 specimens can be seen to have strained the most in the through thickness directions, as they did in QS tension. The D3 specimen has strained most in a direction that nearly bisected the other two, but is still slightly closer to the D1 direction than the D2 direction.

Photos of the compression specimens post-fracture have not been included because they sheared but remained welded together, which did not show useful information. The D1 specimens consistently fractured along a plane that contained the D2 direction, however the D2 specimens fractured along planes that were close to containing the D1 direction, but were all at an angle  $< 30^\circ$  to it. The D3 specimens had a spread of fracture directions that were often closer to containing the D2 direction than the D1 direction.

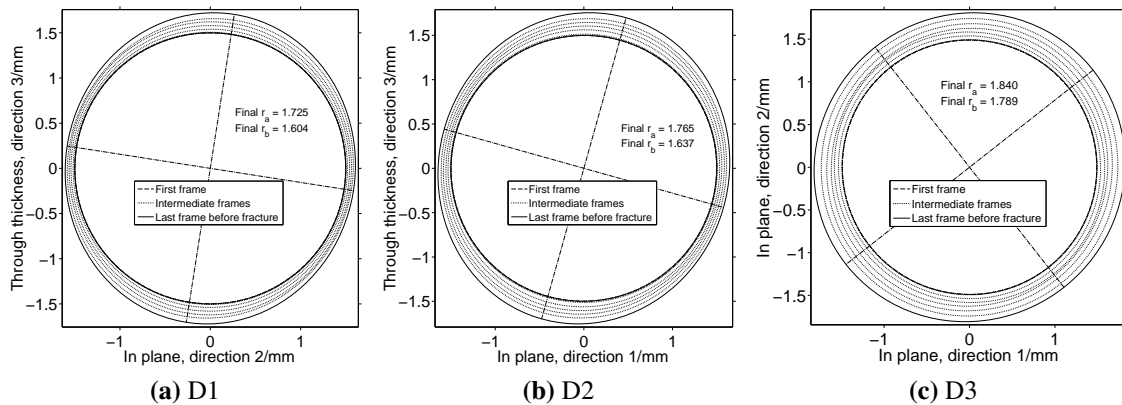


**Figure 6.15:** These figures show the shape of the most strained region in the QS compression specimens in 10 frames, evenly spaced in time, during the experiment.

### 6.1.3 HR tension tests

The HR experiments conducted on Ti-6Al-4V were performed at a relatively early stage in this research which meant that the technique had not been fully optimised to provide the best results. The lighting of the specimens was set so that the edges of the specimens were visible by illumination of their surfaces in some of the views and silhouettes in others. This did not create the consistent sharp contrast and uniformity of illumination that was achieved in the experiments on CP-Zr and steel described in chapter 5 where all the views were silhouettes. Consequently these results are expected to be less accurate than could be achieved in an ideal experiment. Nonetheless, the data presented are still novel and representative of the material behaviour.

Figure 6.16 shows the nominal stress-strain plot for the HR tensile specimens calculated directly by the SHB wave analysis, but with shifting and scaling of the strain dimension so that the plot matched the strain calculated by DIC of the high-speed photos at the sparse locations throughout the experiments. Figure 6.17 shows the true stress in the HR tensile specimens plotted against areal strain for the three directions at the maximum strained position. The D3 specimen can be seen to have a briefly negative strain, which is obviously erroneous, but once significant deformation has taken place the strain is likely to be calculated more accurately. The

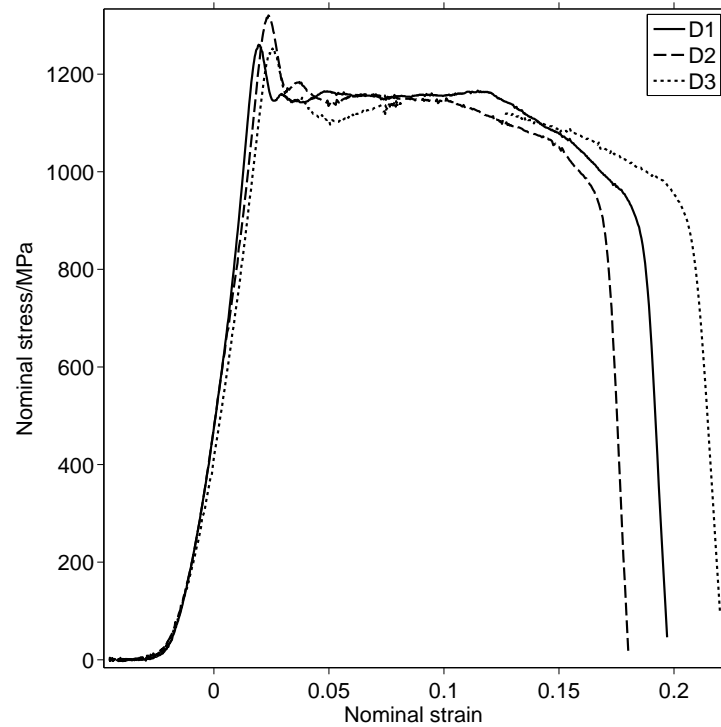


**Figure 6.16:** Nominal stress strain results of the HR tensile specimens calculated by SHB analysis with scaling and shifting applied to make the strain match that obtained from DIC of the high speed photographs.

three directions have very similar flow stresses at HR, as in QS, although the fine detail of the initial yield stresses cannot be determined from such coarse data. The strain to fracture is also difficult to determine owing to the lack of temporal resolution afforded by a 16 frame camera. The positions of the UTS are indicated in the following HR tensile figures by crosses. However, the position of the UTS is not well defined in HR experiments as there is often an initial peak in stress long before necking has started.

Figure 6.18 shows the evolving radii at the neck in the HR tensile specimens. In a similar trend to that shown in the QS results, the D3 specimen has a more circular cross-section than the other material directions for all strain.

Figure 6.19 shows the R ratio calculated at the neck for the three HR tensile specimens. Whilst the data aren't as clear as the QS data (or the HR data for CP-Zr and steel in chapter 5) the D3 specimen is still observed to be less anisotropic than the D1 or D2 directions. The

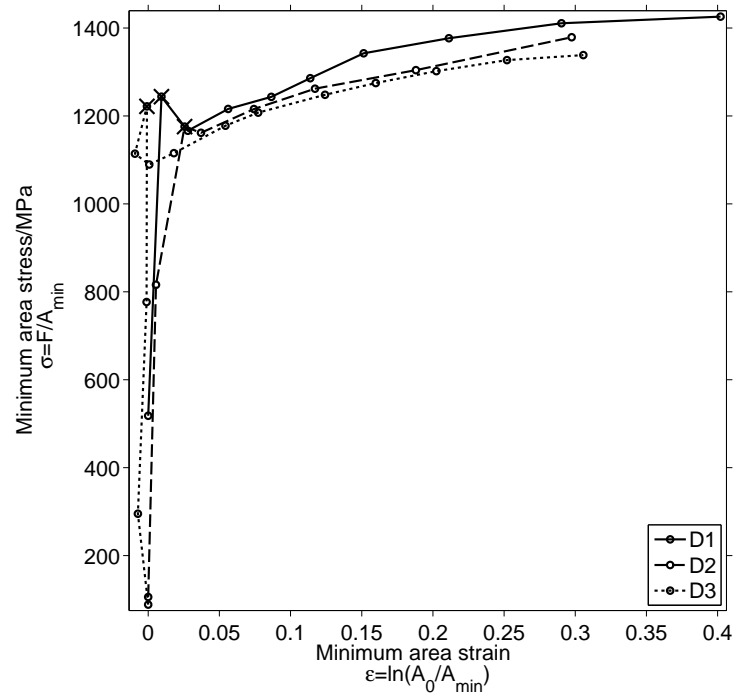


**Figure 6.17:** Mean direct true stress at the minimum cross-sectional area plotted against minimum area strain and mean direct true stress at the maximum cross-sectional area plotted against maximum area strain in the HR tension specimens.

D2 specimen matches its response at the QS strain rate quite well, although the D1 specimen appears to be less anisotropic and it is unlikely that both measurements are accurate. It is tempting to believe that the D1 result here is erroneous as it matches its QS counterpart so poorly.

Figure 6.20 shows the evolving shape of the most strained position in the gauge section for each of the three HR tension specimens for all frames. The D1 and D2 specimens can be seen to strain the most in the through-thickness (D3) direction, whilst the D3 specimen has barely any ellipticity in the final frame before fracture. The D3 specimen here appears to have transitioned from initially circular, to slightly elliptical and then back to circular again before fracture, as seen in its R ratio history. The D1 specimen is significantly more strained than the D2 or D3 directions in its final frame, and this is probably because it failed slightly later than the others did and the final frame time was before fracture occurred, whereas the other two directions were slightly after fracture in the final frame and hence didn't record the total strain

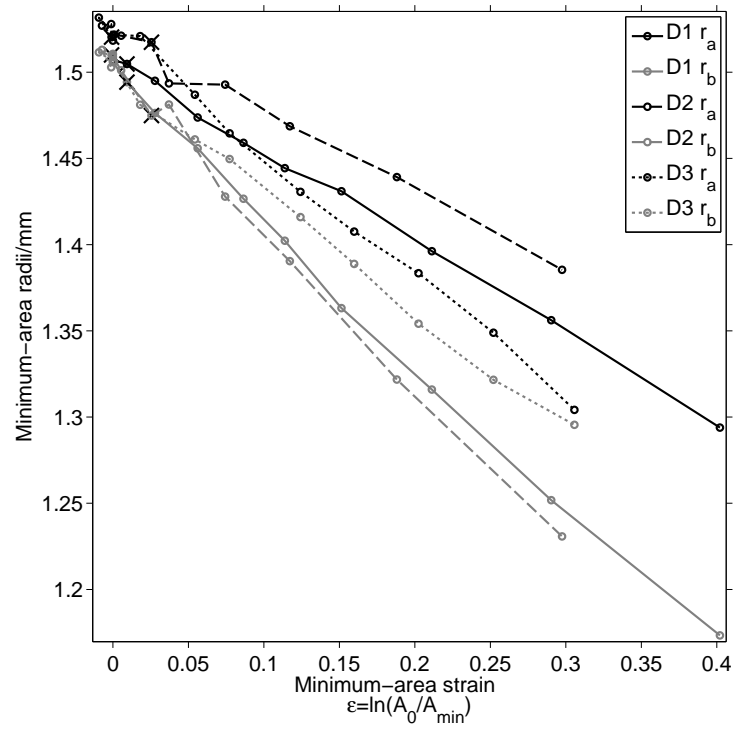


**Figure 6.18:** The semi-minor and semi-major axes lengths at the minimum cross-section against areal strain at the minimum area in the HR tension specimens.

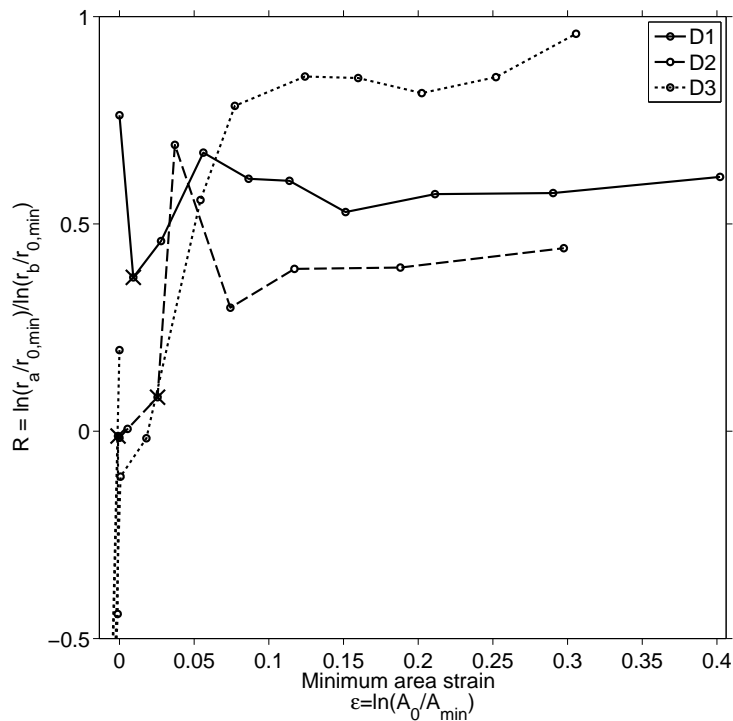


**Figure 6.19:** The R ratio at the minimum cross-sectional area as a function of areal strain at the minimum area in the HR tension specimens.

before fracture very well.

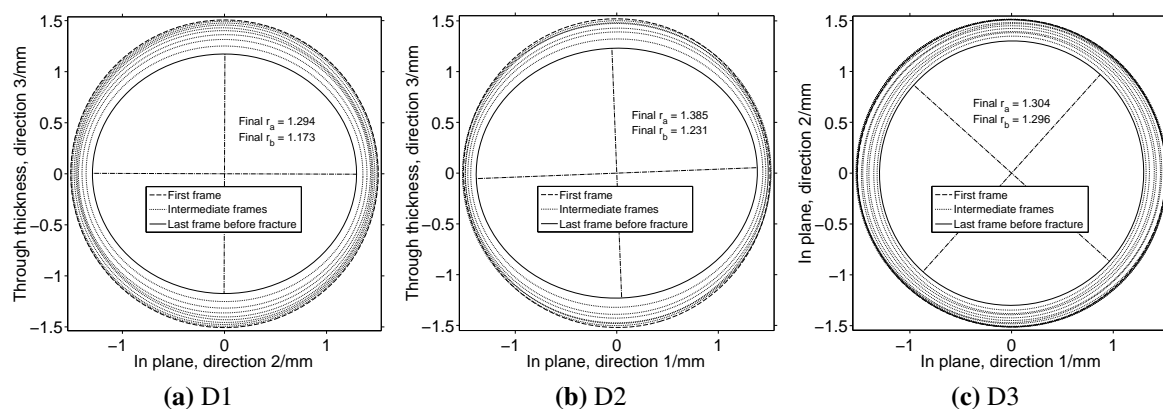


**Figure 6.20:** These figures show the shape of the most strained region in the HR tension specimens in all frames during the experiment.

Figures 6.21, 6.22 and 6.23 show, respectively, photos of the D1, D2 and D3 HR tensile specimens after fracture. Like the QS tensile specimens, there is a definite preferred fracture direction of the D1 and D2 HR tensile specimens on their material directions, but the D3 specimen has virtually no defined fracture direction, probably because of its lower anisotropy than the D1 and D2 directions.

#### 6.1.4 HR compression tests

HR compression tests presented significant challenges owing to the geometry of the configuration. Bars of 15 mm diameter were used to load specimens of only 3 mm gauge diameter, which meant that the mirrors could not be placed very close to the specimen and the specimens did not appear as large in the images as they did in HR tension tests. This reduced the resolution of the recorded images and increased the required depth of field to focus all three views, which necessitated the closing of the aperture and reduced the amount of light reaching the sensors, and this, in turn, increased the noise.

Figure 6.24 shows the true stress-strain plot for the HR compression specimens, as calculated directly by the SHB wave analysis. Similarly, figure 6.25 shows the true stress in the HR

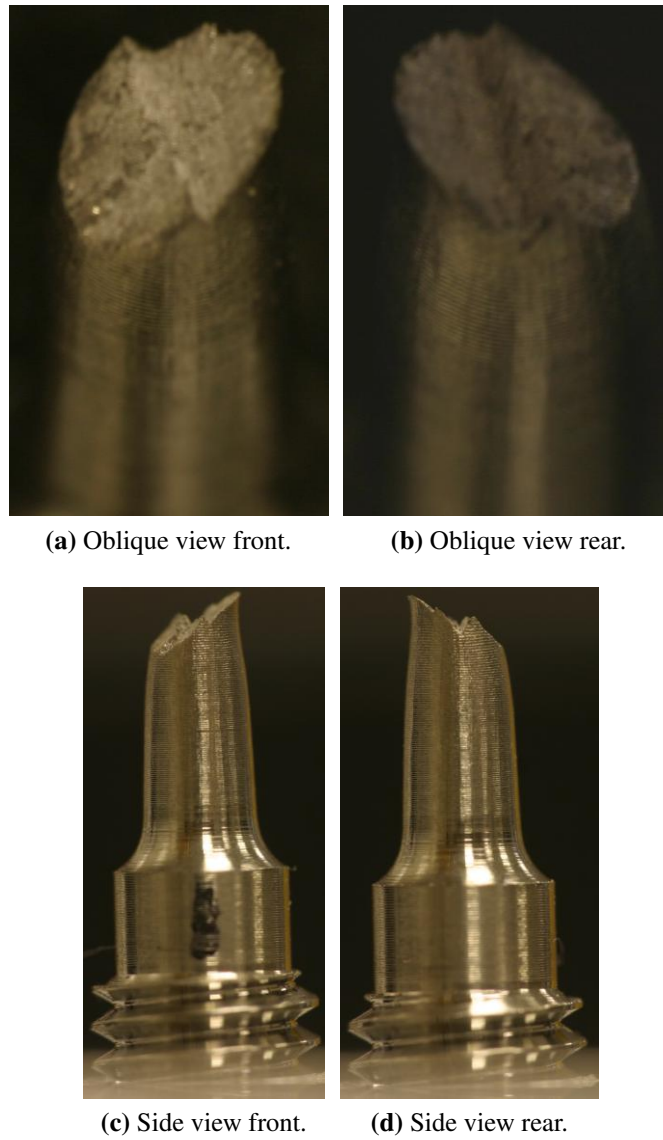


**Figure 6.21:** These photos show the fracture surface of the HR D1 tensile specimen. Note that the fracture surface has formed a plane that contains the in-plane direction and has a step in the middle.

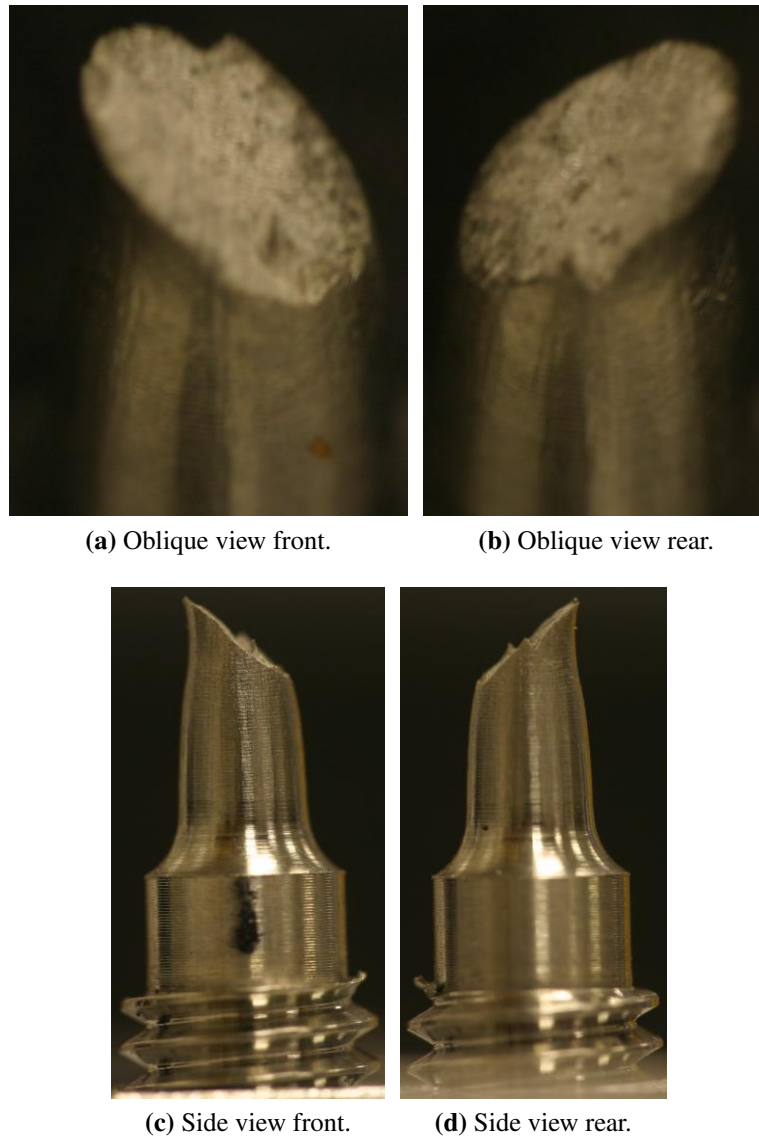


**Figure 6.22:** These photos show the fracture surface of the HR D2 tensile specimen. Note that the fracture surface has formed a plane that contains the in-plane direction and has a step in the middle.

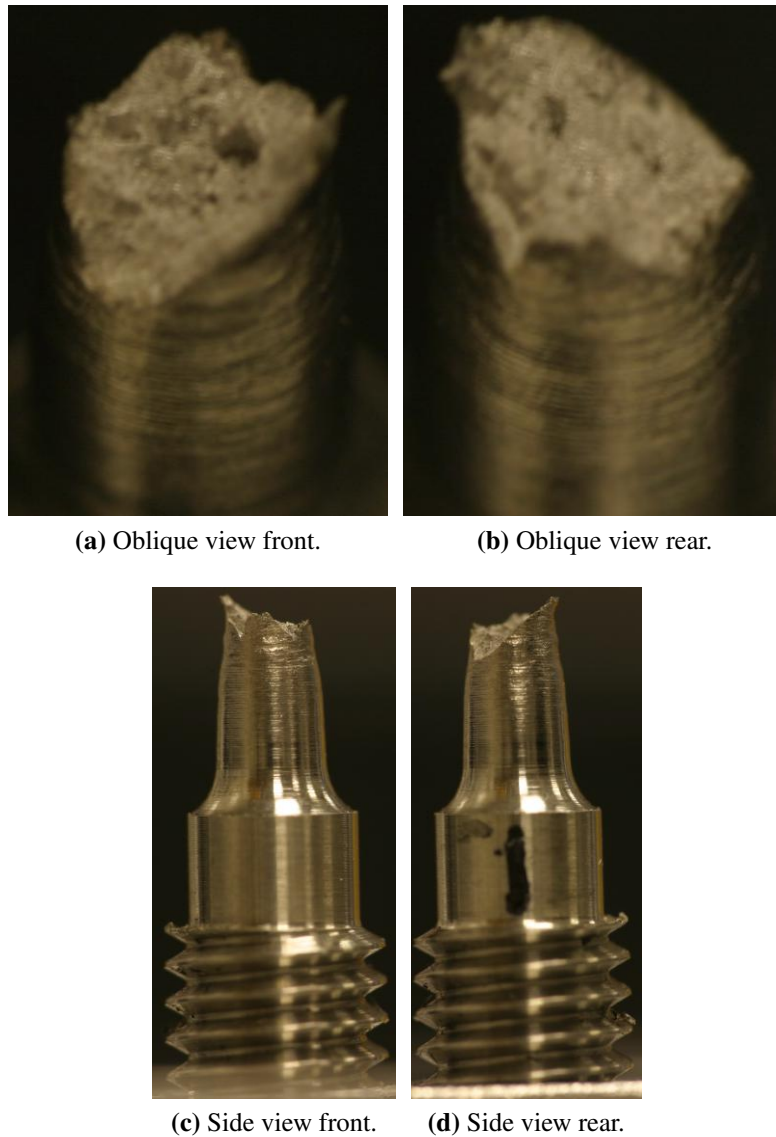


**Figure 6.23:** These photos show the fracture surface of the HR D3 tensile specimen. The fracture plane is more pitted and much less flat than the D1 or D2 specimens and it can't be said to have formed in any particular direction.

compression specimens plotted against areal strain, for the three directions, at the minimum and maximum strained positions. The D3 specimen is clearly weaker than the D1 or D2 specimens, in a similar fashion to the QS compression experiments. The maximum and minimum stresses in the HR compression specimens are much closer to each other for all the specimens than in QS compression, indicating that less barrelling was present at high strain rates.

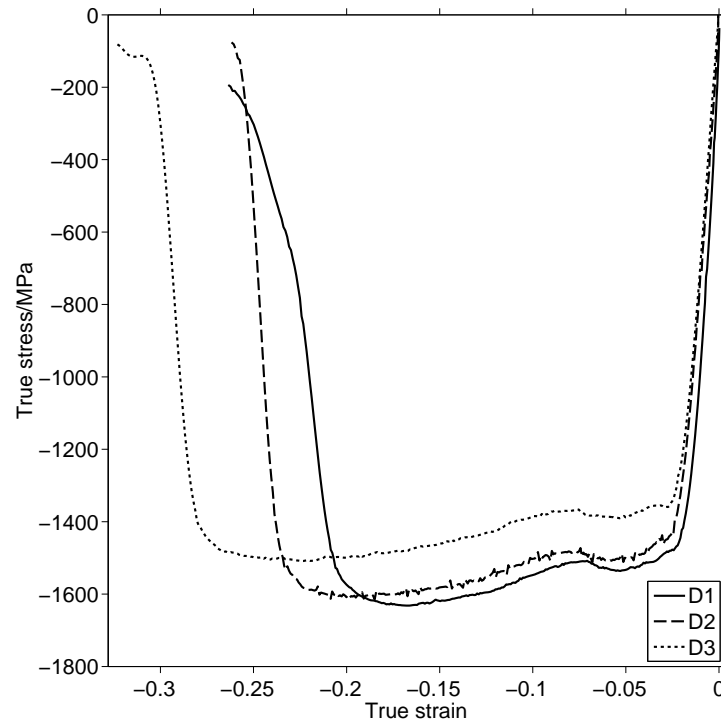


**Figure 6.24:** The true stress-strain results from the three material directions in HR compression, obtained directly from SHB analysis.

Figure 6.26 shows the maximum and minimum radii at the greatest strain position for all three material directions in the HR compression experiments. The radii of the D3 specimen are again nearer to each other than observed in the D2 or D3 directions. The D3 specimen also reaches a significantly greater strain than the other two directions.

Figure 6.27 shows the  $R^{-1}$  ratio calculated in the HR compression specimens at the maximum strain position. Whilst the data are noisy, the overall trends match well with the behaviour seen in QS experiments, in that the D3 specimen is less anisotropic than those taken from the other two directions. The D1 and D3 directions have  $R^{-1}$  ratios ranging approximately from 0.5

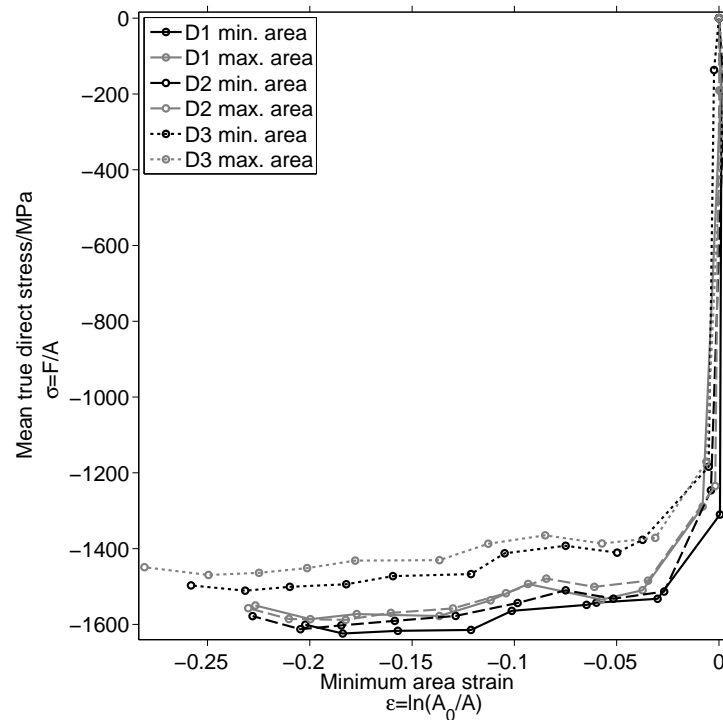
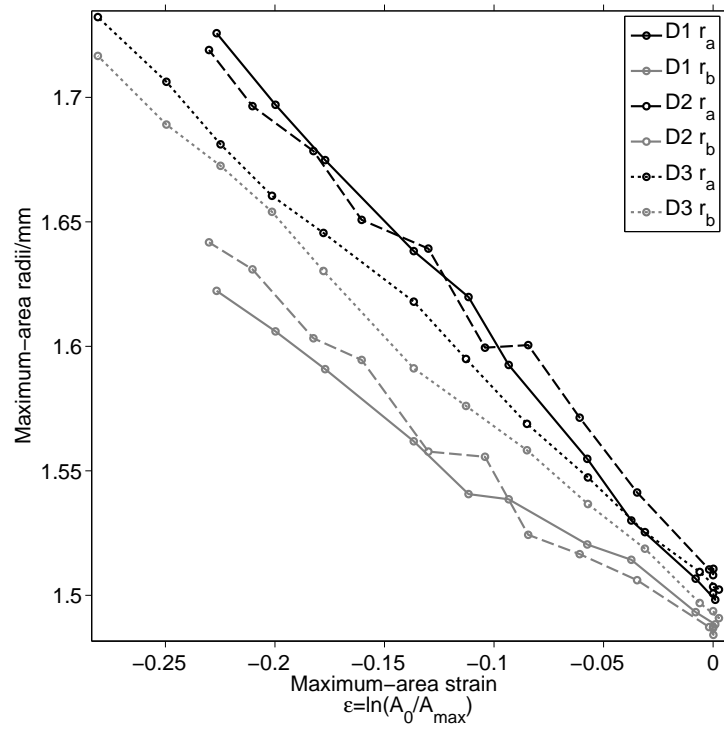


**Figure 6.25:** Mean direct true stress at the minimum cross-sectional area plotted against minimum area strain and mean direct true stress at the maximum cross-sectional area plotted against maximum area strain in the HR compression specimens.

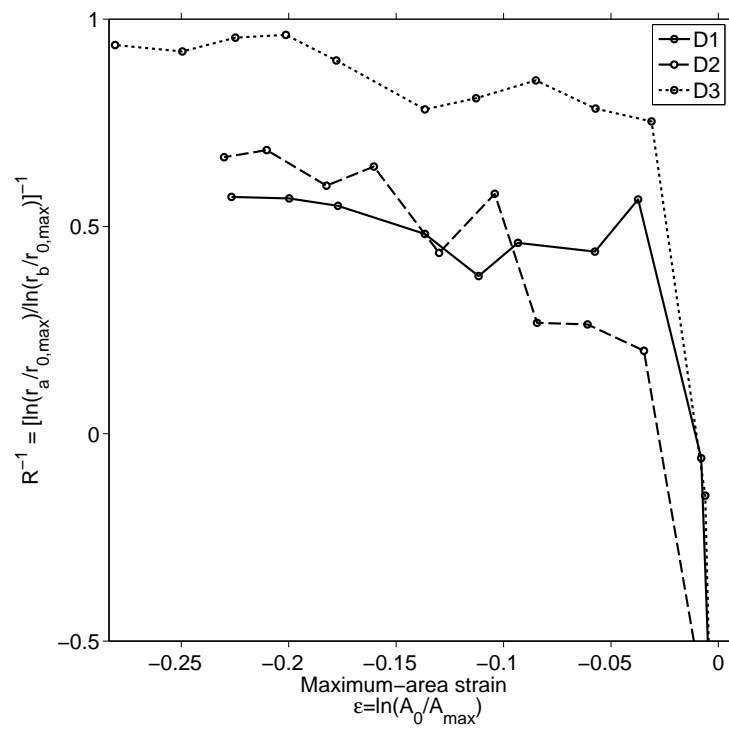
to 0.6 and are observed to increase (become less anisotropic) with increasing strain, exhibiting a similar trend to that displayed by the QS compression specimens.

Figure 6.28 shows the evolution of the cross-sectional shape of the most strained position in each of the three material directions for the HR compression specimens. The D1 and D2 specimens can be seen to have strained the most in the through thickness directions, as they did in all of the other strain rates and directions. Contrary to the other loading rates, the D3 specimen has strained most in the D2 direction.

Photos of the HR compression specimens post-fracture have not been included because they were too badly damaged. However in most of the HR compression specimens a consistent preferred fracture plane orientation with respect to their initial directions was observed. In the D1 and D2 specimens the fracture planes formed in directions that contained the D2 and D1 directions respectively, as they did in QS and HR tension. The D3 specimen also consistently failed along a plane that contained the D1 direction.



**Figure 6.26:** The semi-minor and semi-major axes lengths at the maximum cross-section against areal strain at the maximum area in the HR compression specimens.



**Figure 6.27:** The  $R^{-1}$  at the maximum cross-sectional area as a function of areal strain at the maximum area in the HR compression specimens.

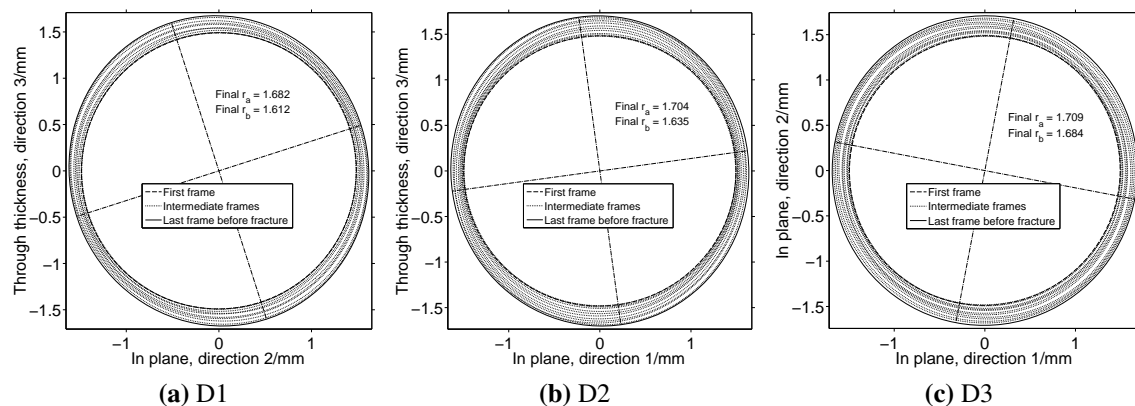


**Figure 6.28:** These figures show the shape of the most strained region in the HR compression specimens in all frames recorded during the experiment.

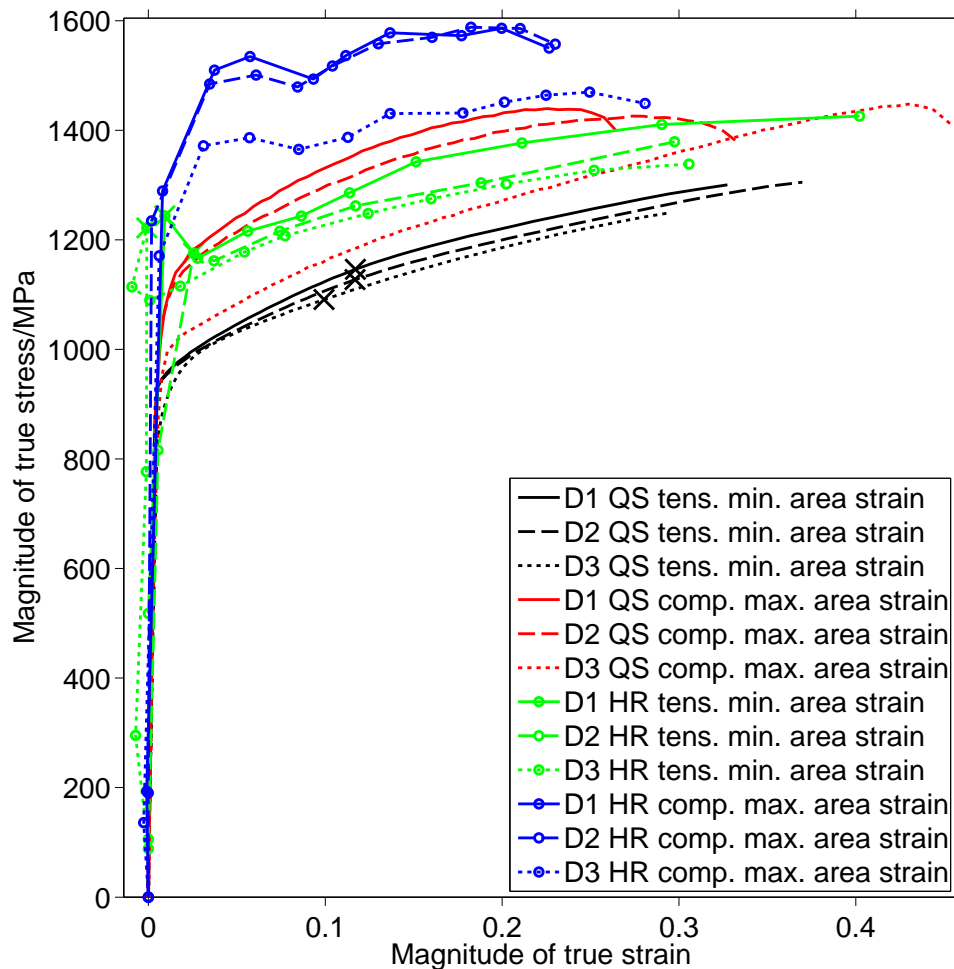
## 6.2 Comparisons of all strain rates and material directions

Comparing the stress-strain behaviour of the materials at all strain rates, material directions and uniaxial loading directions is made easier by plotting the data on a single graph. Figure 6.29 shows the magnitude of true stress and true strain calculated at the cross-section with greatest areal strain in all 12 of the specimens.

Figure 6.30 shows the R ratio (or its inverse in the case of compression) for all of the Ti-6Al-4V specimens.

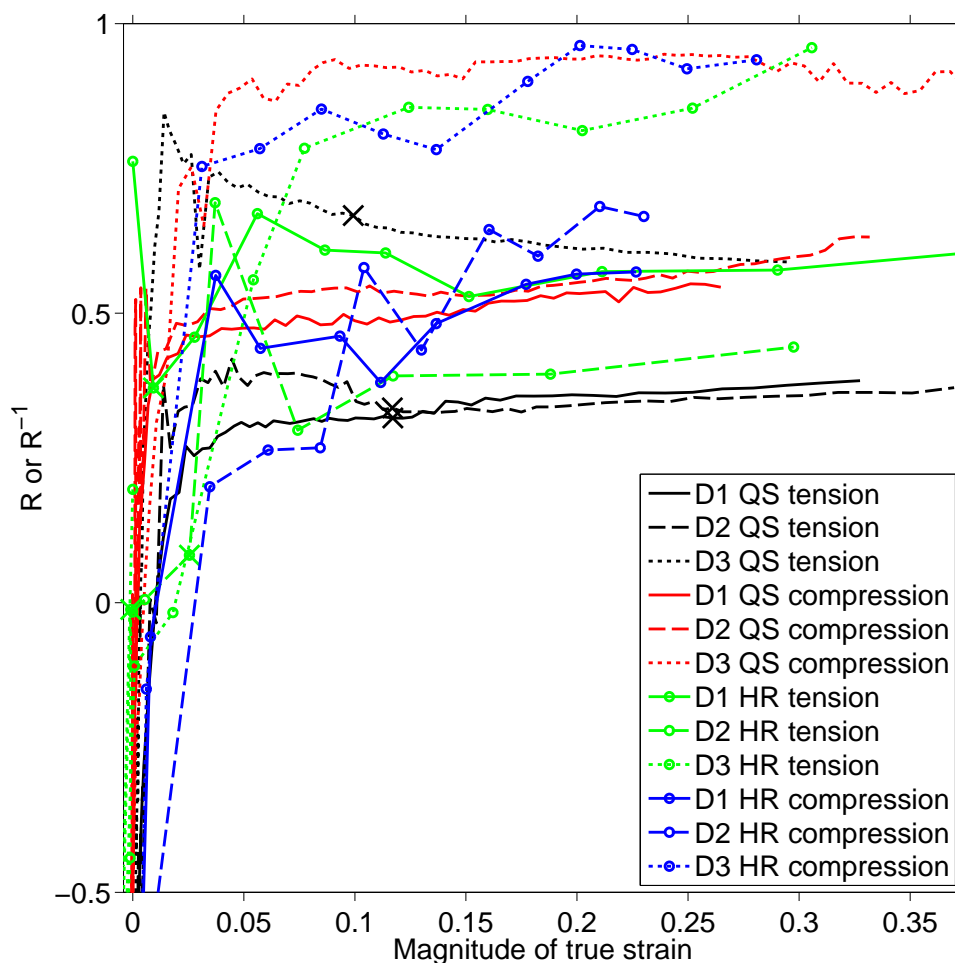
Figure 6.31 shows the true stress-strain histories of the material in graphs separated by material direction. These plots show more clearly how the change in strain rate affects each direction. For instance it can be seen that the D3 specimens have flow stresses that are less strain rate dependent than the D1 and D2 specimens.

Figure 6.32 also shows the R ratios separated into graphs of material direction showing the dependence on strain rate more clearly. D1 and D2 have approximately the same trend in R ratio with strain, gradually increasing, for all strain rates. However D3 has a decreasing R ratio in QS tension, which means that it became more anisotropic upon straining, unlike the QS compression and both HR loading directions where the anisotropy reduced with strain. Also notable in the D1 data is that it is significantly more anisotropic in QS tension than in the other



**Figure 6.29:** The true stress-strain paths for uniaxially loaded specimens of all three material directions at QS and HR strain rates in both compression and tension are plotted here. The magnitude of the stress and the strain for the compression results is shown for comparison with the tensile data.

loading conditions. The D2 direction appears to have two distinct levels of anisotropy, divided between tension and compression (at both strain rates). However, because only one specimen each was tested in HR tension, the D2 tensile specimen results could be anomalous, in which case all three material directions could have more anisotropy in QS tension than in the other loading conditions.



**Figure 6.30:** The R ratios for tension and the  $R^{-1}$  ratios for compression are plotted for all of the Ti-6Al-4V specimens.

### 6.3 Initial yield surface estimation

The results shown in this chapter provide many data for validation of material models. They can also be used to establish some of the parameters that define yield surface functions directly.

In § 1.4, the von Mises, Hill and kinematically hardened von Mises yield surfaces were discussed. As an example of how the data in this chapter may be used to find yield functions, the QS uniaxial yield states will be used to find the best fitting kinematically hardened Hill yield surface. This yield function does not have the flexibility to completely fit all of the data, and so a best fit must be chosen that most closely matches them. The kinematically hardened Hill yield surface is an ellipse in the deviatoric plane, perpendicular to the hydrostatic  $[111]$  direction,

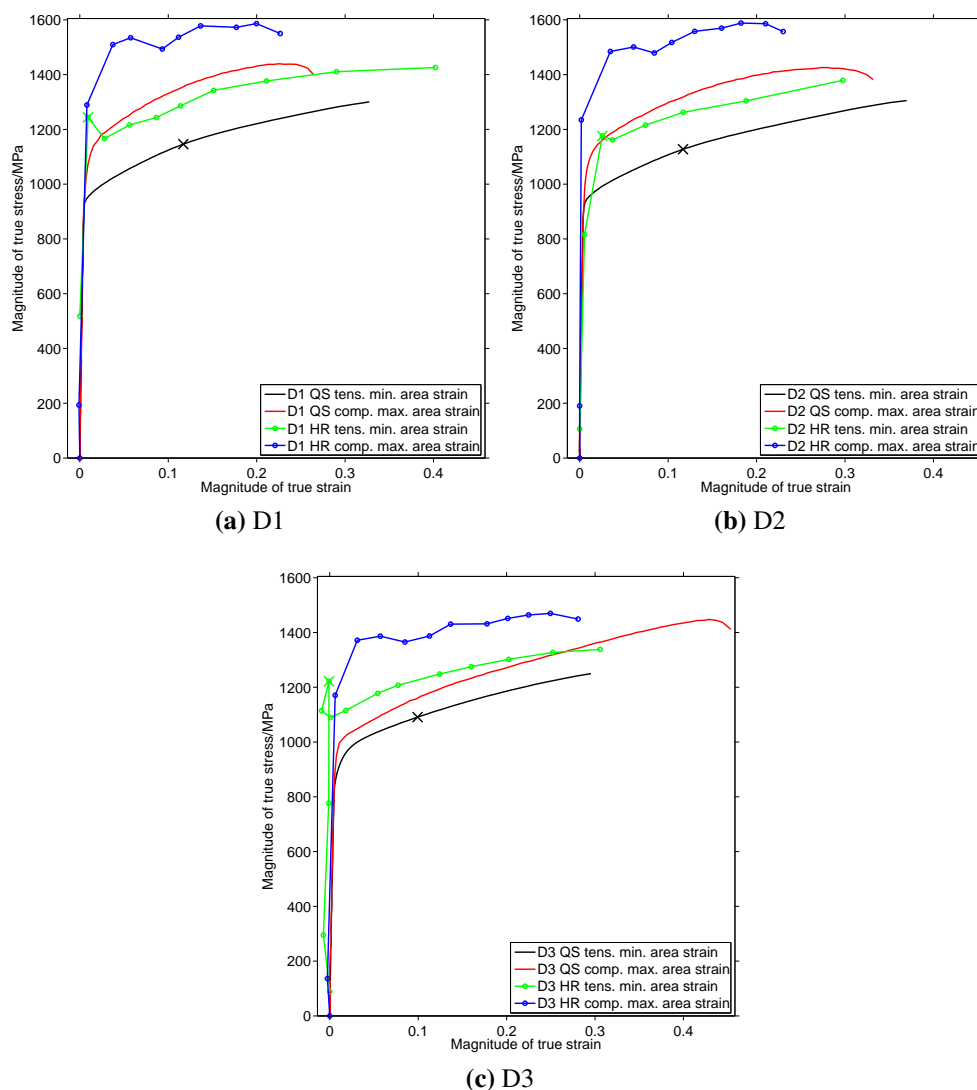


**Figure 6.31:** These figures show the magnitudes of true stress and true strain for the three material directions on separate graphs for comparison of material behaviour at different strain rates.

extended prismatically along the hydrostatic direction in principal stress space. This means that the parameters governing the yield behaviour govern the shape of this ellipse on the deviatoric plane. The yield function matches the experimental data well when the ellipse passes through the uniaxial yield stress states with the same normal directions as the plastic strain increment directions.

The R ratio data at the uniaxial yield stress states has been obtained for specimens undergoing strain hardening. Because this is only an example of the fitting process, a single value of

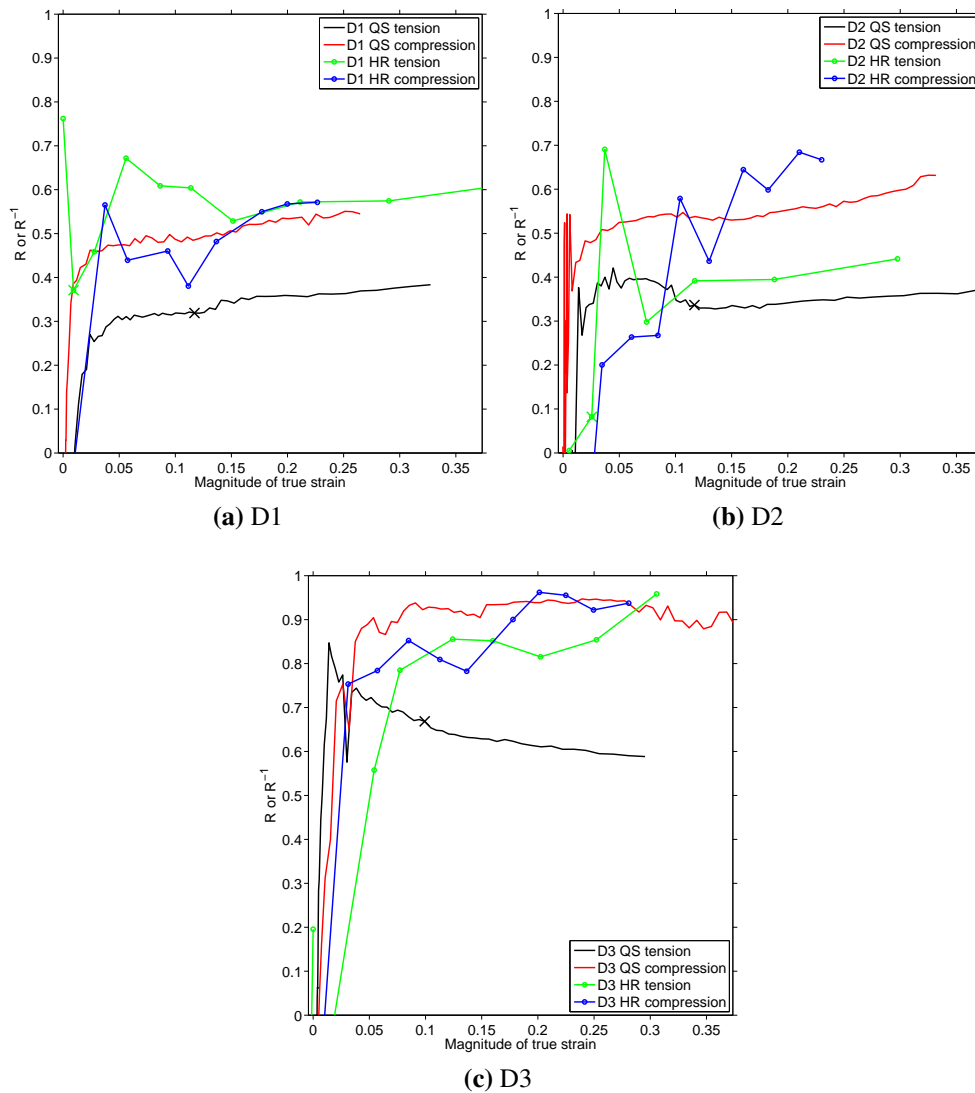


**Figure 6.32:** These figures show the R (and inverted R) ratios for the three material directions on separate graphs for comparison of material behaviour at different strain rates.

total uniaxial strain has been chosen as the state to which the yield function will be fitted. This has been selected as 9 % strain, because all of the QS specimens reached this strain without necking or significant barreling and yet it is still sufficiently large for the R ratio values to be estimated accurately. In addition, at this amount of strain, the total strain is very close to the plastic strain.

At 9 % strain the uniaxial true stress states for material directions D1, D2 and D3 were respectively in tension 1110, 1094 and 1080 MPa and in compression –1315, –1283 and –1150

MPa. And the R ratios were, in the same order,  $R_{D1} = \frac{\varepsilon_2}{\varepsilon_3} = 0.318$ ,  $R_{D2} = \frac{\varepsilon_1}{\varepsilon_3} = 0.376$  and  $R_{D3} = \frac{\varepsilon_1}{\varepsilon_2} = 0.67$  and in compression  $R_{D1} = \frac{\varepsilon_3}{\varepsilon_2} = 2.076$ ,  $R_{D2} = \frac{\varepsilon_3}{\varepsilon_1} = 1.842$  and  $R_{D3} = \frac{\varepsilon_1}{\varepsilon_2} = 1.067$ , from which the strain increment direction may be estimated assuming constant volume (i.e.  $\varepsilon_1 + \varepsilon_2 + \varepsilon_3 = 0$ ) and a constant R ratio, which is not totally accurate, but be sufficient for this example. Projecting the uniaxial stress states and strain increment directions onto the deviatoric plane results in the representation shown in figure 6.33. The principal stress directions and the principal material directions are assumed to be coincident.

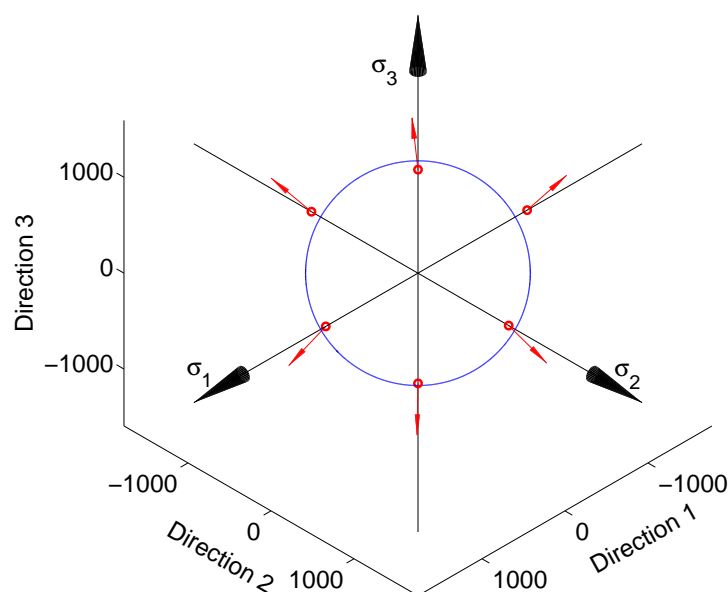


**Figure 6.33:** A view of the deviatoric plane in principal stress space showing the uniaxial yield stress states and the plastic strain increment directions for CR-Ti-6Al-4V loaded quasi-statically at 9 % strain. The data are plotted in red and the mean fit von Mises yield surface is shown in blue.

If a von Mises yield surface were assumed, then the mean distance of these uniaxial yield stress states from the origin in the deviatoric plane would give a yield cylinder radius of 957 MPa, and hence a uniaxial yield stress of 1172 MPa. This would result in the yield surface also shown in figure 6.33.

The uniaxial yield states and the R ratios provide 12 constraints in the deviatoric plane for the fitting of an ellipse: 6 points and 6 tangents. It is possible to simultaneously minimise the distances from the fitted ellipse to these points and tangents, but here the fit to the points will be

compared to the fit to tangents to demonstrate the nature of the constraints applied by each.

The 6 yield point data over-specify the ellipse. The direct-least-squares fitting technique given by Fitzgibbon [77] has been employed to find the best-fitting ellipse. This fit is shown in figure 6.34. The fit can be seen to overestimate tensile yield stresses and underestimate compressive yield stresses, indicating that a more flexible surface would be required to model these data more accurately. The distances from the ellipse to the points have a mean of 61.0 MPa and a variance of 8.3 MPa.

The 6 yield tangent lines, derived from the normal to the strain increment directions and passing through the uniaxial yield stress states, are shown in figure 6.35 in red. To fit an ellipse to these tangent lines, the same geometric fitting process derived in § 3.2.3 was used, and the best fitting ellipse is shown in blue. In a similar fashion to the fit to the yield points, the fit overestimates the tensile yield stresses and underestimates the compressive yield stresses. The distances from the ellipse to the tangent lines have a mean of 62.7 MPa and a variance of 48 MPa.

It is informative to evaluate the two fits to the data not used in making them. The mean distance between the ellipse fitted to the yield point data and the yield tangent lines is 62.5 MPa (variance 130.1 MPa), whilst the mean distance between the ellipse fitted to the yield tangent lines and the yield points is 61.2 MPa (variance 9.3 MPa). The two fits closely match, but the different objectives of minimisation have made them slightly different. The fits are similar because of the low curvature of the ellipse at the uniaxial stress states, relative to other yield functions that may have sharp curvature near these positions, and the agreement between the gradients of the ellipse fitted to the uniaxial stress state points and the gradients of the tangent lines. Both of these reasons serve to bring the points on the ellipse being adjusted by the two different minimisations closer together, arriving at similar fits.

The von Mises surface, the fit to the yield points and the fit to the yield tangents are all shown in figure 6.36. What is immediately qualitatively obvious is the similarity of the best fit

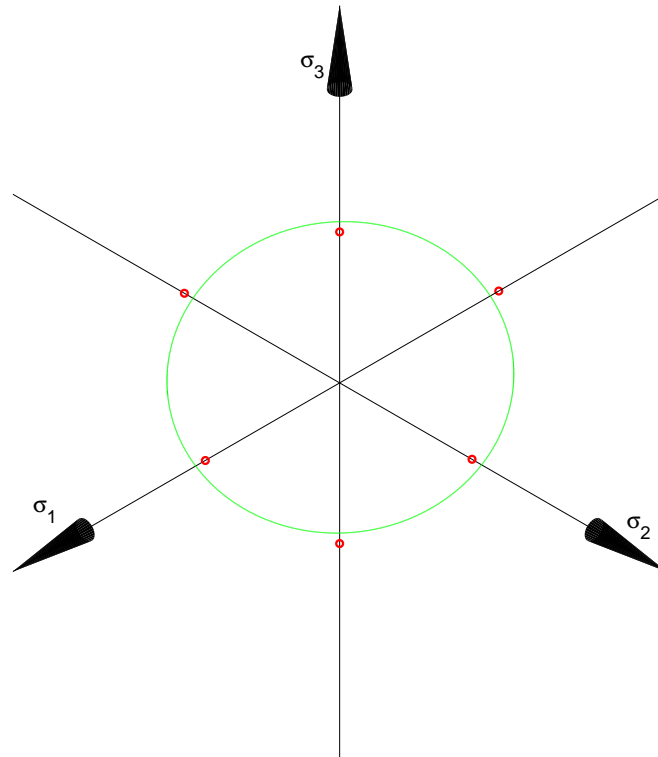


**Figure 6.34:** The same view as in figure 6.33 showing the uniaxial yield stress states in red and the elliptical fit to them, representing a kinematically hardened Hill yield surface, shown in green.

to the yield points and that to the yield tangents, indicating that any deviation from these fits would increase the residual of the least squares fit in both. This demonstrates that the calculated yield surface gradients agree with the uniaxial yield stress values when a Hill yield surface is assumed.

To demonstrate the level of this agreement, a hypothetical material that has exactly the opposite transverse deformation behaviour in the experiments, but the same yield stress values, may be analysed. In this hypothetical material, all of the R ratios from the QS CR-Ti-6Al-4V under analysis in this section have been inverted at the same uniaxial yield stress states. The result of this inversion and the best fit of a kinematically hardened Hill surface to the hypothetical yield tangents can be seen in figure 6.37. It is apparent from this figure that the new fit is much closer to the von Mises surface than the previous fit to the original R-ratio-derived yield tangents. This is indicative that the tangent directions and the yield points for

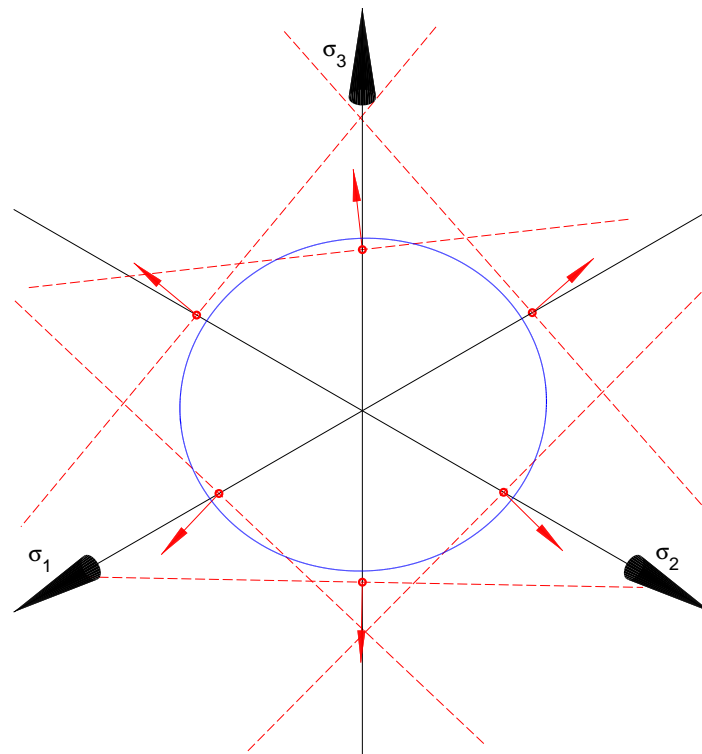


**Figure 6.35:** The same view as in figure 6.33 showing the uniaxial yield stress states and the plastic strain increments in red. Also shown are the tangent lines (dashed) to the yield surface derived from the normal direction to the strain increments and passing through the uniaxial yield stress states. The best fit to these tangents is shown in blue.

the hypothetical material have opposite influences on the yield surface and result in a ‘mean’ surface that is close to the von Mises surface.

The mean distance between the new fit and the hypothetical yield tangents is 74.5 MPa (variance 157.0 MPa). The distances from the yield points to this fit have a mean of 62.2 MPa and a variance of 713.3, suggesting that the fit is much worse at some points than others, and definitely worse than for the original R ratio values. The distances from the hypothetical yield tangents to the fit to the yield points have a mean of 76.0 MPa and a variance of 2191.4 MPa, meaning that the fit to the yield points is very far from the yield tangents in places. The data for the hypothetical material are not self-consistent if a kinematically Hill yield surface can be assumed.

The shape and size of the yield surface depends on the definition of plastic strain, and large plastic strain makes the yield surface smoother. The value of strain used in this section

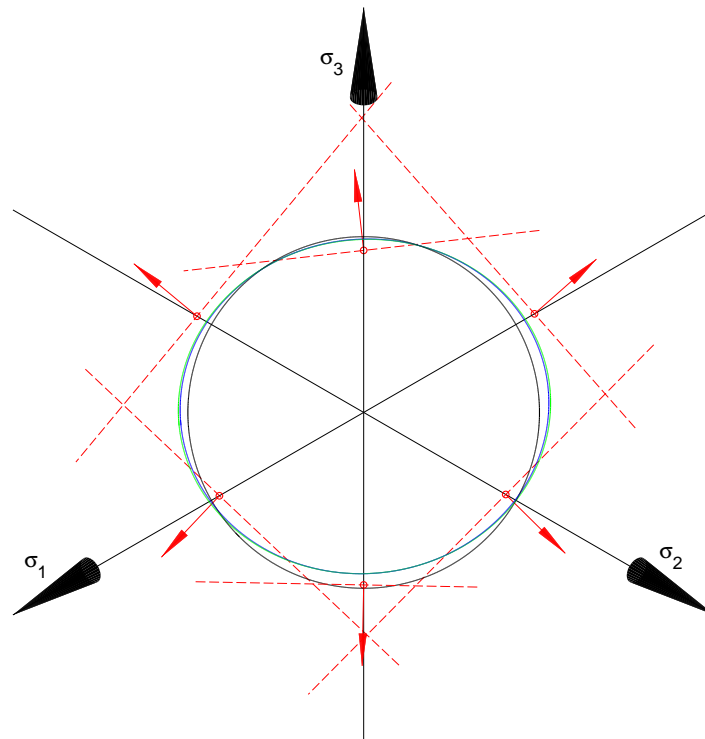


**Figure 6.36:** The same view as in figure 6.33 showing the uniaxial yield stress states, the plastic strain increments and the tangent lines. The best-fit von Mises surface is shown in black, the best fit kinematically hardened Hill surface to the yield points is shown in green and the best fit to the tangent lines is shown in blue.

was large compared the yield strain so that it could be assumed to all be plastic, and so that the measurements of transverse strains were sufficiently accurate to be meaningful. However, the size of the strain used is expected to have reduced the curvature of the yield surface at vertices that are likely to have been present initially in the undeformed material. This means that the yield surface is less sensitive to gradient changes measured by the ratio of transverse strains when the plastic strain is large. As the experimental technique is improved, more accurate measurements of the transverse strain ratios can be made and better estimations of the complex yield surface shape can be made for smaller plastic strains.

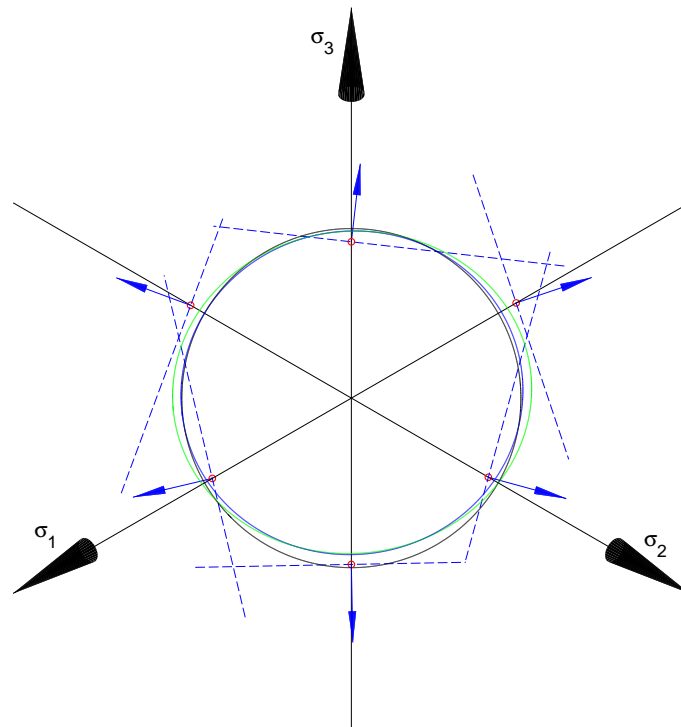


**Figure 6.37:** A deviatoric plane view of a hypothetical material with the same uniaxial yield stress states as the CR-Ti-6Al-4V here, but with inverted R ratios. The strain increments and yield surface tangents are shown in blue, as is the best fit to the tangents. The best fit to the yield points is shown in green and the von Mises surface fitting these points is shown in black.

### 6.3.1 Initial fitting conclusions

This section has demonstrated that the data obtained in these experiments may be used to find a best-fitting kinematically hardened Hill yield surface either through fitting to uniaxial yield stress states in the deviatoric plane or by fitting to lines passing through these points and normal to the plastic strain increment directions, also in the deviatoric plane. The data have proved to be in close agreement when either fitting process is used, showing that, at least with the approximation made by assuming the elliptical nature of the yield surface, the data are self-consistent.

It has been shown that if the R ratios were inverted at the same uniaxial yield stress states, then a surface fitted to the yield tangents from these inverted values would not match the surface fitted to the yield points, and the data would not be self-consistent.

For accurate modelling of the CR-Ti-6Al-4V under investigation, a yield surface that could model the yield values more closely than a kinematically hardened Hill yield surface would be required. The parameters governing this model could be found by simultaneously minimising the distance between the yield surface and the uniaxial yield stress points and the yield tangents at those points. This would ensure that the model accurately captured the behaviour of the stress behaviour and the deformation behaviour too.

## Discussion, Improvements and Future Research

---

### 7.1 Comparison of standard measurements with elliptical cross-section measurement

The current ASTM standard [28] for measuring the  $R_\theta$  ratio (designated r ratio in ASTM terminology) is limited to testing flat specimens. This means that any deviation in principal direction of the material anisotropy from the plate directions cannot be observed. The technique presented in chapter 3 allows the principal directions to manifest themselves as the principal axes of the specimen's elliptical cross-section and hence provides more data on the anisotropic behaviour. There are other disadvantages to using flat specimens, such as canoeing, where the flat specimen warps and takes the shape of a canoe's hull, and pincushion distortion of the cross-section during necking [42], that are both eliminated by using initially axisymmetric specimens.

The ASTM standard also makes use of the measurement of axial strain in combination with width strain because it is frequently difficult to measure the thickness displacement with sufficient accuracy; so the constant volume assumption is made and the r ratio is derived from the axial strain and width strain alone, as described in § 1.4.1. The novel measurement method

presented in this thesis has been designed to have equal accuracy in transverse directions, particularly when the views are evenly spaced around a specimen (see § 3.3). So, the R ratio is calculated from the direct ratio of strains and a constant volume does not have to be assumed, which would be valuable in the application of this technique to polymers or foams.

The ASTM standard presents predictions of the coefficient of variation (CV) of the r value against the CV of the axial strain measurement. It suggests that the r value should be measured above 0.15 engineering strain for accurate results. This is in line with the measurements made in this research, to the extent that R values below an axial strain of approximately 0.15 often vary widely.

The new technique allows the measurement of strain ratio to continue after necking has begun, which increases the accuracy of the R value obtained and also affords the potential for observing changes in the R value with increased strain, as has been observed in certain loading conditions in Ti-6Al-4V.

## 7.2 Measurements of material response

Measuring the evolving elliptical cross-section of anisotropic materials provides data on several properties that are not available in standard uniaxial experiments.

The principal new measurement is the cross-sectional area as a function of axial position. When many measurements are taken during an experiment *in situ*, this allows the calculation of mean direct axial true stress in specimens at any axial position as a function of time. As has been demonstrated in figure 3.27 and figure 3.28 the maximum of this value as a function of strain can be evaluated to provide data on the hardening rate.

The second type of data is the size of the major and minor axes in all cross-sections, again as a function of position and time. These data allow the calculation of orthogonal strains, and hence the strain ratio for the two directions, which is discussed in § 1.4. Because we know how

axes are aligned compared to the material axes, these measurements provide information about the effect of processing on material properties. Compression experiments generally require cylindrical specimens, and up until now no other technique has been presented in the literature that can measure anisotropic behaviour in compression specimens without interrupted tests.

The third type of data that is obtained from these measurements is the direction of anisotropy, present in the orientation of the elliptical measurements. The measurement technique does not rely on prior knowledge of the orientation of the ellipticity, and hence can be used as a measurement of material principal directions. This type of measurement may prove useful in components that have unknown processing routes and the relative strengths of different loading directions are not known. The orientation measurement is also a useful confirmation that the principal material strength directions are as expected in rolled material, such as the Ti-6Al-4V and CP-Zr in this research. The through thickness direction has been observed to have a weaker initial yield strength in tension and compression for Ti-6Al-4V, resulting in more strain in the through-thickness direction during uniaxial experiments conducted in the rolling plane, whereas the CP-Zr specimens exhibited less strain in the through-thickness directions, indicating that the material is stronger through-thickness.

### 7.2.1 Applications for constitutive modelling

There are some situations in which constitutive parameters can directly be inferred from the measurements here without having to use inverse identification methods. In metallic homogeneous alloys, such as Ti-6Al-4V and CP-Zr, the yield function, to a first approximation, can be assumed to take the form of a von Mises surface that has been anisotropically stretched: the Hill yield surface. In this case the normality hypothesis of plasticity can be used to determine orthogonal yield stresses from the strain ratio in a uniaxial experiment. Alternatively, the gradient of the yield function at the uniaxial stress states can be used to determine other parameters of the yield function.

In an isotropic material, the normal vector to the yield stress under uniaxial loading,  $\sigma_1 = \sigma_y, \sigma_2 = 0, \sigma_3 = 0$ , will be in the direction of  $[1 - 0.5 - 0.5]^T$ . If the material exhibits transverse isotropic behaviour, then, in a coordinate system aligned with the material principal axes, two of the initial yield stresses will be equal and the third will be different. Under the transversely isotropic yield stress condition, the direction of the normal vector when loading is applied along either of the two equal yield stresses will be different from that in the isotropic plane direction, whilst loading in the unique yield stress direction will result in a normal vector that has the same direction as the isotropic normal direction. This is explained by figure 1.6, page 12, which shows the normal vectors for uniaxial loading of an isotropic material in 3 orthogonal directions and loading along principal axes of a transversely isotropic material.

The data on flow stresses and R ratios presented in chapter 6 provide the means by which to determine the magnitude and gradient of points on the yield surface for cross-rolled Ti-6Al-4V that change with strain rate and strain hardening. These data have shown that a representative constitutive model must be able to capture the near-transverse isotropy in the D3 direction for all loading directions and strain rates apart from QS tensile loading, which has significant, increasing, anisotropy. The model must also be able to capture the anisotropic behaviour of the D1 and D2 directions which have similar yield surface gradients at all uniaxial stress conditions apart from, again, QS tensile loading, where significantly more anisotropy is evident.

This is the start of the process to determine a constitutive model that can completely capture the yield behaviour of CR-Ti-6Al-4V including its anisotropy and strain dependence. Further experiments would be required to complete the characterisation, which are described in § 7.3.1 below.

It is envisaged that the primary application of data from the techniques presented in this research will be in identification of the parameters governing constitutive models of material behaviour through inverse identification techniques that use numerical modelling of experiments. Elliott [3], for example, has demonstrated how experimental data can be used to find such pa-

rameters when there is coupling between the deformation exhibited and the parameters being modified.

The surface tracking technique developed in chapter 4 has not been applied to all of the experimental data gathered during the tests on CP-Zr, steel and Ti-6Al-4V. This is because the true value in that data is in using it during inverse parameter identification or for direct comparison with simulations of experiments to prove their validity. Also, the surface tracking technique could not be successfully applied to the HR data because there was too much deformation between frames and much more noise than in QS images, so a partial, QS dataset has not been presented. However, the QS data are still available for comparative purposes in the future.

## 7.3 Further research

### 7.3.1 Extensions of the current research

A small amount of microscopy has been conducted on the CR-Ti-6Al-4V plate investigated in this research, [2] figure 1.2. This has shown that there is, indeed, a texture in the hexagonal close-packed (HCP) material, namely one of elongated grains in the rolling directions and a preference for the c-axis of grains to lie in the rolling direction (in-plane), but it does not provide a full microstructural characterisation. For an improved understanding of how the yield surface, which has been better characterised in the current research, is affected by texture, a number of micrographs should be obtained of the material's three principal faces, before deformation, after small deformations (from interrupted specimens) and after fracture has occurred. This will allow better determination of which microstructural mechanisms govern the behaviour observed in this research. An initial inference is that twinning [5] is the cause of the tension-compression asymmetry and the flattening of grains may cause the differences in hardening behaviour in tension at QS strain rates between the three material directions.

The CR-Ti-6Al-4V has been tested by performing uniaxial experiments in three directions that coincided with the plate principal directions. A more complete characterisation of the material would require uniaxial experiments in further directions between these. This would provide more data for inverse parameter identification or model validation.

To improve the characterisation of the yield surface of CR-Ti-6Al-4V further, combined tension-torsion and compression-torsion experiments could be performed on thin walled specimens. If the cross sections were measured in these experiments they could provide estimates of the plastic strain increment directions at yield function locations other than the uniaxial stress states. The changing orientation of the cross-sections in these specimens along the gauge length would not adversely affect the accuracy of the elliptical cross-section measurement technique because it is independent of elliptical orientation.

When the specimens were inserted into the loading devices in the experiments, their orientation was aligned with the camera orientations by eye using a fairly crude marker. This means that there is greater scope for error in the orientation measurements of the principal directions of anisotropy with respect to the plate directions than is ideal. In future, in addition to marking the specimens with their orientation, it might be advisable to include a flat face on one of the shoulders of tension specimens to align it mechanically with the directions of the views, and to have an exact way of visually aligning the markers on the compression specimens with the views. However, the measurement of R ratio was unaffected by orientation because the three view configuration could measure the dimensions of the ellipse regardless of orientation, which is one of the strengths of the technique; the only significant systematic error was in measuring the orientation with respect to material axes.

The CP-Zr and steel data from the experiments in chapter 5 contribute to the wider characterisation of these materials. This is most true for CP-Zr, where its highly anisotropic properties have been investigated before [24] and the results presented complement the current state of characterisation. Micrographs of the steel specimen should be also made to confirm the slightly

unequal properties that have been observed in its transverse material directions. The steel specimen results demonstrate the usefulness of the technique in detecting even mild anisotropy in specimens. The data gathered would prove useful for validation of material models that can describe their respective behaviour.

When the surface tracking technique and the elliptical cross-section measurements are applied simultaneously it is possible to estimate the volume of the specimen as it deforms. If the surface is circumferentially smooth, i.e. it does not become pitted, the accuracy of this measurement could be sufficient to detect voids in the specimen. However this is merely speculative.

The techniques presented could be applied to materials that are longitudinally inhomogeneous. For instance, the strain in specimens of welded joints could be measured using the surface tracking technique and the cross-section measurement technique. However, this would only be possible if the heat affected zone of the material was large enough in the gauge section to be observed.

It may also be possible to measure cross sections that have higher order shapes than ellipses. Given tangent lines a polygonal bounding-hull can always be created which approximates a shape. This could be useful in situations where the cross-section is known to be convex but of an irregular shape. The more views of the specimen that can be acquired, the closer the approximation will be. Formulations to find the best fit for convex analytic shapes with higher orders than conic sections might also be possible, for instance in fitting curves of the form  $f = Ax^4 + By^4 - 1 = 0$  (shown in figure 7.1), but no formulation for these has been investigated here.

### 7.3.2 Improvements to the experimental design and validation

This engineering research project has created tools that will aid research into materials science. There are several aspects of the experimental design that could be improved upon to enhance the accuracy of the techniques in the future.

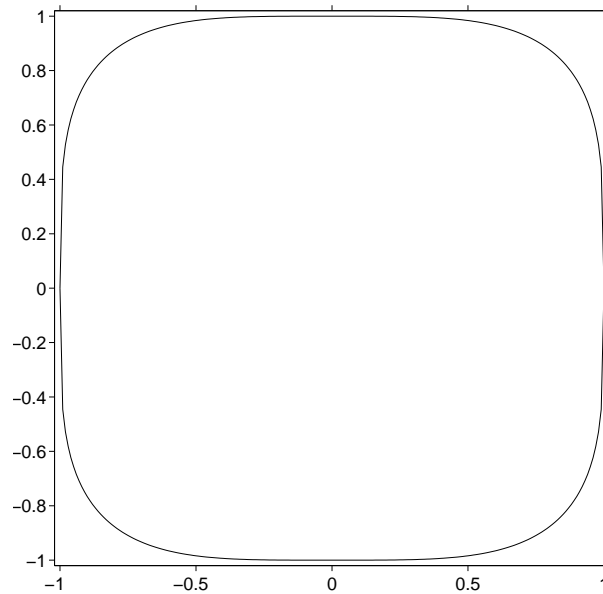


**Figure 7.1:** An example of a higher order function than a conic section,  $f = x^4 + y^4 - 1 = 0$ . It may be possible to measure this shape by a least squares method using an adaptation of the cross-section measurement technique.

The Ti-6Al-4V experiments were performed during the development of the experimental techniques. After those experiments were conducted, it was found that a better way of illuminating high speed experiments was by reflecting flashes from diffuse reflectors such as projector screen fabric. This was the method used in the HR CP-Zr and steel tensile experiments and the CP-Zr Taylor impact experiments, but the HR Ti-6Al-4V specimens were partly illuminated by direct views of the flashes and partly by direct illumination of the specimens, which made overexposure an issue in some parts of the image. Using a diffuse reflector creates an evenly illuminated region behind all three views in the mirrored configuration. The QS photographs of the Ti-6Al-4V specimens were also illuminated by silhouette in the side views but not the centre, because the configuration did not allow simultaneous laser extensometer recording and central silhouette illumination. It should be possible to obtain the Ti-6Al-4V data more accurately if the experiments were repeated with all-silhouetted views.

The interrupted tests carried out on CP-Zr and steel specimens were measured using a coordinate measurement machine (CMM) with a 3 mm diameter probe. The slightly rough surface of the specimens and its concave curvature prevented very accurate measurements of their

dimensions from being recorded. One step towards completing the validation of the elliptical cross-section measurement technique would be to measure these ‘interrupted specimens’ again using a different calibrated method, such as an optical comparator (also known as a shadow graph), which would make the estimations of error in the reconstructions more accurate. The interrupted specimens could also be positioned in the HR apparatus and recorded under HR conditions to estimate the errors present with real elliptical and near-circular specimens, because this has only been done at QS rates in this research.

The elliptical prisms were only photographed in the HR configuration at a single arbitrary angle to estimate the errors in measuring elliptical cross-sections of various aspect ratios. The QS prism measurements were performed at a range of angles to see if there was any significant dependence of accuracy on elliptical orientation. Although no significant dependence was found in QS conditions, the photographs at HR could be taken for the same range of angles to check that there is no dependence on orientation at HR either. Simulations of the measurement of elliptical cross-sections in § 3.3.2 suggest that there will be some dependence of accuracy on orientation when the errors in edge positions are randomly distributed.

The numerical simulations of errors has shown that evenly spaced views, i.e. from cameras placed at  $60^\circ$  or  $120^\circ$ , are more accurate than those spaced at  $45^\circ$ . So the QS data for all the experiments should be more accurate if the cameras were more evenly spaced around the specimen. In the data presented here the QS experiments were performed with cameras at  $45^\circ$ , and these experiments could be repeated.

In several of the HR experiments specimen debris scratched the mirrors, left them coated in lubricant or completely broke them, which meant that mirrors made from aluminium coated microscope slides were used because they were readily available, could be made small enough to fit close to the specimen and were mirrored on the top surface. In the future the data could be made more accurate by using mirrors with a higher reflectivity, such as dielectric mirrors.

The depth of field in the HR experiments using two the mirrors was problematic because the direct central view was closer to the camera than the virtual mirrored views. This meant that the aperture had be kept small so that the specimens could be kept in focus. To overcome this, an optical path extension could be obtained by inserting prisms or mirrors between the central view and the camera lens. Figure 7.2 shows one such configuration, whereby the central view of the specimen has been moved farther from the camera by the insertion of four mirrors. These mirrors could be inserted in the same plane as the two existing ones, as in figure 7.2 or they could be inserted so that the extended optical path is reflected out of this plane and then back into it, which could reduce the risk of obscuring the side views with the extra mirrors. This would alleviate the depth of field problems and may make using mirrors the preferred method for both QS and HR experiments, due to the beneficial factors of simple timing and more efficient use of cameras.

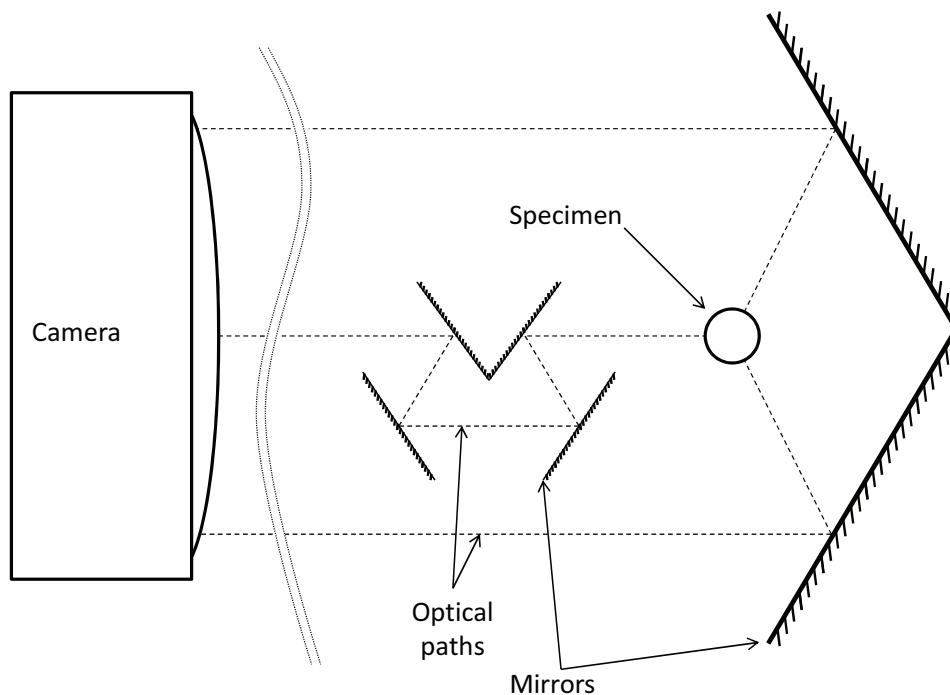


**Figure 7.2:** A suggested improvement to the mirror configuration that provides equal path lengths to the specimen in all three views.

The HR compression bars of the split-Hopkinson bar apparatus could be made thinner to

allow the mirrors to be placed closer to the specimen. However if the path extension was used then this might not be necessary.

It has been mentioned that having more views of a specimen would make the experiment more accurate. This could have been achieved in the current research by using more mirrors to obtain views at more angles. Both the QS and HR experimental configurations have scope for this type of improvement in that there is space for extra mirrors to be inserted that could reflect more views of the specimen. As long as these views were correctly calibrated they would serve to increase the amount of data available for fitting the ellipses and reduce errors in edge detection.

More accuracy could also be achieved by using cylindrical lenses to magnify the specimens only transversely so that their edge positions could be more accurately determined. This would be appropriate for the near-square aspect ratios of digital image sensors where much of the width of the photographs is empty space, or specimen interior that records no useful information in these tests. An optical wedge [99] of prisms could be used in conjunction with the cylindrical lenses to remove the central portion of the specimen before magnification, especially in compression tests where the cross-section doesn't narrow.

On the method of tracking surfaces to estimate displacement there are a number of further sources of error which may need to be investigated in addition to those already stated. These include: errors in detecting the position of features with sub-pixel accuracy; noise in the digital images; lens distortion; changing lighting conditions. One issue not discussed thus far is that of using a perspective camera lens and thus the limited ability to look down the parallel ridges in the specimen surface, apparent in figure 4.1(a), page 85. Ideally a telecentric lens would be used for this purpose, however using a lens with a long focal length should ensure that the light rays are close to parallel, and hence allow the camera to see along the ridges, because the light would fall on the image plane perpendicularly to it. However, as we move further from

the centre of the image, the assumption of perpendicular light rays becomes less valid, and the features on the edge horizon may become less distinct as peaks appear to overlap more.

### 7.3.3 Proposal for removal of fibre-shearing discontinuities

In § 2.2.3 the problems associated with image discontinuity shearing were described. This kind of shearing plagues all kinds of photogrammetric measurement taken by fibre-guided cameras. The distortion is usually assumed to be small for qualitative analysis, but significant when quantitative measurements are required.

To rectify this kind of distortion, it is proposed that a dense checkerboard pattern be photographed. The locations of corners in the pattern can then be found to sub-pixel accuracy using DIC. At a seed location within the image, possibly chosen at random or manually by the user, all corner locations that have a uniform separation from the seed location in orthogonal directions from it can be classified as lying in a single uniform region. Starting with any location that lies outside this region as a new seed location, all corners that have uniform spacing from this new location are classified as lying in a second uniform region and so on, until all points are classified into regions of uniformity. This creates a map of the discontinuities, where the regions meet. To locate the discontinuities to a higher precision than to the nearest corner in the checkerboard pattern, the pattern can be translated by a fraction of the square size and the process repeated. This will provide highly accurate locations for the discontinuity regions.

It is assumed that the discontinuities are straight lines, and that the distortion from one region to the next is translation parallel to the edge of the discontinuity. If this is so, then the distortion may be removed by choosing one of the uniform regions to be the global ‘true’ grid and finding the translation of the other regions required to align them with that global true grid.

From then onwards, for that particular CCD, any coordinates of pixels taken from within uniform regions that are not in the global grid have to be translated by the same amount to align them all correctly.

If the image discontinuity shearing is not translation parallel to the discontinuity, and is instead a general projective transformation (albeit small), then the transformation required for the non-global grid regions will be a general homography, and there will be gaps at the at the discontinuities that would most likely have to be interpolated in any measurement set.

# Conclusions

---

## 8.1 Conclusion

### 8.1.1 Summary

Photogrammetric methods have been developed to measure the edge profile of specimens from photographs of quasi-static (QS) and high strain-rate (HR) experiments robustly and accurately; a method has been developed that uses multiple view geometry to reconstruct the elliptical cross-sectional shape of specimens photographed from three or more angles during loading at strain rates ranging from QS to HR; and a method has been developed that can measure displacement and strain in specimen surfaces with a high resolution by tracking features in the edge profile.

Experiments on nearly-isotropic steel and highly anisotropic CP-Zr have been performed in tension at QS and HR to demonstrate the range of applicability of the cross-section measurement technique and obtain material data that has not been measured before. Experiments have been performed in tension and compression at QS and HR on specimens cut from the principal material directions of a cross-rolled Ti-6Al-4V plate. The elliptical cross-sections of the initially cylindrical Ti-6Al-4V specimens have been measured and the results of these measurements have been presented alongside traditional measures of true stress-strain behaviour.

Validation of the elliptical measurement technique has been obtained through the measurement of elliptical prisms at both QS and HR camera frame rates and exposure times. Further validation has been obtained by the measurement of interrupted specimens of steel and CP-Zr tensions specimens after they had significantly necked. A coordinate measurement machine (CMM) was used to obtain calibrated measurements of the prisms and the interrupted specimens for comparison with the results of the optical technique.

### 8.1.2 Edge detection

The edge detection techniques developed for this research provide methods for robust tracking of the edges of tension and compression specimens with sub-pixel accuracy. In HR experiments the frame rates needed to capture the high speed deformation demand very short exposure times, which reduce the amount of light available for CCDs, and hence the noise level in the intensity values captured in digital images is large. By using a difference-of-boxes technique using a step change template that is very long perpendicular to the edges, their position can be determined accurately even in the presence of large amounts of noise.

The geometry of uniaxial specimens creates opportunities to detect automatically the correct specimen outlines even when multiple highlights from cylindrical surfaces also appear to be edges. By having a sufficiently high frame rate during the recording of specimen photos, the edge detection can be made more efficient by limiting the range in the images over which the edges are searched for, which also prevents the detection of highlights as edges.

### 8.1.3 Elliptical cross-section reconstruction

By measuring the edge profile of a specimen in views from three cameras whose positions are known relative to the specimen, lines were constructed that were tangential to the specimen.

Five of these tangent lines are sufficient to describe the shape of a conic section. In most plastically anisotropic homogeneous materials an initially circular cross-section deforms into an ellipse upon loading. The six tangent lines obtained from all three views over-specify the elliptical shape, which allows a non-linear least-squares solution to be derived to obtain the best fit of an ellipse. If more than three cameras can be used then the extra data can be incorporated into the least-squares minimisation to reduce errors in the fitting introduced by poor edge position measurement. Using this technique at all discernible cross-sections provides a detailed mapping of the specimen cross-section shape along its axis as it deforms.

Assumptions about the design of the experiment that simplify the calibration have been made and their implications for the accuracy of the data have been investigated. It was found that if a lens has a very long focal length, assuming that light rays enter into it without parallax distortion, i.e. they are telecentric, does not impact significantly on the accuracy of the technique. Quantification of the error introduced by this assumption has been given. Practical methods for aligning the three camera views to determine their positions to one another exactly have been given that rely only on a cylinder of known diameter being photographed at the start of an experiment.

The technique has been applied to experiments that require very high frame rates (100,000 fps) with short exposure times (2  $\mu$ s). These experiments require expensive specialised cameras, powerful flashes and sophisticated timing, which often means that only a single camera can be used. An arrangement of mirrors has been presented that provides the functionality of three cameras and removes the need for synchronised timing.

Quantification of the errors in this measurement technique has been made through the measurement of elliptical prisms and interrupted specimens of elliptical and nearly circular cross-section that have all been independently measured using a CMM. The errors in area measurement and aspect ratio measurement have been found to lie within 1% for QS rate experiments and within 5% for HR experiments with elliptical aspect ratios up to 1.5 and within 10%

for aspect ratios less than 2.

### 8.1.4 Obtaining material data from elliptical cross-sections

Making the above measurements during uniaxial loading provides a nearly complete history of surface shape evolution during an experiment at all strain rates. With these data, an abundance of valuable information is available for inverse identification of parameters in constitutive models that can simulate anisotropic behaviour.

These measurements allow the accurate measurement of mean true axial stress in the specimens by recording the real cross-sectional area rather than assuming circularity or a fixed level of anisotropy. They also allow the tracking of the necked region in tension experiments and hence can provide data that are concerned with the most strained region in the gauge length, which have been presented in the experimental results.

Because the technique does not assume an orientation of the specimens before the experiment begins, the principal direction of anisotropy in the material can be recorded by the orientation of the elliptical shape of the cross-section. This is useful for material analysis because it can measure the orientation of the principal axes of anisotropy with respect to the principal manufacturing directions in a single experiment.

The change in major and minor radii of the cross-sections provides data on the strain in those directions. These allow the calculation of a traditional measurement of anisotropy, the ratio of width to thickness strains in sheet metals: the  $R_\theta$  ratio, and also a modification of  $R_\theta$  presented here: the R ratio. Data on CP-Zr, steel and cross-rolled Ti-6Al-4V have been presented that quantifies the R ratio at QS and HR strain rates in tension and also in compression for Ti-6Al-4V which has not been possible before now without interrupted experiments.

Given the major and minor radii of specimens as functions of axial position, the radius of curvature of the specimen profile in its principal directions can be calculated. This means that

a modified Bridgman correction can be made to calculate effective stress in the neck from the current force and the area of the elliptical section.

The cross-section measurement technique has also been applied to Taylor impact experiments in which a cylindrical specimen is fired at a rigid anvil at high speed. In the past, researchers have performed these experiments on anisotropic materials and measured the elliptically deformed surface shape post-impact, but the new technique allows the measurement to be performed *in situ*. Taylor impact experiments have found their modern-day use as a validation tool for constitutive models of high strain-rate behaviour due to the varying strain rates present in the specimen. Measuring elliptical cross-sections *in situ* extends the usefulness of these tests even further by quantifying the shape as the plastic deformation propagates through the specimen.

### 8.1.5 Surface tracking displacement measurement

The accuracy of the edge detection achieved in the QS rate images of Ti-6Al-4V specimens meant that the smooth undulations left by the lathe manufacturing were discernible in the edge profile. This created the opportunity to track the surface to measure its displacement without marking it or using laser speckle.

The significant challenges posed by the tracking problem were: firstly, the edges were subject to noise so that the shape varied from frame to frame; secondly, the frames couldn't be captured at a high enough frame rate so that the displacement was less than a period of the surface shape frequency; thirdly, the surface shape appeared very regular, so false matches were common. Solutions to these problems were developed which used a combination of predicted motion from the cross-head displacement and local filtering of maximum allowable displacements in ranges of time and axial length. This created a guided matching process which could track the dense surface features to quantify the surface displacement with a high spatial resolution.

Strain maps were calculated by averaging the high density displacement data and differentiating it to produce strain fields with a lower resolution, but still with a very high resolution when compared to the strain measurements possible with contacting extensometers or laser extensometers. The measurements were compared to the independent measurement of strain along the specimen calculated by the change in area and found to be in good agreement.

This method allows the high density measurement of displacement and strain without markings, which are required for digital image correlation (DIC), nor laser equipment. Its real advantage is that, when combined with the elliptical cross-section measurement technique, it allows the full measurement of specimen surfaces according to material positions throughout their deformation. This is especially useful when tensile specimens undergo necking and a particular cross-section cannot be compared from one frame to the next because there is no way of knowing to what shape it became.

Simultaneously measuring surface motion and cross-sectional shape provides a full description of specimen surface evolution during uniaxial loading which has not been available before now.

### 8.1.6 Mechanical behaviour of materials

The primary goals of this research have been the development of photogrammetric techniques, but a secondary goal has been the collection of improved characterisation data for cross-rolled Ti-6Al-4V plate.

Uniaxial specimens of cross-rolled Ti-6Al-4V from all three principal material directions have been loaded in compression and tension at QS and HR strain rates whilst applying the elliptical cross-section measurement technique. The ratio of transverse strains, the R ratio, has been measured for all of these types of loading.

---

The unknown thermomechanical processing that the plate had gone through left it with a textured microstructure where the HCP structure of the anisotropic  $\alpha$  grains in the material had a preferred orientation. This texture is evident in the differing initial yield stresses and flow stresses of specimens in different material directions and also in the direction of strain perpendicular to the loading axis.

The experiments performed in this research provide a mapping of the yield surface evolution for uniaxial loading of the principal material directions, which includes the strain hardening and the strain increment directions in tension *and* compression, at QS and HR loading rates. Using these material characterisation data, researchers and engineers developing constitutive models of this particular form of Ti-6Al-4V in the future can ensure that even more aspects of the mechanical behaviour are modelled.

# References

---

- [1] Matthew J. Donachie Jr. *Titanium: A technical guide*. ASM International, 2000. (document), 1.1, 1.3, 1.3
- [2] H Sarsfield. *Development of a Three Dimensional Grain Structure Submodel: Experimental Characterisation and Numerical Modelling of Ti-6Al-4V at Elevated Strain Rates*. PhD thesis, Solid Mechanics and Materials Engineering Research Group, Department of Engineering Science, University of Oxford, April 2007. (document), 1.3, 1.2, 1.3, 1.3, 1.4, 7.3.1
- [3] Ben Elliott. *Inverse Identification of Constitutive Parameters for Simulation of Impact on Rate-Dependent Media*. PhD thesis, Solid Mechanics and Materials Engineering Group, Department of Engineering Science, University of Oxford, 2006. (document), 1.11, 1.7, 7.2.1
- [4] E Wielewski, M R Arthington, C R Siviour, S Carter, F Hofmann, A M. Korsunsky, and N Petrinic. A method for the in situ measurement of evolving elliptical cross-sections in initially cylindrical taylor impact specimens. *The Journal of Strain Analysis for Engineering Design*, 2010. (document), 5.0.1, 5.18, 5.19
- [5] U. F. Kocks, C. N. Tome, and H. R. Wenk. *Texture and Anisotropy: Preferred Orientations in Polycrystals and their Effect on Materials Properties*. Cambridge University Press, 1998. 1.1, 1.3, 1.4, 1.4, 1.4.1, 1.4.1, 1.4.1, 1.6.1, 7.3.1
- [6] HS Yang, XS Su, and B Bai. Analysis of diametral strain in uniaxial tensile and compression testing of round specimens of anisotropic materials. *International journal of mechanical sciences*, 42(12):2395–, 2000. 1.1, 1.4, 1.4.1, 3.1, 5.0.1
- [7] D. S. McDermid, A. W. Bowen, and P. G. Partridge. Superplastic deformation of strongly textured ti-6 al-4 v. *Journal of Materials Science*, 19(7):2378–2386, July 1984. 1.1, 1.3, 1.4, 1.5, 3.1, 5.0.1
- [8] D A Mosher. An orthotropic flow rule for superplastic ti-6al-4v. *Mechanics of materials*, 19(1):59–, 1994. 1.1, 1.4
- [9] G. Lütjering and J.C. Williams. Titanium. In Brian Derby, editor, *Titanium*. Springer, 2007. 1.2, 1.3, 1.3
- [10] Market & Business Development. UK aerospace industry research report. Technical report, Market and Business Development, December 2006. 1.2
- [11] J. Esslinger. Titanium in aero engines. In G. Lütjering, editor, *Proceedings of the 10th World Conference on Titanium*. Wiley-VCH, Weinheim, Germany, 2003. 1.2
- [12] M. Peters, J. Kumpfert, C.H. Ward, and C. Leyens. Titanium alloys for aerospace applications. *Advanced Engineering Materials*, 5(6):419–427, 2003. 1.2
- [13] V.A. Joshi. *Titanium Alloys: An Atlas of Structures and Fracture Features*. Taylor & Francis, Boca Raton, FL, 2006. 1.3

- [14] R Filip. The effect of microstructure on the mechanical properties of two-phase titanium alloys. *Journal of materials processing technology*, 133(1-2):84–, 2003. 1.3
- [15] TIMET. Timet, birmingham/swansea, 2010. Internal literature. 1.3
- [16] I J Polmear. Light alloys metallurgy of the light metals. In Robert Honeycombe and Peter Hancock, editors, *Light Alloys Metallurgy of the Light Metals*. Arnold, 1995. 1.3
- [17] M. R. Bache and W. J. Evans. Impact of texture on mechanical properties in an advanced titanium alloy. *Materials Science and Engineering A*, 319-321:409 – 414, 2001. 1.3
- [18] Y. N. Wang and J. C. Huang. Texture analysis in hexagonal materials. *Materials Chemistry and Physics*, 81(1):11 – 26, 2003. 1.3
- [19] I. Dyson, P. Duo, and N. Petrinic. Deformation and failure of ti64 cross-rolled material, under uniaxial tension and compression at three distinct rates of strain and in three orthogonal directions. UTC report 230, Solid Mechanics Group, Oxford University, 2006. 1.3, 1.4, 1.4, 1.5
- [20] von Mises, R. Mechanics of the plastic deformation of crystals. *Z. Angew. Math. Mech.*, 8:161–185, 1928. 1.4
- [21] R. Hill. A theory of the yielding and plastic flow of anisotropic metals. *Proceedings of the Royal Society of London. Series A, Mathematical and Physical Sciences*, 193(1033):281–297, 1948. 1.4, 1.4.1
- [22] J.L. Bassani. Yield characterization of metals with transversely isotropic plastic properties. *International Journal of Mechanical Sciences*, 19(11):651 – 660, 1977. 1.4, 1.4.1
- [23] F. Barlat and K. Lian. Plastic behavior and stretchability of sheet metals. part i: A yield function for orthotropic sheets under plane stress conditions. *International Journal of Plasticity*, 5(1):51 – 66, 1989. 1.4
- [24] Oana Cazacu, Brian Plunkett, and Frdric Barlat. Orthotropic yield criterion for hexagonal closed packed metals. *International Journal of Plasticity*, 22(7):1171 – 1194, 2006. 1.4, 7.3.1
- [25] W.T. Lankford, S.C. Snyder, and J.A. Bauscher. New criteria for predicting the press performance of deep drawing steels. *Trans. Am. Soc. Metals*, 42:1197, 1950. 1.4.1
- [26] S P KEELER and W A BACKOFEN. Plastic instability and fracture in sheets stretched over rigid punches. *ASM TRANS*, 56:25–48, 1963. 1.4.1
- [27] J. Chakrabarty. *Applied Plasticity, Second Edition*. Springer, 2010. 1.4.1, 1.4.1
- [28] Astm e517-00(2006), "Standard Test Method for Plastic Strain Ratio r for Sheet Metal", 2006. 1.4.1, 1.4.1, 7.1
- [29] W.F. Hosford and W.A. Backofen. Fundamentals of deformation processing,. *Syracuse U. Press*, page 259298, 1964. 1.4.1
- [30] Richard Gedney. Measuring the plastic strain ratio of sheet metals. *The Fabricator*, June 2006. 1.4.1
- [31] Todd M Osman. *ASM Handbook*, volume 8, page 3:12. American Society for Metals, 12 edition, 2000. 1.4.1, 3.1
- [32] H et al Sarsfield. An experimental investigation of rate-dependent deformation and failure of three titanium alloys. *Journal of materials science*, 42(13):5085–, 2007. 1.5

- [33] A. Majorell, S. Srivatsa, and R. C. Picu. Mechanical behavior of ti-6al-4v at high and moderate temperatures—part i: Experimental results. *Materials Science and Engineering A*, 326(2):297–305, March 2002. 1.5
- [34] E. El-Magd and M. Abouridouane. Characterization, modelling and simulation of deformation and fracture behaviour of the light-weight wrought alloys under high strain rate loading. *International Journal of Impact Engineering*, 32(5):741–758, May 2006. 1.5
- [35] P. Follansbee and G. Gray. An analysis of the low temperature, low and high strain-rate deformation of ti-6al-4v. *Metallurgical and Materials Transactions A*, 20:863–874, 1989. 10.1007/BF02651653. 1.5
- [36] Woei-Shyan Lee and Chi-Feng Lin. Plastic deformation and fracture behaviour of ti-6al-4v alloy loaded with high strain rate under various temperatures. *Materials Science and Engineering A*, 241(1-2):48–59, January 1998. 1.5
- [37] L. Wang N. Petrinic. Deformation and failure of ti6/4 specimens subjected to uniaxial tensile loading at three distinct rates of strain. UTC report 168, Solid Mechanics Group, Oxford University, 2001. 1.5
- [38] C. Ingelbrecht and P. Partridge. Superplastic deformation of sheet test pieces machined from ti-6al-4v bar. *Journal of Materials Science*, 21:4071–4080, 1986. 10.1007/BF02431654. 1.5
- [39] C. R. Siviour. *High Strain Rate Properties of Materials Using Hopkinson Bar Techniques*. PhD thesis, Cambridge University, 2005. 1.6
- [40] N. A. Safford. *High Strain Rate Studies with the Direct Impact Hopkinson Bar*. PhD thesis, Cambridge University, 1988. 1.6
- [41] D. R. Drodge. *Mechanical properties of energetic composites*. PhD thesis, Cambridge University, 2009. 1.6
- [42] John M. Holt. *Mechanical Testing and Evaluation*, volume 8 of *ASM Handbook*, chapter Introduction to Mechanical Testing and Evaluation, pages 125–142. ASM International, 2000. 1.6, 1.6.2, 7.1
- [43] PW Bridgman. The stress distribution at the neck of a tension specimen. *Collected experimental papers*, 1964. Harvard University Press. 1.6
- [44] C G'Sell. Video-controlled tensile testing of polymers and metals beyond the necking point. *Journal of materials science*, 27(18):5031–, 1992. 1.6, 3.1
- [45] Martin A. Eisenberg. Anisotropic tensile necking. *International Journal of Plasticity*, 1(1):29 – 38, 1985. 1.6, 1.6, 3.1
- [46] C.S. Hartley, M.A. Eisenberg, D.A. Jenkins, E. Unal, R. Srinivasan, J.J. Lee, and C.F. Yen. Properties of reactor materials at constant true strain rates. Technical Report CR-0235, NUREG, 1981. 1.6, 3.1
- [47] Howard Kuhn. *Mechanical Testing and Evaluation*, volume 8 of *ASM Handbook*, chapter Introduction to Mechanical Testing and Evaluation, pages 143–151. ASM InternationalS, 2000. 1.6.1
- [48] R.S. Hartley, T.J. Cloete, and G.N. Nurick. An experimental assessment of friction effects in the split hopkinson pressure bar using the ring compression test. *International Journal of Impact Engineering*, 34(10):1705 – 1728, 2007. 1.6.1

- [49] Joel W. House and Peter P. Gillis. *Mechanical Testing and Evaluation*, volume 8 of *ASM Handbook*, chapter Testing Machines and Strain Sensors, pages 79–92. ASM International, 2000. 1.6.2, 1.6.2, 1.6.2
- [50] John L. Green, James F. Emslie, and Shun-Chin Chou. The application of laser speckle interferometry to measure strain at elevated temperatures and various loading rates. Technical report, ARMY LAB COMMAND WATERTOWN MA MATERIAL TECHNOLOGY LAB, 1990. 1.6.2
- [51] Kaliat T. Ramesh. *Springer handbook of experimental solid mechanics*, chapter High Rates and Impact Experiments, pages 929–945. Springer, Berlin, 2008. 1.6.2, 1.6.2
- [52] G. Gray. *ASM Handbook*, volume 8, chapter Classic Split-Hopkinson Pressure Bar Testing, page 462:476. American Society for Metals, 12 edition, 2000. 1.6.2
- [53] B. Hopkinson. A method of measuring the pressure produced in the detonation of explosives or by the impact of bullets. *Philos. Trans. A*, 213:437, 1914. 1.6.2
- [54] R.M Davies. A critical study of the hopkinson pressure bar. *Philos. Trans. R. Soc. (London)*, 240:375, 1949. 1.6.2
- [55] H. Kolsky. An investigation of the mechanical properties of materials at very high rates of loading. *Proc. R. Soc. (London)*, 62:676, 1949. 1.6.2
- [56] J. Harding and L. M. Welsh. Tensile testing technique for fibre-reinforced composites at impact rates of strain. *Journal of Materials Science*, 18:1810–26, 1983. 1.6.2
- [57] J Sharpe and N William, editors. *Springer handbook of experimental solid mechanics*. Springer, Berlin, 2008. 1.7
- [58] J Canny. A computational approach to edge detection. *IEEE Trans. Pattern Anal. Mach. Intell.*, 8(6):679–698, 1986. 2.1
- [59] C.G. Harris and M. Stephens. A combined corner and edge detector. *4th Alvey Vision Conference*, 24(6):147151, 1988. 2.1
- [60] J.M.S. Object enhancement and extraction. *Picture Processing and Psychopictorics*, page 75149., 1970. Academic Press, New York. 2.1
- [61] Stephen M. Smith and J. Michael Brady. Susan - a new approach to low level image processing. *Int. J. Comput. Vision*, 23(1):45–78, 1997. 2.1
- [62] Ali J. Tabatabai and O. Robert Mitchell. Edge location to subpixel values in digital imagery. *Pattern Analysis and Machine Intelligence, IEEE Transactions on*, PAMI-6(2):188–201, march 1984. 2.1
- [63] Jian Ye, Gongkang Fu, and Upendra P. Poudel. High-accuracy edge detection with blurred edge model. *Image and Vision Computing*, 23(5):453 – 467, 2005. 2.1
- [64] C Steger. An unbiased detector of curvilinear structures. *IEEE transactions on pattern analysis and machine intelligence*, 20(2):113–, 1998. 2.1
- [65] C Steger. Subpixel-precise extraction of lines and edges. *International Archives of Photogrammetry and Remote Sensing*, XXXIII:141–156, 2000. 2.1
- [66] J. P. Lewis. Fast normalized cross-correlation. In *Vision Interface*, pages 120–123. Canadian Image Processing and Pattern Recognition Society, 1995. 2.1.1
- [67] R. I. Hartley and A. Zisserman. *Multiple View Geometry in Computer Vision*. Cambridge University Press, ISBN: 0521540518, second edition, 2004. 2.2, 2.2.2, 2.2.5, 3.2.2, 3.2.3

- [68] Arin Jumpasut, Nik Petrinic, Ben C.F. Elliott, Clive R. Siviour, and Matthew R. Arthington. An error analysis into the use of regular targets and target detection in image analysis for impact engineering. *Applied Mechanics and Materials (Volumes 13 - 14)*, Advances in Experimental Mechanics VI:203–210, July 2008. 2.2.4
- [69] Gergely Vassy and Tams Perlaki. Applying and removing lens distortion in post production. In *The Second Hungarian Conference on Computer Graphics and Geometry*, 2003. 2.2.5
- [70] Jean-Yves Bouguet. Camera calibration toolbox for matlab. [http://www.vision.caltech.edu/bouguetj/calib\\_doc/](http://www.vision.caltech.edu/bouguetj/calib_doc/) accessed on 09/01/2009, 2009. 2.2.5
- [71] Holger Aretz, Odd Sture Hopperstad, and Odd-Geir Lademo. Yield function calibration for orthotropic sheet metals based on uniaxial and plane strain tensile tests. *Journal of Materials Processing Technology*, 186(1-3):221–235, May 2007. 3.1
- [72] P. D. Alevizos, J. Boissonnat, and M. Yvinec. An optimal  $O(n \log n)$  algorithm for contour reconstruction from rays. In *SCG '87: Proceedings of the third annual symposium on Computational geometry*, pages 162–170, New York, NY, USA, 1987. ACM. 3.1
- [73] Katia Genovese and Carmine Pappalettere. Whole 3d shape reconstruction of vascular segments under pressure via fringe projection techniques. *Optics and Lasers in Engineering*, 44(12):1311–1323, December 2006. 3.1
- [74] G T Gullberg, B M W Tsui, C R Crawford, and E R Edgerton. Estimation of geometrical parameters for fan beam tomography. *Physics in Medicine and Biology*, 32(12):1581–1594, 1987. 3.1
- [75] T. J. Wynn and S. A. Stewart. Comparative testing of ellipse-fitting algorithms: Implications for analysis of strain and curvature. *Journal of Structural Geology*, 27:1973–1985, 2005. 3.2.3
- [76] Walter Gander, Gene H. Golub, and Rolf Strebler. Least-squares fitting of circles and ellipses. *BIT Numerical Mathematics*, 34(4):558–578, December 1994. 3.2.3, 3.2.3
- [77] A. Fitzgibbon, M. Pilu, and R.B. Fisher. Direct least square fitting of ellipses. *Transactions on Pattern Analysis and Machine Intelligence*, 21(5):476–480, May 1999. 3.2.3, 6.3
- [78] Radim Halir and Jan Flusser. Numerically stable direct least squares fitting of ellipses. *WSCG'98, The 6th International Conference in Central Europe on Computer Graphics, Visualization'98*:125–132, 1998. 3.2.3, 3.3.1
- [79] T.H. Eagles. *Constructive Geometry of Plane Curves*. Macmillan and Co., 1885. 3.2.3
- [80] Paul L. Rosin. A note on the least squares fitting of ellipses. *Pattern Recogn. Lett.*, 14(10):799–808, 1993. 3.2.3
- [81] Michael A. Sutton, Jean-Jos Orteu, and Hubert Schreier. *Image Correlation for Shape, Motion and Deformation Measurements*. Springer Science+Business Media, LLC, 2009. 4.1
- [82] F. Hild and S. Roux. Digital image correlation: From displacement measurement to identification of elastic properties—a review. *Strain*, 42(2):69–, 2006. 4.1
- [83] J Sharpe and N William, editors. *Springer handbook of experimental solid mechanics*. Springer, Berlin, 2008. 4.1, 5.5
- [84] R. J. Adrian. Twenty years of particle image velocimetry. *Experiments in Fluids*, 39(2):159–169, August 2005. 4.1

- [85] P Jacquot. Speckle interferometry: a review of the principal methods in use for experimental mechanics applications. *Strain*, 44(1):57–, 2008. 4.1
- [86] V. Tiwari, M. Sutton, and S. McNeill. Assessment of high speed imaging systems for 2d and 3d deformation measurements: Methodology development and validation. *Experimental Mechanics*, 47(4):561–579, August 2007. 4.1
- [87] MA Sutton, WJ Wolters, WH Peters, WF Ranson, and SR McNeill. Determination of displacements using an improved digital correlation method. *Image and Vision Computing*, 1(3):133 – 139, 1983. 4.1
- [88] Andrew Blake and M. Isard. *Active Contours: The Application of Techniques from Graphics, Vision, Control Theory and Statistics to Visual Tracking of Shapes in Motion*. Springer-Verlag New York, Inc., Secaucus, NJ, USA, 1998. 4.1
- [89] Alper Yilmaz, Omar Javed, and Mubarak Shah. Object tracking: A survey. *ACM Comput. Surv.*, 38(4):13, 2006. 4.1
- [90] John MacCormick. *Stochastic Algorithms for Visual Tracking: Probabilistic Modelling and Stochastic Algorithms for Visual Localisation and Tracking*. Springer-Verlag New York, Inc., Secaucus, NJ, USA, 2002. 4.1
- [91] The MathWorks Inc. *MATLAB manual*. Natick, Massachusetts, USA, 7.7.0.47 (r2008b) edition, 2010. 4.2.1, 4.2.4
- [92] Martin A. Fischler and Robert C. Bolles. Random sample consensus: a paradigm for model fitting with applications to image analysis and automated cartography. *Commun. ACM*, 24(6):381–395, 1981. 4.3
- [93] B.J. Tordoff and D.W. Murray. Guided-MLESAC: Faster image transform estimation by using matching priors. *IEEE Transactions on Pattern Analysis and Machine Intelligence*, 27(10), oct 2005. 4.3
- [94] P.L. Rittenhouse and M.L. Picklesimer. Metallurgy of zircaloy-2. part ii. the effects of fabrication variables on the preferred orientation and anisotropy of strain behavior. Technical Report ORNL-2948, Oak Ridge National Lab., Tenn, February 1961. 5.0.1, 5.1
- [95] Geoffrey Taylor. The use of flat-ended projectiles for determining dynamic yield stress. i. theoretical considerations. *Proceedings of the Royal Society of London. Series A, Mathematical and Physical Sciences*, 194(1038):pp. 289–299, 1948. 5.0.1, 5.5
- [96] J. E. Field, S. M. Walley, W. G. Proud, H. T. Goldrein, and C. R. Siviour. Review of experimental techniques for high rate deformation and shock studies. *International Journal of Impact Engineering*, 30(7):725 – 775, 2004. Fifth International Symposium on Impact Engineering. 5.5
- [97] P. J. Maudlin, G. T. Gray, C. M. Cady, and G. C. Kaschner. High-rate material modelling and validation using the taylor cylinder impact test. *Philosophical Transactions: Mathematical, Physical and Engineering Sciences*, 357(1756):pp. 1707–1729, 1999. 5.5
- [98] B. Plunkett, O. Cazacu, R.A. Lebensohn, and F. Barlat. Elastic-viscoplastic anisotropic modeling of textured metals and validation using the taylor cylinder impact test. *International Journal of Plasticity*, 23(6):1001 – 1021, 2007. 5.5
- [99] D A Gorham. A simple technique to improve frame filling in the high-speed photographic recording of symmetrical events. *Journal of Physics E: Scientific Instruments*, 15(5):562, 1982. 7.3.2